

UNIVERSITY OF CALIFORNIA, SAN DIEGO

Investigations of fault creep in southern California using Interferometric Synthetic  
Aperture Radar and GPS

A dissertation submitted in partial satisfaction of the requirements for the Doctor  
of Philosophy in Earth Sciences

by

Suzanne N. Lyons

Committee in charge:

David T. Sandwell, Chair  
Duncan Agnew  
Yehuda Bock  
Kevin Brown  
Xanthippi Markenscoff  
Robert Parker

2002

The dissertation of Suzanne Noelle Lyons is approved, and it is acceptable in quality and form for publication on microfilm:

---

---

---

---

---

---

---

Chair

University of California, San Diego

2002

This dissertation is dedicated to the members of my family, who have always encouraged me to hold on to my dreams and reach for the stars.

"Mercy!" cried Gandalf. "If the giving of information is to be the cure of your inquisitiveness, I shall spend all the rest of my days answering you. What more do you want to know?"  
"The names of all the stars, and of all living things, and the whole history of Middle-earth and Over-heaven and of the Sundering Seas," laughed Pippin. "Of course! What less?"

- J.R.R. Tolkein, *The Return of the King*

## TABLE OF CONTENTS

Signature Page .....	iii
Dedication .....	iv
Epigraph .....	v
Table of Contents .....	vi
List of Figures .....	x
List of Tables .....	xiv
Acknowledgements.....	xv
Vita .....	xviii
Abstract .....	xxii
Chapter 1. An introduction to creep mechanisms, GPS processing and Synthetic Aperture Radar Interferometry .....	1
1.1 Earthquake Prediction.....	1
1.2 The Earthquake Cycle.....	4
1.3 Fault Creep.....	7
1.4 The Global Positioning System (GPS) .....	13
1.4.1 The History of GPS.....	13
1.4.2 How GPS Works.....	15
1.4.3 Error Sources and Corrections .....	18
1.4.4 GPS Applications.....	29
1.5 Radar Systems.....	30
1.5.1 Imaging Radar.....	30
1.5.2 Synthetic Aperture Radar (SAR) .....	36

1.5.3 Synthetic Aperture Radar Interferometry (InSAR).....	44
1.5.4 InSAR Geometry .....	45
1.5.5 Interferometric Errors .....	52
1.5.6 Applications for Interferometry .....	55
1.6 References.....	58
Chapter 2. Creep along the Imperial Fault, Southern California, from GPS measurements.....	62
2.1 Abstract.....	62
2.2 Introduction.....	63
2.3 GPS Methods .....	67
2.4 The Imperial College Network .....	70
2.5 Data Processing.....	72
2.6 Method .....	74
2.7 Results.....	76
2.8 Fault Models .....	82
2.9 Discussion.....	87
2.10 Conclusions.....	90
2.11 Acknowledgements.....	91
2.12 References.....	92
Chapter 3. Fault creep along the southern San Andreas from InSAR, permanent scatterers, and stacking .....	98
3.1 Abstract.....	98
3.2 Introduction.....	99

3.3	Southern San Andreas Fault and Synthetic Aperture Radar.....	100
3.4	Permanent Scatterers.....	105
3.5	Stacking Interferograms.....	115
3.6	Results.....	117
3.7	Fault Models .....	135
3.8	Discussion.....	138
3.9	Atmospheric Effects.....	143
3.10	Conclusions.....	154
3.11	Acknowledgements.....	155
3.12	References.....	155
	Appendix 3.A. Permanent Scatterers - Salton Sea Photo Survey.....	160
	3.A.1 Survey Overview.....	160
	3.A.2 Southeast Region.....	162
	3.A.3 Central Region .....	162
	3.A.4 Northwest Region .....	169
	3.A.5 Northeast Region.....	172
	3.A.6 Conclusions.....	175
	3.A.7 References.....	177
Chapter 4.	Conclusions .....	178
4.1	Fault Creep on California Faults.....	178
4.2	Northern California Faults .....	184
4.3	Central Creeping Section .....	185
4.4	Southern California Faults .....	188

4.5	Conclusions.....	194
4.6	References.....	195
Chapter 5.	3-D estimation of elastic thickness under the Louisville Ridge.....	197
5.1	Abstract.....	197
5.2	Introduction.....	198
5.3	Flexure Theory.....	202
5.4	Method.....	210
5.5	Results and Discussion.....	214
5.6	Conclusions.....	230
5.7	Acknowledgements.....	232
5.8	References.....	232
Epilogue	.....	237

## LIST OF FIGURES

### Chapter 1.

Figure 1.1	Simple earthquake recurrence models .....	6
Figure 1.2	Time history of Parkfield, California, earthquakes .....	8
Figure 1.3	Creep record at the Cienega Winery .....	11
Figure 1.4	Creep retardation near Hollister, California .....	12
Figure 1.5	The basics of GPS .....	16
Figure 1.6	The single difference method .....	20
Figure 1.7	The double difference method .....	21
Figure 1.8	The triple difference method .....	23
Figure 1.9	GPS signal delay due to atmospheric effects .....	24
Figure 1.10	Geometric Dilution of Precision (GDOP) .....	27
Figure 1.11	Multipath effects.....	28
Figure 1.12	The electromagnetic spectrum.....	32
Figure 1.13	Geometry of an imaging radar .....	33
Figure 1.14	Ground range vs. slant range.....	34
Figure 1.15	Diagram of a Synthetic Aperture Radar .....	38
Figure 1.16	Typical backscattering characteristics for various surfaces .....	41
Figure 1.17	Layover and shadowing in SAR images .....	42
Figure 1.18	SAR amplitude image of the Coachella Valley.....	43
Figure 1.19	Geometry of the interferometer .....	46
Figure 1.20	Interferogram of the Coachella Valley .....	48
Figure 1.21	Geometry of InSAR with ground deformation.....	50

Figure 1.22	Interferogram of the Coachella Valley with curvature removed .....	51
Figure 1.23	Deformation interferogram of the Coachella Valley .....	53
Figure 1.24	The limitations of detection using InSAR .....	57

**Chapter 2.**

Figure 2.1	The Salton Sea and Imperial Valley, southern California .....	65
Figure 2.2	Imperial Valley survey sites, 1991-2000.....	71
Figure 2.3	Independent single-epoch solutions for baseline between site S35 and Holt base station.....	77
Figure 2.4	Average horizontal velocities between 1993 and 2000 .....	78
Figure 2.5	Site positions for 1993, 1999, and 2000 with best-fit lines .....	79
Figure 2.6	Average fault-parallel and fault-normal velocities, 1993-2000 .....	80
Figure 2.7	Elastic dislocation model .....	84
Figure 2.8	RMS misfit for models with various parameters.....	85
Figure 2.9	Minimum misfit models vs. observations .....	86
Figure 2.10	Strain rate estimates for various fault models .....	88

**Chapter 3.**

Figure 3.1	Seismicity in the Coachella Valley .....	102
Figure 3.2	Available ERS-1/2 images for the Coachella Valley .....	103
Figure 3.3	Interferograms showing effect of permanent scatterers .....	106
Figure 3.4	Permanent scatterer weights for 37 descending ERS images .....	110
Figure 3.5	Correlation improvement from permanent scatterers.....	113
Figure 3.6	Average LOS interseismic creep velocities, 1993-1999 .....	116
Figure 3.7	Unwrapped LOS velocities spanning Landers .....	121

Figure 3.8	Profiles of Landers displacement from InSAR .....	125
Figure 3.9	Profiles of Interseismic velocities from InSAR.....	127
Figure 3.10	Profiles of Hector Mine velocities from InSAR.....	129
Figure 3.11	Triggered slip from Landers.....	132
Figure 3.12	Triggered slip from Hector Mine .....	133
Figure 3.13	Elastic dislocation model .....	134
Figure 3.14	RMS misfit for interseismic velocity models.....	137
Figure 3.15	Residual interferogram showing atmospheric noise.....	146
Figure 3.16	Residual interferogram showing atmospheric noise.....	148
Figure 3.17	Residual interferogram showing atmospheric noise.....	151
Figure 3.18	Interferogram showing atmospheric noise from topography .....	152

**Appendix 3.A.**

Figure 3.A.1	Average amplitude of Salton Sea side-look complex stack .....	161
Figure 3.A.2	Scattering amplitude of Salton Sea side-look complex stack.....	163
Figure 3.A.3	Southeast Salton survey region.....	164
Figure 3.A.4	Photos of sites 1-3, southeast survey region .....	165
Figure 3.A.5	Photos of sites 4 and 5, southeast survey region .....	166
Figure 3.A.6	Central Salton survey region .....	167
Figure 3.A.7	Photos of sites 6, 7, and 13, central survey region .....	168
Figure 3.A.8	Northwest Salton survey region .....	170
Figure 3.A.9	Photos of sites 8-10, northwest survey region.....	171
Figure 3.A.10	Northeast Salton survey region.....	173
Figure 3.A.11	Photos of sites 11, 12, and 14, northeast survey region.....	174

Figure 3.A.12 Photos of site 15, northeast survey region..... 175

**Chapter 4.**

Figure 4.1 Major faults in California ..... 180

Figure 4.2 Spatial resolution of various creep detectors ..... 181

Figure 4.3 LOS displacement along the Hayward Fault from InSAR..... 186

Figure 4.4 Interferogram of creep near Parkfield, California ..... 187

Figure 4.5 Interferograms of creep near Parkfield, California..... 189

Figure 4.6 Effects of permanent scatterers and filtering on interferograms of  
creep near Parkfield, California ..... 191

Figure 4.7 Inteferogram of creep on Superstition Hills Fault ..... 193

**Chapter 5.**

Figure 5.1 Gravity anomaly over the Louisville Ridge system ..... 199

Figure 5.2 Gravity signal due to a model seamount ..... 204

Figure 5.3 Effects of considering nonlinearity and three-dimensionality in  
gravity models..... 207

Figure 5.4 Spatial coverage of satellite data vs. ship tracks for region G..... 211

Figure 5.5 Nonlinear contribution of topography to the gravity anomaly..... 215

Figure 5.6 RMS misfit for region G vs. crustal density and elastic thickness... 216

Figure 5.7 RMS misfit for each region of the Louisville Ridge ..... 220

Figure 5.8 Elastic thickness vs. age at time of loading..... 223

Figure 5.9 Topographic prediction vs. bathymetry for profile 12 ..... 226

Figure 5.10 Real vs. predicted bathymetry for region G ..... 228

## LIST OF TABLES

### **Chapter 3.**

Table 3.1 Atmospheric error statistics for all interferograms ..... 118

Table 3.2 Atmospheric error statistics for grouped interferograms ..... 120

Table 3.3 Comparison of creep rates for the southern SAF, 1967-2000 ..... 141

### **Chapter 5.**

Table 5.1 Best fitting elastic thickness values ..... 222

Table 5.2 Minimum RMS misfit values within each region..... 231

## ACKNOWLEDGEMENTS

There are so many people who have helped me to get to this point that to mention them all would take almost as many pages as the dissertation itself. First and foremost, I'd like to thank my advisor and committee chair, David Sandwell. From the first day I arrived at Scripps to find him heading toward the beach with a surfboard tucked under one arm, I knew I'd come to the right place. His encouragement and enthusiasm over the last five and a half years have kept me motivated and excited about not only my research, but science in general. He and Yehuda Bock, also my advisor at Scripps, have been completely understanding of all of my endeavors, even when it meant taking off a month here and there to travel to the ocean floor "just because" or to join the Naval Reserves out of a sense of duty to my country. I am indebted to both of them for letting me run on a very, very long leash so that I could explore numerous aspects of both life and scientific research.

I would also like to acknowledge the other members of my dissertation committee, who have all helped me immensely over the past few years. Duncan Agnew and Bob Parker have been with me since the beginning, trying to persuade some of their infinite wisdom to stick in my pea brain. I am sure I have frustrated them almost as much as their homework did to me during my first year. Kevin Brown and Xanthippi Markenscoff sat patiently through long discussions of InSAR, permanent scatterers, and other topics that must have seemed terribly

foreign to them, yet always seemed to ask quality questions that made me stop and think.

I would not have come this far if it hadn't been for my fellow "first-years," Dave McMillan, Eric Hallenborg, and Linda Warren. Those long nights at the chalkboard in the Keller with potluck rice dishes and lots of caffeine will always hold a dear place in my heart. Thanks for the great memories of such a tough time. Dave, thanks for going with me to the hockey games and encouraging me to follow through with what has become one of my main obsessions.

My "labmates" (Bridget Smith, Karen Watson, Lydie Sychoix, Allison Jacobs, and Davis Thomsen) have all managed to keep the Sandwell Lab a lighthearted and relatively laid back place to live and work, and for that I'm eternally grateful. Bridget and Karen, thank you for always being there for a shoulder to lean on or an ear to talk to. I am thankful to call you my friends.

Outside of Scripps, I spent most of my "off time" either boxing or playing hockey. Through this, I have met some of my closest and most treasured friends. At the top of this list is Paul Vaden, who was not only my boxing coach, but my dodgeball partner, my mentor, my psychiatrist, my taskmaster, and, above all else, my friend. Through the last three years of hockey, I have kept my sanity spending most of my time with players from the Heartbreakers, Warriors, P fury, Hurricanes, Ms. Conduct, and numerous other ice and roller hockey teams that I've played with at some time or other. I honestly cannot imagine a better way to spend my Sunday nights, Monday nights, Tuesday nights, Wednesday nights...

Most of all, I want to say thank you to the countless number of people who have continuously encouraged me to pursue my dreams these last twenty-eight years of my life. Family, friends, colleagues, advisors, teachers, teammates...I feel very fortunate to have a strong support network of such caring people. Thank you to all of you. You know who you are.

The text of Chapters Two, Three, and Five, in full, are reprints of the material as it appears in the *Journal of Geophysical Research*. The dissertation author was the primary researcher and author on each of these and the co-authors listed directed and supervised the research that forms the basis for these chapters.

## VITA

- 1994 Summer Research Intern, Lunar and Planetary Institute, Houston, Texas
- 1995 Summer Research Intern, Goddard Space Flight Center, Greenbelt, Maryland
- 1996 Summer Research Intern, University of Hawaii
- 1997 B.S. *cum laude*, Texas A&M University
- 1997-2002 Research Assistant, Scripps Institution of Oceanography, University of California, San Diego
- 2000 Teaching Assistant, Scripps Institution of Oceanography, University of California, San Diego
- 2002 Ph.D., University of California, San Diego

## PUBLICATIONS

- Lyons, S.N. and D.T. Sandwell, Fault creep along the southern San Andreas from InSAR, permanent scatterers, and stacking, in press, *J. Geophys. Res.*, 2002.
- Lyons, S.N., Y. Bock, and D.T. Sandwell, Creep along the Imperial Fault, Southern California, from GPS Measurements, in press, *J. Geophys. Res.*, 2002.
- Lyons, S.N., Y. Bock, and D.T. Sandwell, Near-field deformation of the Imperial Valley, Southern California, from GPS and InSAR measurements, *Vistas for Geodesy in the New Millennium: Proceedings of the IAG 2001 Scientific Assembly, Budapest, Hungary*, (eds. J. Adams and K.P. Schwarz), Heidelberg: Springer-Verlag, 2002.
- Hart, S.R., H. Staudigel, A.A.P. Koppers, J. Blusztajn, E.T. Baker, R. Workman, M. Jackson, E. Hauri, M. Kurz, K. Sims, D. Fornari, A. Saal, and S. Lyons, Vailulu'u undersea volcano: The new Samoa, *Geochem. Geophys. Geosyst.*, 1, Paper number 2000GC000108, December 8, 2000.
- Lyons, S.N., D.T. Sandwell, and W.H.F. Smith, 3-D estimation of elastic thickness under the Louisville Ridge, *J. Geophys. Res.* 105, 13,239-13,252, 2000.
- Herrick, R.R. and S.N. Lyons, Inversion of crater morphometric data to gain insight on the cratering process, *Meteoritics Planet. Sci.* 33, 131-143, 1998.

Wessel, P. and S.N. Lyons, Distribution of large Pacific seamounts from Geosat/ERS-1: Implications for the history of intraplate volcanism, *J. Geophys. Res.* 102, B10, 22,459-22,475, 1997.

Herrick, R.R., V.L. Sharpton, M.C. Malin, S.N. Lyons, and K. Feely, Morphology and Morphometry of Impact Craters. In *Venus II* (eds. S.W. Bougher, D.M. Hunten, and R.J. Phillips), pp. 1015-1046. Tucson: University of Arizona Press, 1996.

#### ABSTRACTS

Blackman, D.K., S.N. Lyons, J. Cann, and J. Morgan, Morphology of a 9 Myr old Oceanic Core Complex: Mid Atlantic Ridge 30°N, 43°W, *Eos Trans. AGU, Fall Meet. Suppl.*, 83, 2002.

Lyons, S.N. and D.T. Sandwell, Evidence for episodes of shallow creep along the southern San Andreas Fault, *Eos Trans. AGU, Fall Meet. Suppl.*, 82, 2001.

Lyons, S.N., Y. Bock, and D.T. Sandwell, Near-field deformation and creep characteristics in the Imperial Valley, *Eos Trans. AGU, Fall Meet. Suppl.*, 81 (poster), 2000.

Lyons, S.N., Y. Bock, and R. Nikolaidis, Rapid static GPS surveys of the Imperial Fault, Southern California, *Eos Trans. AGU, Fall Meet. Suppl.*, 80:F268 (poster), 1999.

Hart, S.R., H. Staudigel, M.D. Kurz, J. Blusztajn, R. Workman, A. Saal, A. Koppers, E.H. Hauri, S.N. Lyons, Fa'afafine volcano: The active Samoan hotspot, *Eos Trans. AGU, Fall Meet. Suppl.*, 80:F1102, 1999.

Phipps Morgan, J., W. Weinrebe, C. Kopp, E.R. Flueh, I. Grevemeyer, H. Borus, R. Hekinian, C.E. Larsen, H. Lelgemann, S.N. Lyons, W.J. Morgan, J. O'Connor, Y. Pan, T. Stender, F. Wolter, Morphology and structure of two 400 km-long volcanic ridges in the Musicians seamount province, *Eos Trans. AGU, Fall Meet. Suppl.*, 80:F1062 (poster), 1999.

Lyons, S.N. and D.T. Sandwell, Elastic thickness under en echelon ridges in the Pacific, *Eos Trans. AGU, Fall Meet. Suppl.*, 79:F919, 1998.

Lyons, S.N. and P. Wessel, Determination of seamount distribution on the Pacific Plate from satellite altimetry, *Eos Trans. AGU, Fall Meet. Suppl.*, 77:F315 (poster), 1996.

Frey, H.V., B.G. Bills, S.N. Lyons, and J.H. Roark, Regional crustal thickness variations on Mars, *Proc. Lunar Planet. Sci. Conf. XXVII*, 381-382, 1996.

Lyons, S.N., H.V. Frey, B.G. Bills, and J.H. Roark, Mars crustal thickness models from Mars50c and GMM-1, *Proc. Lunar Planet. Sci. Conf. XXVII*, 789-790, 1996.

Lyons, S.N., H.V. Frey, B.G. Bills, and J.H. Roark, Crustal thickness models for Mars from GMM-1 and Mars50c, *Eos Trans. AGU, Fall Meet. Suppl.*, 76:F331 (poster), 1995.

Herrick, R.R. and S.N. Lyons, Inversion of impact crater morphometric data, *Proc. Lunar Planet. Sci. Conf. XXVI*, 587-588, 1995.

## FIELDS OF STUDY

Major Field: Earth Science (Geophysics)

Studies in Applied Mathematics

Professors Robert Parker, Glen Ierley, and Jason Phipps-Morgan

Studies in Digital Signal Processing

Professor William Hodgekiss

Studies in Geodynamics

Professors David Sandwell and Jason Phipps-Morgan

Studies in Geophysical Data Analysis

Professors Duncan Agnew and Cathy Constable

Studies in Geophysical Inverse Theory

Professor Robert Parker

Studies in Gravity and Geomagnetism

Professors Robert Parker and Cathy Constable

Studies in Physics of Earth Materials

Professor Duncan Agnew

Studies in Precise Real-Time Positioning and GPS

Professor Yehuda Bock

Studies in Satellite Remote Sensing

Professor David Sandwell

Studies in Seismology

Professor Peter Shearer

Studies in Spatial Referencing and Geodesy and Earthquake Geodesy  
Professor Yehuda Bock

Studies in Earthquake Geodesy  
Professor Yehuda Bock

Studies in Tectonics of the Planets  
Professor Catherine Johnson

## ABSTRACT OF THE DISSERTATION

Investigations of fault creep in southern California using Interferometric Synthetic  
Aperture Radar and GPS

by

Suzanne Noelle Lyons

Doctor of Philosophy in Earth Sciences

University of California, San Diego, 2002

Professor David T. Sandwell, Chair

This dissertation presents an array of remote sensing methods that can be utilized in deformation studies. The main focus is on the detection of creep and how it relates to earthquake hazard assessments. Chapter 1 outlines how both the Global Positioning System (GPS) and Synthetic Aperture Radar Interferometry (InSAR) can be used to detect small creep signatures near strike-slip faults. Chapter 2 presents the results from rapid-static GPS surveys of the dense Imperial Valley geodetic network. Chapter 3 investigates the southern San Andreas Fault, near the Salton Sea, where geodetic monuments are sparse. We utilize InSAR in this region and stack interferograms to isolate the creep signature along the fault. The use of permanent scatterers is introduced and its effects on improving image

coherence are analyzed. Our photographic survey of permanent scatterers in the Coachella Valley/Salton Sea area is presented in Appendix 3A, while Chapter 4 summarizes various studies of creep on California faults. Research from my first two years is presented in Chapter 5, which details how one can determine the elastic thickness of oceanic lithosphere using shipboard bathymetry and satellite gravity.

# Chapter 1

## **An introduction to creep mechanisms, GPS processing, and Synthetic Aperture Radar Interferometry**

*Bah! Only fools, charlatans, and liars try to predict earthquakes.*

-Charles E. Richter

### 1.1 EARTHQUAKE PREDICTION

Present methods of prediction for major earthquakes are not developed enough to provide reliable estimates of occurrence times and, thus, are of little use to city planners and those who deal with public safety. What many people refer to as "earthquake predictions" are actually scientists' attempts at gaining a thorough understanding of earthquake mechanics in order to provide accurate hazard assessments and forecasts. As with any science that directly relates to society's sense of well-being, it is important to remember that even improved earthquake forecasting can have social and economic implications that are as devastating as the earthquake itself.

In 1975, the Chinese government used a foreshock sequence to predict a magnitude 7.3 earthquake near the city of Haicheng and evacuated the town, resulting in relatively light casualties and saving thousands of lives. While many touted this as a new era in earthquake prediction, the excitement was short-lived.

The next year, the Tangshan earthquake in northern China struck without warning, killing 250,000 and disillusioning millions.

Meanwhile, that same year, a psychic named Clarissa Bernhardt predicted in the *National Enquirer* that a major ( $M_L \geq 8$ ) earthquake would occur in North Carolina between January 13 and January 20, 1976. While this would have normally been ignored by the general public, Dr. David Stewart, an assistant professor in geology at the University of North Carolina at Chapel Hill, endorsed the prediction, claiming it was consistent with a pattern of elevation changes he had observed near Wilmington. As a result, the prediction received widespread news coverage and created low-level public panic in the hazard region. Approximately 40% of businesses in the area reported a decline in sales and 40% of the public took action to protect their homes, with 17% stockpiling emergency supplies [*Mileti and Fitzpatrick, 1993*].

No earthquake occurred and, in fact, no seismic activity has ever been reported in the Wilmington area. As a result of endorsing a psychic's prediction without solid scientific evidence, Dr. Stewart eventually lost his position at UNC-Chapel Hill. Unfortunately, this did not deter his prediction endorsements.

In 1989, Stewart supported the claims of Dr. Iben Browning, a 72-year old retired Ph.D. in biology and self-proclaimed climatologist, seismologist, and earthquake expert, that a magnitude 6.5 to 7.5 earthquake would occur near New Madrid, Missouri within 48 hours of December 3, 1990. The New Madrid Fault had produced some of the most violent quakes in North America in 1811 and 1812, so the National Earthquake Prediction Evaluation Council (NEPEC)

organized a study to investigate the claims. Although the team found no scientific evidence to support the prediction and declared it no better than random guessing, the damage had been done. An estimated \$200,000 was spent by state emergency preparedness agencies and more than a dozen schools in four states cancelled classes between December 3 and December 5 in preparation for the earthquake. It never happened, once again causing major disruption to hundreds of thousands of lives.

As a result of incidents like these, most scientific agencies are very careful to limit earthquake hazard analysis to *forecasting* rather than *predictions*. Forecasting is the long-term (years to decades) statements of the probability of one or more earthquakes in a region, while predictions are short-term (hours to days) statements that an earthquake will occur at a given location. Unfortunately, there is a tradeoff between predictions and forecasts. The narrower the time window on predictions, the less disruption to the economy and social structure of the threatened region. However, the paucity of major earthquake events in our historical record makes it difficult to produce even long-range forecasts with small uncertainties.

The most promising earthquake forecast occurred in April 1985. Based on observations that six magnitude 6 earthquakes had occurred along the Parkfield segment of the San Andreas Fault since 1857 with an average repeat time of 22 years, the U.S. Geological Survey predicted (at a 95-percent confidence level) that a moderate earthquake would strike this segment before 1993. This was the first officially recognized earthquake forecast in the United States and as a result, a

huge network of research instruments was deployed in the region to await the earthquake. Unfortunately, the quake that seemed a "sure thing" is now 10 years overdue.

Following the "failure" at Parkfield, it has become obvious that the question of whether or not humans will ever be able to predict earthquakes with any sort of accuracy is more complex than it first appeared. Therefore, it is important to investigate all avenues of research into the mechanics of earthquakes so that we may better understand the forces behind these destructive events and minimize the damage caused by them.

## 1.2 THE EARTHQUAKE CYCLE

The tectonic processes defining the earthquake cycle were first proposed in 1910 by H.F. Reid in his summary of the mechanisms of the 1906 San Francisco earthquake. In this paper, Reid presented his elastic rebound theory, which stated that earthquakes result from the release of strain energy that has been slowly accumulating by the steady motion of the regions on either side of a locked fault [Reid, 1910]. When strain accumulation reaches a critical threshold imposed by the material properties of the rock along a fault, slip will occur along the fault, releasing some of the elastic strain energy. Part of this energy is converted to seismic waves, with the rest usually released in the heating and fracturing of rock. After an earthquake, the elastic strain begins to accumulate again, leading to a cycle of quasi-periodic stressing and failure.

Using Reid's elastic rebound theory as the basis of our understanding of fault slip, we can define three basic models for earthquake prediction: 1) the characteristic (or perfectly periodic) model, 2) the time predictable model, and 3) the slip predictable model [*Shimazaki and Nakata, 1980*]. These models are all shown in Figure 1.1.

The characteristic model (Figure 1.1a) is a simple interpretation of Reid's elastic rebound concept: successive earthquakes each have identical stress drops and occur when the stress on a fault reaches a critical level. This leads to perfect periodicity, in which the amount of slip on the fault for each earthquake is identical and the recurrence interval is constant over time. Unfortunately, this model is rarely observed in nature because it assumes that all fault parameters (friction, strength, etc.) are constant. The most famous case for characteristic fault behavior is along the section of the San Andreas Fault near Parkfield, California (discussed above). This segment is known to have ruptured six times in the past 130 years, with a recurrence interval of about 22 years (Figure 1.2). Although the 1934 event seems to have occurred 10 years early, the consistent recurrence pattern and similar stress drops for each of the last three earthquakes greatly excited researchers in southern California and the region was heavily instrumented in anticipation of the seventh event. According to various models, this most recent earthquake should have occurred in  $1988 \pm 5$  years [*Bakun and McEvilly, 1984*; *Bakun and Lindh, 1985*]. However, at the time of this writing in 2002, scientists were still waiting for the infamous Parkfield prediction to transpire.

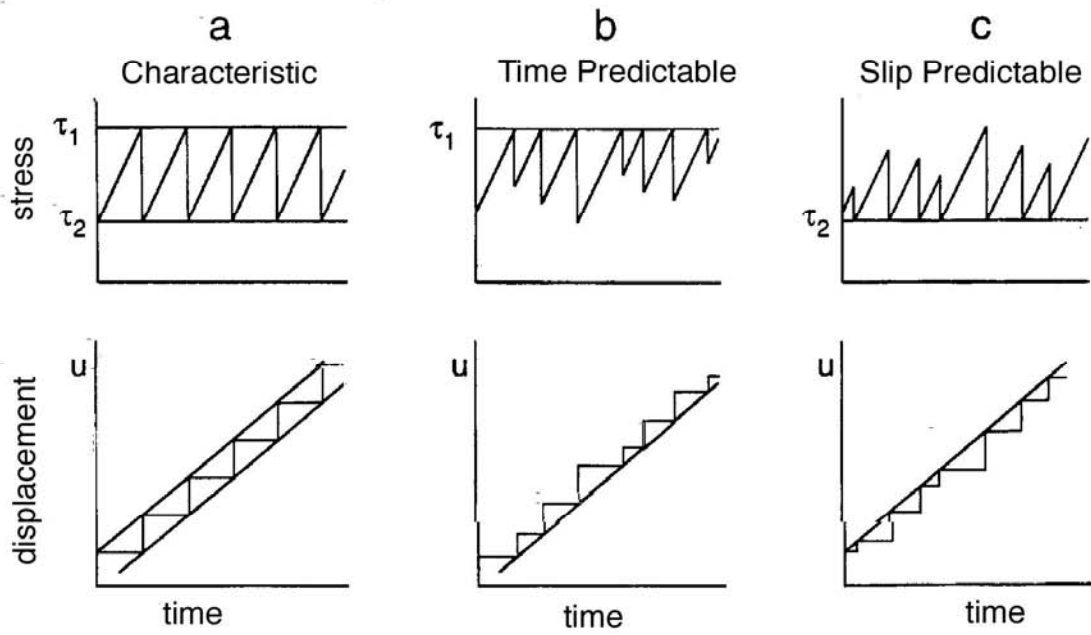


Figure 1.1. Simple earthquake recurrence models. From *Scholz* [1997].

The second model (Figure 1.1b) also assumes that the fault strength is constant, so each earthquake occurs once the shear stress reaches the critical level. However, the stress drop (slip on the fault) can vary with each rupture. Thus, after a large slip, there will be a longer time interval before the next event, in order for the stress level to once again reach the critical point. This is called time predictable, since the time to the next earthquake can be predicted based on the previous events, but the magnitude of the next earthquake is unknown. For time predictable earthquakes, the cumulative slip is linear over time, even though the amount during any particular event varies.

The third model (Figure 1.1c) assumes that earthquakes occur at variable stress states (there is no critical level), but that the stress falls to a constant level of stress, the level of the fault friction. This model is called slip predictable because it can be used to predict the magnitude of an earthquake at any given time, but cannot be used to predict the time of an event.

Although many scientists favor the time predictable earthquake model, there is still not enough evidence to say with any certainty which model is the most accurate. It may be that some fault segments behave according to one model while others adhere to a combination of the three or to a different model altogether.

### 1.3 FAULT CREEP

Creep is defined as an aseismic rupture process that occurs so slowly that no detectable seismic waves are generated. *King et al.* [1973] characterize creep as kinematically similar to faulting, but with low characteristic failure propagation

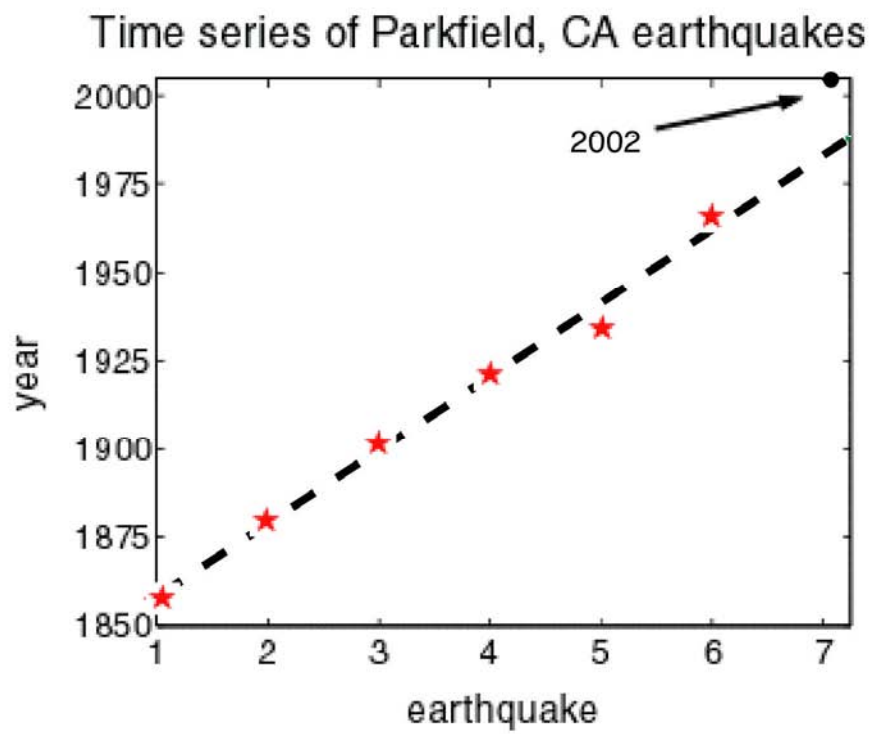


Figure 1.2. The time history of the Parkfield, California, earthquake sequence

rates. Although creep is aseismic due to the slowness of particle motion, it releases considerable amounts of tectonic strain, which may be as much as a low to medium magnitude earthquake. This raises a problem for earthquake predictions: How much does aseismic slip contribute to the release of accumulating strain on a fault?

In general, it is not known how much creep affects strain accumulation on faults, but it could range from zero in the case of "locked" faults with no observable creep to 100% for the central San Andreas Creeping Section [Scholz, 1997]. Along the Imperial Fault, where creep is known to occur [Genrich, 1997; Lyons *et al.*, 1999; Lyons *et al.*, 2002], several earthquake cycles indicate that seismic moment release falls short of the total expected from geodetic and geologic estimates by a factor of 2 to 3 [Anderson and Bonin, 1987].

At the Cienega Winery, 17.5 km southeast of San Juan Bautista, where fault creep was first discovered in 1956 [Steinbrugge *et al.*, 1960], creep has been occurring at a steady rate of 12 mm/yr since 1948. Following two moderate earthquakes ( $M_L=5.3$  and  $M_L=5.2$ ) in 1961, creep ceased at the winery and did not resume until the stress had been restored to its previous level, four years later (Figure 1.3) [Burford, 1988]. This indicates a critical friction level at which slip is initiated along this section of the fault.

In addition to postseismic creep fluctuations, Burford [1988] identified pre-earthquake retardations in creep rates along the San Andreas Fault in central California. The Shore Road creepmeter 10 km NW of Hollister registered a 44-month retardation before the 1979  $M_L=5.9$  Coyote Lake earthquake on the

Calaveras Fault (Figure 1.4). Retardations of 21- and 19-month duration occurred at this location before the 1974 ( $M_L=5.2$ ) and 1984 ( $M_L=6.2$ ) earthquakes, respectively. Thus, there may be a connection between temporary locking of fault surfaces on typically creeping sections of faults and subsequent moderate earthquakes.

Regardless of the exact mechanisms involved in aseismic fault slip, it seems that shallow fault creep is linked to the regional and local processes that accompany, and perhaps promote, moderate earthquakes [Burford, 1988]. Therefore, it is important to study the creep mechanisms along faults such as those in southern California in order to understand the role of aseismic slip in the earthquake cycle.

Traditionally, creepmeters have been used to continuously monitor motions across the surface of faults. Unfortunately, the cost of installation and upkeep on these sites is tremendous. Geologists in the field typically identify creeping faults using cracks and other lines of evidence near the fault trace, then install alignment arrays to monitor the fault motion. However, in regions of thick sediment or fault gouge, identification of creeping sections of faults is difficult. This is where satellite technology such as the Global Positioning System (GPS) and Interferometric Synthetic Aperture Radar (InSAR) has proved invaluable.

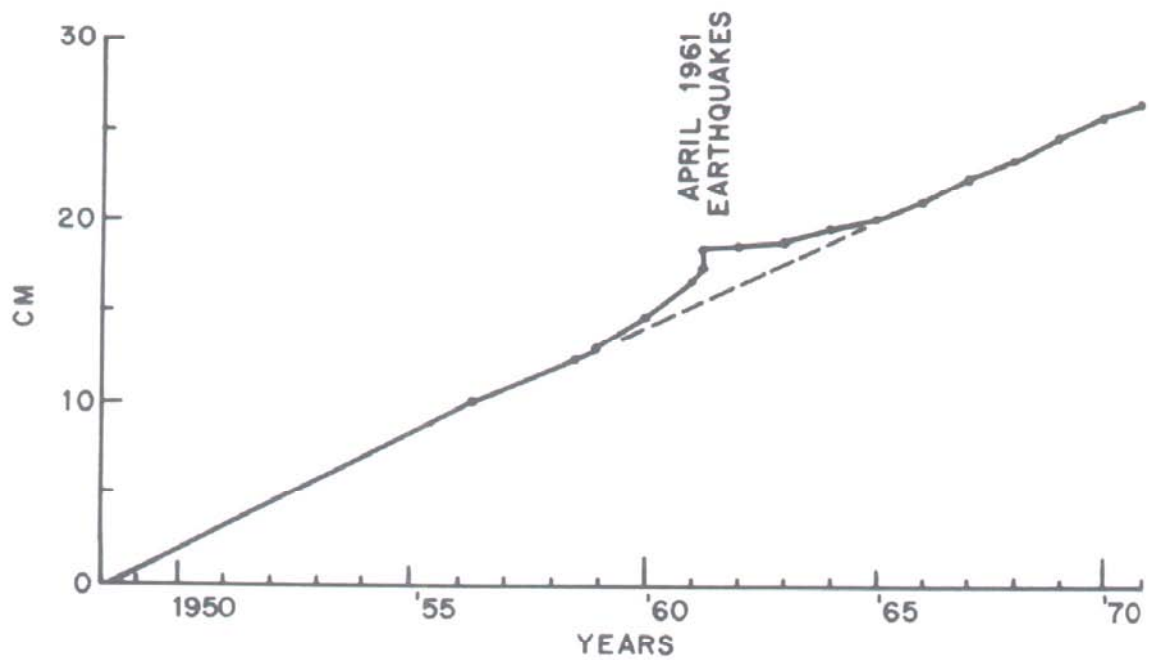


Figure 1.3. Slip at the Cienega Winery, near San Juan Bautista, California, showing a temporary decrease in the creep rate following two April 1961 earthquakes. From *Scholz* [1997].

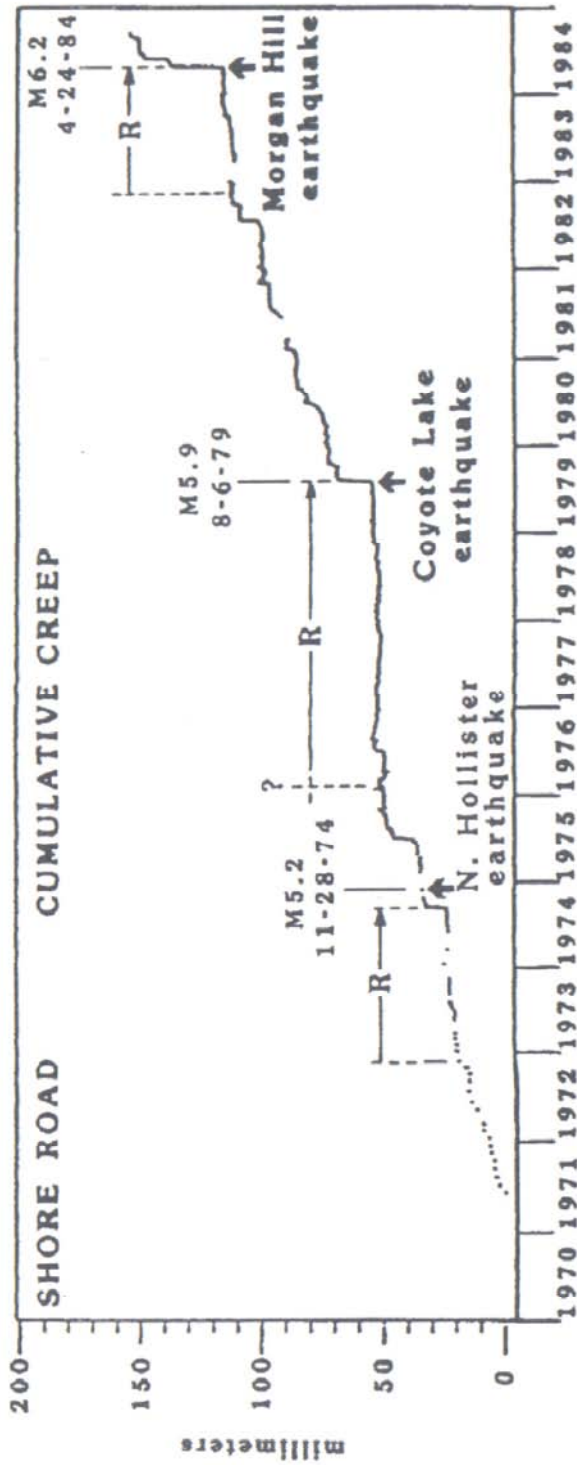


Figure 1.4. Cumulative creep record for 1970-1984 from Shore Road, near Hollister, California. Periods of creep retardation are indicated by arrows labeled "R." From *Burford* [1988].

## 1.4 THE GLOBAL POSITIONING SYSTEM (GPS)

### 1.4.1 THE HISTORY OF GPS

When the Soviet Union launched the first satellite, *Sputnik I*, in 1957, a new technological era was born. Scientists from all over the globe tracked Sputnik's radio signals and at Johns Hopkins University's Applied Physics Laboratory, researchers noticed a Doppler shift in the signals as the spacecraft flew over their receivers. They initially used the Doppler shift in the signals to determine the spacecraft's orbit, but later demonstrated that the principles could be reversed and, if they assumed the satellite was orbiting in a known trajectory, they could determine their position on the earth. Thus, we entered an age of space-based navigation.

The Global Positioning System (GPS) is a satellite radio positioning system designed to provide global all-weather, 24-hour instantaneous position, velocity, and time information. The GPS Nominal Constellation consists of 24 satellites with a minimum of 21 operating 98% of the time. These satellites are in 6 orbital planes (4 per plane) at 20,200 km altitude and 55 degrees inclination. Each satellite is visible for approximately 5 hours above the horizon and has an orbital period of 11 hours 58 minutes, so it will visit the same point in its orbit 4 minutes earlier each day.

There are two types of services available to GPS users: the SPS and the PPS. Civilian users worldwide utilize the Standard Positioning Service (SPS) without restrictions or fees. This uses the Coarse Acquisition (C/A) GPS code

sequence of 1023 pseudo-random binary biphas modulations on a single L1 (1575.42 MHz) carrier frequency. Authorized government users with specially equipped receivers use the Precise Positioning System (PPS). This uses the Precise (P) GPS code sequence of  $10^{14}$  pseudo-random binary biphas modulations on both the L1 and L2 (1227.6 MHz) carrier frequencies. This sequence repeats every 267 days and each one-week segment of the P-code is unique to a particular satellite and is reset each week. PPS users can instantly determine their geocentric position to about 5 meters with a single hand-held satellite receiver, while SPS users achieve 20-30 meter accuracy.

GPS was developed by the Department of Defense primarily for military reasons and serves two main purposes: real-time navigation and high-precision carrier phase positioning. Navigation is the determination of the three-dimensional coordinates of the receiver and the clock offset between the system time and the receiver using a minimum of four pseudorange measurements to four satellites. This typically utilizes a single receiver. Carrier phase positioning employs the more precise carrier phase observations to determine the baselines between two locations. This method, used in surveying, utilizes at least two receivers at a time. Combining the pseudorange with the phase data reduces the noise error and results in much higher positioning accuracy and new on-the-fly processing techniques are providing accuracies of better than a centimeter on moving platforms. This accuracy refers to the relative three-dimensional position between co-observing receivers.

#### 1.4.2 HOW GPS WORKS

GPS positioning uses the travel time of radio signals from a GPS satellite to a receiver on the ground to determine the distance from the satellite to the receiver. Intersecting multiple distances between the different satellites and the receiver, it is possible to triangulate the position of the receiver on the Earth. A receiver must be able to “see” at least four satellites within the GPS Nominal Constellation, which is possible 95% of the time at any location on the Earth due to the configuration of the 24 satellites in the constellation. Each satellite broadcasts a repeating message, indicating the position and orbital parameters of itself and the other satellites. This message (called a “code”) is impressed upon a carrier signal of a certain frequency (either L1 or L2). Both the code and the carrier signal contain important information and can be utilized for precise positioning. The codes have excellent autocorrelation and cross-correlation properties, but very low cross-correlation between two different satellite codes. This is how GPS receivers distinguish between the signals transmitted by different satellites.

At a certain point in time, the specific satellite code (either C/A or P) is generated within both the satellite and the receiver (Figure 1.5). The satellite’s code is then transmitted to the receiver, which compares the incoming code with its generated one. The difference is the time it took for the code to reach the receiver. This time is then multiplied by the speed of light to obtain an estimate of the distance between the satellite and receiver and is called the pseudorange, since

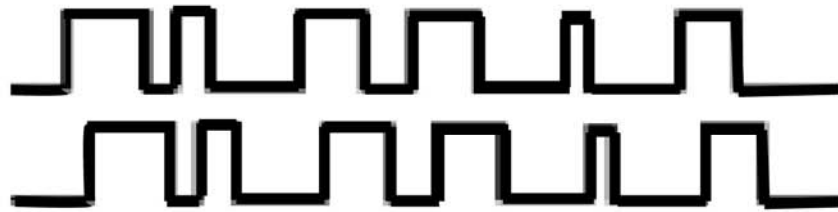
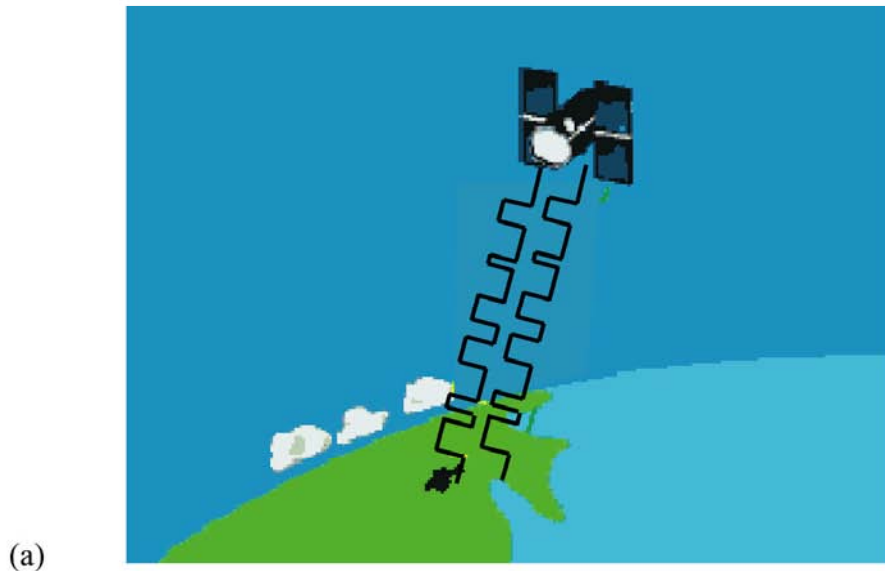


Figure 1.5. Diagram showing the basics of GPS. (a) A specific pseudo-random code is generated by both a satellite and a receiver. The satellite transmits the code to the receiver and the receiver compares the codes. (b) The time difference between the two codes is how long it took for the code to travel from the satellite to the receiver.

there are small errors in the timing of the receiver and satellite clocks. If a receiver,  $k$ , is receiving data from satellite,  $p$ , the general expression for the pseudorange is  $[t_k + \delta t_k - (t^p + \delta t^p)]c = \rho_k^p + I_k^p + T_k^p$ , where  $t_k$  is the time indicated by the receiver,  $\delta t_k$  is the receiver clock error,  $t^p$  is the time indicated by the satellite clock,  $\delta t^p$  is the satellite clock error,  $I_k^p$  is the ionospheric delay,  $T_k^p$  is the tropospheric delay,  $c$  is the velocity of light, and  $\rho_k^p$  is the distance between the receiver and satellite at the time of transmission and reception [Leick, 1990]. This can be rewritten as:

$$(t_k - t^p)c = \rho_k^p + (\delta t^p - \delta t_k)c + I_k^p + T_k^p$$

where the pseudorange is

$$P_k^p = (t_k - t^p)c$$

If the position of the satellite at the time of transmission (called the satellite ephemeris) is known, then the equation for the pseudorange consists of seven unknowns: two clock errors, three receiver coordinates, and the ionospheric and tropospheric delay [Leick, 1990]. The ionospheric and tropospheric delays are computed based on models and the pseudorange to each of the observable satellites have the same clock errors during one measurement epoch, so the offset can be calculated along with the three positional coordinates as long as four satellites are available. This use of the fourth satellite to estimate time offset allows the receiver to work without expensive atomic clocks, while maintaining synchronicity with the satellite clocks to within about 0.1 microseconds.

The carrier phase measurement utilizes the L1 (1575.42 MHz) and/or the L2 (1227.6 MHz) carrier signals. The distance calculated from these signals is

some multiple of 19 or 24 cm (the wavelengths of the L1 and L2 signals, respectively) plus the observed value. This multiple is called the integer ambiguity and must be solved for only after the satellite is locked on by the receiver. Once the receiver has achieved lock, the integer ambiguity is given an arbitrary value and all subsequent measurements are made with respect to this initial value. Thus, if a receiver experiences a “loss of lock” (where the GPS signals are temporarily blocked from the receiver by buildings, etc.), it must reacquire the satellite and be assigned a new initial integer ambiguity. This can cause what is known as a “cycle slip” in the data, where the fractional part of the carrier phase is measured correctly, but the integer value is no longer correct.

#### 1.4.3 GPS ERROR CORRECTION

The most common errors in GPS positional measurements are clock errors (satellite and receiver), orbit errors, localized atmospheric errors, and multipath. All errors except multipath can be minimized through various phase differencing techniques. Processing by differencing takes advantage of the correlation of the error between receivers, satellites, and epochs (or some sort of combination of the three) in order to improve positional accuracy [*Dept. of the Army, EM 1110-1-1003, 1996*].

The simplest way to reduce errors is with single differencing. Single differencing is usually done between receivers or between satellites. Single differencing between receivers (Figure 1.6a) involves calculating the differences between the carrier phase observations by two receivers of the same satellite at the

same instant in time (called an “epoch”). Single differencing essentially eliminates satellite clock errors and much of the orbit errors and atmospheric delays, but it requires a detailed parameterization of the receiver clock errors.

The basic phase equation is given by:

$$\varphi_k^p(t) = \varphi^p(t) - \varphi_k(t) + N_k^p(1) + \text{noise}$$

where  $\varphi_k^p(t)$  is the carrier phase observable in units of cycles for satellite  $p$  and receiver  $k$ ,  $\varphi^p(t)$  is the received phase of satellite  $p$  measured at receiver  $k$ ,  $\varphi_k(t)$  is the receiver phase, and  $N_k^p(1)$  is the integer ambiguity at the first epoch [Leick, 1990]. Thus, if two receivers,  $k$  and  $m$ , observe the same satellite  $p$  at the same epochs (Figure 1.6a), the single difference phase observation can be written:

$$\varphi_{km}^p = \varphi_k^p(t) - \varphi_m^p(t) = -\frac{f}{c} \{ [\rho_k^p(t) - \rho_m^p(t)] - [\varphi_k(t) - \varphi_m(t)] \} + N_{km}^p$$

where  $f$  is the frequency of the signal and the initial ambiguity is

$$N_{km}^p = N_k^p - N_m^p.$$

Single differencing between satellites (Figure 1.6b) occurs when the difference between phase observations of two satellites by the same receiver is calculated. This eliminates the receiver clock errors and, as such, is sometimes used as a precursor to double differencing.

Double differences are the differences of two single differences for two different satellites at the same epoch (see Figure 1.7). This eliminates the receiver clock errors and is the usual technique adopted in GPS data processing. If two receivers,  $k$  and  $m$ , observe two satellites,  $p$  and  $q$ , at the same time, the double difference phase equation is:

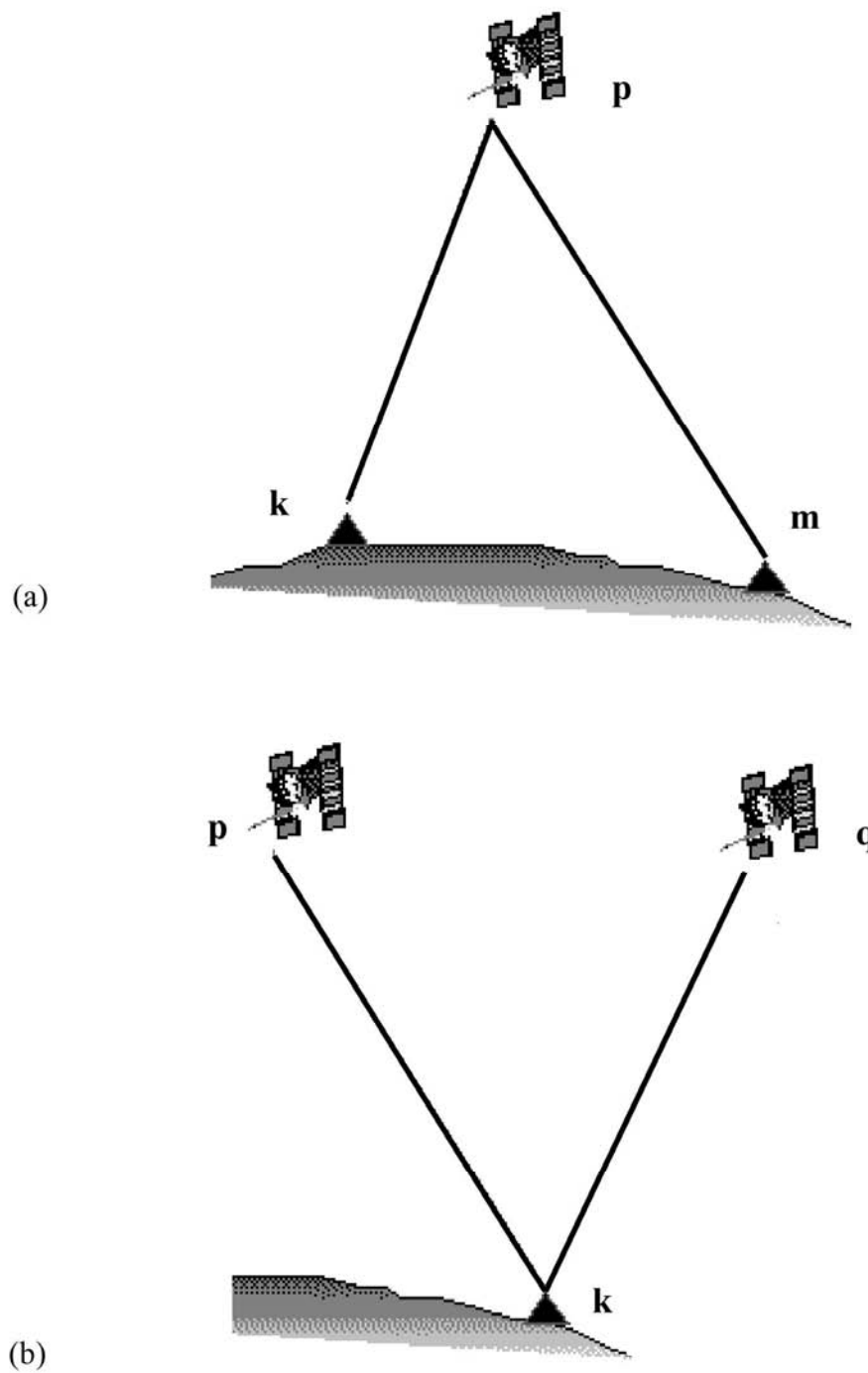


Figure 1.6. The single difference. (a) Two receivers observe the same satellite at the same epoch. (b) One receiver observes two satellites at the same epoch.

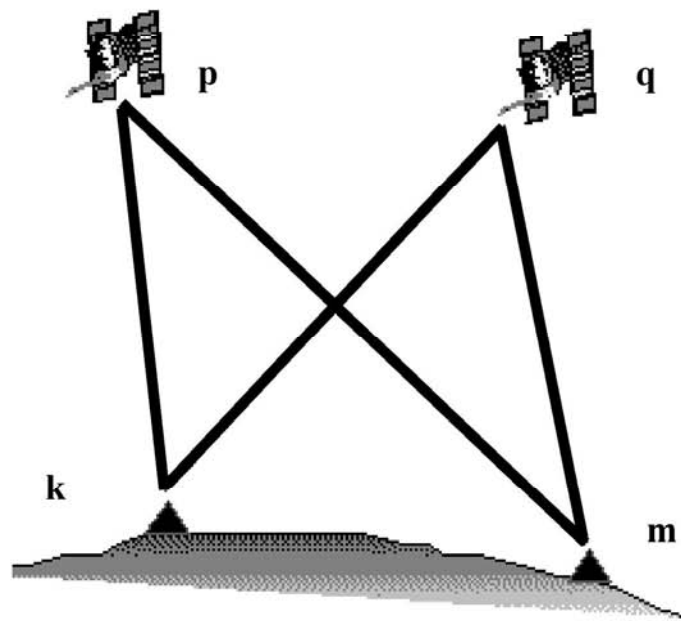


Figure 1.7. The double difference. Two receivers observe two satellites at the same time.

$$\varphi_{km}^{pq} = \varphi_{km}^p(t) - \varphi_{km}^q(t) = -\frac{f}{c} \{ [\rho_k^p(t) - \rho_m^p(t)] - [\rho_k^q(t) - \rho_m^q(t)] \} + N_{km}^{pq}$$

where the integer ambiguity has become

$$N_{km}^{pq} = N_{km}^p - N_{km}^q.$$

The triple difference is the difference between two double differences at two subsequent epochs (see Figure 1.8):

$$\begin{aligned} \varphi_{km}^{pq} &= \varphi_{km}^{pq}(t+1) - \varphi_{km}^{pq}(t) \\ &= -\frac{f}{c} \{ [\rho_k^p(t+1) - \rho_m^p(t+1)] - [\rho_k^q(t+1) - \rho_m^q(t+1)] \} \\ &\quad + \frac{f}{c} \{ [\rho_k^p(t) - \rho_m^p(t)] - [\rho_k^q(t) - \rho_m^q(t)] \} \end{aligned}$$

Note that the triple difference does not depend on the initial integer ambiguity,  $N$ , since the unknown is constant in time and, therefore, the triple difference is used to detect and fix cycle slips and loss of lock. The cycle slip creates an individual outlier in the triple-difference residuals, which can easily be detected and removed automatically. A cycle slip in the double difference solution is a step function and is usually eliminated manually during processing. Thus, triple differences are advantageous in that the processing and editing of data can be fully automated. However, eliminating too much data can degrade the solution, so the majority of processors utilize double differencing techniques and handle cycle slips manually in order to maximize the amount of data used in the position solution.

Atmospheric delay of the GPS signal occurs as the signal passes through the charged particles of the ionosphere and the water vapor in the troposphere (Figure 1.9). If not properly modeled and removed, these delays can cause errors in the final position estimates. Since ionospheric delay is dependent upon the

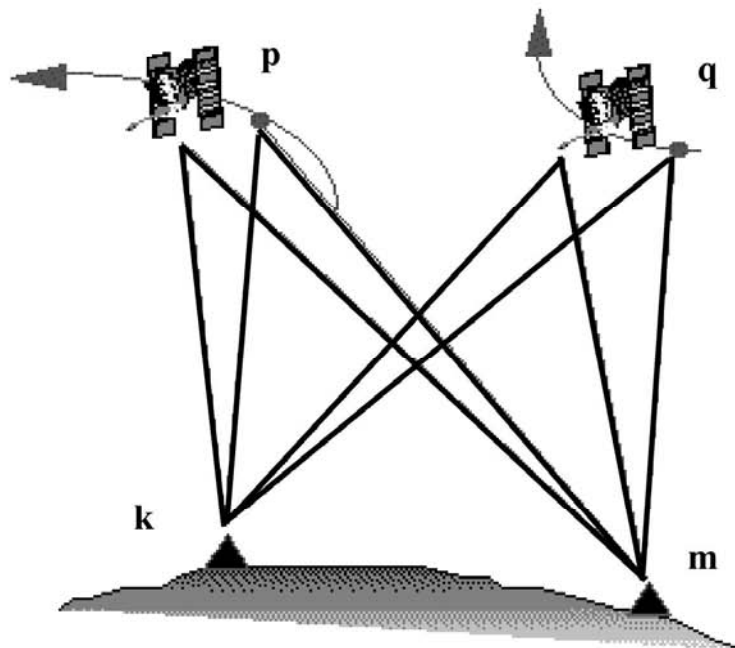


Figure 1.8. The triple difference. Two receivers observe two satellites from one epoch to the next.

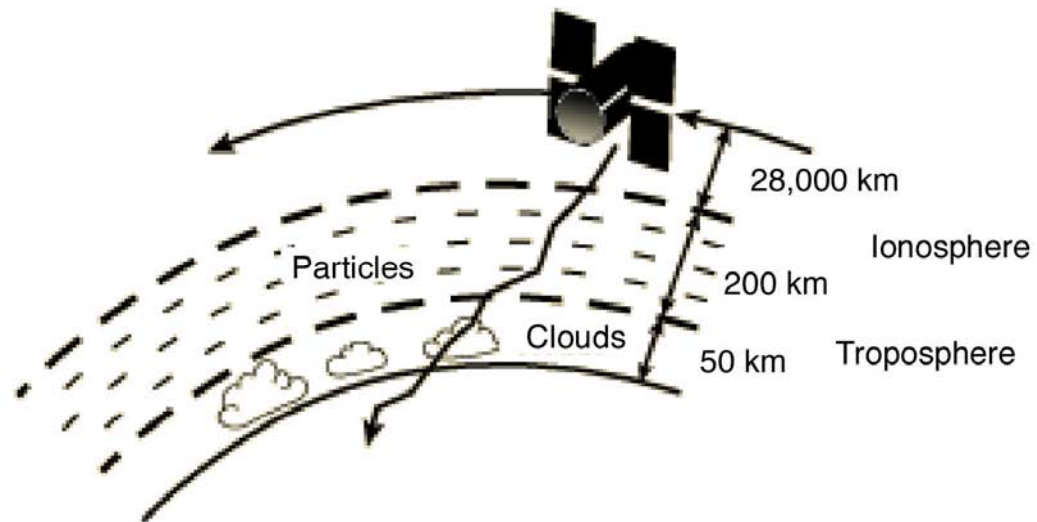


Figure 1.9. Diagram showing the delay of the GPS signal due to the ionosphere and troposphere. Image from Trimble Navigation Limited, 2002.

signal's wavelength, ionospheric errors are eliminated through the use of both the L1 and L2 carrier phase frequencies. Tropospheric delay, however, is not as simple and the spatial and temporal variability of water vapor content causes modeling complexities over long baselines. For short baselines of a few kilometers, the ionospheric and tropospheric effects are highly correlated, since the signal is traveling through essentially the same part of the atmosphere. Thus, double differencing cancels out most of the atmospheric errors.

The same holds true for satellite ephemeris (orbit) errors. The projection of the orbit error is sufficiently similar for co-observing receivers along short baselines that double differencing eliminates the errors.

The most challenging step in GPS processing is the calculation of the integer ambiguities. If the receivers are stationary, the satellites will be in roughly the same relative positions to the receiver for a period of time and the system of equations is singular. However, over time, the satellite geometry with respect to the receiver will change sufficiently to determine the integer ambiguities. Originally this took a few hours of continuous data collection. Now, when performing rapid-static surveys (discussed in Chapter 2), only about 10 minutes of satellite lock is required. Once the initial ambiguity has been computed, it is possible to move the receiver and, as long as the satellite lock is not lost, centimeter accuracy solutions can be calculated within 1-2 minutes at subsequent survey sites.

It is important that the satellites must be spaced far enough apart during the data collection phase that the timing difference is adequate to calculate the

unknown location precisely. This is called the “geometric dilution of precision” (GDOP) and is shown in Figure 1.10. Most high-quality receivers will calculate the GDOP of the available satellites and automatically choose the configuration that provides for the best geometry (lowest GDOP). In most cases, the larger the number of satellites, the smaller the GDOP.

In measuring the distance from the satellite to the receiver based on the signal's travel time, it is assumed that the emitted signal travels directly from the satellite to the receiver antenna. This is not always the case, however, since there are reflected signals from both the ground and other objects near the antenna that interfere with the direct signal (Figure 1.11a). This reflection of signals, known as multipath, creates an uncertainty about the true signal arrival time and can introduce significant (centimeter to meter) errors into the final positioning solution. However, multipath can be reduced in multiple ways.

The simplest way to alleviate multipath effects is through site selection. Buildings, bodies of water, and trees can cause severe multipath errors, so setting up receivers in areas that offer an unobstructed view of the sky (e.g., mounting the antenna on top of a building or mountain or placing the antenna in a field) will greatly reduce these errors. The use of choke rings (Figure 1.11b) will eliminate multipath signals reflected from objects below the antenna. However, the antenna will still receive reflected signals that hit the antenna from the top (e.g., bouncing off a building). These multipath signals usually travel a distance of at least 10 meters longer than the direct path, so they can be isolated from the direct signal and reduced without affecting the true signal.

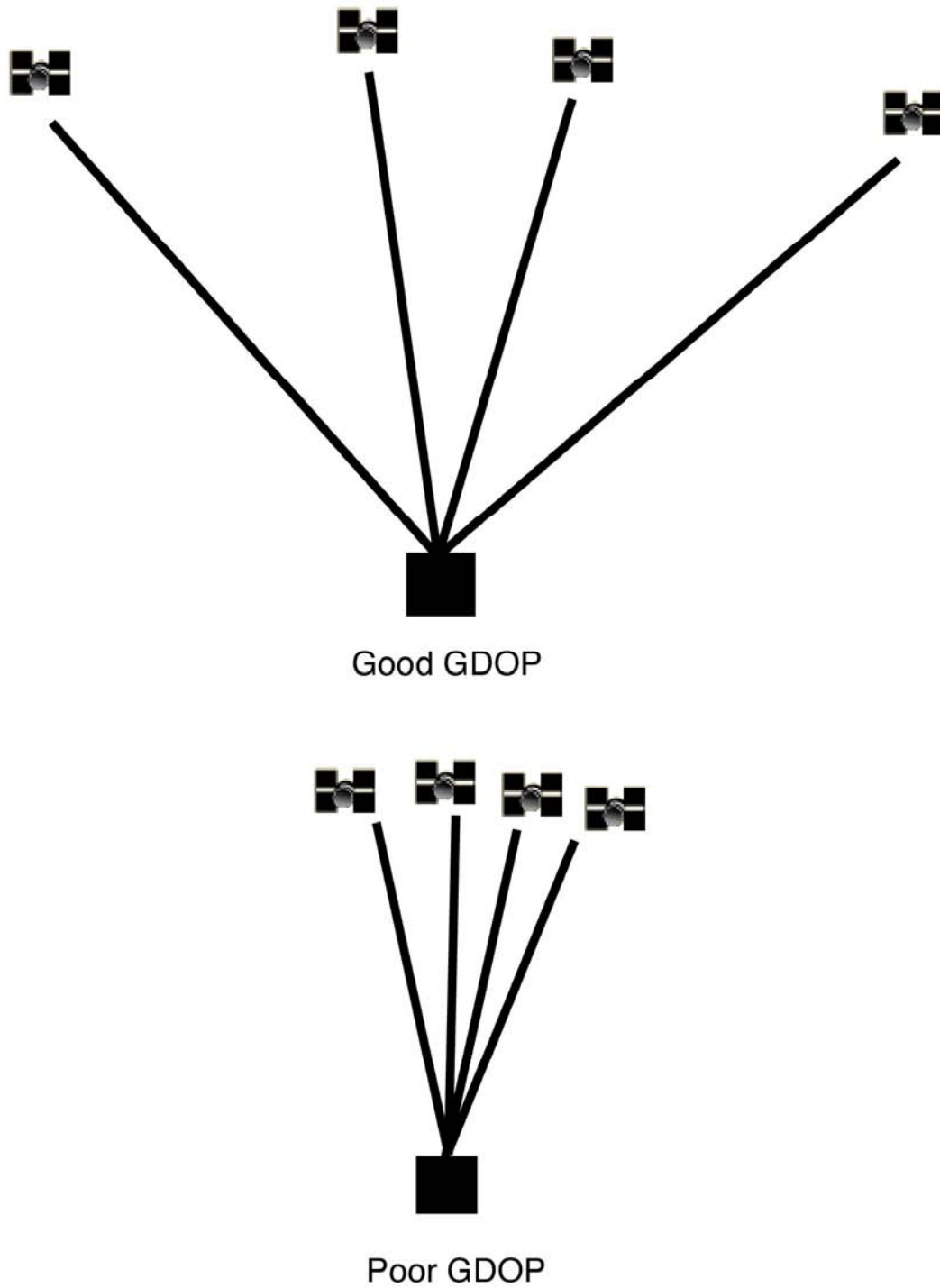
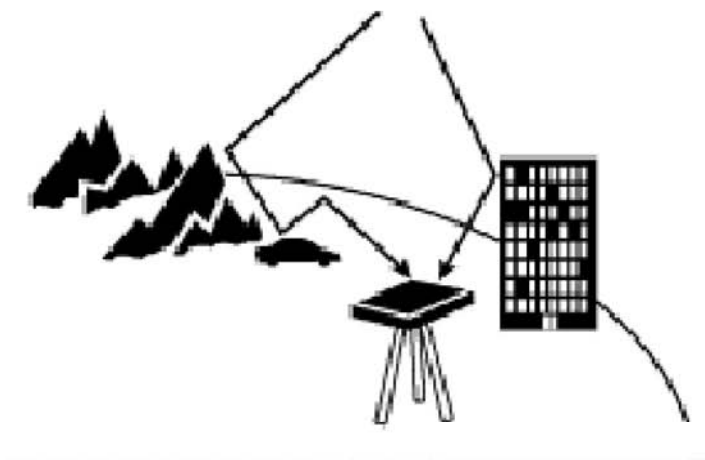


Figure 1.10. Geometric Dilution of Precision (GDOP), a composite measure reflecting the effect of the satellite geometry on the GPS solution. A good GDOP leads to more reliable results.



(a)



(b)

Figure 1.11. (a) Multipath effects from objects surrounding a GPS receiver. Multipath occurs when a signal arrives at a receiver's antenna by way of two or more different paths. The signals interfere with each other at the antenna and cause error in the range (distance between satellite and receiver) calculation. (b) Trimble choke ring used to reduce multipath.

Errors in the satellite clock, satellite orbit, receiver clock, ionosphere, troposphere, and the multipath usually amount to up to 10 m of range error if there are no corrections. This results in a positional accuracy of ~20 m for simple handheld receivers. Using the differential correction techniques discussed above can improve the solution accuracy to the sub-centimeter level. This is discussed further in Chapter 2.

#### 1.4.4 GPS APPLICATIONS

So who uses GPS? GPS has a wide variety of applications, from industry to science to transportation to recreation. Basically, GPS can be used anywhere except where the signal cannot be received (e.g., in most buildings, underwater, and in caves). Airborne receivers are used for navigation by commercial and military aircraft. Marine GPS systems are used by commercial fishermen, recreational boaters, and military and scientific research ships for accurate navigation. On land, the applications are even more varied. Surveyors, wildlife managers, mappers, search and rescue teams, geologists, and geophysicists all use GPS for positioning and location information vital to their jobs. Recreationally, hikers, hunters, skiers, campers, and basically anyone who needs to keep track of his or her location can utilize the Global Positioning System. Newer cars even come equipped with GPS systems for trip planning or to avoid getting lost. Any time the location of a person or object needs to be known, GPS is a viable solution. The accuracy with which the position is needed (i.e., centimeter level or meter

level) will depend on the application and will determine the type of processing and equipment needed.

## 1.5 RADAR SYSTEMS

### 1.5.1 IMAGING RADAR

Before the development of imaging radar, remote sensing technology consisted of camera systems that were sensitive either to reflected solar radiation or to thermal radiation emitted from the Earth's surface. These passive imaging systems used natural radiation, meaning that an absence of sunlight due to clouds or night would hinder the collection of data. With the advent of active radar systems, such as Side-Looking Airborne Radar (SLAR), radar altimetry, and Synthetic Aperture Radar (SAR), the weather and/or time of day is no longer a limitation on imaging.

Active radar is one in which the satellite transmits a beam of electromagnetic radiation in the microwave band (1 cm to 1 m or 300 MHz-30 GHz, Figure 1.12) obliquely onto the earth. The radar then measures the backscattered radiation (strength and roundtrip time) that is reflected off the Earth's surface. This data is converted to digital form to be used for image processing. Since the radar provides its own illumination, it can record data at any time of the day or night.

Imaging radar emits waves within the microwave band of the spectrum. Since attenuation by atmospheric molecules (water vapor or oxygen) is dependent on frequency, the radar waveband is carefully chosen to minimize atmospheric

interference. Between 1-10 GHz (3-30 cm), the transmissivity approaches 100%, which makes the radar system virtually unaffected by clouds or precipitation. By choosing the correct waveband, an active radar system can operate unhindered in all weather conditions.

The two main types of radar images are the circularly scanning plan-position indicator (PPI) images – used mainly for monitoring air traffic – and the side-looking images – used in remote sensing. These side-looking images are divided into two groups: the real aperture radar systems (SLAR and SLR) and the synthetic aperture radar (SAR) systems.

The real aperture systems use a long, straight antenna mounted on an aircraft or satellite moving at some velocity and altitude. The antenna transmits pulses of electromagnetic energy perpendicular to the flight path (along-track direction) of the platform (Figure 1.13). These pulses reflect off a narrow region (called the footprint) and are scattered in numerous directions, including back toward the satellite. The antenna height,  $W_a$ , and the wavelength,  $\lambda$ , determine the width of this footprint (known as the swath width). The slant range is the line-of-sight distance measured from the antenna to the target, while the ground range is the horizontal distance measured along the surface from the ground track (nadir line) to the target (Figure 1.14). The edge of the footprint closest to the nadir line is the near range and the edge of the footprint farthest from the nadir line is the far range.

The angle measured between the direction the antenna is pointing and the nadir line is the look angle. This varies across the image swath and is relatively

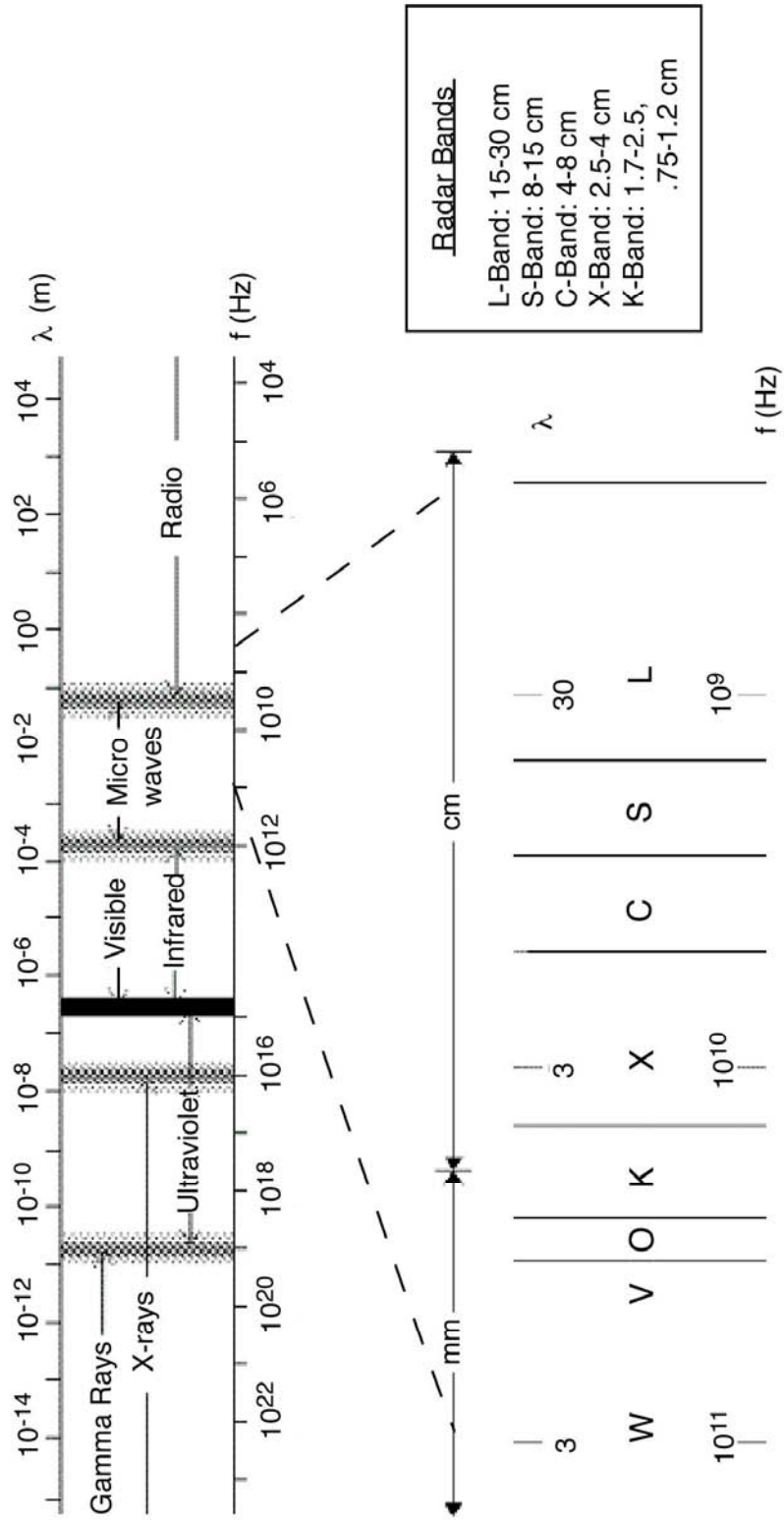


Figure 1.12. The electromagnetic spectrum

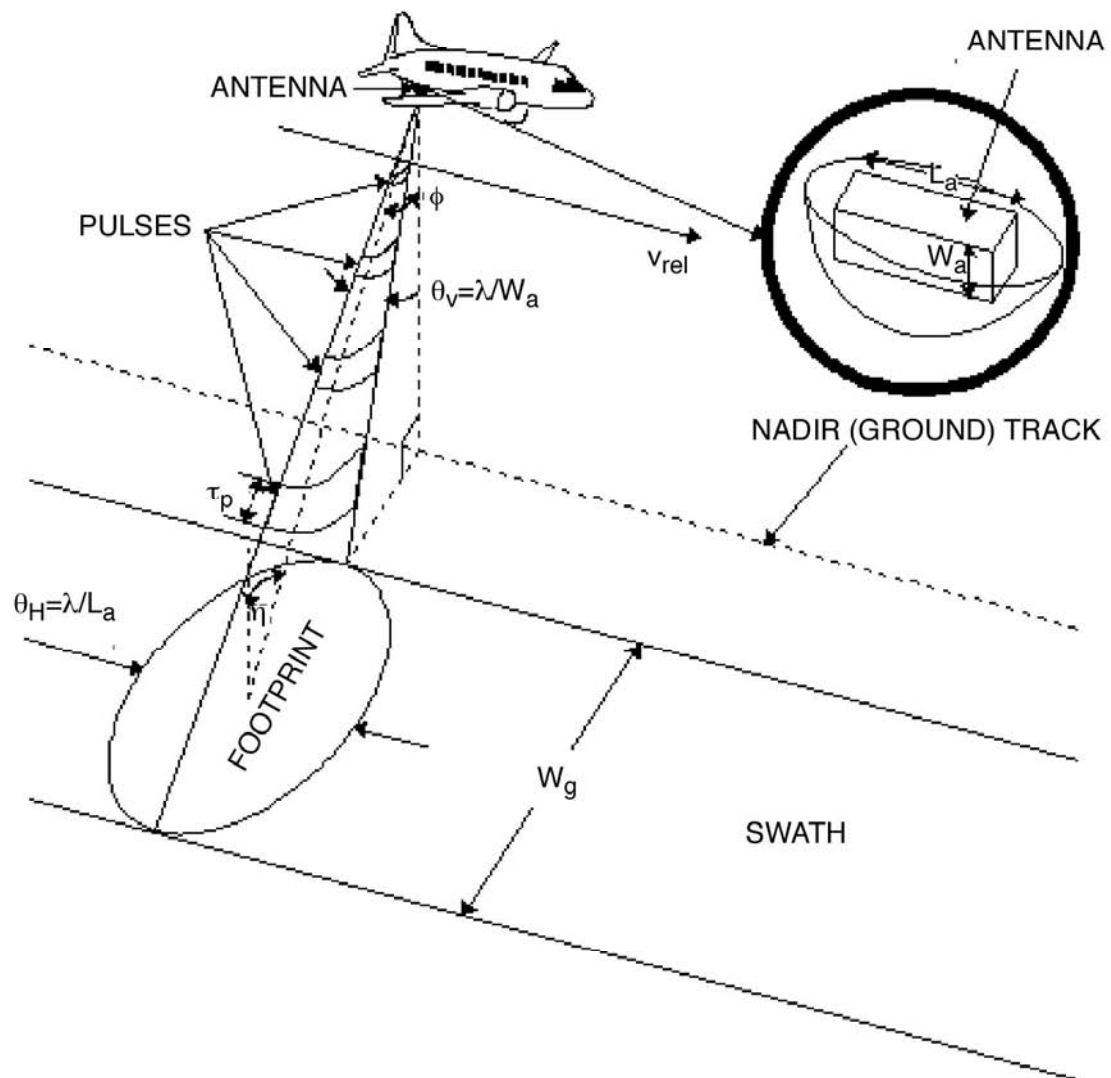


Figure 1.13. Geometry of an imaging radar.

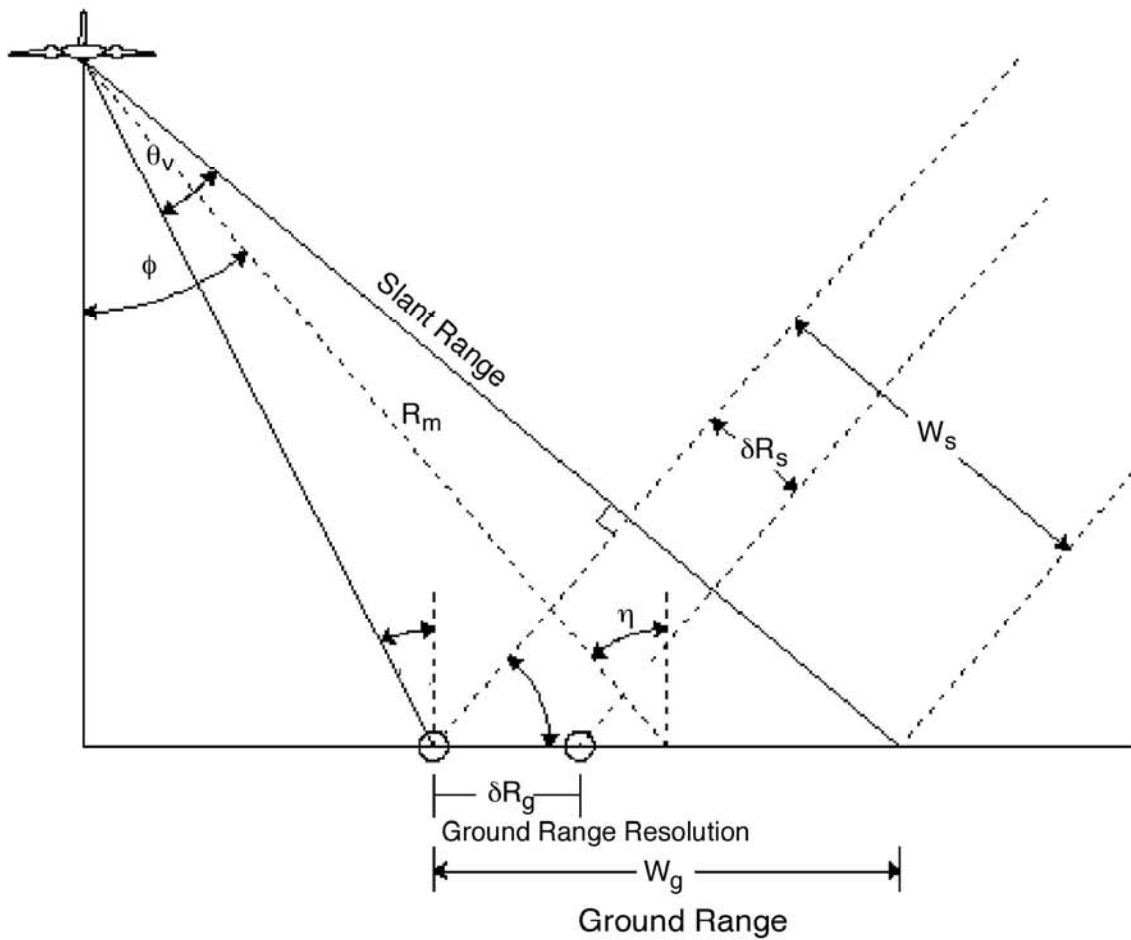


Figure 1.14. Diagram illustrating ground range vs. slant range. Ground range resolution is the minimum distance required for the satellite to distinguish two separate points on the ground.

small in the near range and relatively large in the far range. The incidence angle is the angle between the axis of the radar beam and the normal to the local topography. These two angles are sometimes used synonymously, but that is only valid for a simplified geometry in which the Earth's curvature and the local topography are neglected.

The vertical beamwidth of the emitted pulses is  $\theta_v = \lambda/W_a$ , which gives a ground swath width of:

$$W_g = \frac{\theta_v \times R_m}{\cos \eta} = \frac{\lambda R_m}{W_a \cos \eta}$$

where  $\eta$  is the incidence angle of the beam at the midpoint of the swath and  $R_m$  is the slant range from the antenna to the swath midpoint (see Figure 1.14).

The range (ground) resolution of this system,  $\delta R_g$ , is defined as the minimum ground distance between two points that can still be distinguished as separate points (Figure 1.14). If the pulse duration is  $\tau_p$ ,  $c$  is the speed of light, and  $\delta R_s$  is the slant range resolution, then the range resolution is given by:

$$\delta R_g = \frac{\delta R_s}{\sin \eta} = \frac{c\tau_p}{2\sin \eta}$$

Unfortunately, to obtain a useful resolution requires a pulse duration that would be too short to provide a decent echo signal-to-noise ratio (SNR), so most researchers apply a pulse compression technique along with matched filtering (see *Curlander and McDonough*, 1991), which produces both a high signal-to-noise ratio and better range resolution:

$$\delta R_g = \frac{c}{2B_R \sin \eta}$$

where  $B_R$  is the frequency bandwidth of the transmitted radar pulse.

The azimuth resolution is the same as the range resolution, except it is in the direction of the flight path. Two objects on the ground with the same slant range,  $R_s$ , can only be imaged separately if they are not within the radar beam at the same time. Thus, if the angular spread of the radar beam is  $\theta_H = \frac{\lambda}{L_a}$  (Figure 1.13), where  $L_a$  is the length of the radar antenna in the azimuth direction, we can determine the real aperture azimuth resolution:

$$\delta x_a = R_s \theta_H = \frac{2R_s \lambda}{L_a}$$

Thus, to improve resolution (smaller  $\delta x_a$ ), a longer antenna is required. Unfortunately, this can pose some problems, as a typical radar system such as ERS-1/2 operating in the C-Band at an altitude of 785 km would require a satellite antenna of almost 2 km in length to achieve a ground resolution of 25 meters! This is where synthetic aperture radar (SAR) comes in. It is the ability of the SAR to produce fine-scale images without cumbersome antennae that distinguishes it from other radar systems.

### 1.5.2 SYNTHETIC APERTURE RADAR

The observation by Carl Wiley in 1951 that two point targets at different angles along-track will have different speeds at any instant relative to the platform eventually led to the creation of SAR. When a detector moves with respect to a source of waves, a shift in frequency occurs, known as the Doppler effect. If the emission source is moving away from the observer at a velocity  $v$ , the observed

frequency is  $f_o = \frac{1 - (v/c)}{1 + (v/c)}^{1/2} f$  with the signs of  $v/c$  reversed for a source moving toward an observer. Thus, an approaching source has an apparent frequency that is *higher* than the actual emitted frequency and a receding source exhibits a *lower* frequency than the actual frequency. This can be observed by listening to a train whistle as it approaches the station. As the train gets nearer, the pitch of its whistle increases until the train finally reaches the observer, at which point the actual frequency of the whistle is heard, which then lowers as the train departs.

In the same way, objects on the ground experience this “Doppler shift” in frequency, with each point exhibiting a different shift. By comparing the Doppler-shifted frequencies to a reference frequency, many returned signals can be “focused” on a single point. This effectively increases the length of the antenna that is imaging that particular point by creating a synthetic aperture.

For a point target at  $x$  with a slant range of  $R_s$  (Figure 1.15), the Doppler shift relative to the transmitted signal frequency is:

$$f_D = \frac{2v_{rel} \sin \theta}{\lambda} = \frac{2v_{rel} x}{\lambda R_s}$$

where  $v_{rel}$  is the relative velocity,  $\theta$  is the angle off broadside, and  $\lambda$  is the wavelength of the signal. The azimuth resolution,  $\delta x_a$ , is then related to the resolution of the Doppler frequency measurement,  $\delta f_D$  by:

$$\delta x_a = \frac{\lambda R_s}{2v_{rel}} \delta f_D.$$

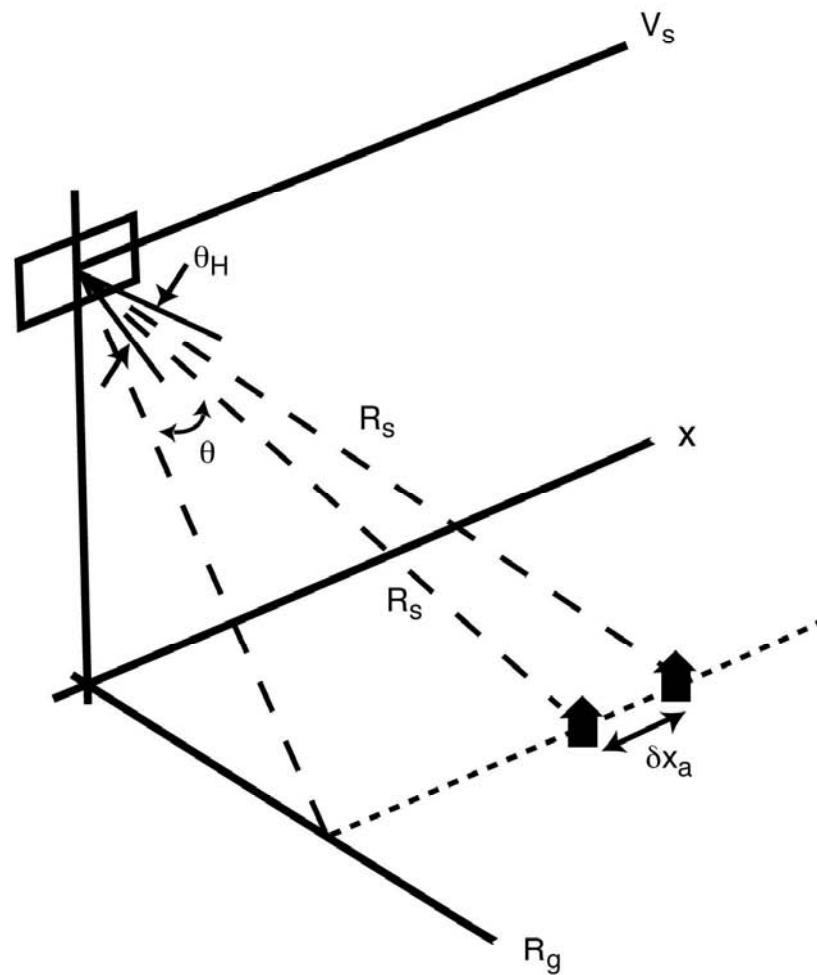


Figure 1.15. Diagram of a Synthetic Aperture Radar.  $R_s$  is the slant resolution,  $R_g$  is the ground resolution, and  $\delta x_a$  is the azimuth resolution. From *Curlander and McDonough* [1991].

This Doppler frequency resolution is limited by the time during which any particular target remains in the radar beam. Thus, the time span,  $S$ , of the waveform is:

$$S = \frac{1}{\delta f_D} = \frac{R_s \theta_H}{v_{rel}} = \frac{R_s \lambda}{L_a v_{rel}}$$

which results in a synthetic aperture azimuth resolution of:

$$\delta x_a = \frac{\lambda R_s}{2v_{rel}} \delta f_D = \frac{\lambda R_s}{2v_{rel}} \frac{L_a v_{rel}}{R_s \lambda} = \frac{L_a}{2}$$

assuming that the Doppler shift is constant during the entire time span. This assumption does not always hold true, but the modern SARs do achieve resolution very near this value. Thus, the use of a synthetic aperture bypasses the requirement of an outrageously long antenna for high azimuth resolution.

When looking at a SAR image, it seems to closely resemble that of an optical image. However, the SAR records both the amplitude and the phase of the image. The phase information is needed for interferometry (discussed below). The amplitude of each pixel in the image is a representation of the amount of backscatter detected by the radar. Darker areas represent low backscatter, while brighter areas represent high backscatter. The amount of reflected energy at a particular pixel is dependent upon many factors, including the wavelength of features within the target area, the moisture content of the area, the polarization of the pulses, the pulse wavelength used, and the angle of reflection. As a simple rule of thumb: the brighter the pixel, the rougher the imaged surface. Figure 1.16 shows the typical backscatter for different surfaces.

An obvious difference between SAR images and optical images is the geometric distortion due to the angle of the radar and of the target. Unlike an optical image, which has a central perspective projection, a SAR locates images as a function of distance from the antenna. Thus, two points on a SAR image will look closer together than they really are. The distance in slant range,  $D_s$ , is approximately equal to the ground distance multiplied by the sine of the look angle,  $\theta$ . Thus, the slant range distance is always smaller than the corresponding ground range and the slant range (SAR image) view compresses the terrain in the near range more than in the far range. Translating between the two presentations becomes important when one wants to overlay targets onto the SAR image (such as plotting GPS station locations).

Imaging slopes with radar can result in some very odd relief, which can be decoded by understanding the effects of layover and shadowing. Layover occurs because the top of a vertical object is closer to the radar than the bottom (Figure 1.17). Shadowing is caused by the angle of the radar beam. Since the radar beam is at an angle, there will be a region of ground behind a vertical structure that the beam cannot reach and, thus, cannot return any signal. This results in a black area called a shadow. Figure 1.18 shows a typical SAR amplitude image of the Salton Sean and Coachella Valley. Layover of the mountainous terrain is obvious in the lower left (southwest) corner.

The applications of Synthetic Aperture Radar in remote sensing encompass numerous disciplines. Oceanographers and climatologists have used SAR to

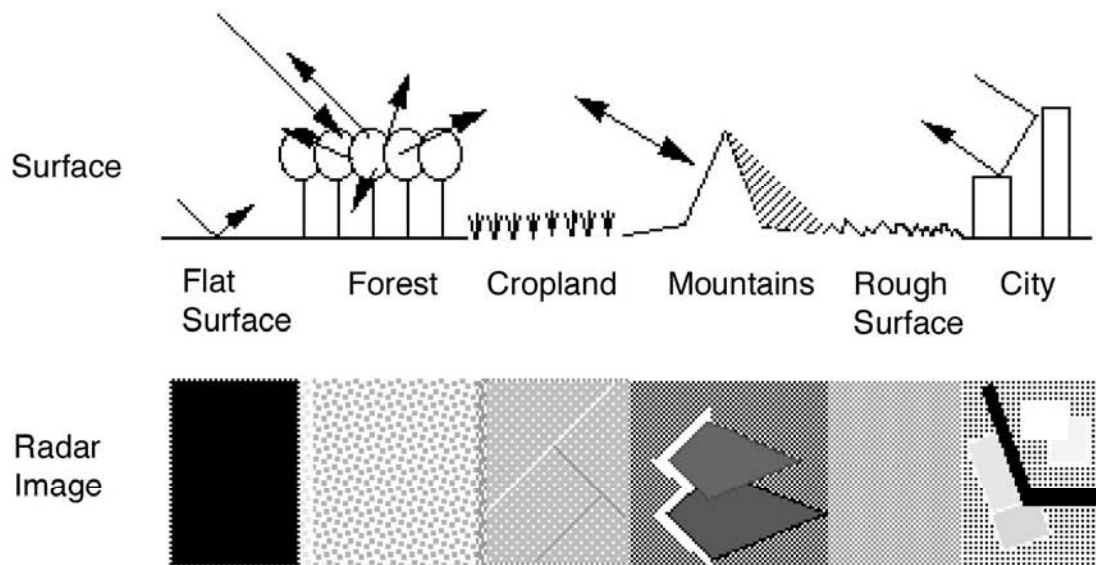


Figure 1.16. Typical backscatter characteristics for various surface types.

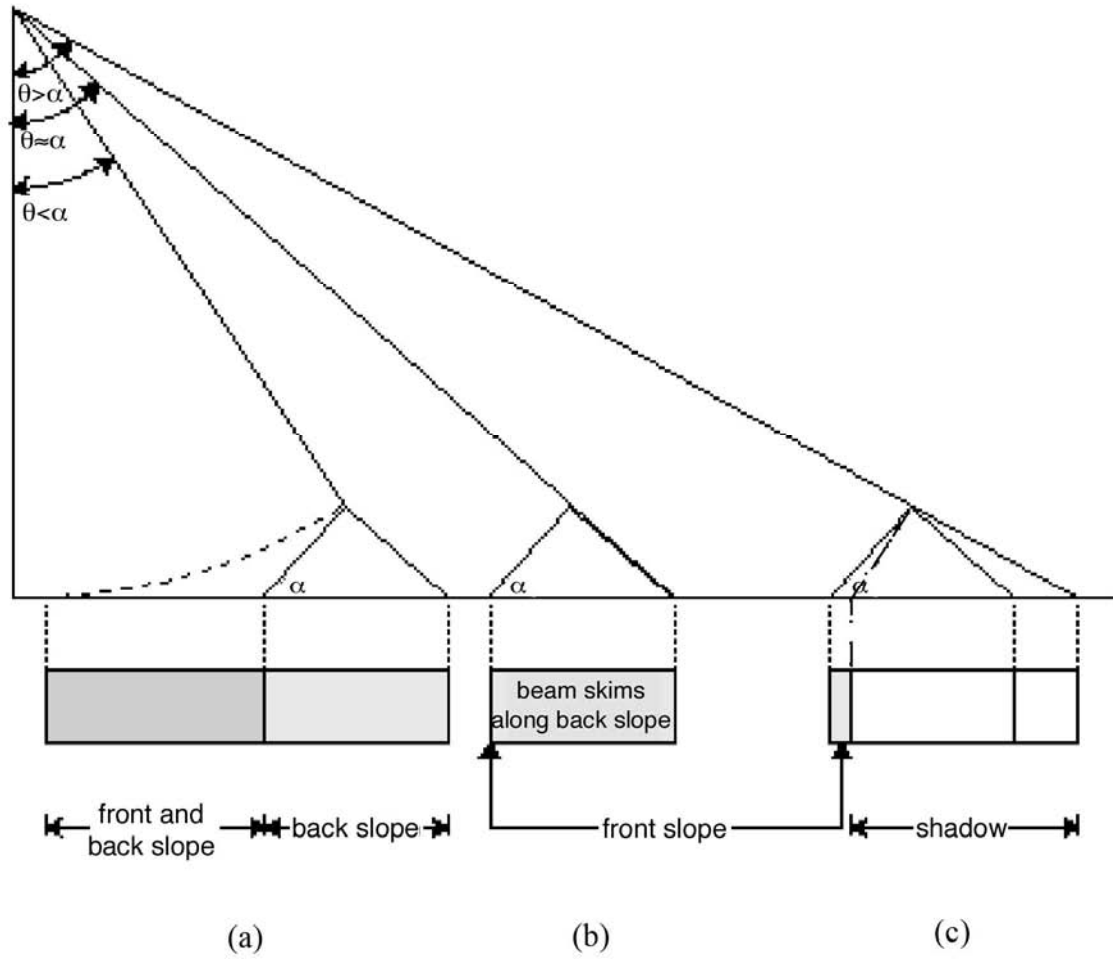


Figure 1.17. Diagram showing layover and shadowing in SAR images.



Figure 1.18. SAR amplitude image of the Coachella Valley/Salton Sea area. Layover is apparent in the southwest (lower left) corner.

model ocean waves and to classify different types of sea ice and track their motions. Geologists and geophysicists utilize SAR imagery in mineral exploration and for locating oil and gas deposits. Water content in the atmosphere can be determined through the use of SAR interferometry (differencing a pair of SAR images to determine the change in ground elevation between passes). But the most influential use in the geophysics community has been the use of SAR interferometry (InSAR) for the development of high-resolution digital elevation models (DEMs) and the isolation of small-scale ground movements due to earthquakes and human activity.

### 1.5.3 SYNTHETIC APERTURE RADAR INTERFEROMETRY (INSAR)

The first experiments in using SAR interferometry for topographic mapping were performed by *Graham* in 1974, but it was over a decade after this initial paper before SAR came to the forefront of geophysical research. In 1986, *Zebker and Goldstein* demonstrated single-pass interferometry using two SAR antennae mounted on an aircraft. In 1988, *Gabriel and Goldstein* introduced repeat-pass interferometry using three different L-band observations from SEASAT. In 1991, the European Space Agency (ESA) launched ERS-1, carrying a C-band SAR system with a repeat time of 35 days. With the launching of ERS-2 in 1995, it was possible to set up a tandem mission, which combines data sets from the two satellites acquired one day apart. This dual satellite configuration has

made numerous advances possible over the last decade and led to a plethora of publications in various fields utilizing SAR interferometry.

SAR interferometry (InSAR) is used to provide information about three-dimensional objects using the phase differences between radar images acquired from slightly different positions. The phases of images with differences of position (e.g., two radars on one platform) or time (e.g., one radar receiving data at two different times) can be compared and used to create a new image called an interferogram. Interferometry utilizes the real (Re) and imaginary (Im) parts of the complex radar signal such that:

$$\phi = \arctan \frac{\text{Im}}{\text{Re}}$$

$$A = \sqrt{\text{Im}^2 + \text{Re}^2}$$

where  $\phi$  is the phase and  $A$  is the amplitude of each SAR image. The difference in the phase of the two images is the interferogram, where the pattern of fringes represents phase values from 0 to  $2\pi$ .

#### 1.5.4 INSAR GEOMETRY

The standard observational geometry for the simplest case of single-pass interferometry is shown in Figure 1.19a (from *Zebker and Goldstein, 1986*). An airplane carries two antennas, A1 and A2, separated by a baseline  $B$ , oriented at an angle  $\alpha$  with respect to the horizon. The path difference between the observed point, P, and the two antennas is  $\rho - (\rho + \delta\rho)$ .

Repeat pass interferometry (Figure 1.19b) utilizes the same geometrical approach, but instead of using two antennas on the same platform, it requires one

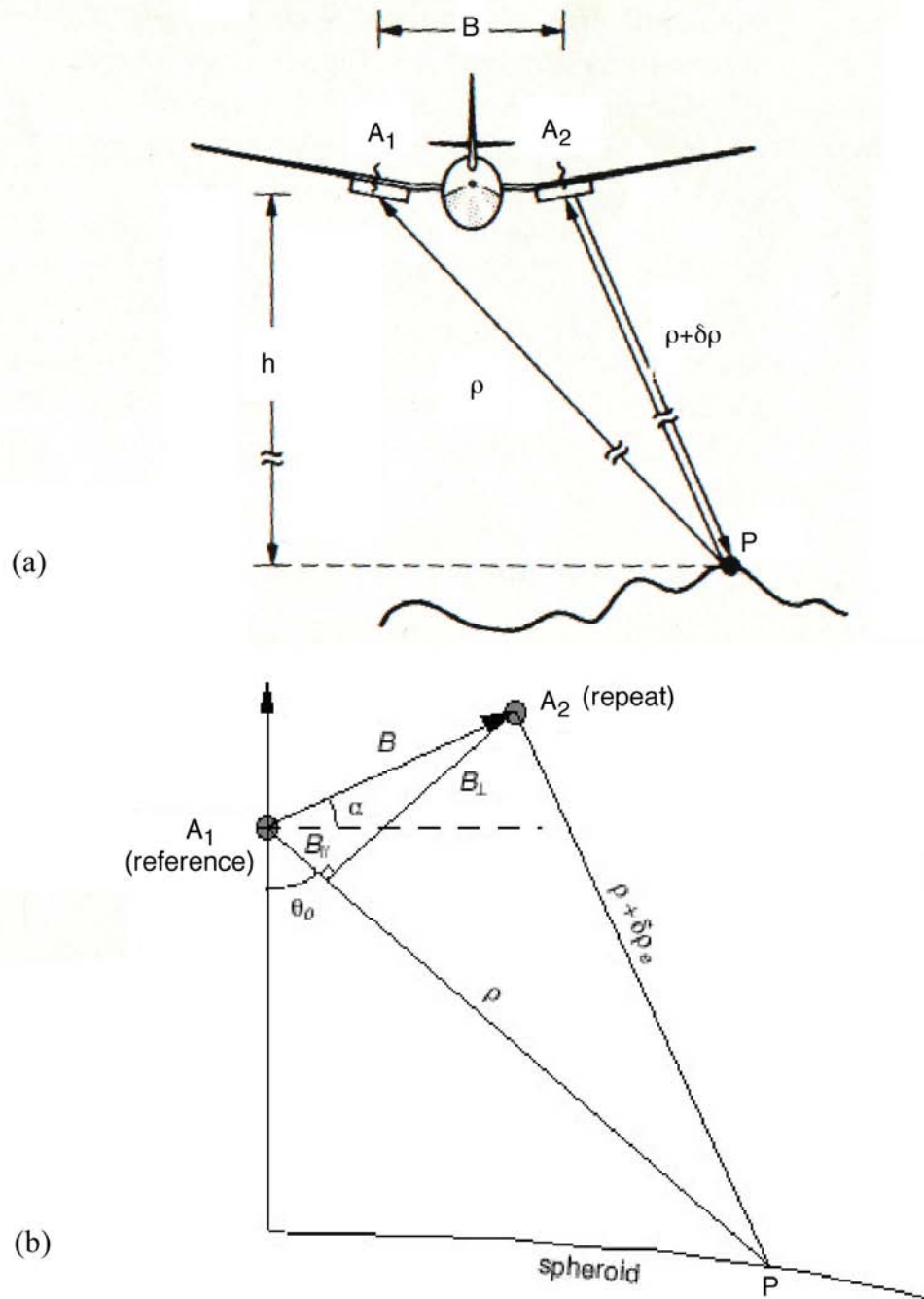


Figure 1.19. Geometry of the interferometer. In single-pass interferometry (a), a wave transmitted from  $A_1$  is received by  $A_1$  and  $A_2$ . Knowledge of  $\rho$ ,  $\delta\rho$ ,  $B$ , and  $\theta$  will determine height,  $h$ , of the radar above each point in the image. (b) The geometry of repeat-pass interferometry is identical to that of single-pass, but consists of a satellite imaging an area at two different times (reference and repeat). In this setup, with the absence of topography, the range change between the reference and repeat passes,  $\delta\rho_e$ , is due to a spheroidal Earth. Adapted from *Zebker and Goldstein* [1986] and *Price* [1999].

antenna visiting a region at two distinct times. This method is useful when attempting to detect crustal deformation over various time periods (e.g., earthquakes, aseismic creep, subsidence) or when trying to characterize atmospheric differences at two imaging times. Assuming the backscattering characteristics for the target,  $P$ , are essentially equal for the reference and repeat images, the induced phase change  $\phi$  between the reference and repeat pass will be proportional to the sum of a curved Earth ( $\delta\rho_e$ ), a topographic ( $\delta\rho_t$ ), and a deformation ( $\delta\rho_d$ ) contribution to the range change:

$$\phi = \frac{4\pi}{\lambda} (\delta\rho_e + \delta\rho_t + \delta\rho_d).$$

Figure 1.20 shows an interferogram of the Salton Sea and Coachella Valley in southern California. This interferogram includes contributions from the Earth's curvature, the topography, and deformation, with one fringe representing 2 phase change.

Following *Zebker et al.* [1994] and *Price and Sandwell* [1998], the phase contribution due to a spheroidal Earth,  $\delta\rho_e$ , can be found by applying the parallel ray approximation

$$\delta\rho_e = B \sin(\theta_0 - \alpha)$$

where  $\theta_0$  is the look angle, defined by  $\cos\theta_0 = \frac{(r_1^2 + \rho^2 + r_2^2)}{2\rho r_1}$  such that  $r_1$  is the distance from the center of the earth to the satellite reference pass ( $A_1$ ) and  $r_2$  is the distance from the center of the earth to the target point  $P$ . This expression for  $\delta\rho_e$  is simply the parallel component of the baseline,  $B_{\parallel}$ .

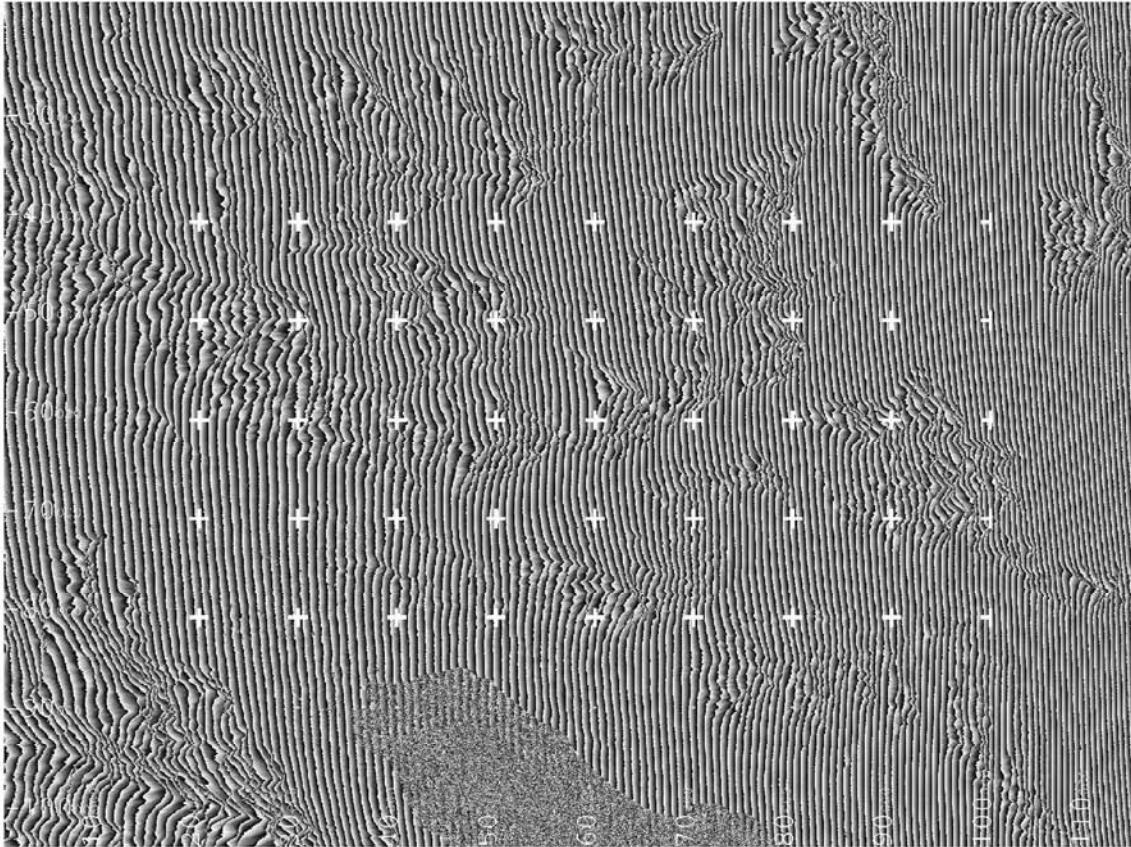


Figure 1.20. Interferogram of the Coachella Valley/Salton Sea area. The fringes are the result of topography, the Earth's curvature, and deformation. Each fringe represents  $2\pi$  phase change.

The geometry for a repeat-pass interferogram for a spheroidal Earth with topography and surface deformation is shown in Figure 1.21. In this setup,  $\rho$  is the range from the "reference" satellite pass to a point on the Earth's surface located at elevation  $z$ ,  $\rho + \delta\rho_e + \delta\rho_t$  is the range from the "repeat" satellite pass to the same location,  $\rho + \delta\rho_e + \delta\rho_t + \delta\rho_d$  is the range from the repeat pass to the same piece of Earth if that point had been displaced by an amount  $D$ ,  $\theta$  is the look angle,  $\alpha$  is the baseline elevation angle, and  $B$  is the baseline length. For satellite-derived SAR images, since the spacecraft is at an altitude of almost 800 km, the three range rays can be considered parallel to each other so that  $\delta\theta_d$  is approximately zero. The contribution to the phase from the topography is  $\delta\rho_t$  and the phase contribution from the displacement of the point is  $\delta\rho_d$ .

Figure 1.22 highlights the same area of the Salton Sea and Coachella Valley as Figure 1.20, but has the effects of geometry and the Earth's curvature ( $\delta\rho_e$ ) removed. These residual fringes are due to contributions from the topography and deformation.

The range difference for the topographic contribution can be written:

$$\delta\rho_e + \delta\rho_t = -B \sin(\theta_0 + \delta\theta_t - \alpha) = -B(\sin(\theta_0 - \alpha)\cos(\delta\theta_t) + \cos(\theta_0 - \alpha)\sin(\delta\theta_t))$$

where  $\delta\theta_t$  is the angular distortion due to topography and is very small due to the height of the satellite above the Earth. Thus

$$\delta\rho_e + \delta\rho_t = -B(\sin(\theta_0 - \alpha) + \delta\theta_t \cos(\theta_0 - \alpha)) = -(B_{\perp} + \delta\theta_t B)$$

where  $B_{\perp}$  is the perpendicular component of the baseline. This relation shows that the topographic effect is directly proportional to the perpendicular baseline length.

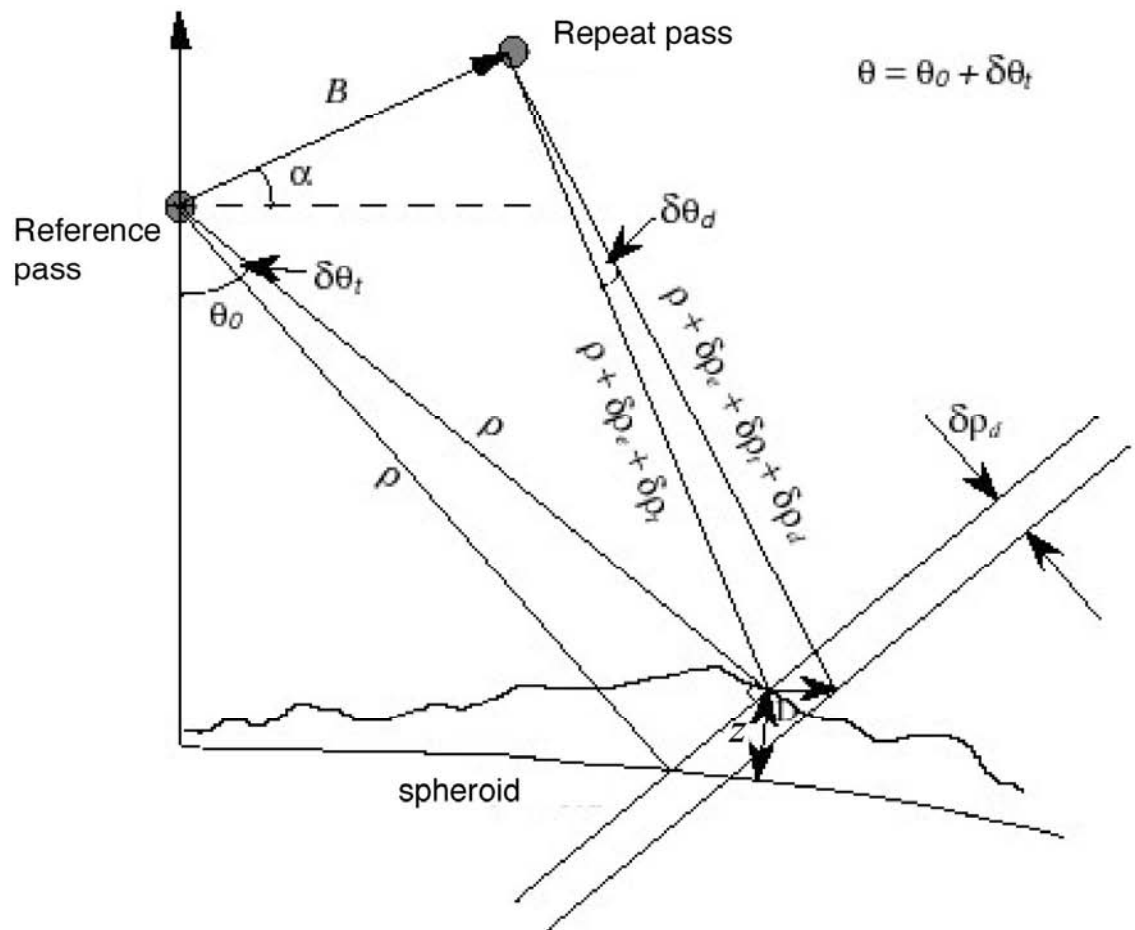


Figure 1.21. InSAR geometry similar to Figure 1.19b, but for a spheroidal Earth with topography and deformation. From Price [1999].

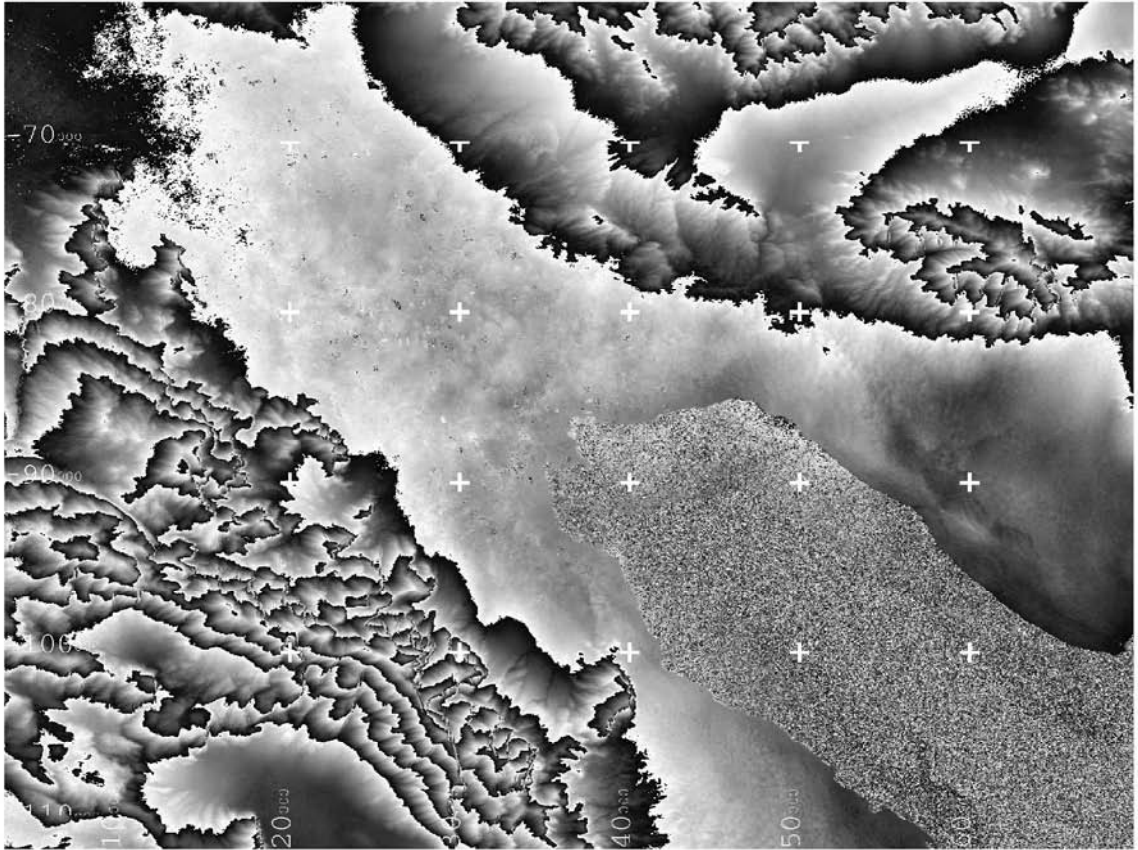


Figure 1.22. Same as Figure 1.20, but with the effects of geometry and the Earth's curvature removed. These fringes are due to contributions from topography and any deformation that has taken place between imaging times.

Once the topographic and flat earth (geometric) phase contributions are removed, the resultant phase is essentially due to deformation:

$$\delta\rho_d = \delta\rho - \delta\rho_e - \delta\rho_t = \delta\rho + B_{\parallel} + \delta\theta_{,B}$$

The deformation in the Salton Sea/Coachella Valley region over a three-year time period spanning the Landers (1992) earthquake is shown in Figure 1.23. Unfortunately, the phase containing this deformation signal is given in modulo  $2\pi$ , meaning that it ranges from 0 to  $2\pi$ . This is called the wrapped phase. In order to calculate elevation or deformation at each pixel, it is necessary to unwrap the phase, or solve for the correct integer ambiguity that needs to be added to each phase measurement to get the correct slant range distance. Phase unwrapping is one of the most difficult steps in interferometry and, thus, has been the focus of numerous studies (e.g., *Ghiglia et al.*, 1987; *Goldstein et al.*, 1988; *Zebker et al.*, 1994b; *Fornaro et al.*, 1996 and many others). Unfortunately, unwrapping the phase can often result in the loss of signal in noisy areas of an interferogram, even if there are fringes that can be visually detected in the wrapped phase. Thus, it is sometimes preferred to leave the phase wrapped when analyzing interferograms in areas of low coherence.

### 1.5.5 INTERFEROMETRIC ERRORS

The resultant phase change,  $\delta\rho_d$ , is only an approximation to the deformation, however. It is actually composed of signal from displacement, atmospheric delay, orbit errors, and noise. Orbital errors depend on the relative, rather than the absolute, positions of the orbits; therefore, residual long-

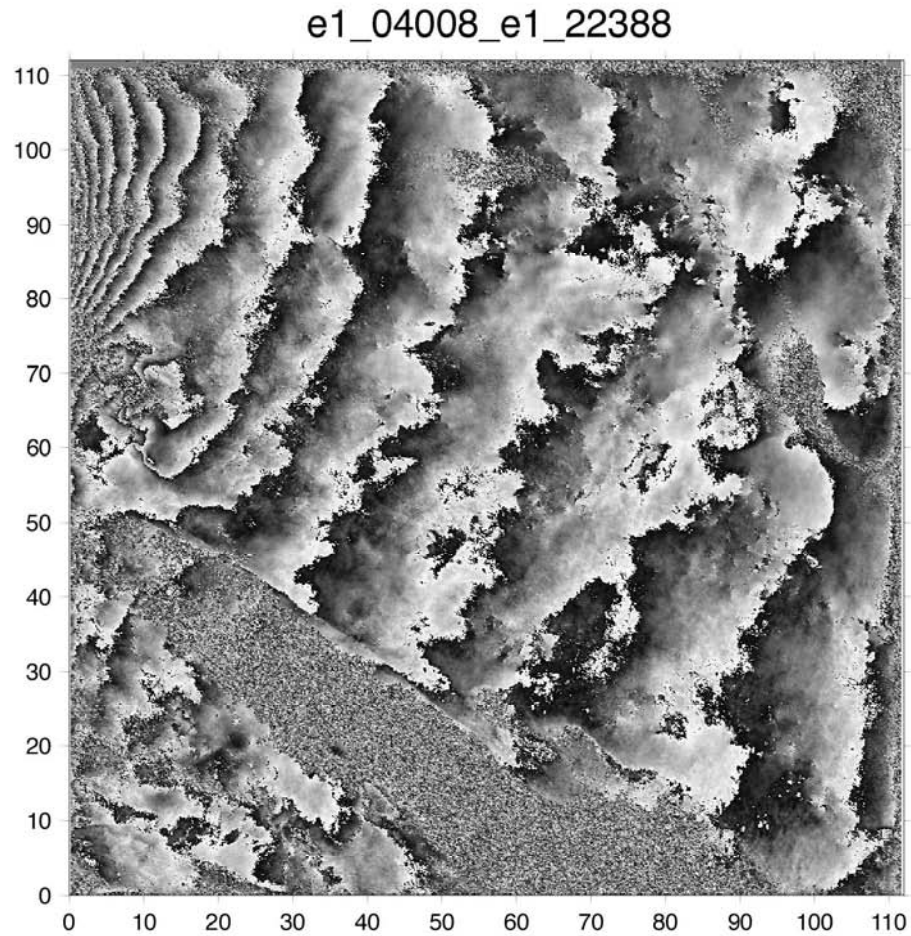


Figure 1.23. Interferogram of the Coachella Valley/Salton Sea region covering a three-year period that spans the Landers earthquake. The topography and error estimates have been removed, so the resultant signal is due to deformation.

wavelength fringes in areas where deformation is small can be attributed to errors in the slave orbit [Massonnet and Feigl, 1998]. To estimate the orbit errors in an interferogram, we choose four points spaced as far apart as possible and count the residual fringes between them. This provides us with a linear gradient that approximates the vertical and lateral deviation of the slave orbit. We remove this gradient from our interferogram, leaving the deformation signal and the atmospheric effects. As the radar signal passes through the Earth's atmosphere, it is delayed due to the water vapor content. This delay varies over the image and can create residual signal that can be mistaken for deformation. Comparing multiple interferograms can help to identify images that are heavily affected by atmospheric disturbances (thunderstorms, cold fronts, etc.) in an effort to isolate those images. Assuming that the atmospheric noise is not correlated on a daily timescale, it is also possible to minimize the atmospheric effects by stacking multiple interferograms to boost the deformation signal and reduce the noise.

The length of the baseline determines the effectiveness of interferometry for specific applications. Increasing baseline length leads to greater sensitivity to height changes (since the topographic contribution is proportional to the perpendicular baseline). However, it also causes decorrelation in the phase and a lower level of coherence. The coherence is a measure of the correlation of the phase information returned from a specific target in the reference image and its corresponding phase in the repeat image. The coherence ranges from 0 to 1 and is a measure of the reliability of the phase. A coherence value of zero means that the cell is totally decorrelated and the measurement is useless, while a coherence value

of 1 implies total correlation of all pixels within the cell. If the baseline reaches its critical length, it will lose all coherence. This critical baseline,  $B_c$ , is defined as:

$$B_c = \frac{\lambda r}{2\delta R_g \cos^2 \theta}$$

where  $r$  is the range and  $\delta R_g$  is the resolution in range. For the ERS-1/2 satellites, the critical baseline is ~1200 meters.

Coherence can also be lost as patches of ground move or there is a change in the dielectric properties of an area over time. This will cause the phase of the signal returned from that patch of ground to be uncorrelated with the phase of previously returned signals. In this case, it is impossible to recover the interferometric phase in that region. This is known as "phase decorrelation" and can be due to numerous natural and man-made activities (e.g., farming, floods, urban activity). Loss of coherence can also be due to thermal noise in the system electronics.

### 1.5.6 APPLICATIONS FOR INTERFEROMETRY

Since the launch of ERS-1, the variety of applications for InSAR has skyrocketed. While topographic mapping was one of the main issues when SAR interferometry was introduced by Graham in 1974 and continues to be an active area of research today, it is the use of interferometry for detecting movements of the Earth's surface that has excited most geophysicists. InSAR can detect deformation due to earthquakes, volcanoes, and landslides, as well as slow subsidence caused by hydrologic variations or petroleum extraction. Thus, it can

be utilized to detect and monitor both natural and anthropogenic landscape changes.

The magnitude of the deformation and the spatial scale over which the movement occurs determine whether or not a signal is measurable by radar interferometry. The limits of detectability include: the pixel size, swath width, the gradient of deformation, and the phase and atmospheric noise levels. On a logarithmic plot of magnitude vs. width (Figure 1.24), these parameters form a truncated parallelogram, with events falling within the parallelogram being detectable by InSAR. The bounds are not hard limits, however, since some processing techniques can overcome each limit. Typical events that fall within the limits are multi-year interseismic slip along faults, glacial displacement, and volcanic deflation. The success of InSAR in studying the displacement at various phases in the earthquake cycle has enabled scientists to gain a better understanding of the mechanics of earthquakes and will hopefully lead to improved hazard assessments for the regions that will be affected by these events.

This dissertation focuses on the use of geodetic measurements to detect aseismic fault creep in the Salton Trough. Chapter 2 introduces rapid-static GPS surveying of a dense network of sites across the Imperial Fault. Standard fault models are used to determine the slip distribution with depth based on the surface displacements. Chapter 3 investigates stacking interferograms of the Coachella Valley and Salton Sea in order to detect creep along the southern San Andreas over the last decade, including triggered slip due to the Landers and Hector Mine earthquakes. Chapter 3 also introduces the concept of permanent scatterers and

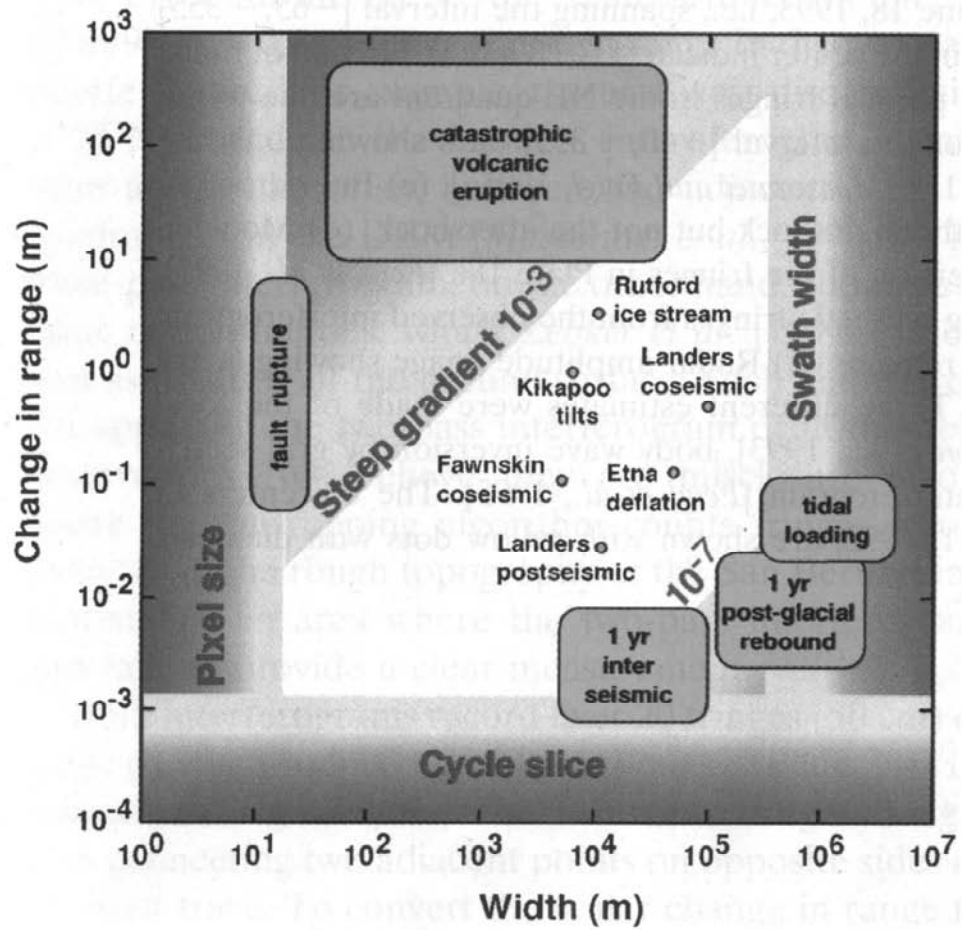


Figure 1.24. The limitations of detection using InSAR. See text for details. From *Massonnet and Feigl* [1998].

how they can be used to improve coherence in interferograms. Appendix 3A presents a photographic survey of permanent scatterers in the Salton Sea region to illustrate the types of objects that produce consistent backscatter in SAR images. Chapter 4 summarizes creep detection methods and results for faults in California and wraps up the main portion of this dissertation. Chapter 5 is based on earlier research and utilizes gravity measurements based on satellite altimetry and shipboard bathymetric data to determine the effective elastic thickness of the lithosphere below the Louisville Ridge. Thus, a wide range of geodetic tools is presented to study various deformation processes of the Earth's lithosphere.

## 1.6 REFERENCES

- Anderson, J.G. and P. Bonin, Earthquake recurrence models and historical seismicity in the Mexicali-Imperial Valley, *Bull. Seism. Soc. Am.*, 77, 562-578, 1987.
- Ashjaee, J. and N. Ashjaee, Basics of High-Precision Global Positioning Systems, Topcon Positioning Systems, 1998.
- Atlantis Scientific, Theory of Synthetic Aperture Radar, [http://www.atlsci.com/library/sar\\_theory.html](http://www.atlsci.com/library/sar_theory.html), 1997.
- Bakun, W. and A. Lindh, The Parkfield, California, earthquake prediction experiment, *Science*, 229, 619-624, 1985.
- Bakun, W.H. and T.V. McEvelly, Recurrence models and Parkfield, California, earthquakes, *J. Geophys. Res.*, 89, 3051-3058, 1984.
- Burford, R.O., Retardations in fault creep rates before local moderate earthquakes along the San Andreas fault system, central California, *Pageoph.*, 126, 499-529, 1988.
- Curlander, J.C. and R.N. McDonough, *Synthetic aperture radar: systems and signal processing*, New York: Wiley, 1991.

- Department of the Army, NAVSTAR Global Positioning System Surveying, EM 1110-1-1003, 1996.
- Elachi, C., Radar Images of the Earth from Space, *Scientific American*, 247, 54-61, 1982.
- Ford, J.P et al., Guide to Magellan Image Interpretation, NASA Report, Pasadena, CA, Nov. 1, 1993, 148 pp.
- Fornaro, G., G. Franceschetti, and R. Lanari, Interferometric SAR phase unwrapping using Green's formulation, *IEEE Trans. Geosci. Remote Sens.*, 34, 720-727, 1996.
- Freeman, T., What is Imaging Radar?, Jet Propulsion Laboratory, <http://southport.jpl.nasa.gov/desc/imagingradarv3.html>, 1996.
- Gabriel, A.K. and R.M. Goldstein, Crossed orbit interferometry: theory and experimental results from SIR-B, *Int. J. Remote Sens.*, 9, 857-872, 1988.
- Genrich, J.F., Y. Bock, and R.G. Mason, Crustal deformation across the Imperial Fault: Results from kinematic GPS surveys and trilateration of a densely-spaced, small-aperture network, *J. Geophys. Res.*, 102, 4985-5004, 1997.
- Gens, R. and J.L. van Genderen, Review article: SAR interferometry - issues, techniques, and applications, *Int. J. Remote Sens.*, 17, 1803-1835, 1996.
- Ghiglia, D., G. Mastin, and L. Romero, Cellular-automata method for phase unwrapping, *J. Opt. Soc. Am.*, 4, 267-280, 1987.
- Goldstein, R.M., H.A. Zebker, and C.L. Werner, Satellite radio interferometry: Two-dimensional phase unwrapping, *Radio Sci.*, 23, 713-720, 1988.
- Graham, L.C., Synthetic interferometer radar for topographic mapping, *Proceedings of the IEEE*, 62, 763-768, 1974.
- King, C.-Y., R.D. Nason, and D. Toucher, Kinematics of fault creep, *Phil. Trans. of the Royal Soc. of London, Series A*, 274, 355-360, 1973.
- Leick, A., *GPS Satellite Surveying*, New York:Wiley, 1990, 352 pp.
- Lyons, S.N., Y. Bock, and R. Nikolaidis, Rapid static GPS surveys of the Imperial Fault, Southern California, *EOS, AGU Fall Meeting Supplement*, 80:F268, 1999.

- Lyons, S.N., Y. Bock, and D.T. Sandwell, Creep along the Imperial Fault, Southern California, from GPS Measurements, in press, *J. Geophys. Res.*, 2002.
- Massonnet, D. and K.L. Feigl, Radar interferometry and its application to changes in the Earth's surface, *Reviews of Geophys.*, 36, 441-500, 1998.
- Massonnet, D., M. Rossi, C. Carmona, F. Adragna, G. Peltzer, K. Feigl, and T. Rabaute, The displacement field of the Landers earthquake mapped by radar interferometry, *Nature*, 364, 138-142, 1993.
- Mileshosky, B., What is Synthetic Aperture Radar? Document #SAND99-0018, <http://www.sandia.gov/radar/whatis.html>, 1999.
- Mileti, D.S. and C. Fitzpatrick, *The Great Earthquake Experiment*, Boulder, Colorado: Westview Press, 1993.
- Price, E., Coseismic and Postseismic Deformations Associated With the 1992 Landers, California, Earthquake Measured by Synthetic Aperture Radar Interferometry, Ph.D. thesis, Univ. of California, San Diego, CA, 1999.
- Price, E.J. and D.T. Sandwell, Small-scale deformations associated with the 1992 Landers, California, earthquake mapped by synthetic aperture radar interferometry phase gradients, *J. Geophys. Res.*, 103, 27,001-27,016, 1998.
- Rees, W.G., *Physical Principles of Remote Sensing*, New York: Cambridge University Press, 1996, 247 pp.
- Scholz, C., *The Mechanics of Earthquakes and Faulting*, New York: Cambridge University Press, 1997, 439 pp.
- Shimazaki, K. and T. Nakata, Time-predictable recurrence model for large earthquakes, *Geophys. Res. Lett.*, 7, 279-282, 1980.
- Steinbrugge, K.V., E.G. Zacher, D. Tocher, C.A. Whitten, and C.N. Claire, Creep on the San Andreas fault, *Bull. Seism. Soc. Am.*, 50, 389-415, 1960.
- Trimble Navigation Systems, All About GPS, <http://www.trimble.com>, 2002.
- Zebker, H. and R. Goldstein, Topographic mapping from interferometric SAR observations, *J. Geophys. Res.*, 91, 4993-5001, 1986.
- Zebker, H.A., P.A. Rosen, R.M. Goldstein, A. Gabriel, and C.L. Werner, On the derivation of coseismic displacement fields using differential radar interferometry: The Landers earthquake, *J. Geophys. Res.*, 99, 19,617-19,634, 1994.

Zebker, H.A., J.F. Vesecky, and Q. Lin, Phase wrapping through fringe-line detection in synthetic aperture radar interferometry, *Appl. Opt.*, 33, 201-208, 1994b.

## Chapter 2

### Creep along the Imperial Fault, Southern California, from GPS

#### Measurements

*Nature shows us only the tail of the lion. But I do not doubt that the lion belongs to it even though he cannot at once reveal himself because of his enormous size.*

-Albert Einstein

Suzanne N. Lyons, Yehuda Bock, and David T. Sandwell

Reprint from *Journal of Geophysical Research*, 2002.

#### 2.1 ABSTRACT

In May of 1999 and 2000, we surveyed with GPS 46 geodetic monuments established by Imperial College, London, in a dense grid (half-mile spacing) along the Imperial Fault, with three additional National Geodetic Survey sites serving as base stations. These stations were previously surveyed in 1991 and 1993. The Imperial College sites were surveyed in rapid-static mode (15-20 minute occupations), while the NGS sites continuously received data for 10 hours per day. Site locations were calculated using the method of instantaneous positioning and velocities were determined relative to one of the NGS base stations. Combining our results with far-field velocities from the Southern California Earthquake Center, we fit the data to a simple elastic dislocation model with 35 mm/yr of right-lateral slip below 10 km and 9 mm/yr of creep from the surface down to 3

km. The velocity field is asymmetrical across the fault and could indicate a dipping fault plane to the northeast or a viscosity contrast across the fault.

## 2.2 INTRODUCTION

An important issue for both earthquake physics and earthquake hazards mitigation is the depth and extent of aseismic fault slip. Some faults remain locked over the entire thickness of the seismogenic zone throughout the earthquake cycle and thus can store maximum seismic moment while other faults slide freely from the surface to the base of the seismogenic zone and, therefore, may be less hazardous [Bürgmann *et al.*, 2000]. This slow movement of the Earth's surface at a fault is known as creep.

Fault friction models (e.g., *Weertman*, 1964; *Savage and Burford*, 1971; *Tse and Rice*, 1986) relate slip at depth to surface displacement. Therefore, one can examine the spatial distribution of crustal displacement over a long period of time (> 5 years) to detect the interseismic signal and determine if a fault is creeping during that time. Creep can be gradual (months to years) or it can occur in short episodes known as “creep events” (lasting hours to days). While creepmeters have excellent temporal sampling, they lack the spatial coverage needed to determine the depth variations in aseismic slip. In contrast, most geodetic measurements lack temporal resolution but, if sufficiently dense, they can be used to infer the slip distribution with depth [*Thatcher*, 1983; *Harris and Segall*, 1987; *Lorenzetti and Tullis*, 1989; *Savage*, 1990; *Savage and Lisowski*, 1993]. Dense geodetic networks, such as the one along the Imperial Fault in

southern California [Mason, 1987], are well suited for observing the near-field spatial distribution of slip that primarily reflects the shallow component of slip on a fault.

Located southwest of the Salton Sea (Figure 2.1), the Imperial Valley has experienced numerous large seismic episodes this century: April 19, 1906 ( $M=6.0+$ ), June 22, 1915 ( $M_L=6.1$  and  $6.3$ ), May 28, 1917 ( $M=5.5$ ), January 1, 1927 ( $M=5.8$ ), May 19, 1940 ( $M_L=7.1$ ), and October 15, 1979 ( $M_L=6.9$ ) [Genrich *et al.*, 1997]. Most of the motion from these earthquakes has occurred along the Imperial Fault, a right-lateral strike-slip fault which runs for 69 km through the eastern portion of El Centro and the western side of Holtville, south into the Mexicali Valley (Figure 2.1). A relatively fast-moving fault, the estimated average slip rate along the Imperial Fault ranges from 15-20 mm/yr based on shoreline deposits [Thomas and Rockwell, 1996] to 35-43 mm/yr based on conventional geodetic surveys [Bennett *et al.*, 1996; Genrich *et al.*, 1997; Wdowinski *et al.*, 2001]. Geodetic rates indicate the Imperial Fault accommodates almost 80% of the total plate motion between the North American and Pacific Plates. The earthquake recurrence interval for the Imperial Fault is on the order of 40 years for  $M_L=6.0$  and 700 years for  $M_L=7.0+$  [Southern California Earthquake Center, 1999, available at [http://www.scecdc.scec.org/group\\_e/release.v2](http://www.scecdc.scec.org/group_e/release.v2)].

The Imperial Fault was first identified from coseismic motion during the 1940 earthquake. Surface rupture from this quake occurred along more than 40 km of the trace. Ellsworth [1990] estimates 60 km of rupture, with displacement

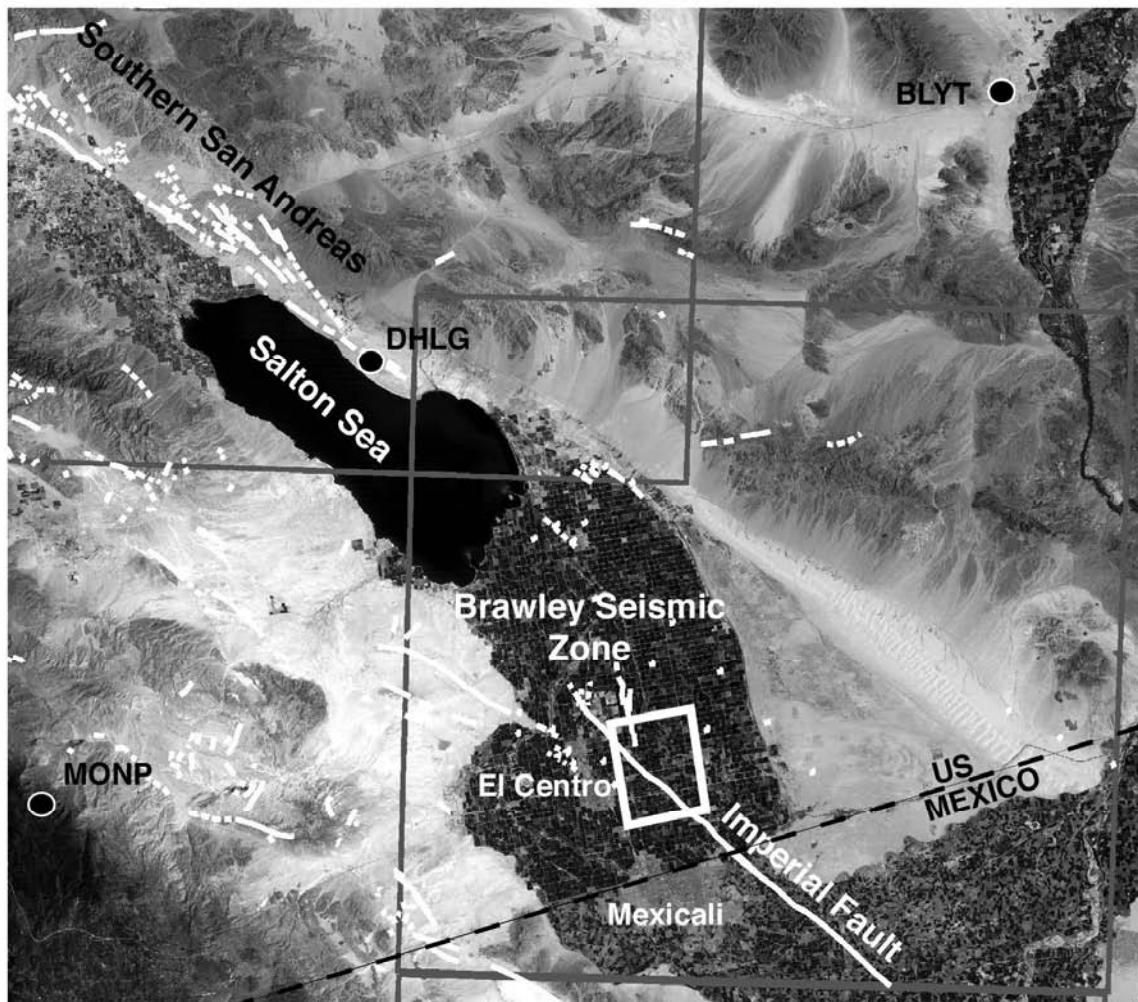


Figure 2.1. The Salton Sea and Imperial Valley, southern California. Major faults are in white, white box indicates GPS survey region, and large gray boxes highlight Synthetic Aperture Radar (SAR) coverage from ERS-1/2.

ranging from about 75 cm near El Centro to 4.5 meters at the Mexican border. Elastic half-space models were used to estimate an additional postseismic creep of 75 cm along the northern section and 1.5 m along the southern part [Reilinger, 1984].

The 1979 Imperial Valley earthquake caused coseismic slip along 30.5 km of the fault trace, with geodetic data yielding displacement ranging from 13 cm along the northern and southern sections of the fault to 48 cm on a 10-km section straddling the U.S.-Mexico border [King and Thatcher, 1998]. The postseismic slip was on the order of 30 cm over the next six months [Sharp *et al.*, 1982].

While it is common practice to determine slip rates and displacement during coseismic events along faults such as the Imperial [e.g., Hartzell and Heaton, 1983; Archuleta, 1984; King and Thatcher, 1998], it is the moment accumulation rate [Savage and Simpson, 1997] during the long interseismic period that may be the key to earthquake prediction. The moment accumulation rate per length of fault is proportional to the slip rate times the height of the locked portion of the fault. Most of this accumulated seismic moment (and elastic energy) is released during the infrequent major events. Thus, according to the elastic rebound theory [Reid, 1969], there is an increased likelihood of a major earthquake in regions with high localized strain rates. In creeping sections of faults, some of the accumulated shear strain is continuously released, which might lower the risk of major earthquake events. Therefore, interseismic near-field deformation characteristics of major southern California faults may provide insight into hazard assessments for this region.

*Wdowinski et al.* [2001] analyzed velocities compiled by the Southern California Earthquake Center (SCEC) Crustal Deformation Working Group from GPS measurements, triangulation, trilateration, and electronic distance measurements [SCEC, 1999] and found a well-defined belt of high strain rate ( $0.5 \mu\text{strain/year}$ ) along the Imperial Fault. This shear belt is characterized by a high level of microseismicity ( $>200$  events in 1997 [Richards-Dinger and Shearer, 2000]), indicating that a large part of the interseismic deformation occurs within the brittle upper crust ( $7.5 \pm 4.5$  km) [Wdowinski et al., 2001].

Along the Imperial Fault, studies of pre-1979-earthquake slip rates using creepmeter measurements [Goultly et al., 1978; Cohn et al., 1982; Louie et al., 1985] yielded only 2-5 mm/yr of fault creep. However, using EDM surveys of fault-crossing lines, *Genrich et al.*, [1997] found an average of 10-14 mm/yr of creep between 1987 and 1993. They attributed this high rate to triggered slip from the 1987 Superstition Hills earthquake, which would imply that current rates would be closer to pre-1979 estimates.

### 2.3 GPS METHODS

During the interseismic period, the relative ground motion across the fault is quite small ( $< 35$  mm/yr), especially for stations close to the fault trace, so it is important to obtain precise positions. By using continuous Global Positioning System (GPS) data, it is possible to determine the location of specific points over small apertures such as the Imperial College network to millimeter accuracy and precision [Bock et al., 2000]. While continuous GPS has high resolution for

displacement at each site, it is difficult to get effective spatial coverage without extremely dense GPS arrays. This is not too problematic in the Los Angeles basin, where taxpayers are willing to spend large amounts of money for earthquake research, but in desert areas such as the Imperial Valley, the cost of installing a dense network of permanent GPS sites becomes unrealistic. Thus, we are forced to use alternate methods for acquiring displacement data.

In areas of sparse GPS, the use of interferometric SAR (InSAR, gray boxes, Figure 2.1) measurements seems ideally suited for observing the shallow component of fault slip [Zebker et al., 1994; Peltzer et al., 1996; Rosen et al., 1996; Massonnet and Feigl, 1998; Vincent, 1998]. The InSAR method works well in arid regions such as north of the Salton Sea, where phase coherence is retained over long periods of time [Lyons et al., 2000; Sandwell and Agnew, 1999]. However, in the farmland of the Imperial Valley, interferograms formed from available SAR images appear noisy due to the loss of phase coherence over time and it is extremely difficult to discern the near-field deformation across the faults in these areas. Therefore, we turn to a more practical method of GPS survey to obtain data in irrigated areas near major faults: the rapid-static survey.

Kinematic GPS surveying yields the greatest number of observation points in the least amount of time compared to static GPS surveying. One station is "fixed" while the other receiver is moved from observation point to observation point. Kinematic GPS determines the position of this roving receiver relative to the known stationary base site at every epoch. The integer cycle, doubly differenced phase ambiguities are resolved, leaving only the three station position

parameters to be solved for at each epoch [*Genrich and Bock, 1992*]. Using dual frequency receivers, only 1-2 minutes at each observation point is required to achieve relative horizontal positional accuracies at the centimeter level for baselines up to ~10 km [*Hofmann-Wellenhof et al., 1997*]. While quite promising for maximizing the number of observation points in minimal time (important in applications such as the generation of high resolution topographic maps), kinematic GPS requires that phase lock be maintained on five or more satellites throughout the entire survey (or recovered in post-processing). Although on-the-fly ambiguity resolution techniques are available, kinematic GPS surveying suffers from initialization and re-initialization problems that limit the ability to resolve reliably and continuously integer-cycle phase ambiguities throughout the survey [*Bock et al., 2000*].

Rapid static surveying, on the other hand, involves fast ambiguity resolution through the utilization of dual frequency receivers and good satellite geometry [*Blewitt, 1993*]. Thus, loss of lock does not affect the solution since the integer cycle phase ambiguities can be reacquired at any time during the survey [*Genrich and Bock, 1992*]. In rapid static mode, as in kinematic mode, one station is stationary while the other receiver roams from site-to-site. *Genrich and Bock* [1992] used a combination of kinematic and rapid static techniques to determine movement across the San Andreas Fault in central California. They showed that, by computing the baseline epoch-by-epoch after resolving for phase ambiguities, it is possible to achieve millimeter horizontal precision with brief (~10 minutes)

occupation times for a short-range ( $< 1$  km) survey during periods of good satellite geometry.

## 2.4 THE IMPERIAL COLLEGE NETWORK

Although various geodetic surveys were performed in the Imperial Valley as early as 1939, these used classic positioning techniques (trilateration and triangulation) on a coarse grouping of stations [*Snay and Drew*, 1988]. In the 1970's and 1980's, under a grant from the U.S. Geological Survey, the Imperial College (IC) of London constructed a dense grid of survey markers in the Imperial Valley near El Centro to monitor motion along the Imperial Fault [*Mason*, 1987]. This network consists of buried monuments in a pattern coinciding with agricultural roads running north-south and east-west every half mile. These stations are identified according to location: the first digit is a letter indicating the north-south position and the second two digits identify the east-west position [*Crook et al.*, 1982].

Various sections of this grid have been surveyed since the last major earthquake in 1979. The most recent studies have used GPS positioning techniques and focused on the main section of the grid (Figure 2.2) [*Genrich*, 1992; *Genrich et al.*, 1997; *Lyons et al.*, 1999; *Lyons et al.*, 2000].

The 1991 survey of *Genrich* [1992] included 67 IC stations with 5 local National Geodetic Survey (NGS) stations and was performed in kinematic mode, with the NGS stations serving as a static base network to maintain sufficient network control and redundancy. Unfortunately, due to poor satellite geometry,

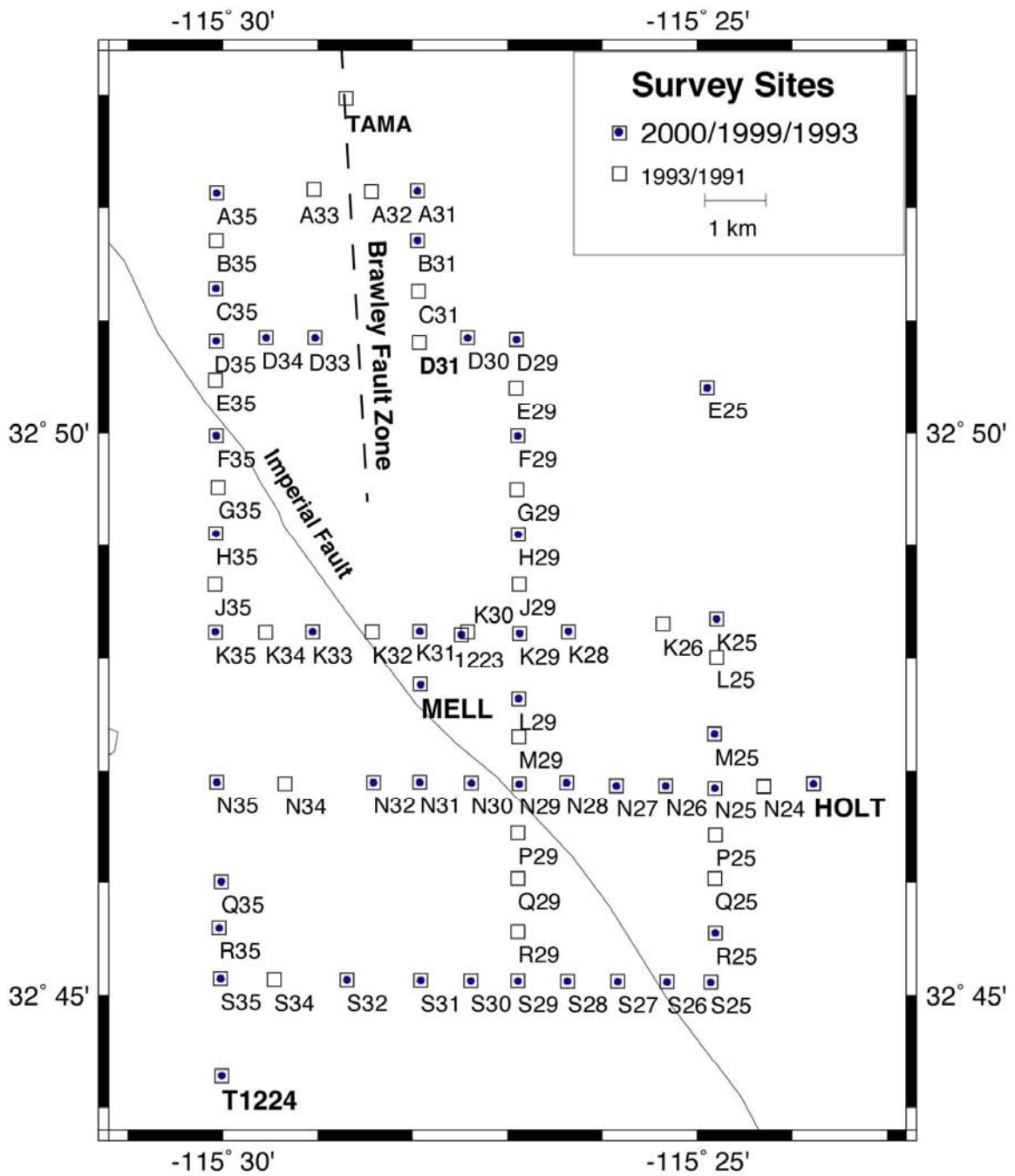


Figure 2.2. Sites surveyed between 1991 and 2000 along the Imperial Fault. NGS stations are shown in bold. Numbers indicate east-west position and letters indicate north-south position.

we were unable to use the data in our analysis. In 1993, *Genrich et al.* [1997] resurveyed the 72 stations using five dual-frequency, full carrier wavelength L2 codeless receivers. Due to improved receiver technology and satellite geometry, they employed the rapid-static procedure, discussed above, where integer cycle ambiguities are resolved during each session, so maintaining phase lock on the satellites in between site occupations is unnecessary.

In May of 1999 and 2000, we resurveyed 46 of these sites in the IC network in rapid-static mode, with 3 additional NGS sites serving as static base stations [*Lyons et al.*, 1999; *Lyons et al.*, 2000]. Thirteen of the IC sites were reoccupied during each survey to determine the precision of the measurements. Occupation time at each site was 15-20 minutes. Three NGS stations were continuously receiving data during the 10 hours of surveying each day and provided a relative reference frame for the IC sites.

## 2.5 DATA PROCESSING

Typically, the processing of field GPS data includes parameter estimation from several hour spans of data sampled every 30 seconds. Site positions are determined by batch least squares or other multi-epoch estimation methods [e.g., *Bock et al.*, 1997]. These techniques often require many epochs of dual-frequency data in order to resolve phase ambiguities and frequently do poorly with short observation spans. Outliers due to multipath and other site-specific errors, receiver losses of lock, and phase cycle slips can strongly influence the final

positioning when using these methods, by complicating reliable integer-cycle ambiguity resolution.

This can be avoided by using a new method of precise GPS processing called instantaneous positioning [*Bock et al.*, 2000]. Estimates of the position of an unknown site are found relative to a known fixed site up to several tens of kilometers away with only a single epoch of data. The positions (and zenith delay parameters) are estimated independently for each observation epoch, thereby avoiding the cleaning and repairing of the input GPS observables for outliers, receiver losses of lock, and phase cycle slips. Receiver loss of lock and phase cycle slips are irrelevant at the single-epoch level since ambiguity resolution is instantaneous and independent at each epoch. Outliers are determined from the single-epoch positions using the interquartile range of the suite of solutions for that site. The interquartile range is a measure of spread or dispersion. It is the difference between the 75<sup>th</sup> percentile (often called Q3) and the 25<sup>th</sup> percentile (Q1). The formula for the interquartile range is therefore simply  $Q3 - Q1$ . Although not used extensively, the interquartile range is a robust measure of scatter and is the preferred method of measuring dispersion in distributions with outliers.

For short to intermediate length baselines, the instantaneous positioning method provides comparable precision to batch processing methods while requiring only a fraction of the amount of data. Since the phase ambiguities and site coordinates are determined independently at each epoch, the solution rate can equal the sampling rate. *Bock et al.* [2000] demonstrated that for small aperture

networks such as the one in this study, averaging instantaneous positions estimated over a 15-20 minute interval is sufficient to achieve 1 mm horizontal position precision. Thus, for studies of fault movement in regions with dense GPS networks, such as the Imperial Valley, a combination of rapid-static surveying and instantaneous positioning provides the most efficient means of precise position estimation.

## 2.6 METHOD

Combining daily orbit solutions, our local static data, and data obtained from three Southern California Integrated GPS Network (SCIGN, <http://www.scign.org>) sites for the survey time period, we determined daily positions for the base stations using the GAMIT software [King and Bock, 1995]. The three SCIGN sites used for the 1999 and 2000 analysis were MONP, BLYT, and DHLG (Figure 2.1, circles). As each of these sites was installed after 1994, for the 1993 survey we used the more westerly SCIGN sites of PIN1, ROCH, SIO2 and SIO3 (<http://sopac.ucsd.edu/maps/>).

Each SCIGN station was tightly constrained to its International Terrestrial Reference Frame 1996 (ITRF96) value [Sillard *et al.*, 1998], with an *a priori* 1 mm standard deviation in each component. The base station coordinates were allowed to adjust freely and daily base station positions were solved in batch mode relative to this SCIGN reference network. One of the base stations (HOLT) was then tightly constrained and all site data was processed epoch-by-epoch relative to the base station network. Unlike Genrich *et al.* [1997], we processed all of the

survey data using instantaneous positioning (discussed above and in *Bock et al.* [2000]) rather than the batch least-squares method. We defined anomalous solutions as three times the interquartile range and removed these points from the suite of position estimates at each site. Final site positions were determined by the median of the remaining estimates.

Precision for a single-epoch solution is in the centimeter range, with precision for the suite of estimates at the millimeter level (Figure 2.3). The precision of the vertical component is generally about a factor of five to ten less than the horizontal component, so we focused on horizontal displacements. Uncertainties for the suite of estimates were ascertained using an empirical relationship derived from *Bock et al.* [2000], in which they determine the baseline scatter associated with various baseline lengths (50 m, 14 km, and 37 km) for different collection times (1, 10, 30, 120, 720, 2880, and 11520 epochs). We used Figure 11 in *Bock et al.* [2000], which shows the interquartile range for short distances based on a 12-week analysis of PIN1-PIN2 (50 m). From this, we interpolated to determine the weights for our single-epoch uncertainties based on the number of data points at each site. Sigma estimates for position were derived from this interquartile range ( $\sigma = \text{IQR}/1.35$ ), assuming the errors were normally distributed (after outliers were excluded). For site S35 (Figure 2.3), the single-epoch sigma values for the north ( $\sigma_n$ ) and east ( $\sigma_e$ ) positions are 5.47 mm and 6.24 mm, respectively, while the vertical standard deviation ( $\sigma_u$ ) is 32.18 mm. The standard deviations for the suite of estimates are  $\sigma_n=1.47$ ,  $\sigma_e=1.45$ , and  $\sigma_u=11.55$

mm. Velocity errors were then defined as  $\sigma_{V_N} = \frac{\sqrt{\sigma_{P1_N}^2 + \sigma_{P2_N}^2}}{t}$ , where  $\sigma_{V_N}$  is the uncertainty in the north component of the average velocity (and likewise for the east component), determined from the positional variances,  $\sigma_{P1_N}^2$  and  $\sigma_{P2_N}^2$ , and  $t$  is the time interval (years).

## 2.7 RESULTS

Results from the 1993-2000 GPS surveys are shown in Figures 2.4-2.6. The horizontal velocity field (Figure 2.4) is coherent and indicates that, relative to the base station HOLT, the eastern side of the fault acts as a relatively stationary block, while the western section experiences a northwesterly motion of about 15 mm/yr. The station positions for 1993, 1999, and 2000 are consistent with linear motion of the sites over the studied time interval. Figure 2.5 shows the positions of four stations over the three survey years, with the best-fit slope for each site. The slopes for the western sites (N30 and Q35) are different from those of the eastern stations (B31 and S26), but all demonstrate a relatively constant velocity over the survey period.

By decomposing the station velocities into their fault-normal and fault-parallel components, we can more accurately assess the nature of interseismic displacement. The fault normal velocities (Figure 2.6, top) indicate a small, steady compression of ~3 mm/yr on the eastern side of the fault, with a slight shift in velocities across the fault. The southwest corner of the survey area indicates a

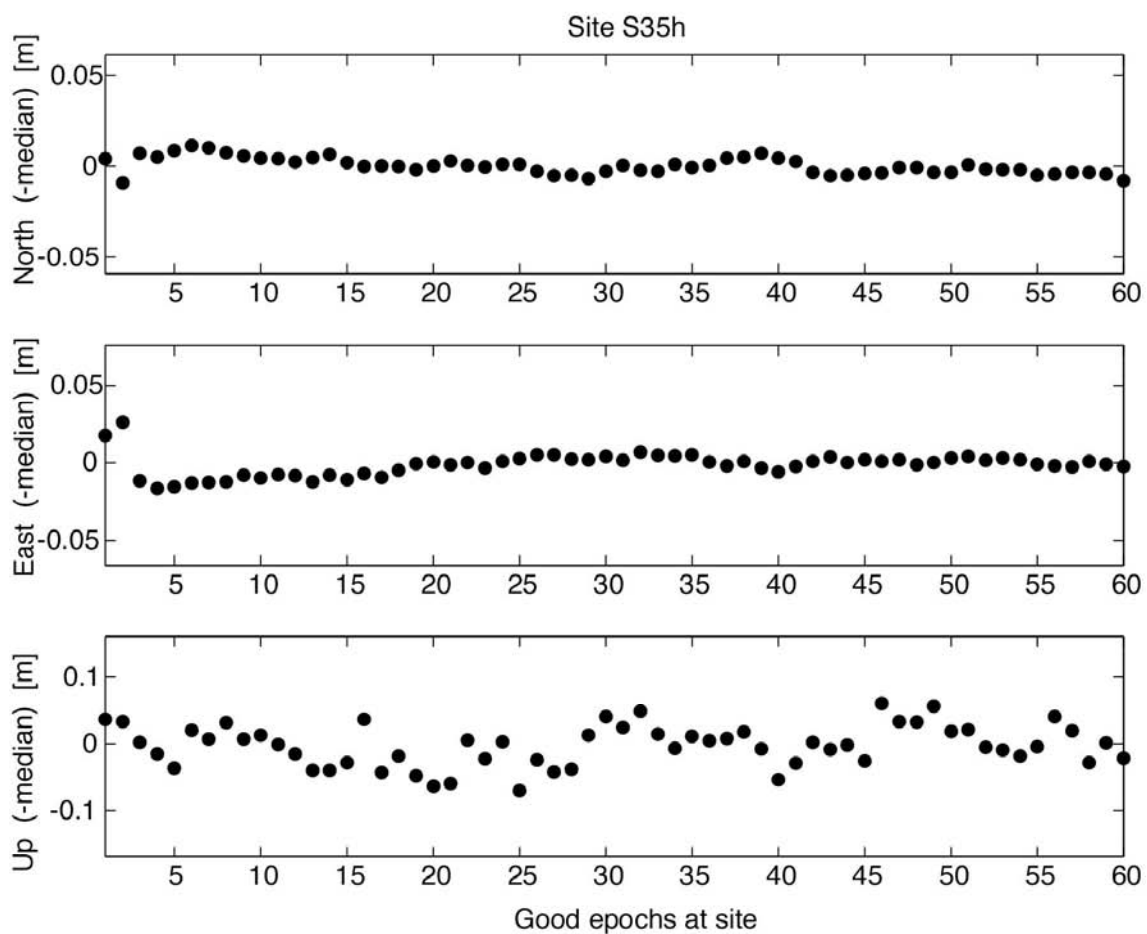


Figure 2.3. Independent single-epoch solutions (every 15 seconds) for baseline between sites S35 and HOLT. The horizontal single-epoch precision is 8 mm, with a decrease by a factor of 10 in the vertical. By stacking numerous epoch solutions, we can reduce the horizontal scatter to  $<1$  mm for the base stations and  $\sim 2$  mm for the roving stations.

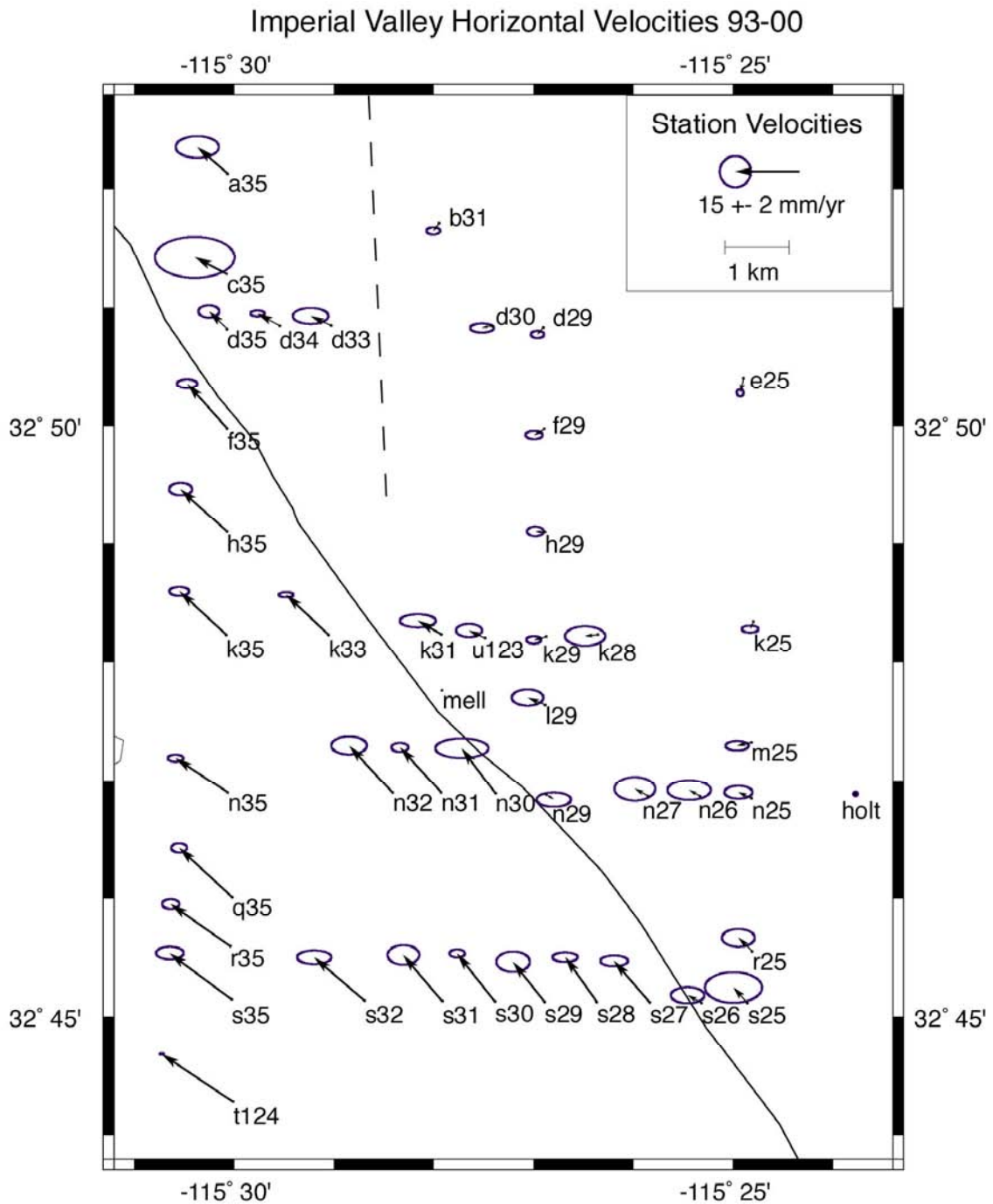


Figure 2.4. Average horizontal velocities between 1993 and 2000 with 95% confidence ellipses. Velocities are relative to the NGS benchmark HOLT and represent the average interseismic motion over the last decade. The velocity fields for both 1993-1999 and 1993-2000 indicate the eastern side of the fault acts as a relatively stationary block, while the western section experiences a northwesterly motion of about 15 mm/yr.

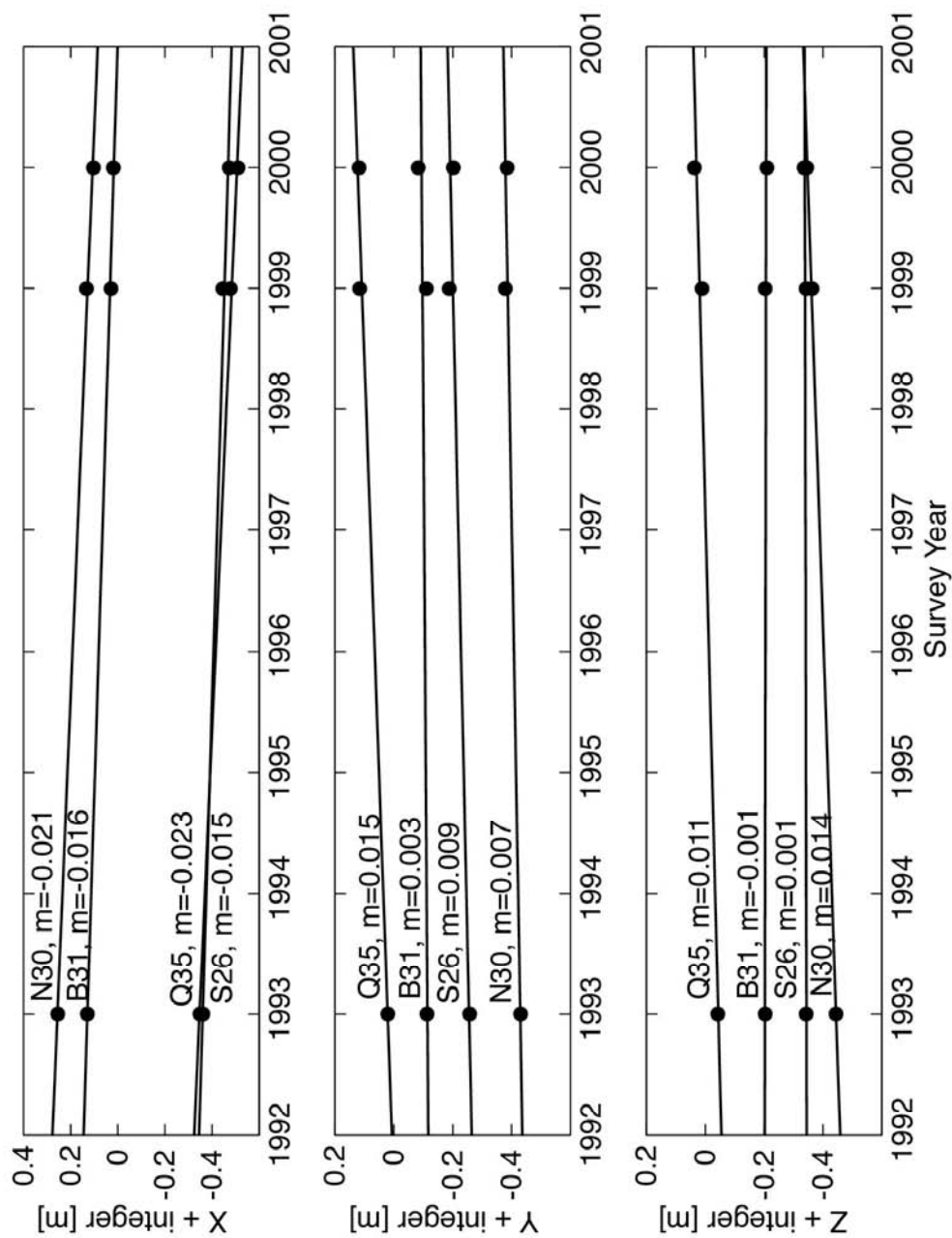


Figure 2.5. Relative ITRF site positions for a variety of sites in the Imperial network with least-squares "best-fit" lines. The consistency of motion in the near-field for sites on either side of the fault at both short (0.5 km, S26 and N30) and long (4.5 km, B31 and Q35) distances indicates a relatively linear motion throughout the interseismic period.

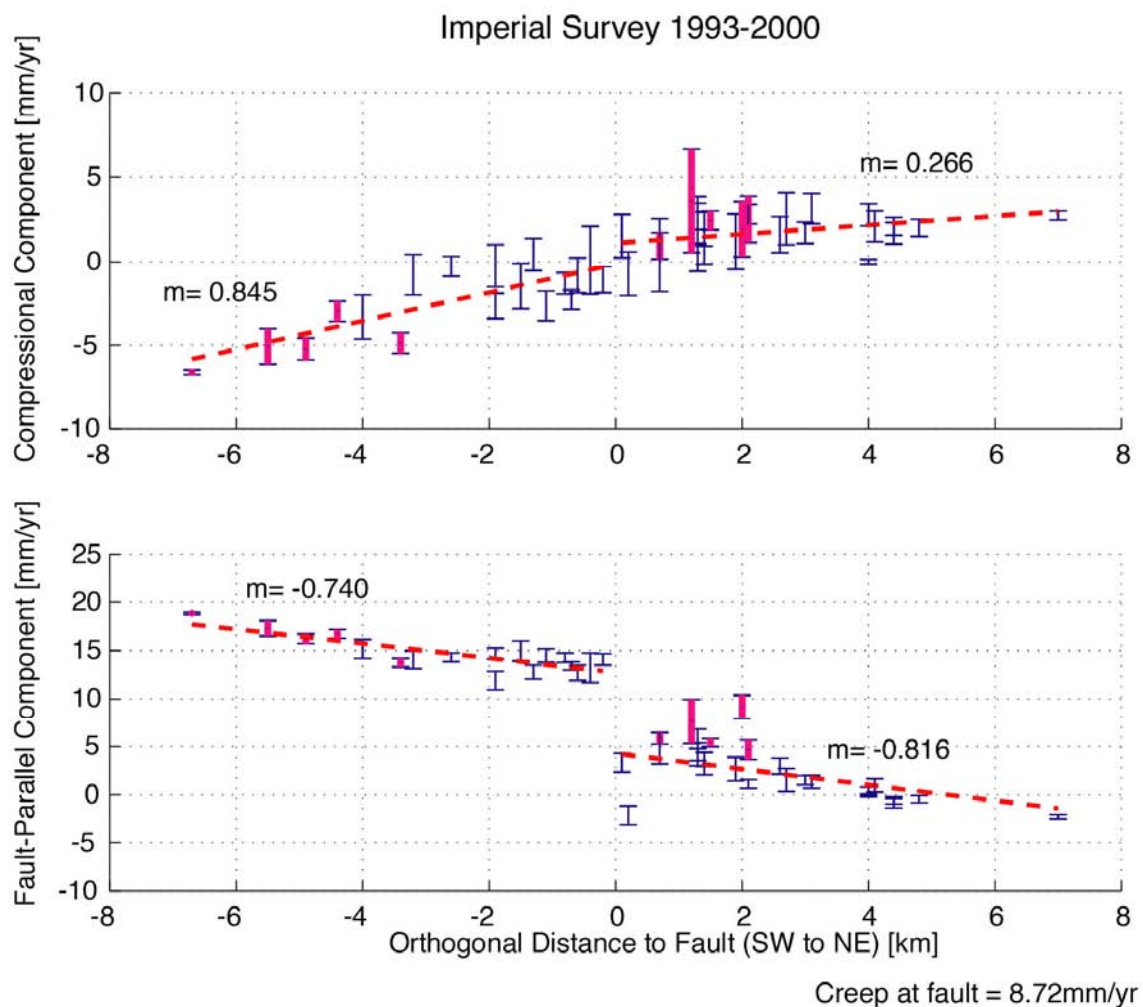


Figure 2.6. Average fault-parallel and fault-normal velocities vs. distance from the fault for 1993-2000. Dashed lines indicate the least-squares fit, with slopes as indicated. The fault strike is defined as  $323^{\circ}$ , measured clockwise from north. The fault-normal velocities (top) indicate a small southwest component ( $10 \pm 2.3$  mm/yr) of relative motion across the entire region. Much of this could be related to the Heber Geothermal Field. See text for details. The fault-parallel component (bottom) shows increasing velocity with distance on either side of the fault, a sign of elastic strain accumulation, with a large jump in velocities at the fault, indicating creep of  $9.0 \pm 1.4$  mm/yr. Results for 1993-1999 are similar.

dilatation of 5-6 mm/yr. This is most likely caused by effects from the Heber Geothermal Field (32°43'N, 115°32'W). *Mason* [1987] found horizontal displacements near this production zone and *Genrich et al.* [1997] attributed a westward deviation of ~7 mm/yr between their model and site T1224 to this geothermal area. Removal of the sites near the geothermal field (thick lines west of the fault - negative orthogonal distance - in Figure 2.6) causes the best-fit slope for the compressional component on the western side of the fault to be reduced from 0.85 to 0.29, a value that is similar to that of the eastern block of sites.

The fault-parallel component (Figure 2.6, bottom) shows increasing velocity with distance on either side of the fault, with a jump of ~9 mm/yr at the fault trace. Sites in the northwest section of our survey area (thick lines east of the fault in Figure 2.6) appear to have the same compressional component as the surrounding region. However, the fault-parallel motion is higher than other sites east of the fault and could be due to the Brawley Seismic Zone. The Brawley Seismic Zone (BSZ) runs north-south between D33 and B31 (see Figure 2.2) and represents a zone of broad deformation in the region. East and southeast of the BSZ, station velocities are near zero and the velocity jump across the fault (e.g., site S26-S27) is ~9.5 mm/yr. However, between the BSZ and the Imperial Fault, velocities reach 9 mm/yr (site A35) and the velocity jump across the fault (site C35-F35) is only ~6 mm/yr. Thus, some of the plate motion across this boundary is accommodated in the northern section of the Imperial Fault by the Brawley Seismic Zone.

Velocities for the Imperial Fault reach two-thirds of the full plate motion within 10 km of the fault. This is consistent with estimates from earlier geodetic surveys [*Snay and Drew, 1988*] and from the SCEC crustal motion map version 2.0 [*SCEC, 1999; Wdowinski et al., 2001*], which revealed interplate deformation over a zone at least 50 km wide north of the Imperial Valley and concentrated within 20 km across the Imperial Fault.

## 2.8 FAULT MODELS

To determine the variation of slip with depth using geodetic data (our GPS data plus far-field velocities derived from sparse continuous GPS coverage [*SCEC, 1999*]), we adopted the fault model originally proposed by *Weertman [1964]* and subsequently developed by *Savage and Lisowski [1993]*. The model consists of two plates sliding past each other with a far-field plate velocity of  $V$ . The simplest model has a fault that slips freely between minus infinity and a deep locking depth of  $D$  (Figure 2.7, solid curve). Our data show evidence for shallow creep between the surface of the earth and some shallow locking depth  $d$ . We use the model of *Savage and Lisowski [1993]* to evaluate this shallow creep signature. In their model, shallow creep occurs when the far-field tectonic stress plus the local stress concentration due to the deep fault slip exceeds the fault strength. Fault strength depends on the coefficient of friction ( $\sim 0.85$  for most rocks [*Byerlee, 1978*]) times the normal stress, where normal stress has a component due to lithostatic pressure plus an unknown tectonic component of normal stress. The details of the model are found in *Savage and Lisowski [1993]*. The unknown parameters are the deep

locking depth  $D$  and the tectonic normal stress. If there is no shallow creep, the displacement follows the smooth arctangent function (Figure 2.7, solid curve, surface locked). If there is combined shallow slip and deep slip (Figure 2.7, dashed curve, surface creep), the displacement field will have a local abrupt transition superimposed on the broad displacement field.

We varied the deep locking depth (7 to 15 km) and the tectonic normal stress (-10 to 50 MPa) to find the corresponding creeping depths. Based on previous estimates of the secular slip rate on the Imperial Fault [Bennett *et al.*, 1996; Working Group on California Earthquake Probabilities, 1995], we used  $V=35$  mm/yr. We estimated the slip rate on the surface at the fault trace to be 9 mm/yr, (Figure 2.6) and then calculated the stress rate for each  $D-d$  pair from Savage and Lisowski [1993] equation A13. We determined the surface velocity caused by the slip on the upper segment of the fault and calculated the rms-misfit to the geodetic measurements (plus an unknown constant).

Figure 2.8 shows the RMS misfit between the GPS-derived velocities and the forward models for the range of locking depths and corresponding creeping depths. The minimum misfit values for  $D=8-12$  km are plotted as crosses, with the minimum misfit for all models at  $D=10$  km,  $d=2.9$  km (star). The dashed contour line represents the minimum RMS value plus 10% and illustrates that there is a wide range of "reasonable" models for our data. The corresponding best-fit forward models for  $D=8-12$  km are shown in Figure 2.9, along with the minimum misfit model for a non-creeping fault ( $D=7$  km,  $RMS=0.43$ ). The creeping models have a lower misfit than the model without creep and are more consistent with the

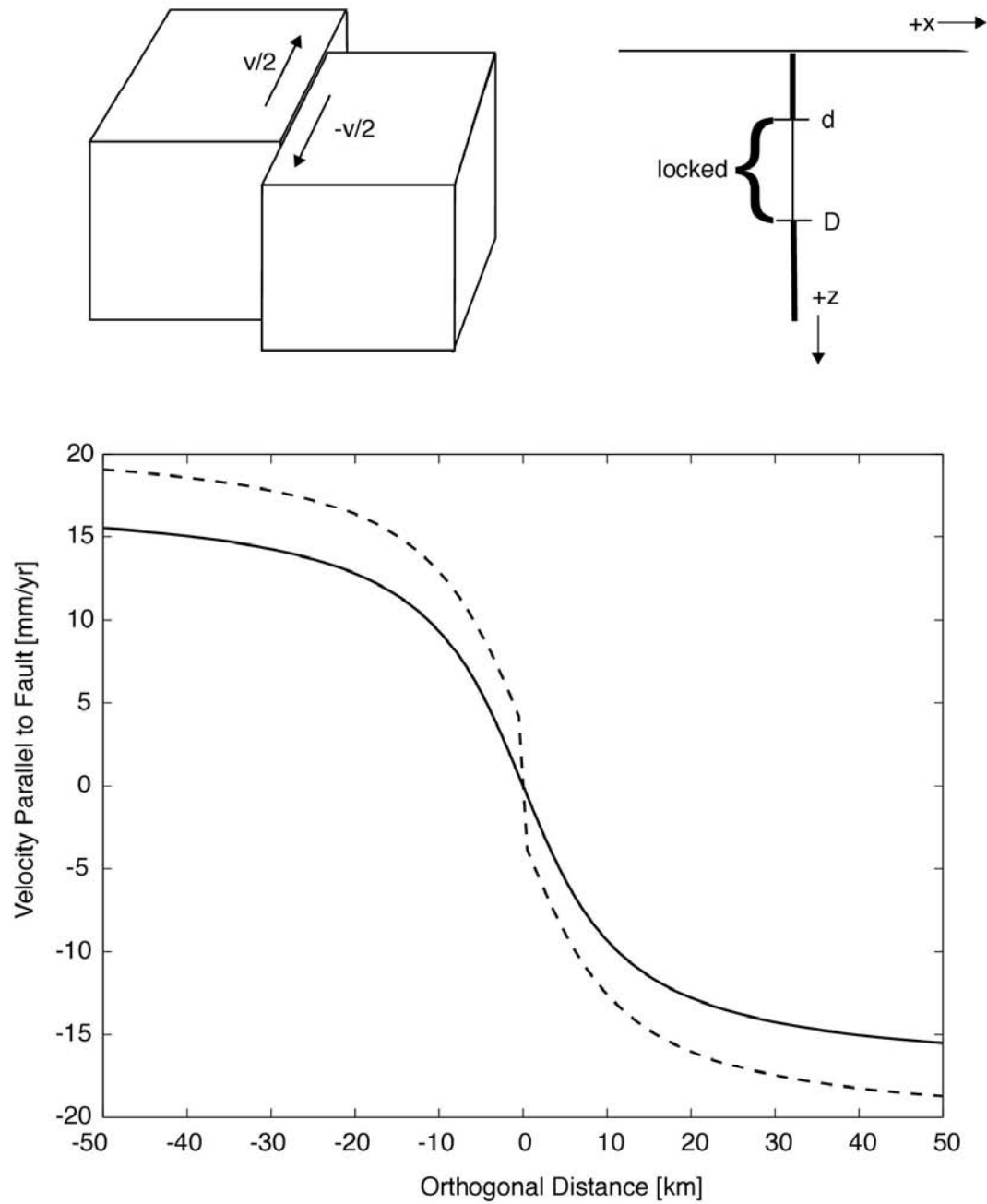


Figure 2.7. Elastic dislocation model using the model of *Savage and Lisowski* [1993]. (top) A right-lateral, strike-slip fault in which two blocks slide past each other with velocity  $V$ . (bottom) The resultant deformation signature across the fault if (solid line) the fault is locked from the surface to depth  $D$  and slips freely below  $D$ , and if (dashed line) the fault is locked only between  $d$  and  $D$ .

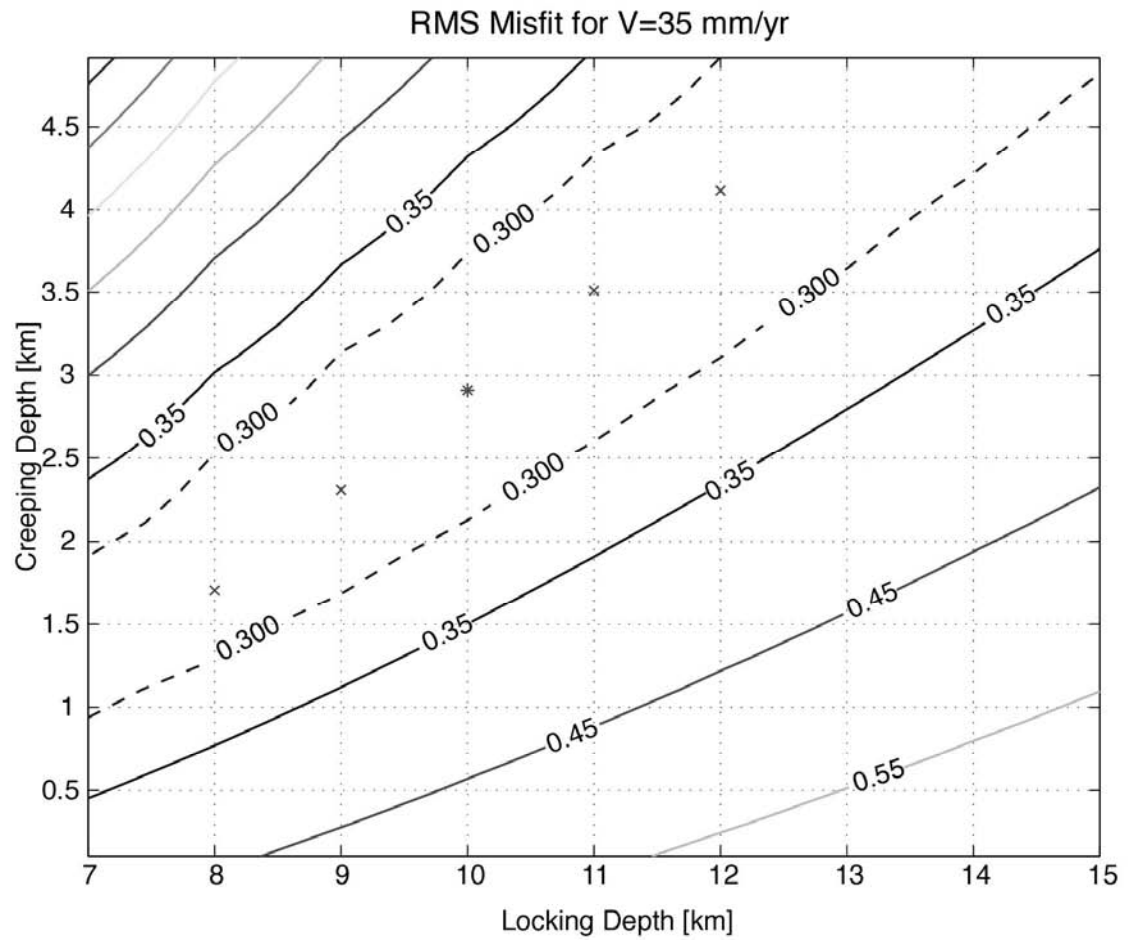


Figure 2.8. RMS misfit for models with varying locking depths and creeping depths. Crosses indicate the minimum misfit model at  $D=8-12$  km. Star ( $D=10$  km) is the minimum misfit of all models.

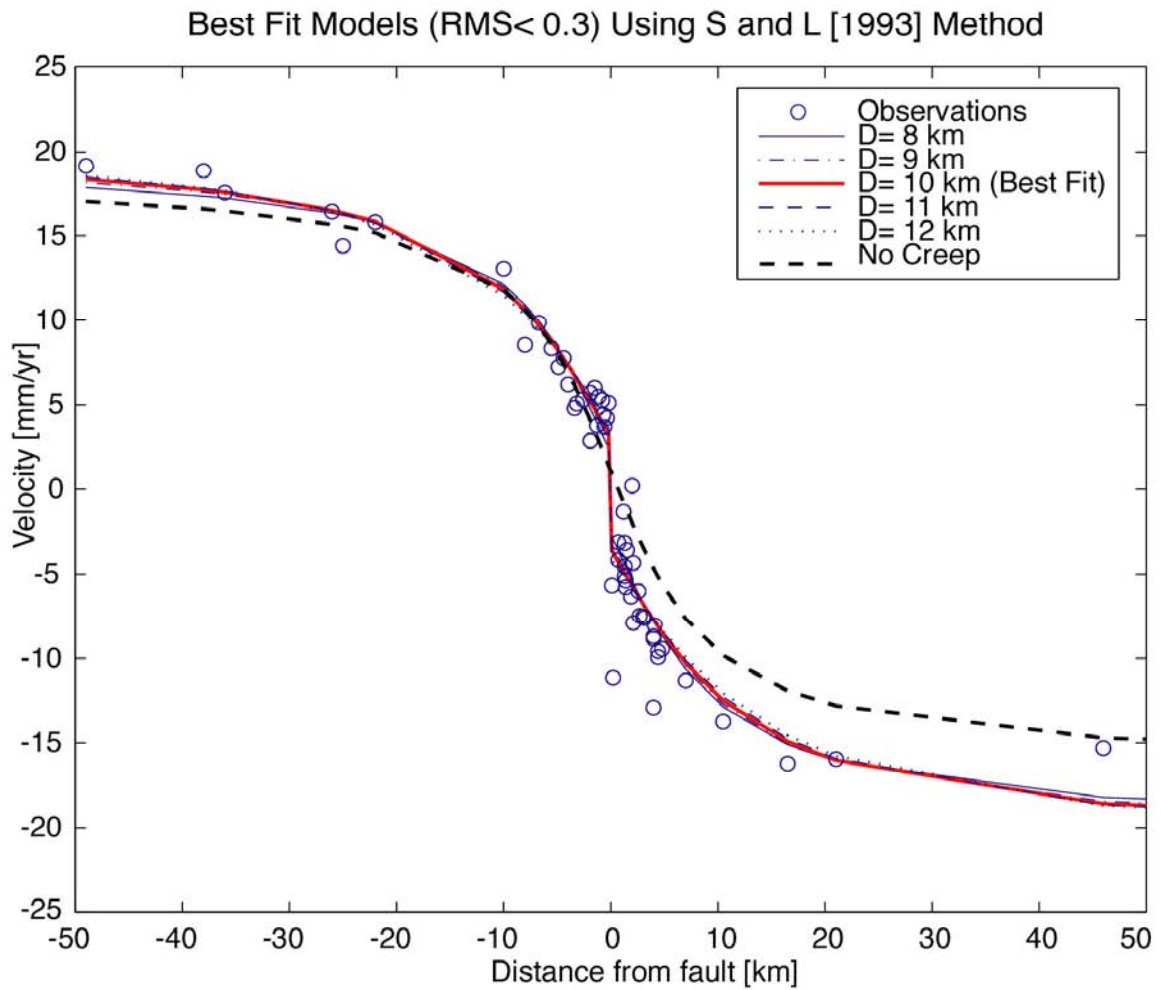


Figure 2.9. Minimum misfit models from Figure 2.8, plotted with average fault-parallel velocities with distance from the fault (circles) from both our surveys (near-field <10 km) and the SCEC estimates (far-field >10 km). Dashed line is minimum misfit model without creep.

overall deformation pattern across the fault. However, it is difficult to distinguish between the creeping models, indicating a range of locking and creeping depths that fit the geodetic data.

Thus, we look at the strain rate for a range of deep slip rates and depths ( $\mu=30$  GPa). This is shown in Figure 2.10, with the expected strain rates for our minimum misfit models plotted as crosses. The 2001 study by *Wdowinski et al.*, which used the SCEC velocity field, version 2.0 [SCEC, 1999] to determine the shear strain rates along the San Andreas Fault System, revealed a well-defined belt of high strain rate along the Imperial Fault, with a maximum strain of  $\dot{\tau}_{\max} = 0.53 \mu\text{strain/yr}$ . The shaded box in Figure 2.10 represents models which would produce strain rates of 0.3-0.53  $\mu\text{strain/yr}$  for  $V=30-40$  mm/yr. Our minimum misfit model for  $D=10$  km,  $d=2.9$  km (best fit for all models) is the only one that coincides with this shaded region. Therefore, we choose this as the most reasonable model for the Imperial Fault.

## 2.9 DISCUSSION

The pattern of deformation across the Imperial Fault indicates that there is combined shallow slip and deep slip (Figure 2.9). However, the deformation is not symmetrical across the fault, which could indicate that the fault plane is dipping to the northeast. Previous refraction surveys [*Fuis et al.*, 1982] along the Imperial Fault, along with strong ground motion data [*Archuleta*, 1984] from the 1979 Imperial Valley earthquake and subsequent elevation surveys [*Reilinger and Larsen*, 1986] indicate that this section of the fault is dipping  $80^\circ$  down to the east.

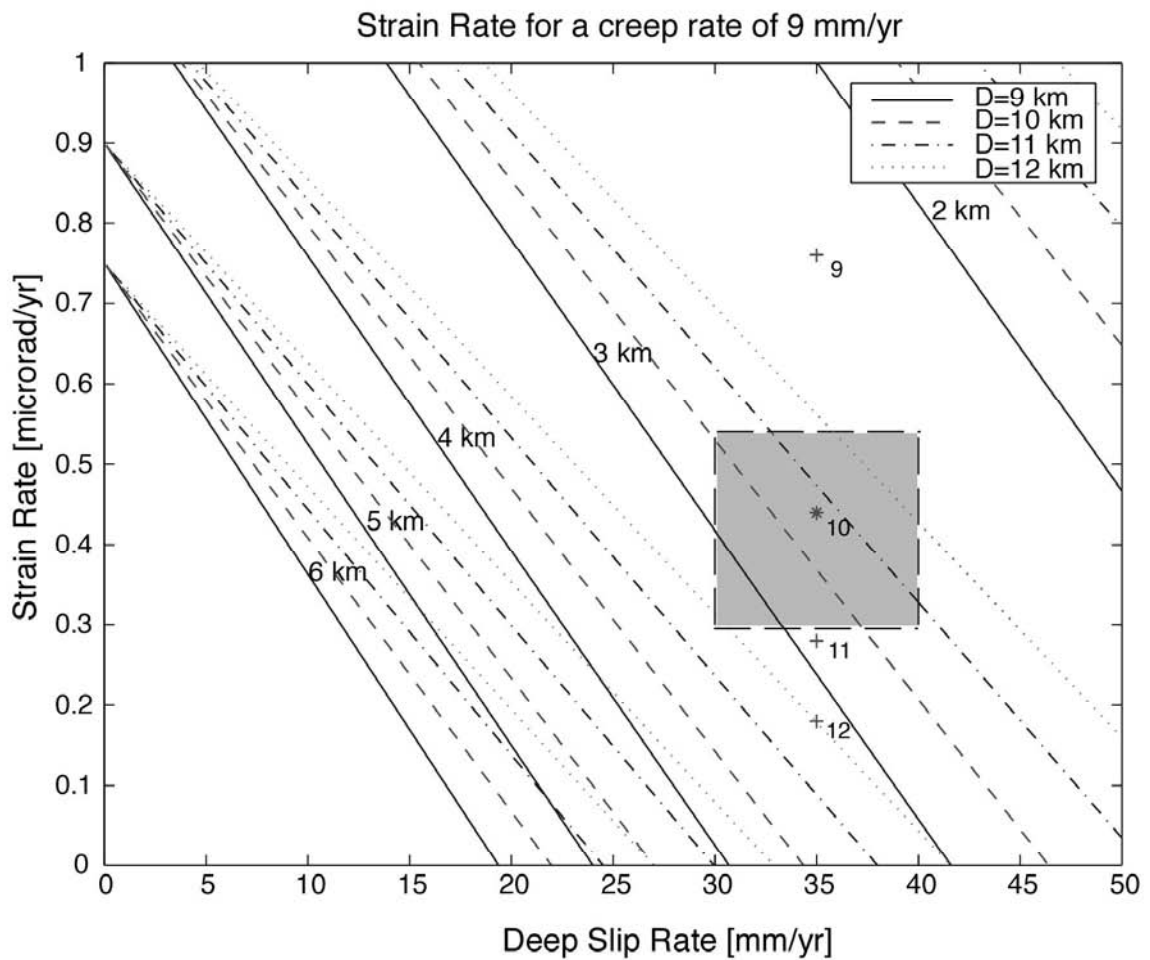


Figure 2.10. Strain rate estimates for various fault models. Minimum misfit models from Figure 2.8 are plotted as crosses, with best-fit model represented by the star. Shaded region coincides with strain estimates for the Imperial Fault from *Wdowinski et al.* [2001].

However, there are not enough data points east of the fault (only one station 20-60 km from the fault) for us to determine this with any certainty.

Another possible explanation for the asymmetry can be inferred from *Malservisi et al.* [2001], who showed that, for the Eastern California Shear Zone (ECSZ), a high viscosity contrast between the Basin and Range Province and the Sierra Nevada block produces an asymmetric surface velocity field across this region. While the eastern "weak" side of the ECSZ appears to accommodate most of the deformation in the region, the cold western side behaves as a strong, almost rigid block, with a flat velocity field 20-100 km from the fault and a steep gradient within 20 km of the fault. This is similar to what we see along the Imperial Fault (Figure 2.9), with the southwestern side of the fault appearing to behave in a weaker fashion than the northeastern side. Without more knowledge of the heat flow within this region and more detailed modeling, however, it is difficult to discern whether heat flow, fault geometry, or a combination of the two contributes to the asymmetric deformation across the Imperial Fault.

Fitting frictional fault models to the data, we find that the data fits well with a model in which the Imperial Fault is creeping down to ~3 km at a surface rate of 9 mm/yr, with 35 mm/yr of right-lateral free slip below 10 km. The locking depth is similar to the best-fit models from 1979 coseismic data [*Olsen and Apsel*, 1982; *Hartzell and Helmberger*, 1982; *Hartzell and Heaton*, 1983; *King and Thatcher*, 1998] and is consistent with prior GPS results [*Genrich et al.*, 1997] and seismicity catalogs [*Johnson and Hill*, 1982; *Richards-Dinger and Shearer*, 2000]. The creep rate is higher than previous studies of pre-1979 earthquake rates using

creepmeter measurements (2-5 mm/yr) [Goultly *et al.*, 1978; Cohn *et al.*, 1982; Louie *et al.*, 1985] and is closer to the post-Superstition Hills estimates by Genrich *et al.* [1997].

## 2.10 CONCLUSIONS

By investigating the creep characteristics over different faults in southern California, it might be possible to discern characteristics specific to certain fault types. The tectonic implications of fault creep are still debated, with some investigators believing creep is the first step in failure leading to major earthquakes (preseismic slip) [Nason, 1973], while others argue that creep reduces stress buildup along faults, therefore precluding very large earthquakes along the creeping section [Prescott and Lisowski, 1983; Bürgmann *et al.*, 2000]. Regardless, most models of earthquake generation use creep to load asperities on a fault, which subsequently fail in earthquakes. Thus, creep studies are important in determining seismic hazard along active faults in southern California.

The density of GPS measurements along the Imperial Fault makes it possible for us to assess the nature of the near-field motion of this fault over time. Our results for the Imperial Fault show a coherent velocity field in which the fault has been creeping 9 mm/yr over the last decade. The increase in creep rate since 1979 could be due to an underestimate in prior creep rates caused by the use of creepmeters in earlier studies versus our geodetic means, as has been reported by Lisowski and Prescott [1981] and Langbein *et al.* [1983]. However, it may also imply a longer-term increase in creep rates since the last major earthquake and a

corresponding decrease in the hazard for another major earthquake along this section of the Imperial Fault.

Our next step will be to use Interferometric Synthetic Aperture Radar (InSAR) and permanent scatterers [*Haynes, 1999; Ferretti et al., 2000; Ferretti et al., 2001*] along the Imperial and Cerro Prieto Faults, to look at the entire deformation field in these regions. By comparing the InSAR results with our GPS measurements and an updated SCEC crustal motion map (version 3.0), we should get a clearer indication of the behavior of these major faults in southern California and, perhaps, the risk associated with them.

## 2.11 ACKNOWLEDGEMENTS

The authors would like to thank the numerous students who comprised the Imperial Fault survey teams of 1999 and 2000. Some of the figures were created using the GMT software of *Wessel and Smith [1991]*. Reviews by Roland Bürgmann, Tim Dixon, and Mike Lisowski led to a considerable improvement in our slip model and in the final version of this paper. This work was supported by a Department of Defense, National Defense Science and Engineering Graduate Fellowship (S.N. Lyons), NASA Earth Systems Science Fellowship (S.N. Lyons), and NSF Earth Sciences grant NSF EAR-0105896 (D.T. Sandwell). This research was also supported by the Southern California Earthquake Center. SCEC is funded by NSF Cooperative Agreement EAR-8920136 and USGS Cooperative Agreements 14-08-0001-A0899 and 1434-HQ-97AG01718. The SCEC contribution number for this paper is 681.

## 2.12 REFERENCES

- Archuleta, R. J., A faulting model for the 1979 Imperial Valley earthquake, *J. Geophys. Res.*, *89*, 4559-4585, 1984.
- Bennett, R. A., W. Rodi, and R. E. Reilinger, Global Positioning System constraints on fault slip rates in southern California and northern Baja, Mexico, *J. Geophys. Res.*, *101*, 21,943-21,960, 1996.
- Blewitt, G., Advances in Global Positioning System technology for geodynamics investigations: 1978-1992, in *Contributions of Space Geodesy to Geodynamics Technology, Geodyn. Ser.*, vol 25, edited by D.E. Smith and D.L. Turcotte, 195-213, AGU, Washington, D.C, 1993.
- Bock, Y., R. Nikolaidis, P. J. de Jonge, and M. Bevis, Instantaneous geodetic positioning at medium distances with the Global Positioning System, *J. Geophys. Res.*, *105*, 28,223-28,253, 2000.
- Bock Y., S. Wdowinski, P. Fang, J. Zhang, S. Williams, H. Johnson, J. Behr, J. Genrich, J. Dean, M. van Domselaar, D. Agnew, F. Wyatt, K. Stark, B. Oral, K. Hudnut, R. King, T. Herring, S. Dinardo, W. Young, D. Jackson, and W. Gurtner, Southern California Permanent GPS Geodetic Array: Continuous measurements of crustal deformation between the 1992 Landers and 1994 Northridge earthquakes, *J. Geophys. Res.*, *102*, 18,013-18,033, 1997.
- Bürgmann, R., D. Schmidt, R.M. Nadeau, M. d'Alessio, E. Fielding, D. Manaker, T. V. McEvelly, and M. H. Murray, Earthquake potential along the northern Hayward fault, California, *Science*, *289*, 1178-1182, 2000.
- Byerlee, J. D., Friction of rocks, *Pure Appl. Geophys.*, *116*, 615-626, 1978.
- Cohn, S.N., C. R. Allen, R. Gilman, and N. R. Goult, Preearthquake and postearthquake creep on the Imperial Fault and the Brawley fault zone, in *The Imperial Valley, California, Earthquake of October 15, 1979, U.S. Geol. Surv. Prof. Paper*, *1254*, 15-24, 1982.
- Crook, C. N., R. G. Mason, and P. R. Wood, Geodetic measurements of horizontal deformation on the Imperial Fault, *U.S. Geol. Surv. Prof. Paper*, *1254*, 183-191, 1982.
- Ellsworth, W. L., Earthquake history, 1769-1989, in *The San Andreas Fault System, California*, edited by R.E. Wallace, *U.S. Geol. Surv. Prof. Paper*, *1515*, 152-187, 1990.

- Ferretti, A., C. Prati, and F. Rocca, Nonlinear subsidence rate estimation using permanent scatterers in differential SAR interferometry, *IEEE Trans. Geos. Remote Sens.*, 38, 2202-2212, 2000.
- Ferretti, A., C. Prati, and F. Rocca, Permanent scatterers in SAR interferometry, *IEEE Trans. Geos. Remote Sens.*, 39, 2001.
- Fuis, G. S., W. D. Mooney, J. H. Healey, G. A. McMechan, and W. J. Lutter, Crustal structure of the Imperial Valley region, *U.S. Geol. Surv. Prof. Paper, 1254*, 25-50, 1982.
- Genrich, J.F., Geophysical applications of GPS kinematic techniques, Ph.D. thesis, Univ. of Calif., San Diego, 1992.
- Genrich, J.F. and Y. Bock, Rapid resolution of crustal motion at short ranges with the Global Positioning System, *J. Geophys. Res.*, 97, 3261-3269, 1992.
- Genrich, J.F., Y. Bock, and R. G. Mason, Crustal deformation across the Imperial Fault: Results from kinematic GPS surveys and trilateration of a densely-spaced, small-aperture network, *J. Geophys. Res.*, 102, 4985-5004, 1997.
- Gouly, N. R., R. O. Burford, C. R. Allen, R. Gilman, C. E. Johnson, and R. P. Keller, Large creep events on the Imperial Fault, California, *Bull. Seismol. Soc. Am.*, 68, 517-521, 1978.
- Harris, R. A., and P. Segall, Detection of a locked zone at depth on the Parkfield, California, segment of the San Andreas fault, *J. Geophys. Res.*, 92, 7945-7962, 1987.
- Hartzell, S. H., and T. H. Heaton, Inversion of strong ground motion and teleseismic waveform data for the fault rupture history of the 1979 Imperial Valley, California, earthquake, *Bull. Seismol. Soc. Am.*, 73, 1553-1583, 1983.
- Hartzell, S. H., and D. V. Helmberger, Strong-motion modeling of the Imperial Valley earthquake of 1979, *Bull. Seismol. Soc. Am.*, 72, 571-596, 1982.
- Haynes, M., New developments in wide-area precision surveying from space, *Mapping Awareness*, 13, 40-43, 1999.
- Hofmann-Wellenhof, B., H. Lichtenegger, and J. Collins, GPS: Theory and practice, Springer-Verlag/Wien, New York, 389 pp., 1997.
- Johnson, C. E. and D. P. Hill, Seismicity of the Imperial Valley, in *The Imperial Valley, California, Earthquake of October 15, 1979*, *U.S. Geol. Surv. Prof. Paper, 1254*, 15-24, 1982.

- King, N.E. and W. Thatcher, The coseismic slip distributions of the 1940 and 1979 Imperial Valley, California, earthquakes and their implications, *J. Geophys. Res.*, *103*, 18,069-18,086, 1998.
- King, R.W. and Y. Bock, Documentation of the GAMIT GPS Analysis Software, v.9.4, Mass. Inst. of Technol., Cambridge, and Scripps Inst. of Oceanogr., La Jolla, Calif., 1995.
- Langbein, J., A. McGarr, M.J.S. Johnston, and P. W. Harsh, Geodetic measurements of postseismic crustal deformation following the 1979 Imperial Valley earthquake, California, *Bull. Seism. Soc. Am.*, *73*, 1203-1224, 1983.
- Lisowski, M. and W. H. Prescott, Short-range distance measurements along the San Andreas fault system in central California, 1975 to 1979, *Bull. Seismol. Soc. Am.*, *71*, 1607-1624, 1981.
- Louie, J. N., C. R. Allen, D. C. Johnson, P.C. Haase, and S.N. Cohn, Fault slip in Southern California, *Bull. Seism. Soc. Am.*, *75*, 811-833, 1985.
- Lorenzetti, E. and T. E. Tullis, Geodetic predictions of strike-slip fault model: Implications for intermediate- and short-term earthquake prediction, *J. Geophys. Res.*, *94*, 12343-12361, 1989.
- Lyons, S. N., Y. Bock, and R. Nikolaidis, Rapid static GPS surveys of the Imperial Fault, Southern California, *EOS, AGU Fall Meeting Supplement*, 80:F268, 1999.
- Lyons, S. N., Y. Bock, and D. T. Sandwell, Near-field crustal deformation and creep characteristics in the Imperial Valley, *EOS, AGU Fall Meeting Supplement*, 81, p. F328, 2000.
- Mason, R. G., Geomensor surveys in the Imperial Valley, California, report, Geol. Dept., Imperial College, London, 1987.
- Massonnet, D., and K.L. Feigl, Radar interferometry and its applications to changes in the Earth's surface, *Reviews of Geophys.*, *36*, 441-500, 1998.
- Nason, R. D., Fault creep and earthquakes on the San Andreas Fault, in *Proceedings, Conference of Tectonic Problems of the San Andreas Fault System*, R. L. Kovach and A. Nur, eds., Stanford Univ. Publ. in Geol. Sci. 13, pp. 275-285, 1973.
- Olson, A.H., and R.J. Apsel, Finite faults and inverse theory with applications to the 1979 Imperial Valley earthquake, *Bull. Seism. Soc. Am.*, *72*, 1969-2001, 1982.

- Peltzer, G., P. Rosen, F. Rogez, and K. Hudnut, Postseismic rebound in fault step-overs caused by pore fluid flow, *Science*, 273, 1,202-1,204, 1996.
- Prescott, W. H. and M. Lisowski, Strain accumulation along the San Andreas Fault system east of San Francisco Bay, California, *Tectonophysics*, 97, 41-56, 1983.
- Reid, H.F., The mechanics of the earthquake, in *The California earthquake of April 18, 1906, Report of the State Earthquake Investigation Commission*, vol. 2, Carnegie Inst. Publ. 87, 192 pp., 1910. (Reprinted, 1969)
- Reilinger, R., Coseismic and postseismic vertical movements associated with the 1940 M 7.1 Imperial Valley, California, earthquake, *J. Geophys. Res.*, 89, 4531-4537, 1984.
- Reilinger, R., and S. Larsen, Vertical crustal deformation associated with the 1979 M=6.6 Imperial Valley, California earthquake: Implications for fault behavior, *J. Geophys. Res.*, 91, 14,044-14,056, 1986.
- Richards-Dinger, K. B. and P. M. Shearer, Earthquake locations in southern California obtained using source specific station terms, *J. Geophys. Res.*, 105, 10,939-10,960, 2000.
- Rosen, P. A., S. Hensley, H.A. Zebker, F.H. Webb, and E. Fielding, Surface deformation and coherence measurements of Kilauea Volcano, Hawaii from SIR-C radar interferometry, *J. Geophys. Res.*, 101, 23,109-23,125, 1996.
- Sandwell, D., and D. Agnew, Strain accumulation and fault creep on the southern San Andreas Fault: 1992 to present, *EOS, AGU Fall Meeting Supplement*, 80, 1999.
- Savage, J.C., Equivalent strike-slip earthquake cycles in half-space and lithosphere-asthenosphere earth models, *J. Geophys. Res.*, 95, 4873-4879, 1990.
- Savage, J.C., and R. O. Burford, Discussion of paper by C. H. Scholz and T. J. Fitch, Strain accumulation along the San Andreas Fault, *J. Geophys. Res.*, 76, 6469-6479, 1971.
- Savage, J.C., and M. Lisowski, Inferred depth of creep on the Hayward Fault, central California, *J. Geophys. Res.*, 98, 787-793, 1993.
- Sharp, R. V. et al., Surface faulting in the central Imperial Valley, in *The Imperial Valley, California, Earthquake, October 15, 1979, U. S. Geol. Surv. Prof. Pap.*, 1254, 119-144, 1982.

- Sillard, P., Z. Altamimi, and C. Boucher, The ITRF96 realization and its associated velocity field, *Geophys. Res. Lett.*, 25, 3223-3226, 1998.
- Snay, R.A. and A. R. Drew, Supplementing geodetic data with prior information for crustal deformation in the Imperial Valley, California, Technical Report, no. 6, University of Stuttgart, 1988.
- Southern California Earthquake Center Crustal Deformation Working Group, SCEC Horizontal Deformation Map v.2.0, [http://www.scecdc.scec.org/group\\_e/release.v2](http://www.scecdc.scec.org/group_e/release.v2), 1999.
- Thatcher, W., Nonlinear strain buildup and the earthquake cycle on the San Andreas Fault, *J. Geophys. Res.*, 88, 5893-5902, 1983.
- Thomas, A. P. and T. K. Rockwell, A 300- to 500-year history of slip on the Imperial Fault near the U.S.-Mexico border: missing slip at the Imperial fault bottleneck, *J. Geophys. Res.*, 101, 5987-5997, 1996.
- Tse, S. T. and J. R. Rice, Crustal earthquake instability in relation to depth variation of frictional slip parameters, *J. Geophys. Res.*, 91, 9452-9572, 1986.
- Vincent, P., Application of SAR Interferometry to low-rate crustal deformation, Ph.D., Univ. of Colorado, 1998.
- Wdowinski, S., Y. Sudman, and Y. Bock, Distribution of interseismic deformation along the San Andreas fault system, southern California, *Geophys. Res. Lett.*, 28, 2321-2324, 2001.
- Weertman, J., Continuous distribution of dislocations on faults with finite friction, *Bull. Seism. Soc. Am.*, 54, 1035-1058, 1964.
- Wessel, P. and W.H.F. Smith, Free software helps map and display data, *EOS Trans. AGU*, 72, 445-446, 1991.
- Working Group on California Earthquake Probabilities, Seismic hazard in southern California: probable earthquakes, 1994 to 2024, *Bull. Seism. Soc. Am.*, 85, 379-439, 1995.
- Zebker, H. A., P.A. Rosen, R.M. Goldstein, A. Gabriel, and C.L. Werner, On the derivation of coseismic displacement fields using differential radar interferometry: The Landers earthquake, *J. Geophys. Res.*, 99, 19,617-19,643, 1994.

This chapter, in full, is a reprint of the material as it appears in the *Journal of Geophysical Research*, Lyons, Suzanne; Bock, Yehuda; Sandwell, David, 2002.

The dissertation author was the primary investigator and author of this paper and the co-authors directed and supervised the research.

## Chapter 3

### **Fault Creep Along the Southern San Andreas from InSAR, Permanent Scatterers, and Stacking**

*The important thing in science is not so much to obtain new facts as to discover  
new ways of thinking about them.*

-William Bragg, Sr.

Suzanne Lyons and David Sandwell

Reprint from *Journal of Geophysical Research*, 2002.

#### 3.1 ABSTRACT

Interferometric Synthetic Aperture Radar (InSAR) provides a practical means of mapping creep along major strike-slip faults. The small amplitude of the creep signal ( $< 10$  mm/yr), combined with its short wavelength, makes it difficult to extract from long time span interferograms, especially in agricultural or heavily vegetated areas. We utilize two approaches to extract the fault creep signal from 37 ERS SAR images along the southern San Andreas Fault. First, amplitude stacking is utilized to identify permanent scatterers, which are then used to weight the interferogram prior to spatial filtering. This weighting improves correlation and also provides a mask for poorly correlated areas. Second, the unwrapped phase is stacked to reduce tropospheric and other short-wavelength noise. This combined processing enables us to recover the near-field ( $\sim 200$  m) slip signal

across the fault due to shallow creep. Displacement maps from 60 interferograms reveal a diffuse secular strain buildup, punctuated by localized interseismic creep of 4-6 mm/yr LOS (12-18 mm/yr horizontal). With the exception of Durmid Hill, this entire segment of the southern San Andreas experienced right-lateral triggered slip of up to 10 cm during the 3.5-year period spanning the 1992 Landers earthquake. The deformation change following the 1999 Hector Mine earthquake was much smaller ( $< 1$  cm) and broader than for the Landers event. Profiles across the fault during the interseismic phase show peak-to-trough amplitude ranging from 15-25 mm/yr (horizontal component) and the minimum misfit models show a range of creeping/locking depth values that fit the data.

### 3.2 INTRODUCTION

Standard models of the earthquake cycle [e.g., *Tse and Rice, 1986*] assume that above a depth of about 30 km, plate boundary deformation occurs on discrete faults. Over a period of many earthquake cycles, the displacement is uniform with depth such that the sum of the preseismic, coseismic, postseismic, and interseismic deformation is equal to the geologic displacement. The depth and extent of surface creep is an important issue for both earthquake physics and earthquake hazards mitigation. Some faults remain locked over the entire thickness of the seismogenic zone throughout the earthquake cycle and so can store maximum seismic moment. Other faults slide freely from the surface to the base of the seismogenic zone and, therefore, may be less hazardous [*Bürgmann et al., 2000*]. This slow movement of the Earth's surface at a fault is known as creep.

Fault friction models (e.g., *Weertman, 1964; Savage and Burford, 1971; Tse and Rice, 1986*) relate slip at depth to surface displacement. Therefore, one can examine the spatial distribution of crustal displacement over a long period of time ( $> 5$  years) to detect the interseismic signal and determine if a fault is creeping during that time. Creep can be gradual (months to years) or it can occur in short episodes known as “creep events” (lasting hours to days). While creepmeters have excellent temporal sampling, they lack the spatial coverage needed to determine the depth variations in aseismic slip. Networks of other geodetic measurements, such as continuous GPS receivers or survey-mode GPS sites, can provide adequate temporal coverage of the coseismic, postseismic, and interseismic motions along the North American-Pacific plate boundary, but the network must be sufficiently dense for accurate determination of the average slip distribution with depth [*Thatcher, 1983; Harris and Segall, 1987; Lorenzetti and Tullis, 1989; Savage, 1990; Savage and Lisowski, 1993*]. Interferometric synthetic aperture radar (InSAR) complements these systems by providing complete 200-m spatial resolution, but at a much lower sampling rate ( $\geq 35$  days) than other instruments.

### 3.3 SOUTHERN SAN ANDREAS FAULT AND SYNTHETIC APERTURE RADAR

The San Andreas Fault has shown evidence for both steady creep and triggered creep over the last few decades [*Louie et al., 1985; Vincent et al., 1998; Sandwell and Agnew, 1999*]. The southern San Andreas (Figure 3.1) has

undergone four large slip events between 1000 and 1700 A.D. [Sieh, 1986] and has an earthquake recurrence interval of about 230 years. It has been 300 years since the last major earthquake on this segment, suggesting a significant seismic event along the San Andreas Fault is overdue. The seismicity in this area is low and not on the fault (Figure 3.1) [Richards-Dinger and Shearer, 2000] and the fault has been known to undergo both continuous creep at 1-2 mm/yr and triggered slip due to earthquakes [Louie *et al.*, 1985; Bilham and Williams, 1985; Rymer *et al.*, 2002]. Thus, it makes for a very interesting region in which to study crustal deformation. Unfortunately, GPS coverage in this region is sparse, so we must rely on Interferometric Synthetic Aperture Radar (InSAR) to determine the small-scale interseismic deformation.

The 9-year archive of SAR data and precise orbital tracking data from the ERS-1 and ERS-2 spacecraft (European Space Agency) was used to recover the slip history of the southern San Andreas Fault (Figure 3.2). This involved two modes of processing. First, 25 ERS-1/2 pairs having short time spans and moderate baseline lengths (100-300 m) were stacked to recover the topographic phase (thick lines in Figure 3.2) [Sandwell and Sichoix, 2000]. Then, ERS-1/2 pairs having long time spans (200-3000 days) and short baselines ( $\leq 186$  m; median baseline = 70 m) were used to recover crustal motion. Since this area has more than 2500 m of relief, the accurate development and removal of topographic phase is a critical step in the processing. A comparison with 81 GPS monuments shows the vertical accuracy for the digital elevation model (DEM) using this method is 10

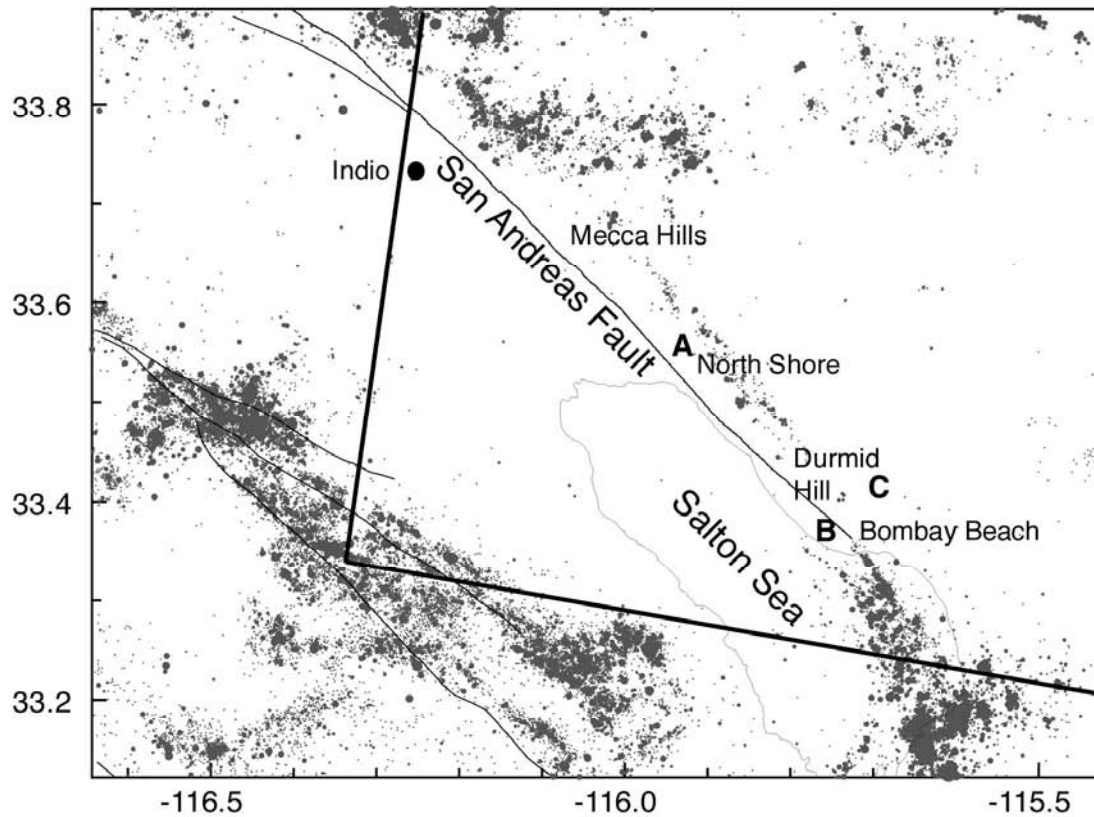


Figure 3.1. Map view of seismicity in the Coachella Valley. Earthquake locations along the southern San Andreas are offset by  $\sim 5$  km to the northeast of the fault. Locations from *Richards-Dinger and Shearer* [2000]. Letters are for reference with later figures. Solid lines indicate Synthetic Aperture Radar (SAR) frame from ERS-1/2.

Figure 3.2. Diagram of available ERS-1 and ERS-2 images of a 120 km by 120 km area containing the southern San Andreas Fault and Salton Sea. These 42 images span almost nine years and include the Landers and Hector Mine ruptures. All images are aligned with the master image (E1\_23390) so interferograms can be formed from any pair of images. Phase gradients from pairs with medium baseline difference (50-300 m) and short time difference (<70 days) are stacked to construct a high accuracy digital elevation model (examples shown by thick lines). Pairs with short baseline difference (<186 m) and long time span are used for monitoring small displacements after topographic phase removal (thin lines). For clarity, not all interferogram pairs are shown.



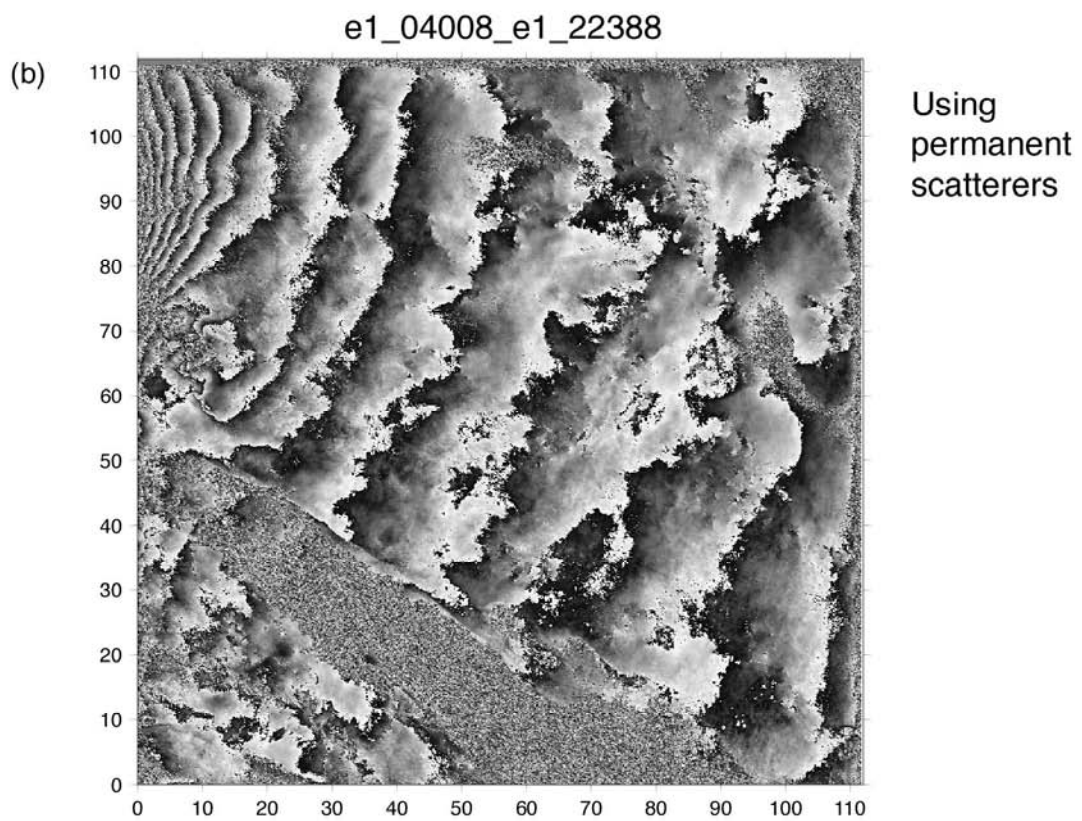
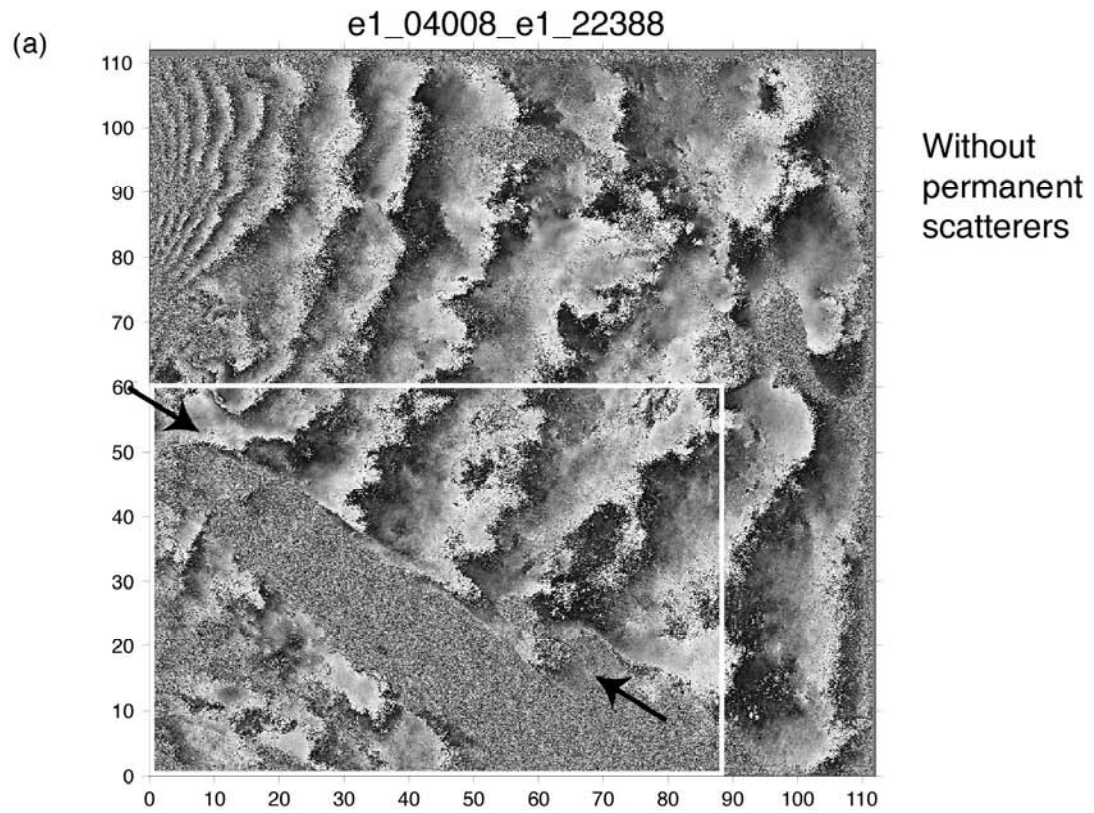
m at 25-m horizontal postings. This topography error maps into less than 13 mm for interferometric baselines shorter than 186 m.

While most of the Salton Sea area is arid and, thus, retains phase coherence over long periods of time, the agricultural areas in the Coachella Valley cause significant decorrelation between SAR images. In the farmland of the Imperial Valley and northwest of the Salton Sea, interferograms formed from available SAR images appear noisy and it is difficult to discern the small-scale deformation across the faults in these areas. Of the sixty interferograms formed from our SAR images, most had high coherence in the region northeast of the fault and showed consistent far-field movement (Figure 3.3), along with small amounts of fault creep (arrows in Figure 3.3a). However, southwest of the fault, in the Coachella Valley, the interferograms were highly decorrelated and it was difficult to assess the character of motion across the valley. Thus, while one can qualitatively see creep along this section of the San Andreas, the full “picture” of the near-field is muddled by the incoherent farmland.

### 3.4 PERMANENT SCATTERERS

Decorrelation of the phase in repeat SAR images is caused by cultivation, irrigation, and vegetation growth. However, these agricultural areas also contain isolated reflectors (buildings, roads, drainage channels, etc.) that remain coherent over long periods of time. If these permanent scatterers can be isolated from the generally decorrelated areas [Ferretti *et al.*, 2000; Ferretti *et al.*, 2001; Haynes, 1999], they can be used as a data mask (discussed later) or to simulate a dense

Figure 3.3. (a) Interferogram of the southern San Andreas fault zone (box) processed using the standard method. Indio is in the western part of the image and the Salton Sea cuts toward the southeast. This interferogram spans 3.5 years and includes deformation from the 1992 Landers event (fringes in upper left). Each fringe corresponds to 28 mm of deformation. Creep can be seen along the San Andreas Fault (black arrows). (b) Interferogram processed from the same images, but using permanent scatterers to weight the pixels during multilook averaging.



GPS network. Analysis of the interferograms at these “stable” points can yield the relative motion over time, which can then be used to create a deformation field. *Ferretti et al.* [2001] demonstrated the technique using more than 30 co-registered SAR images in their test regions (Camiore, Milano, and Paris). In their study, after geometric alignment, each amplitude image was scaled using a calibration factor supplied by ESA. The amplitude images were averaged to form the mean of the stack,  $m_A$ . They then computed the standard deviation from the mean,  $\sigma_A$ , to form the amplitude dispersion index,  $D_A$ , at each pixel, such that  $D_A = \frac{\sigma_A}{m_A}$ . Points of low amplitude dispersion ( $D_A < 0.25$ ) were labeled “permanent scatterers.” From this subset of points, *Ferretti et al.* [2001] jointly estimated the digital elevation model (DEM) errors, line-of-sight (LOS) velocities, and linear atmospheric contributions (see *Ferretti et al.*, 2001 for details). This secondary analysis involved an iterative, least-squares procedure to effectively unwrap the phase and isolate the time series of crustal deformation.

Our analysis of 37 SAR images along the Southern San Andreas Fault initially followed the approach of *Ferretti et al.* [2000] to identify the permanent scatterers. However, we deviated from their technique when using this information. We began by calculating the amplitude dispersion from the stack of SLC images, but rather than use a calibration factor from ESA, we calculated the average calibration factor for each image using the ratio of the amplitude of each image (mean of all pixels) to the mean amplitude of the entire set. Each SAR image was divided by this calibration factor to equalize the brightness between images, and we calculated the scattering amplitude,  $s$ , which is the inverse of the

amplitude dispersion,  $D_A$  (Figure 3.4). Stable areas with low dispersion have a high scattering amplitude and, thus, have higher phase stability, while bodies of water, such as the Salton Sea in Figure 3.4, have zero phase stability and so the scattering function,  $s^2$ , is close to zero. A photographic survey of the Salton Sea region to illustrate types of landscapes and structures that make good scatterers is presented in Appendix 3.A.

Interferogram formation typically involves the following steps: cross-multiplication of the aligned single-look complex SAR images; removal of all known phase effects due to Earth curvature, topography, orbital geometry, etc.; and multi-look (boxcar or Gaussian) filtering of the real and imaginary parts of the interferogram to boost the signal-to-noise ratio [Massonnet and Feigl, 1998; Rosen *et al.*, 2000]. Rather than isolate the permanent scatterers using a threshold and treat them as an array of known points [Ferretti *et al.*, 2001], we modified the filtering step using the scattering function at each pixel ( $s_j^2$ ) (Figure 3.4). We multiplied the real and imaginary parts of each pixel by  $s_j^2$  and then filtered each component with a Gaussian filter oriented approximately along the fault (N47.5° W), such that the width of the filter along the fault,  $\sigma_{\text{par}} = 0.5 \times 285$  m), is greater than the width of the filter perpendicular to the fault,  $\sigma_{\text{perp}} = 0.5 \times 84$  m). Pixels with high  $s$ -values are given more “confidence” and weighted more than those with high dispersion (low  $s$ -value) prior to spatial filtering of the interferogram,  $C$ ,

$$\langle C(\mathbf{x}) \rangle = \langle R(\mathbf{x}) \rangle + i \langle I(\mathbf{x}) \rangle$$

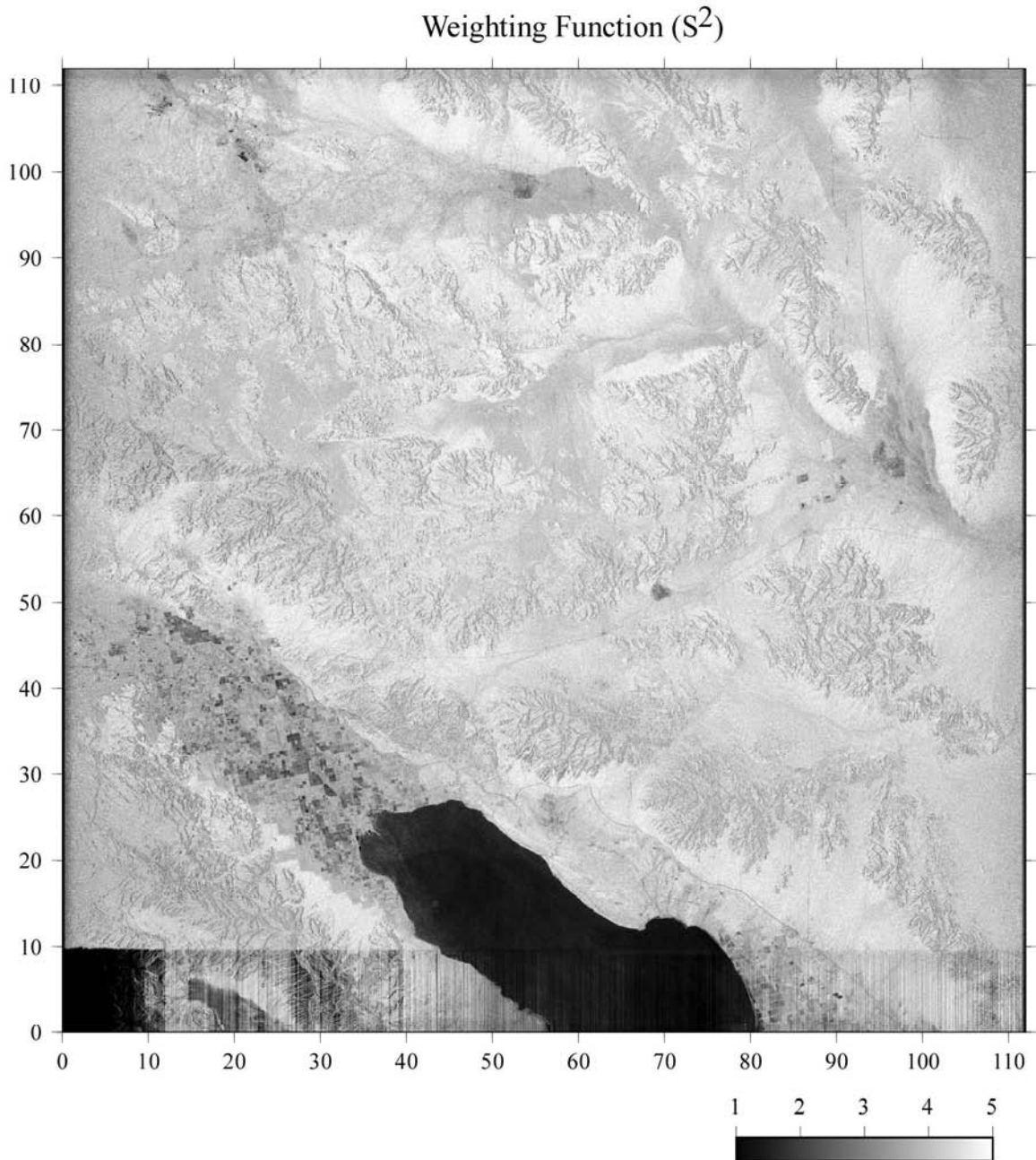


Figure 3.4. Permanent scatterer weights ( $s^2$ ) from a stack of 37 descending ERS images. Bright regions are "stable" and considered highly reliable, while black regions experience sporadic, random motion (plowing of fields, overlay effects of mountains) and are used as masks in the weighting process, as described in the text.

where  $\langle \rangle$  denotes the Gaussian convolution filter. This weighting boosts both the real and imaginary parts of the amplitude of stable areas prior to filtering, but does not alter the phase of the pixel, since the phase is:  $\phi = \tan^{-1} \frac{\langle s^2 \text{Im}(C) \rangle}{\langle s^2 \text{Re}(C) \rangle}$ .

Figure 3.3 illustrates the qualitative improvement in phase recovery by using the weighting and filtering method versus using normal interferometric methods. This interferogram spans 3.5 years and includes the Landers earthquake. Figure 3.3a was formed using the standard interferometric techniques with a nearly isotropic Gaussian filter ( $\sigma_{0.5}=84$  m azimuth,  $\sigma_{0.5}=105$  m ground range, see *Sandwell and Price* [1998]). The fringe edges are rough and highly pixellated, and the Coachella Valley creates a decorrelated barrier between the fringes of the northeast section and those in the southwest region. Figure 3.3b shows the resultant interferogram after weighting the amplitude components by the square of the scattering index and filtering with the Gaussian filter oriented along the fault. The fringes in this interferogram are much more highly defined and areas within the Coachella Valley are more coherent than before. In the northwest region of the valley, the fringe pattern is almost continuous across the valley, with only minor pixellation.

To look more quantitatively at the effects of the weighting, we determined the correlation between two SAR images used in a four-year interferogram spanning the interseismic period (July 1995 through June 1999). Although the coherence measurement may seem to be a more relevant measure of the impact of the permanent scatterers technique, we wanted to examine the difference on a

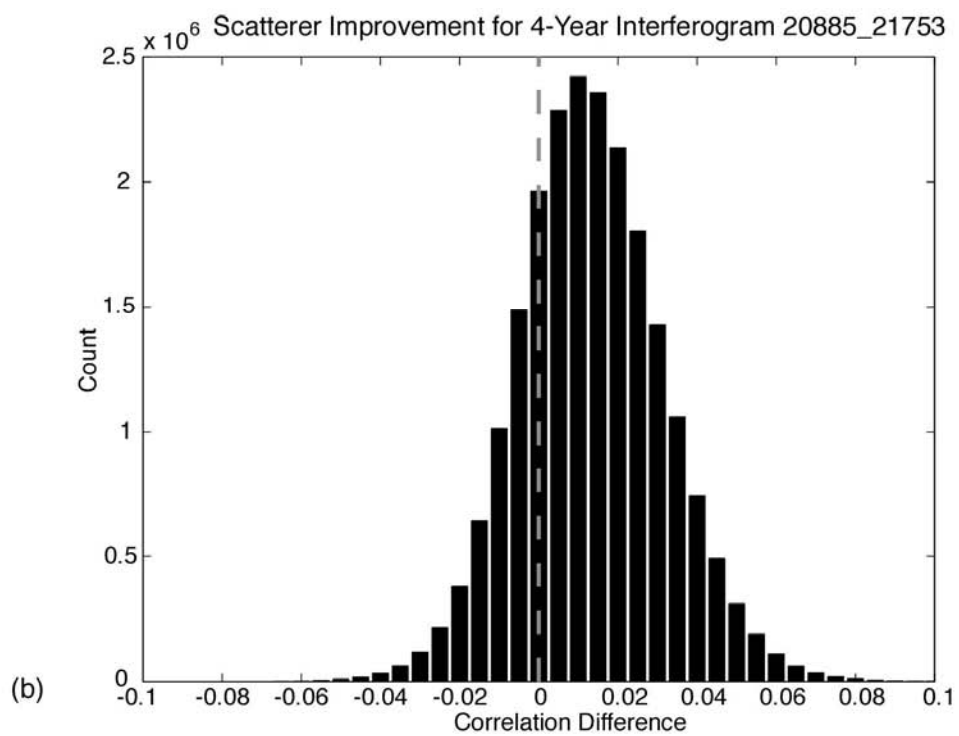
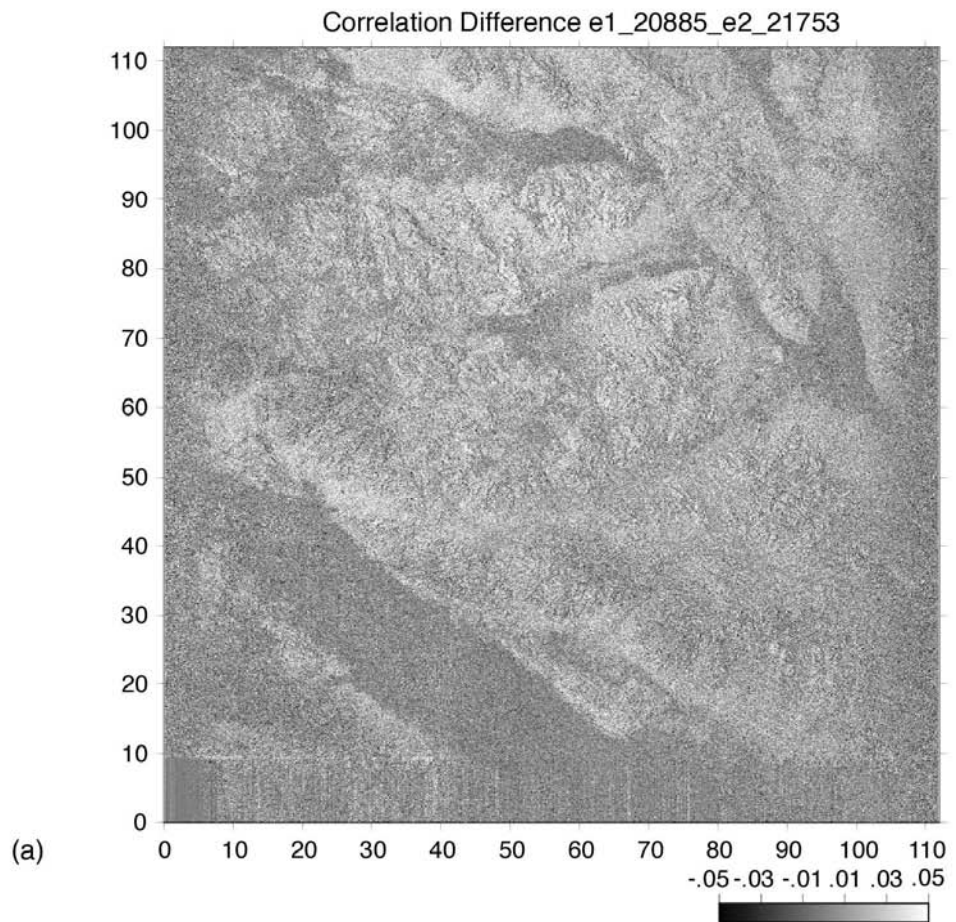
pixel-by-pixel basis, so we found the correlation of the image pair for both our weighted permanent scatterers technique ( $\gamma_{wps}$ ) and the standard technique ( $\gamma_{std}$ ).

The correlation value is defined as simply  $\gamma = \frac{\langle A_{12} \rangle}{\sqrt{\langle A_1 \rangle \langle A_2 \rangle}}$ , where  $A_1$ ,  $A_2$ , and  $A_{12}$

are the amplitudes of the reference image, the repeat image, and the interferogram between the two, respectively.

The difference between these values,  $\gamma_{wps} - \gamma_{std}$ , for the four-year interferogram is shown in Figure 3.5. The top image (Figure 3.5a) shows the distribution of correlation improvement and demonstrates a positive correlation difference (improvement) for the weighting technique in most regions. This is supported by the histogram of the region (Figure 3.5b) which shows a normal distribution, offset by  $\sim 0.01$ . The vast majority of pixels were either unchanged or experienced an improvement in the correlation due to the scatterers (mean =  $\sim 0.014$ , median =  $\sim 0.015$ ). Areas of complete decorrelation with no permanent scatterers within the footprint of the convolution will not be improved using this technique and also areas of perfect correlation cannot be improved. Therefore, we expect the most improvement from this permanent scatterer weighting and filtering method will come from areas where the correlation is marginal ( $\sim 0.2$ ). In highly decorrelated areas, it may be preferable to use only the permanent scatterer points and discard the other data (similar to *Ferretti et al.* [2001]). Further experimentation is needed in areas of varying correlation to determine the optimum masking, weighting, and filtering technique that will maximize the

Figure 3.5. (a) Difference between the correlation of a 4-year interferometric pair (E1\_20885 to E2\_21753) using the permanent scatterer weights versus using the standard method. This demonstrates a positive correlation difference (improvement) for the weighting technique in most regions. (b) Histogram of (a), showing a normal distribution, offset by  $\sim 0.01$ . mean =  $\sim 0.014$ , median =  $\sim 0.015$



correlation of the data while still maintaining a useful spatial resolution along the fault.

### 3.5 STACKING INTERFEROGRAMS

Interferometric "signal" is composed of topographic height variations, surface deformation, orbit errors, and signal delay variability within the image due to the atmosphere. To isolate the creep signal, we first removed the topographic phase from each interferogram. The surface deformation is composed of both long-wavelength (far-field) motion and short-wavelength (near-field) creep. We estimated the far-field motion using the Southern California Earthquake Center (SCEC) velocity model [SCEC, 1999] for the region (based on continuous GPS stations) and interpolated for velocities between stations. After removing this long-wavelength signal, our resultant signal should be comprised of orbit error, tropospheric error, and creep. For each of the sixty interferograms, we unwrapped the phase and attempted to manually bridge gaps in the data. Since the orbit error is nearly a plane over a 100 km distance [Massonnet and Feigl, 1998], we removed a plane estimating the best-fit linear gradient across the unwrapped phase data from each phase array. Most of these unwrapped interferograms showed evidence for fault creep, but the line-of-sight signal was very small and it was difficult to obtain reliable measurements from a single interferogram. Assuming the tropospheric errors are random, stacking multiple interferograms should reduce this noise, leaving the creep signal. Figure 3.6 shows the unwrapped interseismic interferogram stack with the SCEC velocity model and orbit error estimate

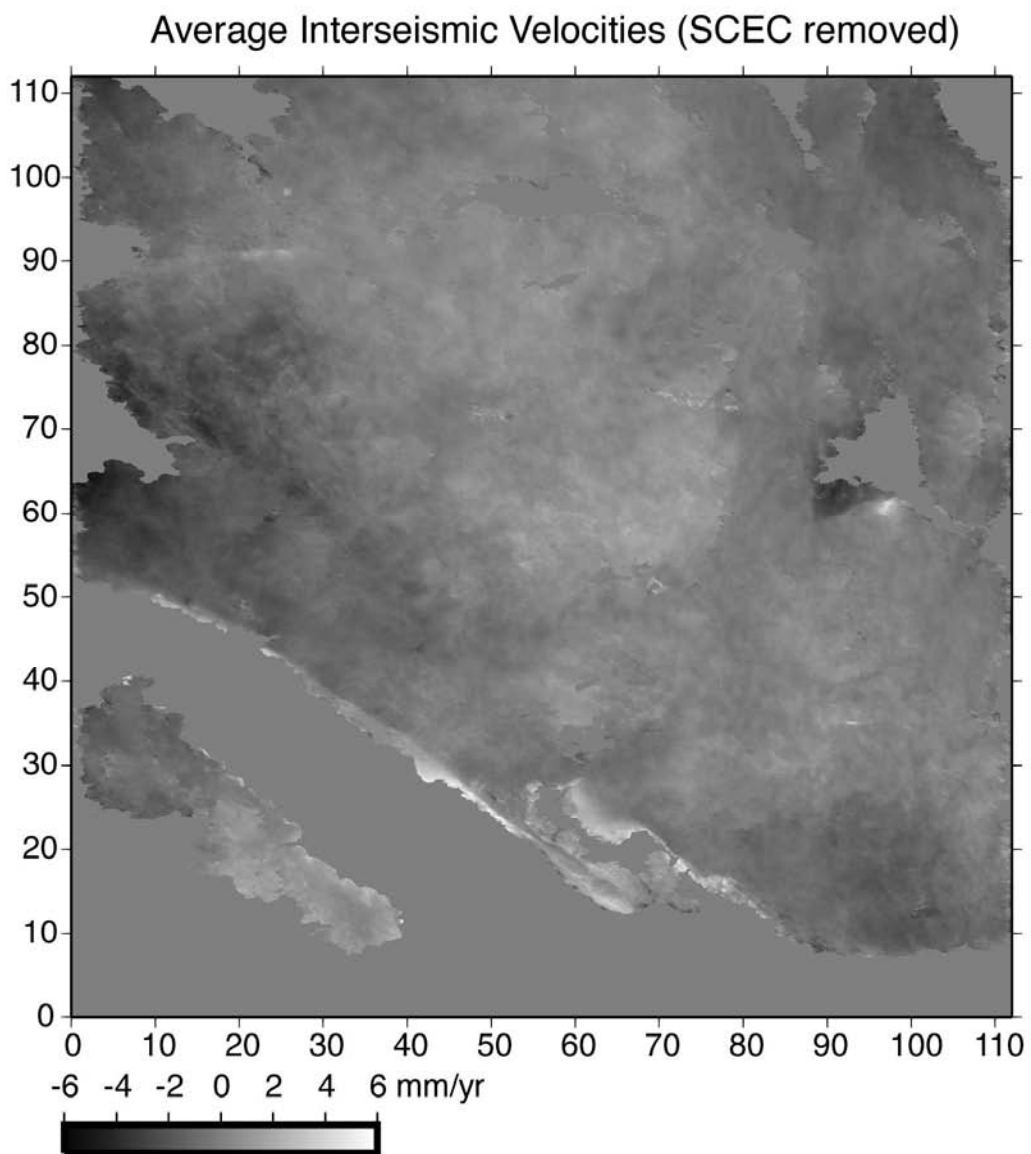


Figure 3.6. Average LOS interseismic creep velocities for 1993-1999. The far-field velocity model and the orbit error model have been removed from each interferogram prior to stacking.

removed. The resultant signal is the average over seven years of data (1993-1999) and shows creep along the northwest and southeastern sections of the fault region.

### 3.6 RESULTS

To look for evidence of triggered slip along this segment of the San Andreas Fault due to the Landers and Hector Mine earthquakes, we divided the set of interferograms into three different time periods (Table 3.2): Landers (1992-1996), Interseismic (1993-1999), and Hector Mine (1997-2000). Twelve interferograms spanned more than one time period, so they were not used in the stacks. The SCEC velocity model was added back into each stack before modeling.

For the Landers stack, we used four interferograms encompassing both the earthquake and three and a half years of postseismic motion (April 22, 1992 to February 10, 1996). The average line-of-sight (LOS) velocity during this 3.5-year period is shown in Figure 3.7a, with red indicating 5 mm/yr line-of-sight (LOS) motion (away from the satellite or northwest) and blue indicating -5 mm/yr LOS (toward the satellite or southeast). The sharp jump across the fault indicates that some sections of the fault experienced creep during the Landers quake, while other regions along the fault appear to be locked to the surface. To look more quantitatively at the spatial distribution of slip along the fault, we extracted 38 profiles across the length of the fault region (numbered lines in Figure 3.7a).

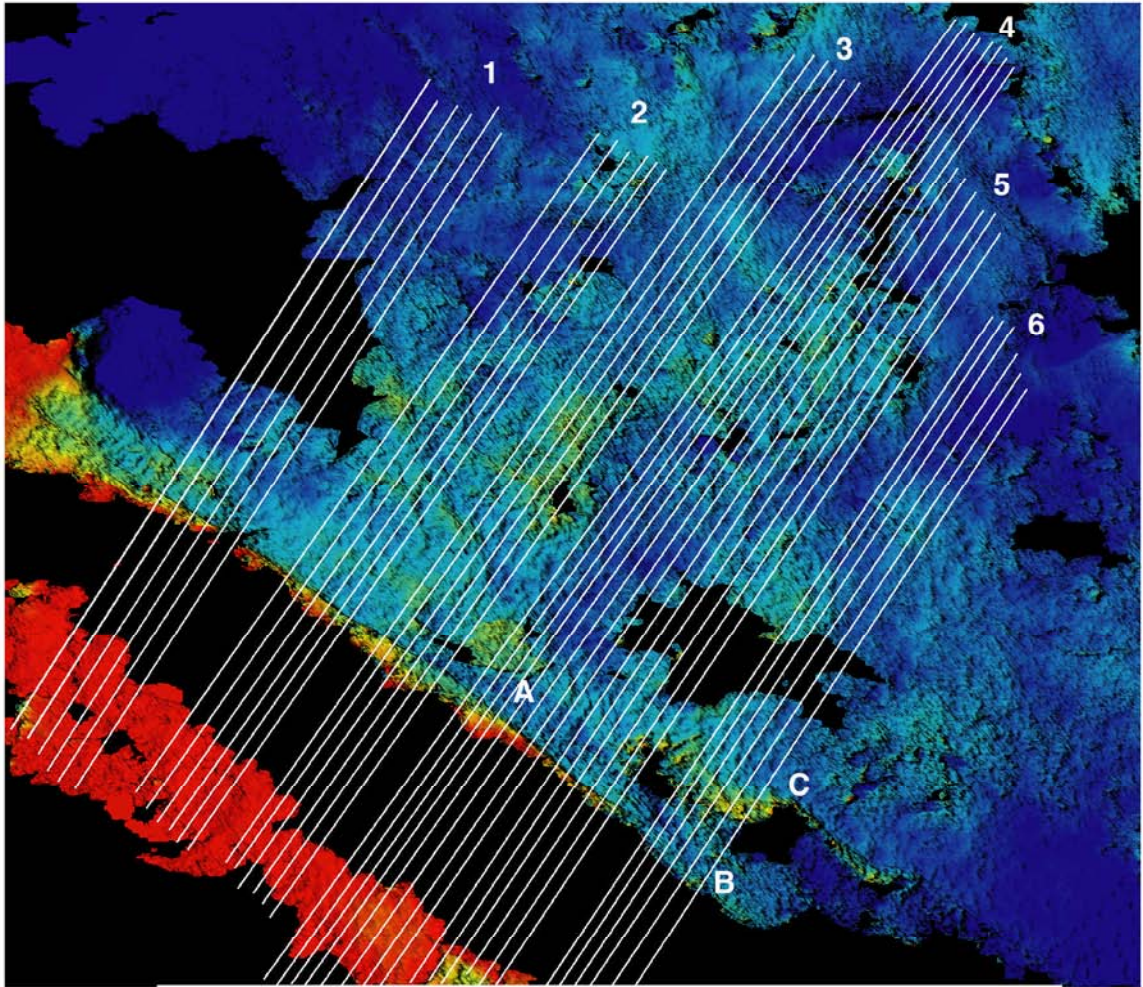
Table 3.1. Atmospheric error statistics for all interferograms. Mean and standard deviation for each interferogram after subtracting the deformation signal (Entire Stack, which has been corrected for orbit error). The standard deviation of the atmospheric signal for most of the interferograms is <15 mm.

<b>Image</b>	<b>Time Span</b>	<b># data used</b>	<b>mean [mm]</b>	<b><math>\sigma</math> [mm]</b>
<b>Entire Stack (Deformation)</b>	1.00	12822657	-0.40	1.41
e1_04008_e1_22388	3.51	12729530	2.30	10.73
e1_04008_e2_02715	3.52	12640483	1.36	11.08
e1_04008_e2_04218	3.80	12724527	-0.52	15.02
e1_04008_e2_27765	8.31	12476377	1.91	14.02
e1_04509_e1_20885	3.13	12429082	-0.23	13.59
e1_04509_e1_21753	7.44	12580644	1.78	12.11
e1_04509_e2_23757	7.44	12580644	1.78	12.11
e1_04509_e2_25260	7.73	12719124	2.22	14.60
e1_08517_e1_20384	2.27	12652573	1.79	8.05
e1_08517_e1_23390	2.84	12743944	3.95	8.69
e1_08517_e2_09228	3.90	12787240	2.15	8.65
e1_08517_e2_13737	4.76	12772228	2.45	7.12
e1_08517_e2_15240	5.05	12763131	1.66	6.01
e1_08517_e2_15741	5.15	12716073	5.15	12.17
e1_08517_e2_19749	5.91	12558454	0.21	8.20
e1_08517_e2_28266	7.54	12621014	2.09	8.39
e1_09018_e1_23891	2.84	12753806	1.83	7.23
e1_09018_e2_04218	2.85	11593768	2.74	7.80
e1_20384_e1_25394	0.95	12810794	1.26	7.26
e1_20384_e2_09729	1.73	12798180	0.38	5.21
e1_20384_e2_19749	3.64	12794909	-0.48	4.57
e1_20384_e2_24258	4.51	12747593	-2.97	10.56
e1_20885_e2_21753	3.93	12795837	-0.47	9.20
e1_22889_e2_05721	0.48	12812462	0.34	7.52
e1_22889_e2_24258	4.03	12783303	0.17	6.56
e1_23390_e2_13737	1.92	12767254	-0.53	6.67
e1_23390_e2_15741	2.30	12808346	3.22	7.66
e1_23390_e2_26262	4.32	12691101	-0.73	8.70
e1_23891_e2_23256	3.64	12735269	1.34	6.33
e1_23891_e2_27765	4.51	12690805	5.22	10.14
e1_25394_e2_10731	0.96	12814597	-1.40	6.26
e1_25394_e2_24258	3.55	12762393	-3.24	13.34
e2_03216_e2_14739	2.20	12797624	1.44	6.12
e2_03216_e2_21753	3.55	12761718	0.08	5.97
e2_03216_e2_24258	4.02	12756666	2.40	15.20
e2_05721_e2_14238	1.63	12804551	0.90	9.28
e2_05721_e2_24258	3.55	12780326	1.31	14.07
e2_09729_e2_15240	1.05	12804438	-0.12	5.66
e2_09729_e2_28266	3.55	12797232	-1.65	7.26
e2_10230_e2_26262	3.07	12771967	-1.74	9.64
e2_10731_e2_11733	0.19	12821784	0.91	7.75
e2_10731_e2_14238	0.67	12812598	-0.85	7.07
e2_10731_e2_19749	1.73	12795239	-0.39	4.61
e2_11733_e2_14238	0.48	12812037	-1.81	9.69
e2_11733_e2_19749	1.53	12799322	-1.28	8.57
e2_11733_e2_24258	2.40	12795679	-3.53	9.86
e2_13737_e2_15741	0.38	12787232	4.55	11.37
e2_13737_e2_28266	2.78	12781273	-1.18	6.29
e2_14238_e2_19749	1.05	12776497	0.32	6.65
e2_14238_e2_24258	1.92	12810522	-1.25	7.74
e2_14739_e2_21753	1.34	12763047	-1.70	9.19
e2_14739_e2_24258	1.82	12732988	-0.90	7.37
e2_15240_e2_26763	2.21	12745648	5.21	11.63
e2_15741_e2_26763	2.11	12605092	0.58	13.27
e2_19749_e2_24258	0.86	12761928	-2.17	10.27
e2_19749_e2_28266	1.63	12780606	0.12	5.84
e2_21753_e2_23757	0.38	12813805	0.74	8.09
e2_23256_e2_26262	0.58	12795684	-0.31	8.68
e2_23256_e2_27765	0.86	12598397	4.51	12.16
e2_23757_e2_25260	0.29	12808983	-1.89	5.82
Median	2.78	12771967	0.34	8.39
SCEC Phase Model	1.00	21504000	0.26	0.51

Table 3.2. Same as Table 3.1, but with each interferogram categorized into its corresponding time category. The standard deviation of the atmospheric signal for most of the interferograms is <10 mm.

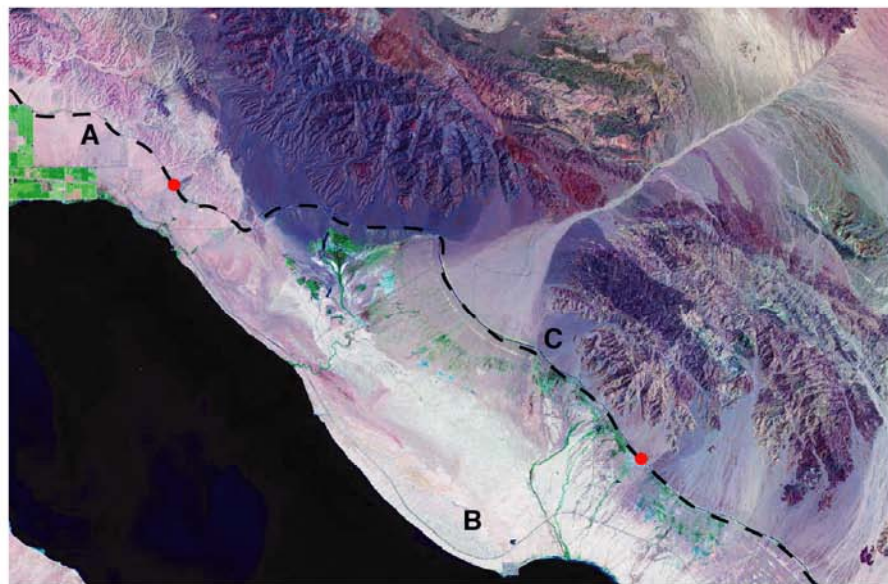
<b>Image</b>	<b>Time Span</b>	<b># data used</b>	<b>mean [mm]</b>	<b><math>\sigma</math> [mm]</b>
<b>Interseismic Stack</b>	1.00	16036454	-0.39	0.98
e1_08517_e1_20384	2.27	15661458	1.38	8.53
e1_08517_e1_23390	2.84	15839799	4.50	9.64
e1_08517_e2_09228	3.90	15949683	1.71	7.86
e1_08517_e2_13737	4.76	15917989	2.16	8.13
e1_08517_e2_15240	5.05	15882854	1.24	6.25
e1_08517_e2_15741	5.15	15726075	5.90	10.23
e1_08517_e2_19749	5.91	15418444	-0.84	9.49
e1_09018_e1_23891	2.84	15797617	2.08	8.28
e1_09018_e2_04218	2.85	14556996	3.16	8.04
e1_20384_e1_25394	0.95	16007701	1.65	7.91
e1_20384_e2_09729	1.73	15972479	0.12	5.44
e1_20384_e2_19749	3.64	15958108	-1.07	6.84
e1_20885_e2_21753	3.93	15970992	-3.59	12.94
e1_22889_e2_05721	0.48	16011506	0.99	7.96
e1_23390_e2_13737	1.92	15904598	-1.23	7.79
e1_23390_e2_15741	2.30	15996066	3.74	7.37
e1_23891_e2_23256	3.64	15794977	0.24	8.38
e1_25394_e2_10731	0.96	16013454	-1.71	6.78
e2_03216_e2_14739	2.20	15973252	1.18	6.15
e2_03216_e2_21753	3.55	15891411	-1.80	8.01
e2_05721_e2_14238	1.63	15974680	0.70	9.88
e2_09729_e2_15240	1.05	15978842	0.12	6.59
e2_10731_e2_11733	0.19	16030262	-0.11	8.50
e2_10731_e2_14238	0.67	16008501	-1.68	8.38
e2_10731_e2_19749	1.73	15962245	-0.92	4.94
e2_11733_e2_14238	0.48	16007444	-1.68	9.97
e2_11733_e2_19749	1.53	15972968	-0.90	8.16
e2_13737_e2_15741	0.38	15946210	5.89	12.09
e2_14238_e2_19749	1.05	15934429	0.61	7.52
e2_14739_e2_21753	1.34	15898121	-3.40	10.77
<b>Hector Stack</b>	1.00	16000194	-1.05	5.22
e2_11733_e2_24258	2.40	15899373	-3.23	8.97
e2_13737_e2_28266	2.78	15841896	-0.49	8.69
e2_14238_e2_24258	1.92	15941333	-1.45	5.90
e2_14739_e2_24258	1.82	15762022	-0.32	7.61
e2_15240_e2_26763	2.21	15787982	7.33	11.32
e2_15741_e2_26763	2.11	15506748	1.34	11.22
e2_19749_e2_24258	0.86	15869345	-3.56	10.03
e2_19749_e2_28266	1.63	15885884	0.80	6.15
e2_21753_e2_23757	0.38	15973780	0.91	8.88
e2_23256_e2_26262	0.58	15928559	-1.09	8.72
e2_23256_e2_27765	0.86	15507135	5.50	12.64
e2_23757_e2_25260	0.29	15964596	-2.18	6.52
<b>Landers Stack</b>	1.00	14578153	-0.87	4.77
e1_04008_e1_22388	3.51	14371067	2.52	6.82
e1_04008_e2_02715	3.52	14252541	1.49	7.43
e1_04008_e2_04218	3.80	14335058	-1.35	13.45
e1_04509_e1_20885	3.13	14023711	-0.13	12.91
Median	1.92	15814939	0.12	8.13

Figure 3.7. (a) Unwrapped line of sight (LOS) displacement for a stack of interferograms encompassing the Landers event. Red is 5 mm/yr LOS motion (away from the satellite); blue is -5 mm/yr LOS (motion toward the satellite). Black areas indicate regions without good point scatterers (high dispersion) and are masked out. White lines correspond to the profiles used in modeling the fault behavior (Figures 3.8-3.10). Thirty-eight profiles are used to estimate the locking depth of the shallow portion of the fault. (b) Aerial photography of sections 5 and 6 near the Bombay Beach/Durmid Hill region of the Salton Sea. Pixel resolution is 64 m and covers a 40 km x 32 km area. The Coachella Canal is shown as a thick dashed line. Red dots signify the endpoints of the unlined section of the canal. Image courtesy of the U.S. Geological Survey.



-5 0 5 mm/yr

(a)



(b)

Because the creep appears to vary in magnitude from northwest to southeast, we divided the profiles into six groups. These profile groups were used to model the fault movement at depth.

Since our displacement measurements are in the radar line-of-sight (LOS) reference, we must convert to fault-parallel horizontal motion prior to modeling. If we define  $\phi$  to be the azimuth of the southern San Andreas ( $\sim 312.5^\circ$  [Bilham and Williams, 1985]),  $\theta$  as the incidence angle ( $23^\circ$  for ERS in the center of the SAR frame), and  $\alpha$  as the azimuth of the line-of-sight vector ( $103^\circ$  for descending ERS tracks), we can write the LOS displacement for a descending pass as:

$$\begin{bmatrix} LOS_d \end{bmatrix} = \begin{bmatrix} -\sin\alpha \sin\theta & -\cos\alpha \sin\theta & -\cos\theta \end{bmatrix} \begin{bmatrix} x \\ y \\ z \end{bmatrix}.$$

If we then assume a vertical fault plane with purely horizontal strike-slip motion,  $s$ , we can rewrite the x and y components as:

$$\begin{aligned} x &= s \sin\phi \\ y &= s \cos\phi \end{aligned}$$

and the relationship between the line-of-sight and fault-parallel motion becomes:

$$LOS_d = s(-\sin\alpha \sin\theta \sin\phi - \cos\alpha \sin\theta \cos\phi) = 0.3401 s$$

Care must be taken when converting from LOS to strike-slip values using this assumption of purely horizontal motion, as any vertical motion would be converted to strike-slip displacement. For example, one mm of subsidence would map into  $\sim 2.7$  mm NW motion, while one mm of uplift would map into 2.7 mm of SE motion. Field observations along the southern San Andreas, however, have shown evidence of purely dextral motion with only minimal ( $\sim 1$  mm) vertical slip

in scattered areas [Rymer, 2000; Rymer *et al.*, 2002] so our assumption should be valid for this region.

Figures 3.8-3.10 show the resultant profile groups for the Landers, Interseismic, and Hector stacks, respectively. The Landers stack (Figure 3.8) reveals fault creep in every group over the 3.5-year period except for group 6 at the southernmost end near Durmid Hill. Durmid Hill is a 4 km wide and 20 km long hill at the southern terminus of the San Andreas Fault (B in Figure 3.7). Its formation has been attributed to transpression along the San Andreas [Bilham and Williams, 1985; Sylvester *et al.*, 1993] and leveling data has shown that Durmid Hill is growing aseismically at a rate of 1-2 mm/yr [Sylvester *et al.*, 1993]. Previous creepmeter studies have revealed episodic creep near Durmid of 1-3 mm/yr from 1967-1984 [Bilham and Williams, 1985] and triggered creep in 1992 from the Joshua Tree ( $1.5 \pm 1$  mm) and Landers (3.9 mm) events [Bodin *et al.*, 1994]. Although a prominent creep signal is not seen in our profiles, the scatter of the points near the fault makes it difficult to isolate a signal of this magnitude in the Durmid Hill region, so we do not rule out the possibility of very small creep in this area.

The average interseismic velocity from 1993-1999 is shown in Figure 3.9. A sharp jump in velocities at the fault in group 1 (far northwest) indicates creep of 3-5 mm/yr LOS (9-15 mm/yr horizontal) in this region, but it is not as apparent in groups 2 and 3. Toward the middle of the region (group 4), there is evidence of ~6 mm/yr LOS (18 mm/yr horizontal) of surface slip, continuing southeast through group 5 and the Desert Beach/North Shore region (A in Figure 3.7). The far

Figure 3.8. Horizontal displacement over 3.5 years for profile groups from the stack of 4 interferograms used in Figure 3.7 (Landers event), compared with preliminary models. Zero distance corresponds to the mapped fault location. Solid lines are "best fit" models with 17 mm/yr strike-slip applied to an elastic half-space having a free-slip plane below depth  $D$  and slip from the surface to a depth  $d$ . For comparison, dashed line is  $D=6$ ,  $d=0.9$ , dash-dot line is  $D=8$ ,  $d=2.9$ , and dotted line is  $D=6$ ,  $d=1.9$ . "Bad" points (decorrelated areas) are defined by a scattering amplitude of  $<2$  and are masked out.

## Landers Stack

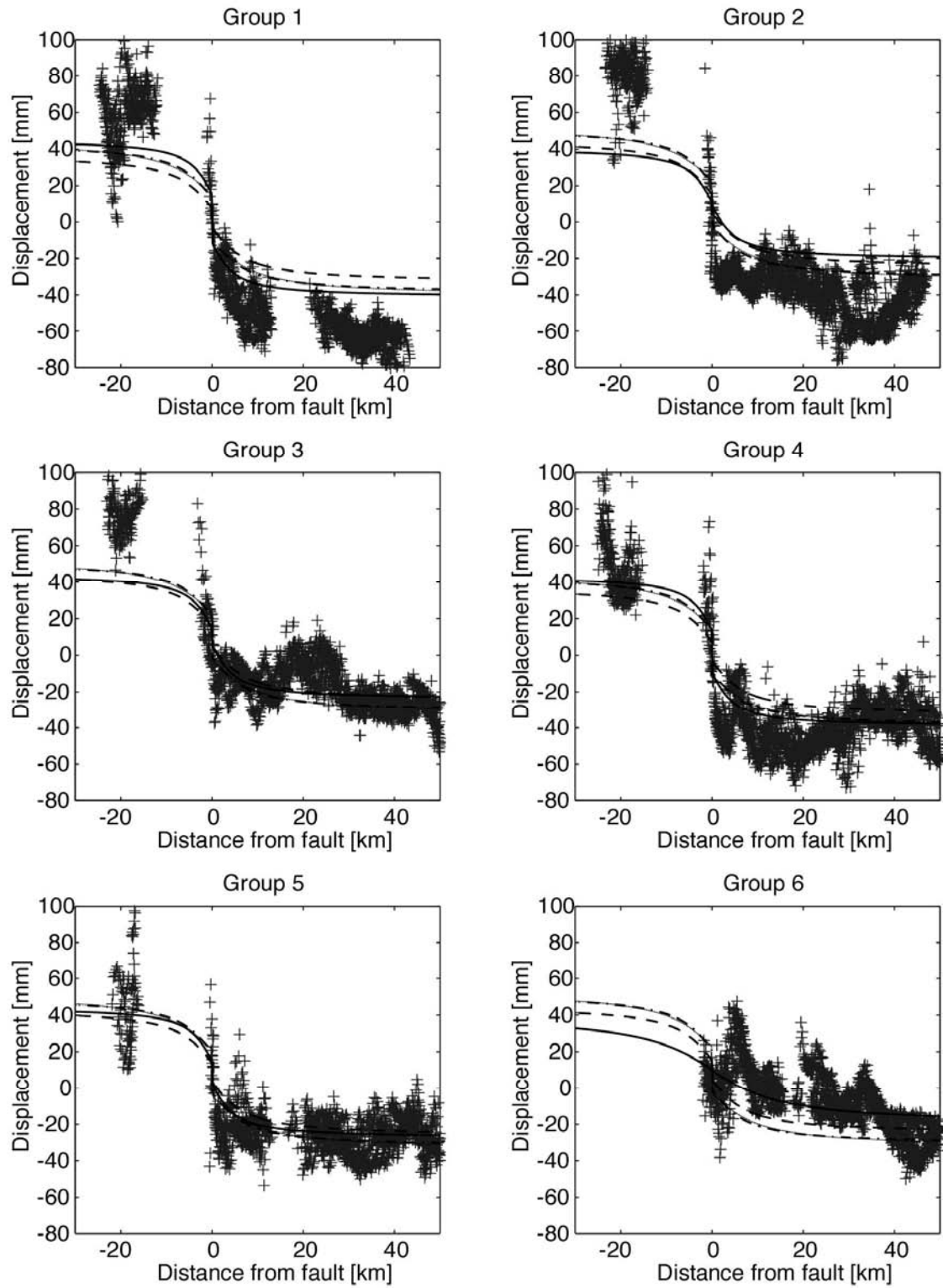


Figure 3.9. Same as Figure 3.8, but for the stack of 28 interseismic interferograms, time averaged over 1993-1999.

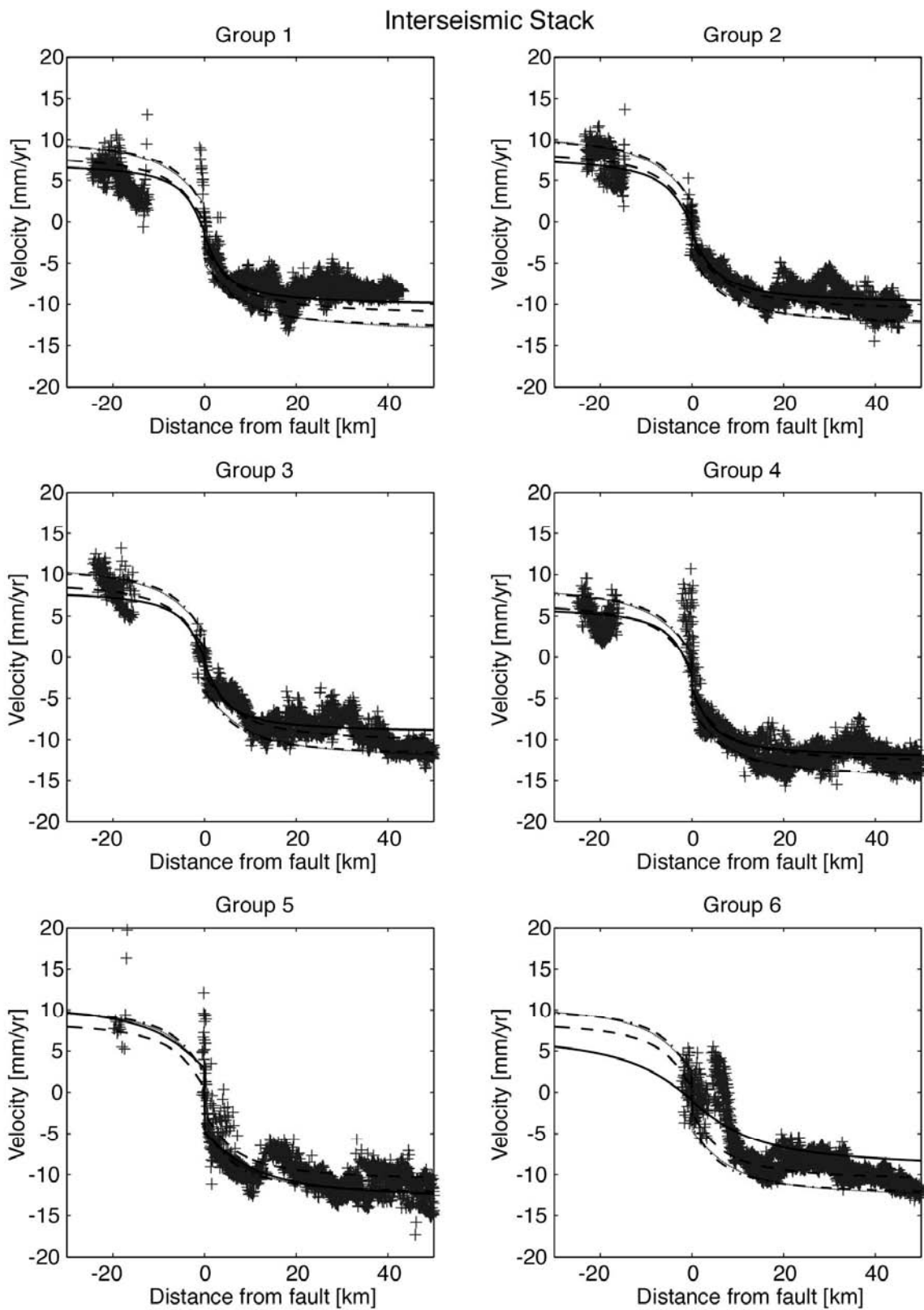
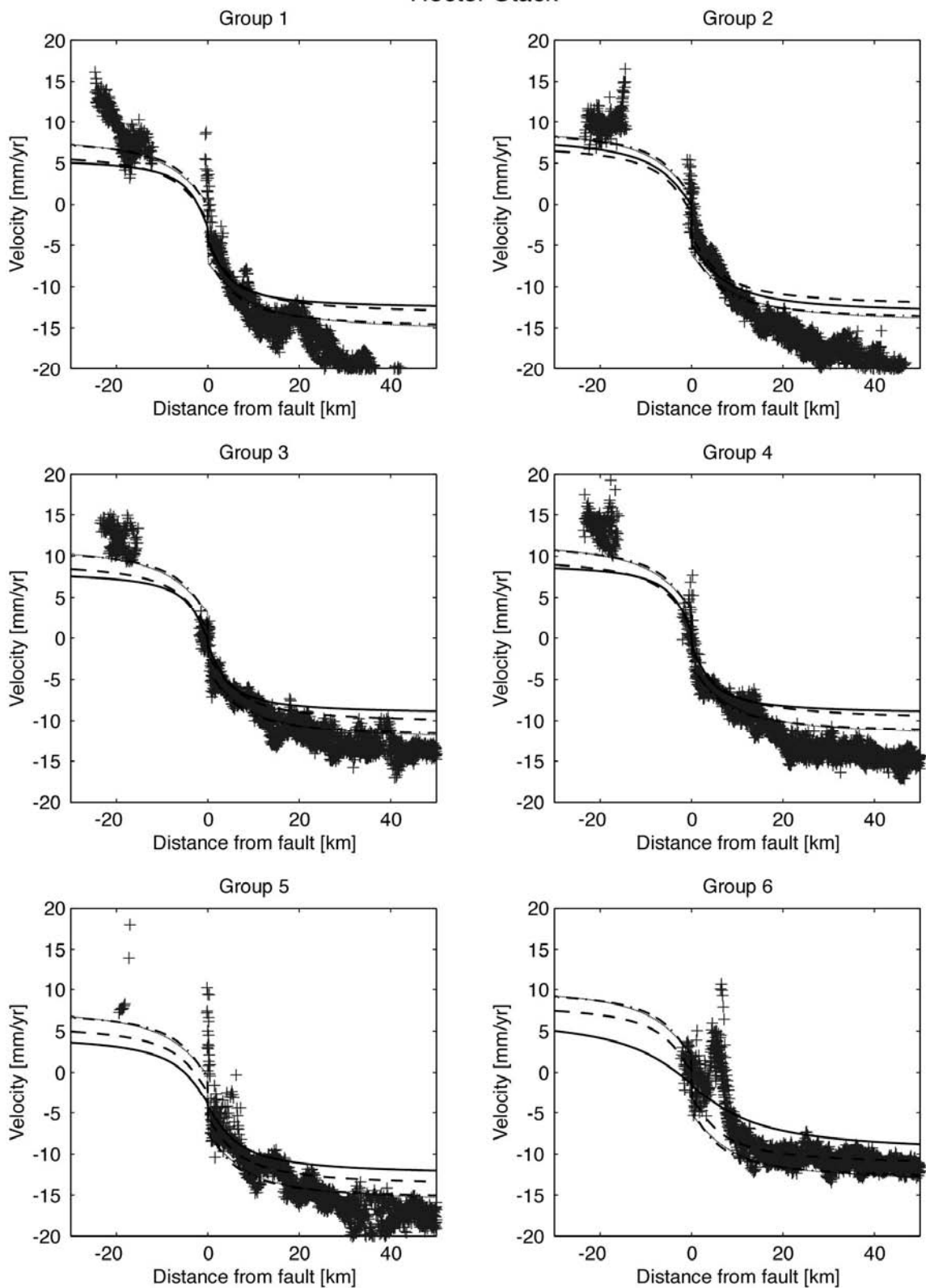


Figure 3.10. Same as Figure 3.9, but for the stack of 12 Hector Mine interferograms, time averaged over three years.

## Hector Stack



southeast segment of the fault (group 6), between Durmid Hill and Bombay Beach (B in Figure 3.7), does not show distinct signs of creep.

The profiles for the Hector Mine stack yielded similar results (Figure 3.10) to the interseismic stack. We used 12 interferograms (Table 3.2) spanning three years (July 19, 1997 to September 16, 2000), including one year of postseismic data. Groups 1, 4, and 5 showed 4-6 mm/yr LOS (12-18 mm/yr horizontal) of creep, with a reduced rate for section 2 and no creep for groups 3 and 6.

To determine the amount of triggered slip due to the Landers event, we subtracted the average interseismic displacement from the Landers stack for the 3.5 year time-period. The result is shown in Figure 3.11 and ranges from -20 to 30 mm LOS. Near the fault, the displacement varies from a 50 mm LOS (14.7 cm horizontal) slip difference in the northwest (arrow Figure 3.11) to nearly zero in the southeast near Durmid Hill. For the main segment of our survey region, triggered slip due to the Landers earthquake amounts to 15-35 mm LOS (4.5-10 cm horizontal) over the three and a half year period.

To see if there is a similar pattern for the Hector Mine earthquake, we subtracted the average interseismic velocities for a three-year period from our Hector stack. This gives an approximation of the slip due to Hector Mine during 1999-2000. The results (Figure 3.12) reveal over a centimeter of LOS motion across the entire region, but very little near-field triggered creep across the fault.

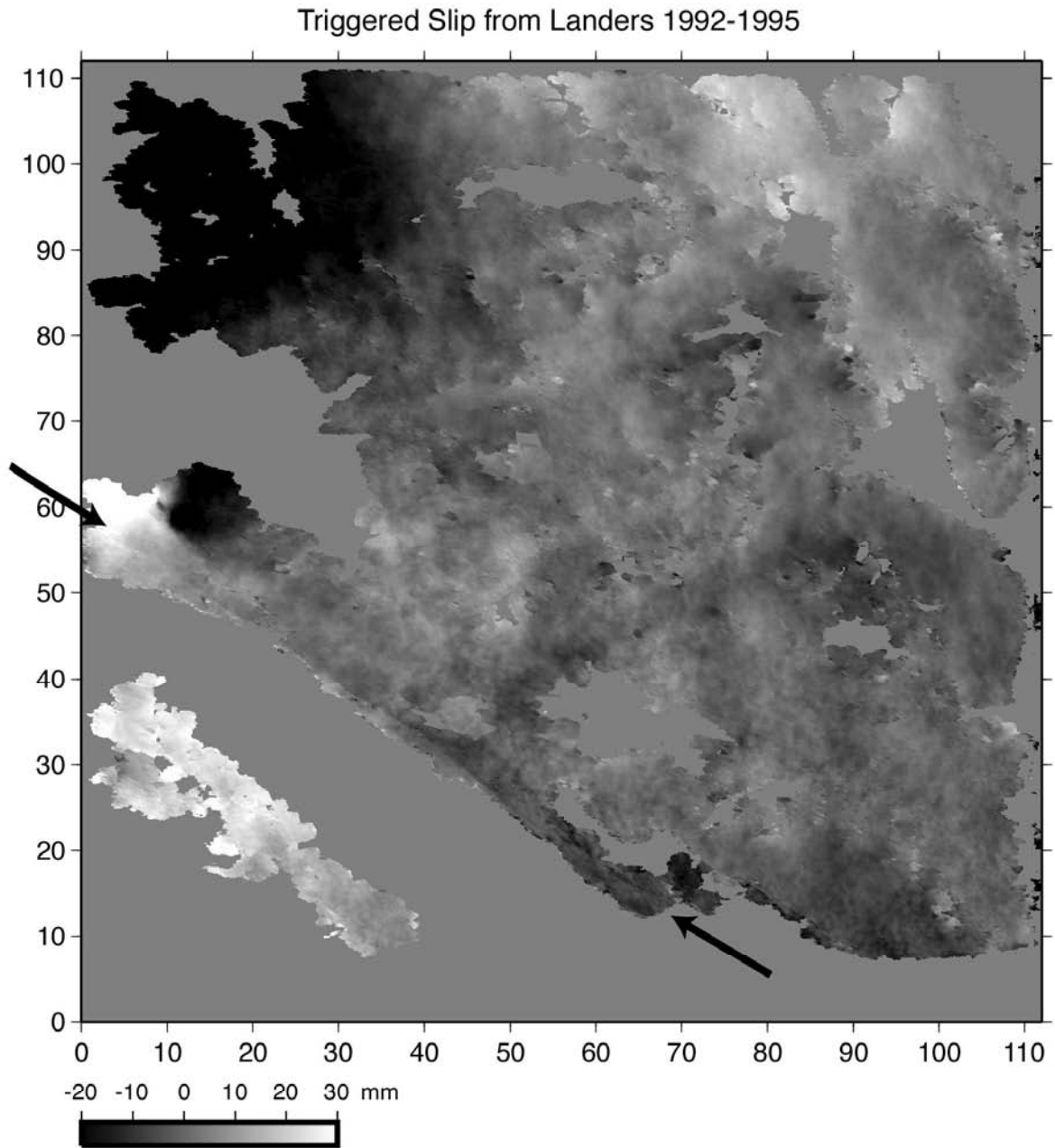


Figure 3.11. Triggered slip from the Landers earthquake for 1992-1995. Image was formed by removing the average interseismic signal for the 3.5-year timespan from the Landers stack. Triggered slip ranges from 5 cm LOS (14.7 cm horizontal) in the northwest (arrow) to zero in the southeast.

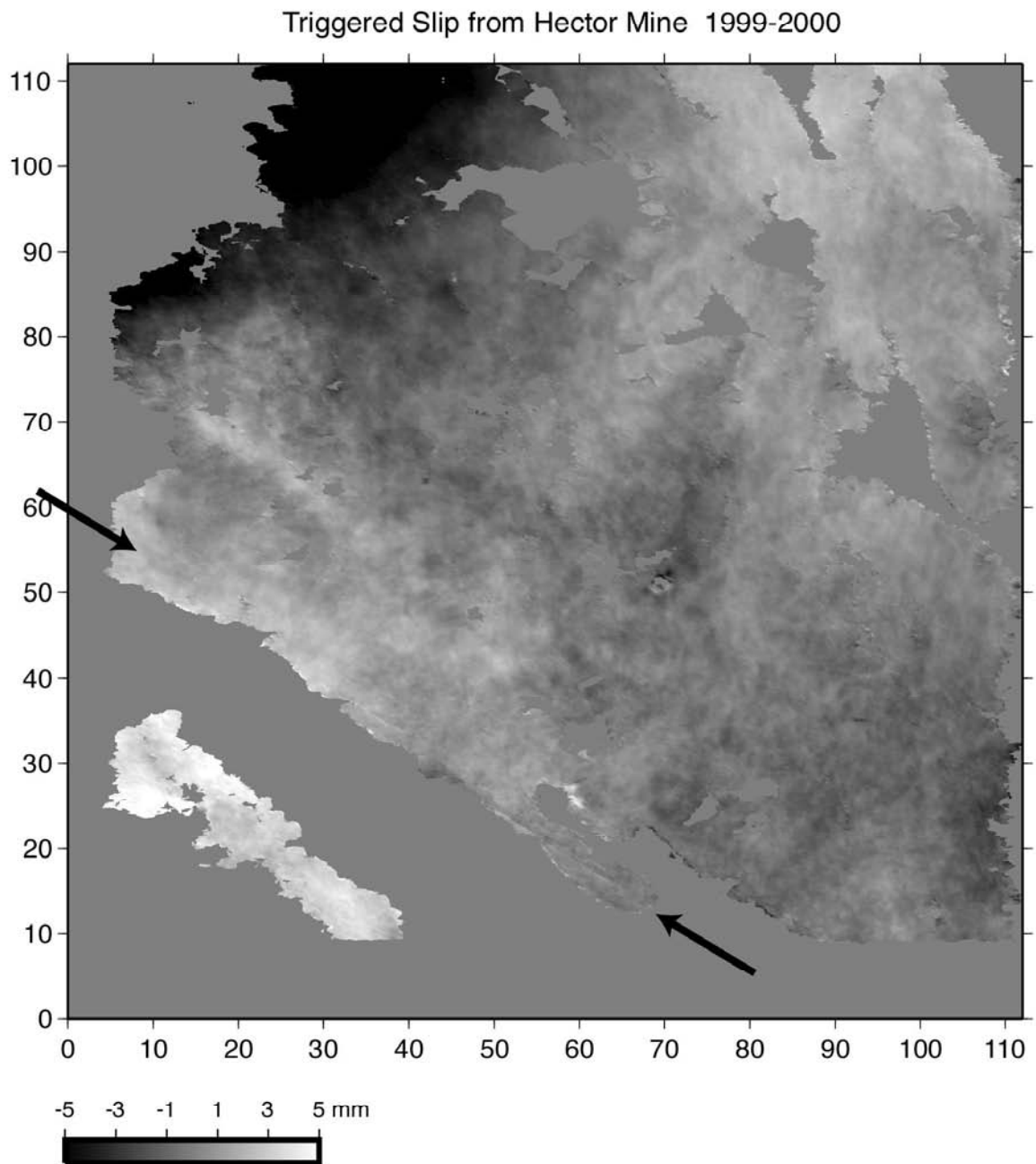


Figure 3.12. Same as Figure 3.11, but for the Hector Mine earthquake and one year of postseismic signal. Values are much smaller than for Landers and the far-field effect is more noticeable.

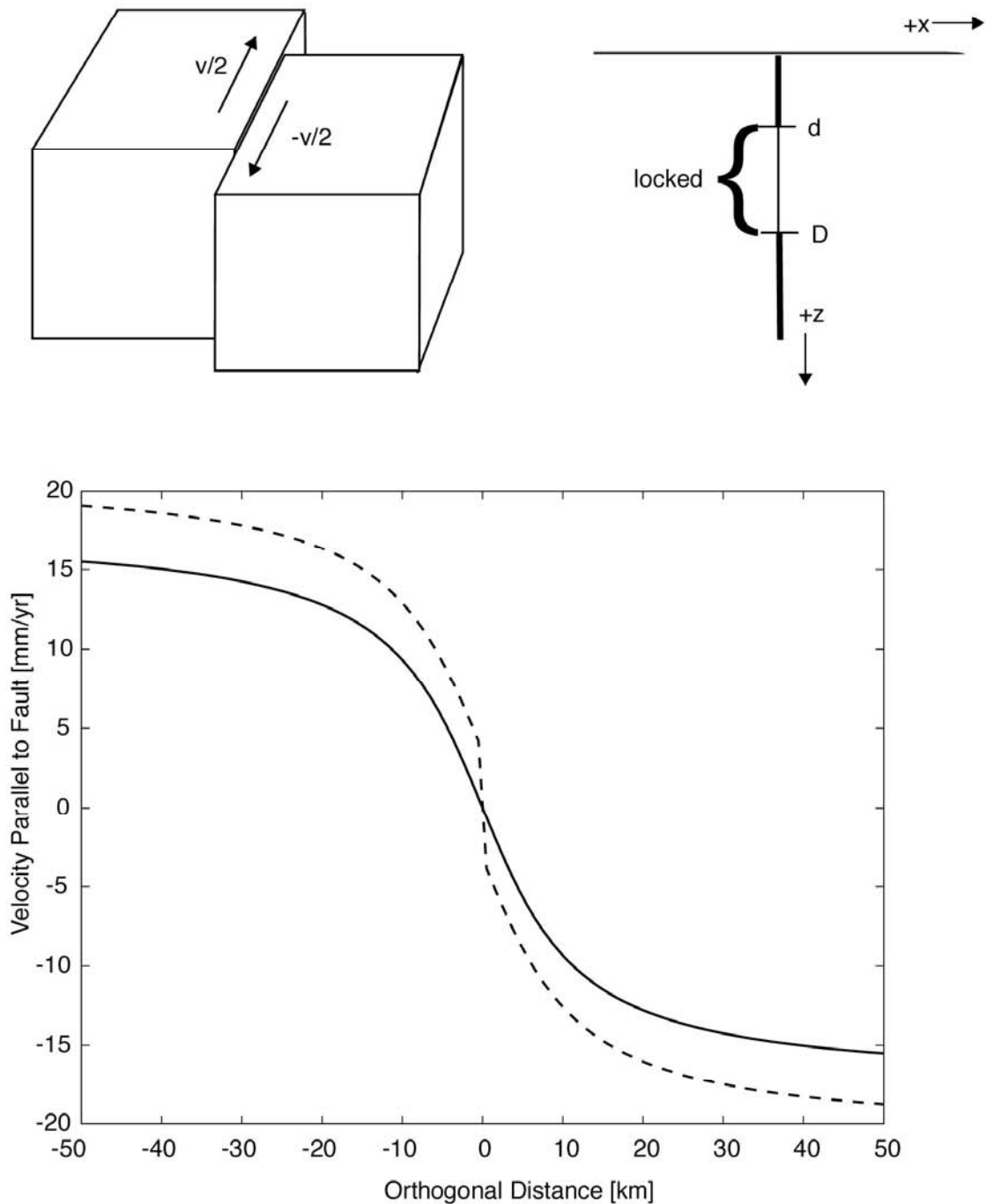


Figure 3.13. Simple elastic dislocation model. (top) A right-lateral, strike-slip fault in which two blocks slide past each other with velocity  $v$ . (bottom) The resultant deformation signature across the fault if (solid line) the fault is locked from the surface to depth  $D$  and slips freely below  $D$ , and if (dashed line) the fault is locked only between  $d$  and  $D$ . Note that this is a zero-stress boundary condition on the unlocked areas of the fault plane so displacement is continuous everywhere.

### 3.7 FAULT MODELS

We adopted the fault model originally proposed by *Weertman* [1964] and subsequently developed by *Savage and Lisowski* [1993] to determine the distribution of slip with depth for this section of the San Andreas. The model consists of two plates sliding past each other with a far-field plate velocity of  $V$ . The simplest model has a fault that slips freely between minus infinity and a deep locking depth of  $D$  (Figure 3.13). Our data show evidence for shallow creep between the surface of the Earth and some shallow locking depth  $d$ . We use the model of *Savage and Lisowski* [1993] to evaluate this shallow creep signature. In their model, shallow creep occurs when the far-field tectonic stress plus the local stress concentration due to the deep fault slip exceeds the fault strength. Fault strength depends on the coefficient of friction ( $\sim 0.85$  for most rocks [*Byerlee*, 1978]) times the normal stress, where normal stress has a component due to lithostatic pressure plus an unknown tectonic component of normal stress. The details of the model are found in *Savage and Lisowski* [1993]. The unknown parameters are the deep locking depth  $D$  and the tectonic normal stress. If there is no shallow creep, the displacement follows a smooth arctangent function (Figure 3.13, solid curve, surface locked). If there is combined shallow slip and deep slip, the displacement field will have a local abrupt transition superimposed on the broad displacement field (Figure 3.13, dashed curve, surface creep).

We varied the deep locking depth (4 to 12 km) and the tectonic normal stress (-10 to 50 MPa) to find the corresponding creeping depths. Previous estimates of the secular slip rate for the southern San Andreas Fault vary from

$V=12$  mm/yr [Wdowinski *et al.*, 2001] to  $V=26$  mm/yr [Bennett *et al.*, 1996; Working Group on California Earthquake Probabilities, 1995]. Using velocities from continuous GPS stations in the Coachella Valley and surrounding areas [SCEC, 1999], we estimated the far-field velocity as 17 mm/yr and ran our modeling program using deep slip rates of both 17 mm/yr and 26 mm/yr. Using the profiles across the fault during the interseismic phase (Figure 3.9), we estimated the slip rate on the surface at the fault trace to be 12 mm/yr, and then calculated the stress rate for each  $D-d$  pair from Savage and Lisowski [1993] equation A13. We determined the surface velocity caused by the slip on the upper segment of the fault and calculated the root mean square (RMS) misfit to the geodetic measurements (plus an unknown constant). To account for the large number of far-field measurements versus the near-field data, we weighted the misfit between the model and observations such that the misfit is equal to 1 at the fault and falls off by  $\frac{1}{\sqrt{|x|}}$  with distance,  $x$ , from the fault. We tested the effect of varying both the surface slip rate value (5-20 mm/yr) and the coefficient of friction (0.85, 0.4) and found the differences in misfit values negligible.

Figure 3.14 shows the interseismic RMS misfit between the GPS-derived velocities and the forward models for the range of locking depths and corresponding creeping depths using  $V=17$  mm/yr. The minimum misfit for each region is plotted as a circled cross, and its corresponding forward model is shown in Figure 3.9 (solid line). The dashed contour line in Figure 3.14 represents the minimum RMS value plus 10% and illustrates that there is a wide range of "reasonable" models for our data (shaded areas). For comparison, Figures 3.8-3.10

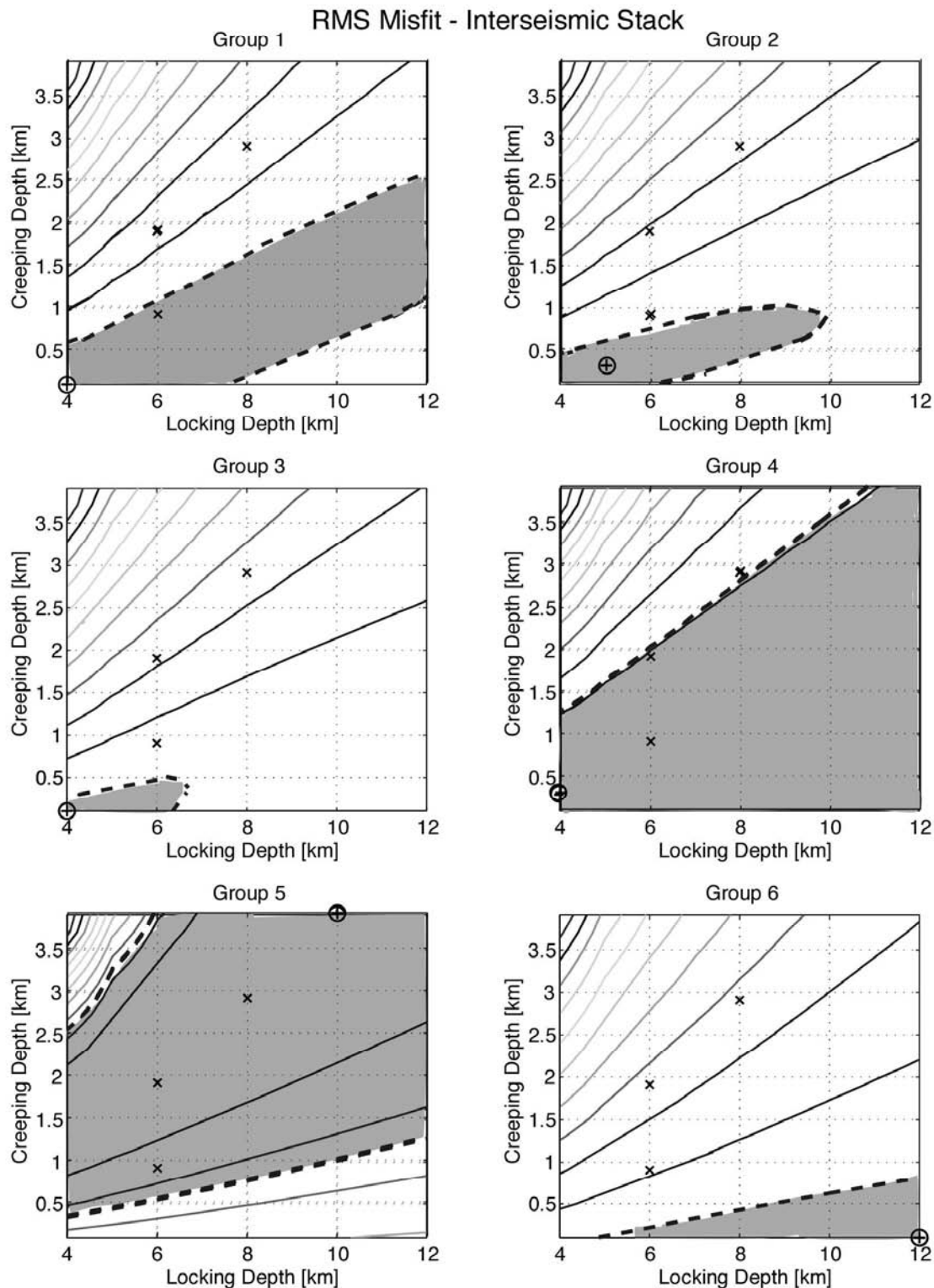


Figure 3.14. RMS values for weighted misfit between observations and models for the interseismic stack. Circled cross indicates the minimum misfit parameters; x's indicate other model values plotted in Figure 3.9. Shaded areas are minimum misfit plus 10%.

show the forward models for  $[D=6, d=0.9]$  (dashed line),  $[D=8, d=2.9]$  (dash-dot line), and  $[D=6, d=1.9]$  (dotted line). These parameter values are marked with an 'x' in Figure 3.14. Note that, for the two models with a locking depth of 6 km, altering the creeping depth changes the model significantly. However, the models for  $D=6, d\sim 2$  (dotted) and  $D=8, d\sim 3$  (dash-dot) are virtually identical, illustrating the tradeoff between locking depth and creeping depth values and the need for other sources of information (seismic, etc.) to constrain the locking depth of the fault in order to define the creeping depth. Once the locking depth is well constrained, it becomes easier to determine the most reasonable creeping depth using this model. Unfortunately, for this section of the southern San Andreas, seismicity is extremely low, so determining the locking depth is difficult. *Wdowinski et al.* [2001] give a value of  $3.8 \pm 3.3$  km for the Coachella Valley, based on the relocations by *Richards-Dinger and Shearer* [2000], while *Hauksson and Jones* [2000] show the majority of seismic events in the Coachella Valley occur  $\leq 6$  km depth, with a few as deep as 10-15 km.

### 3.8 DISCUSSION

The sequence of interferogram stacks reveals a diffuse secular strain buildup that is punctuated by localized fault creep. With the exception of the far southeast section near Durmid Hill, this entire segment of the San Andreas Fault appears to creep over the time interval encompassing the 1992 Landers earthquake. Slip is continuous for more than 60 km from Durmid Hill to Indio and the line-of-sight component of right-lateral offset ranges from 12 to 35 mm (which

maps into 3.5-10 cm of strike-slip motion) for the 3.5 year period. This triggered slip following the earthquake relieves much of the added stress that *Stein et al.* [1992] and *King et al.* [1994] predicted for the Coachella segment of the San Andreas due to the Landers event. Their Coulomb stress change model predicted that 7 cm of slip would be required to compensate for the added stresses on the fault due to Landers, with another 30 cm required to relieve the long-term stress change (equivalent to a  $M=5.7$  earthquake). Although they concede that these numbers may be overestimates, there is still a clear indication that a significant amount of the stress load related to Landers has been released aseismically along the fault over the last decade. Although this shallow creep reduces the seismic moment on the slipping section, it is important to note that stress is transferred to the deeper locked segment, bringing it closer to failure.

From 1993 until mid-1999, aseismic slip was mainly confined to two regions: northwest of Indio and between North Shore (A in Figure 3.7a) and Durmid Hill. The time history of the deformation during this period is not well determined from interferometry, although creepmeters and strainmeters along the fault suggest that this creep is episodic [*Bodin et al.*, 1994]. Following the 1999 Hector Mine earthquake, the near-field slip pattern does not alter much, though we do see increased slip during 1999-2000 of over a centimeter LOS in the far-field. To the southeast of Durmid Hill, toward Bombay Beach, there appears to be no sign of fault creep over the past decade, but a small signal may be hidden in our data.

Previous studies of the southern San Andreas by *Louie et al.* [1985] and *Bilham and Williams* [1985] covering 1967-1984 have indicated much lower values (0-3 mm/yr) of time-averaged creep for the southern San Andreas. *Bilham and Williams* also noticed an apparent relationship between the observed creep rate and the strike of the fault, with creep occurring along sections of similar strike (N47.5W). This pattern was also seen in the geologic observations of triggered slip following the Landers [*Rymer*, 2000] and Hector Mine [*Rymer et al.*, 2002] earthquakes. However, our results indicate that after 1992, the reverse pattern is true, with the fault appearing locked in the previously creeping sections and vice versa (see Table 3.3 for comparison). Since all of the sections of the southern San Andreas appear to have undergone triggered slip due to the Landers quake, the apparent switch between locking and creeping sections after the event could indicate an equalization of stress along the fault over the entire time span (1967-2000). The magnitude of slip across the fault in our study is 3-4 times the earlier ones obtained by creepmeters and could reflect either an underestimation of creep rates using creepmeters vs. geodetic means (as has been reported by *Lisowski and Prescott* [1981] and *Langbein et al.* [1983]) or a longer-term increase in the average creep rate since the Landers earthquake. Geologically derived slip measurements are also generally underestimates of slip since the distributed shear across the entire fault zone is not always manifest on the cracks [*Bodin et al.*, 1994].

All of the stacks show evidence of an apparent LOS velocity increase of ~5 mm/yr northeast of the fault in group 6 (C in Figure 3.7). The motion occurs along

Table 3.3. Comparison of creep rates for the southern San Andreas Fault from 1967-2000.

	<i>Bilham &amp; Williams</i>	<i>Louie et al.</i>	<i>Rymer et al.</i>	This Paper		Segment #	
	Triggered 1968/1978 [mm]	Average 1967-1984 [mm/yr]	Average 1967-1984 [mm/yr]	Triggered 1992/1999 [mm]	Interseismic (1993-1999) [mm/yr]		
					LOS		Horizontal
Indio	0/0	2	1.4-1.8	0-10/-			
					3-5	9-15	1
Canal	0/0	0	0-3	0/0	0-2	0-6	2
Mecca Hills	9.5/4	3	1.7-3.1	0-20/0-10	0-2	0-6	3
North Shore	~0/0	0	0	0/0	5-7	15-20	4
					5-7	15-20	5
Durmid	5/2.5	2	-	0-2/~0	~0	~0	6

a 2-5 km wide strip just downstream of the intersection of Salt Creek and the Coachella Canal (along dashed line in Figure 3.7b). A LOS increase translates to either northwest relative motion (horizontal component) or deflation (vertical component). The deformation occurs off the fault, suggesting a largely vertical component of motion. If this signal were due to erosion from stream flow, we would see decorrelation in this area of the interferograms, similar to the black areas southwest of point C in Figure 3.7a. But a regional slumping or long-term deflation would cause a coherent relative increase in the LOS signal on the northeast side of the fault, similar to that in Figure 3.7a.

There are multiple possibilities as to the cause of this subsidence. The Coachella Valley has a delicate water balance and the Water District consistently pumps groundwater to supply the fields and houses in the region. Thus, the most likely cause of ground subsidence is a groundwater extraction rate that exceeds the resupply rate. However, an interesting correlation exists between the area of subsidence and the leaking section of the Coachella Canal.

The Coachella Canal is 122 miles long and is a major branch of the All-American Canal system. Its turnout is 37 miles downstream from Imperial Dam. When the canal was constructed in 1948, it was earth-lined except for the last 38 miles, from Lake Cahuilla southward to near North Shore (A in Figure 3.7), which were concrete-lined. In 1980, to save an estimated 132,000 acre-feet of water annually which had been lost through seepage (14% of its capacity), the first 49 miles of the Coachella Branch were replaced with a 48-mile long concrete-lined canal [*Coachella Valley Water District*, 2001]. This leaves almost 35 miles of

unlined canal along the Salton Sea between Niland and North Shore (dashed line between red dots in Figure 3.7b), which loses an estimated 9,000 acre-feet of water per year [*U.S. Bureau of Reclamation*, 2001]. This unlined section follows the same route as the upslope origination of the signal seen in the interferometry, thus corroborating that the almost 6 mm/yr vertical motion is caused by a net loss of groundwater near the canal, perhaps due to mining.

### 3.9 ATMOSPHERIC EFFECTS

As discussed earlier, once the topographic phase and orbit errors are removed from an interferogram, the resultant signal is composed of the deformation signal and the atmospheric delay. To qualitatively assess the nature of atmospheric delay in this region, we assume that the deformation signal is a secular trend that is common to all interferograms (i.e. pairs of SAR images) while the atmospheric water vapor signal is mostly uncorrelated among individual SAR images. This is not always the case since, as we have seen, creep can be episodic and triggered slip can occur after nearby earthquakes, causing deformation signals that occur in only a few interferograms. However, for our analysis of the atmospheric effects, we use only interseismic interferograms, remove the average interseismic signals, and focus on signals greater than ~10 km from the fault.

There are two types of signals due to atmospheric water vapor [*Hanssen*, 2001]. The first is due to turbulent mixing in the atmosphere and is largely uncorrelated with topography. The second signal is caused by a change in the vertical stratification of the troposphere between the lowest and highest elevations

in the area. This signal is highly correlated with topography. The turbulent mixing in the neutral part of the atmosphere is predominantly from effects of the water vapor in the troposphere [Hanssen, 2001] and the phase delay is independent of radar frequency, rendering multi-wavelength measurements (such as those used to correct GPS ionospheric errors) useless. Relative humidity changes of 20% can lead to 100 mm of error in deformation maps, independent of baseline parameters [Zebker *et al.*, 1997]. Thus, the average of many interferograms is needed to minimize tropospheric effects and isolate the deformation signal. In many cases, the turbulent mixing signal appears as ripples in the image due to gravity waves. Gravity (or internal) waves are oscillations in the atmosphere which can occur as weather fronts are formed, from flow instability in the jet stream, as air flows over mountains, and as large-scale clouds form. They are responsible for mountain lee waves and clear air turbulence and have been the topic of numerous SAR studies (e.g., Chunchuzov *et al.*, 2000; Vachon *et al.*, 1995). Atmospheric gravity waves usually cause local variations of <1 cm in interferograms, and typically have wavelengths of 3-10 kilometers [Vachon *et al.*, 1994; Mattar *et al.*, 1997].

The tropospheric signal for an interferogram can be isolated from the secular deformation signal by subtracting the stacked signal (i.e. scaled by the time interval between the reference and repeat SAR acquisitions). Previously, only ERS-1 to ERS-2 tandem interferograms (i.e., 1-day time interval) were used to isolate tropospheric effects, in order to minimize temporal decorrelation and to exclude any deformation signal [Hanssen, 2001]. Here we wish to investigate the optimal sampling strategy needed to separate the deformation and atmospheric

signals using an actual set interferograms. We assume that stacking  $N$  interferograms reduces the noise in the stacked image by  $\frac{1}{\sqrt{N}}$ . Thus, we can stack many interferograms over long time spans to minimize tropospheric effects and isolate the deformation signal. This allows us to cover a much broader range of both baselines and time scales and will hopefully provide a more complete characterization of the nature of the tropospheric effects for the region.

First, we show the result of removing both the interseismic deformation signal and a residual plane from three interferograms formed from three SAR acquisitions (Figure 3.15). Atmospheric residuals range from -15 to 15 mm, and are independent of the time span between images. We selected this interferogram triplet such that two of the three display common patterns while the third does not so the characteristic atmospheric signal can be isolated to a single SAR acquisition time. In the first example (Figure 3.15), images (a) and (b) both display atmospheric "ripples" having a characteristic wavelength of 15-20 km, but the signal is not observed in interferogram (c). We conclude that e1\_09018 is the source of the gravity waves.

Similarly, the example shown in Figure 3.16 has shorter-wavelength ripples (2-3 km) in interferograms (a) and (c) but not in (b). We conclude that the ripples come from SAR acquisition e2\_11733. In addition to the ripples, interferograms (a) and (b) display wide blotches of the same sign on the western part of the area (labeled A); this atmospheric signal comes from e2\_10731. The blotch signals in e2\_10731 are probably due to precipitating cumulonimbus clouds [see *Hanssen et al.*, 1999], while the rolls in e2\_11733 are likely gravity waves.

Figure 3.15. Residual interferograms displaying atmospheric noise. The interseismic stack and any ramps (orbit error) have been removed from interferograms (a) e1\_09018\_e1\_23891, (b) e1\_09018\_e2\_04218, and (c) e1\_23891\_e2\_23256. Residuals range from -15 to 15 mm, regardless of interferogram time span. Comparison indicates the large rippling in (a) and (b) is due to image e1\_09018. This signal is not correlated with topography and is indicative of gravity waves in the troposphere.

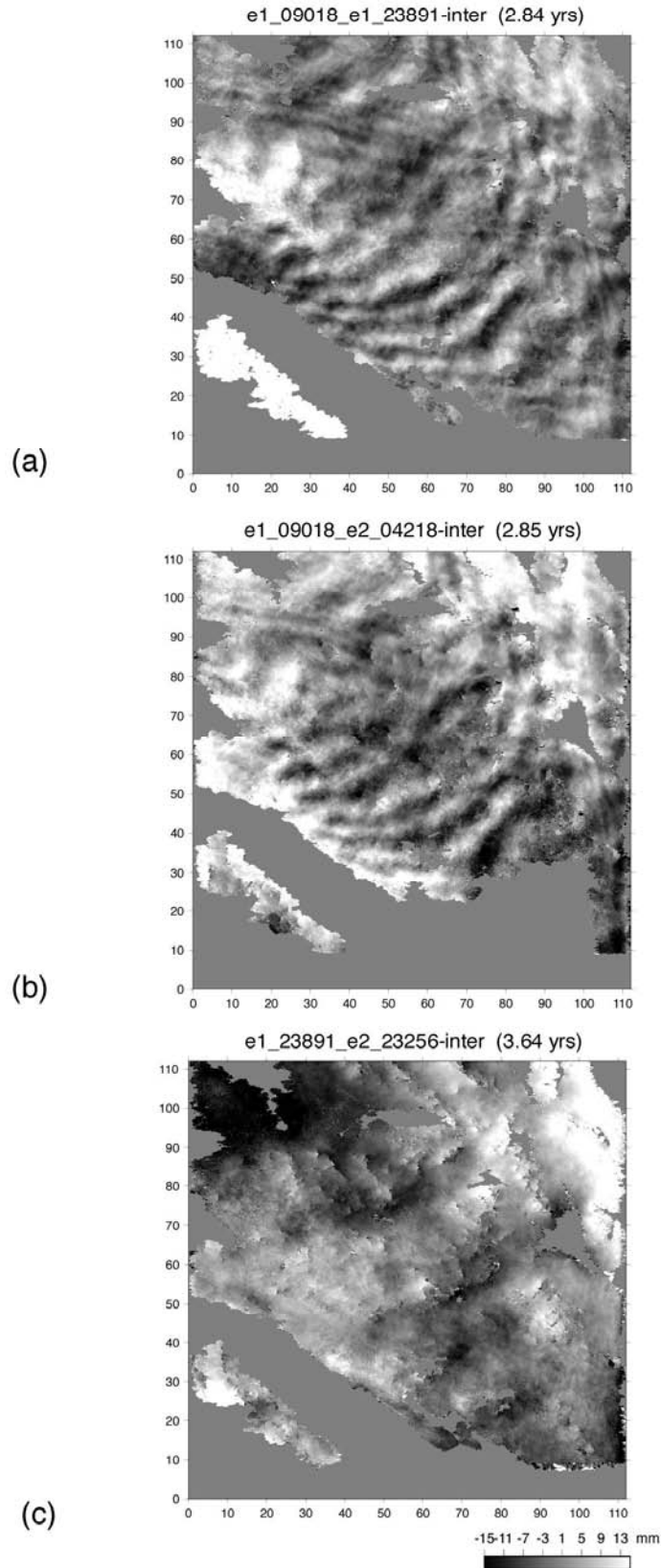
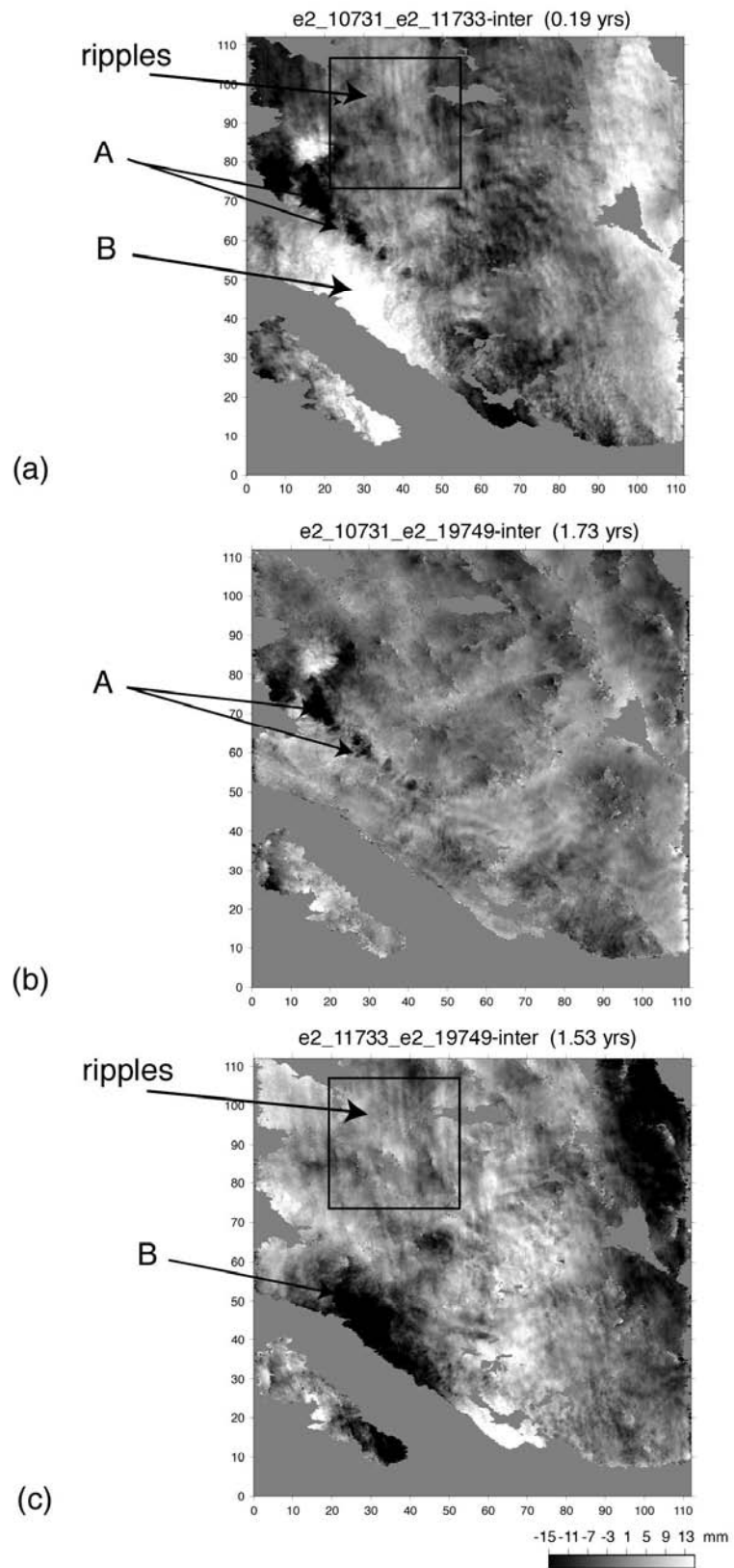


Figure 3.16. Same as Figure 3.15, but for (a) e2\_10731\_e2\_11733, (b) e2\_10731\_e2\_19749, and (c) e2\_11733\_e2\_19749. Comparison of images shows atmospheric "ripples" in e2\_11733 and large "blotches" in the western regions of e2\_10731 (labeled A). E2\_19749 does not show any predominant error patterns. As in Figure 3.15, the signal is not correlated with topography and thus is mainly from effects of water vapor in the troposphere.



One can observe other large scale signals that are common to (a) and (c) that are related to a larger scale atmospheric phenomenon (label B).

In most instances, using ERS data, one cannot isolate the atmospheric signal to a particular SAR acquisition either because the signals are chaotic or because not all elements of the triplet can be constructed. Such an example is shown in Figure 3.17 where atmospheric ripples are apparent (lower panels). We are able to isolate some long-wavelength atmospheric signal in images e1\_08517 and e2\_15240 and short-wavelength atmospheric signal in images e1\_20384 and e2\_09729. However, there is no distinct pattern to indicate a definitive cause for the variations in atmospheric signal. Thus, the signal is probably distributed among all of the SAR acquisitions.

The final interferogram examples (Figure 3.18) display atmospheric signals that are highly correlated with topography and are thus related to vertical stratification in the troposphere at elevations less than the highest peak (~2500 m). The center panel (b) in Figure 3.18 is the topography derived from a USGS grid and a stack of 25 short time span interferograms [*Sandwell and Sichoix, 2000*].

Note the correlation between the interferograms and topography is more complicated than a simple scale factor, perhaps reflecting spatial variations in the vertical stratification. While correlation with topography could also be due to topographic error, we rule this out as a possibility because the topographic error is less than 10 m [*Sandwell and Sichoix, 2000*]. For baselines of 134 and 82 m (Figures 3.18a and 3.18c), the topographic phase error is less than 3.8 mm and 2.3 mm, respectively, while the observed phase variations are more than 30 mm. A

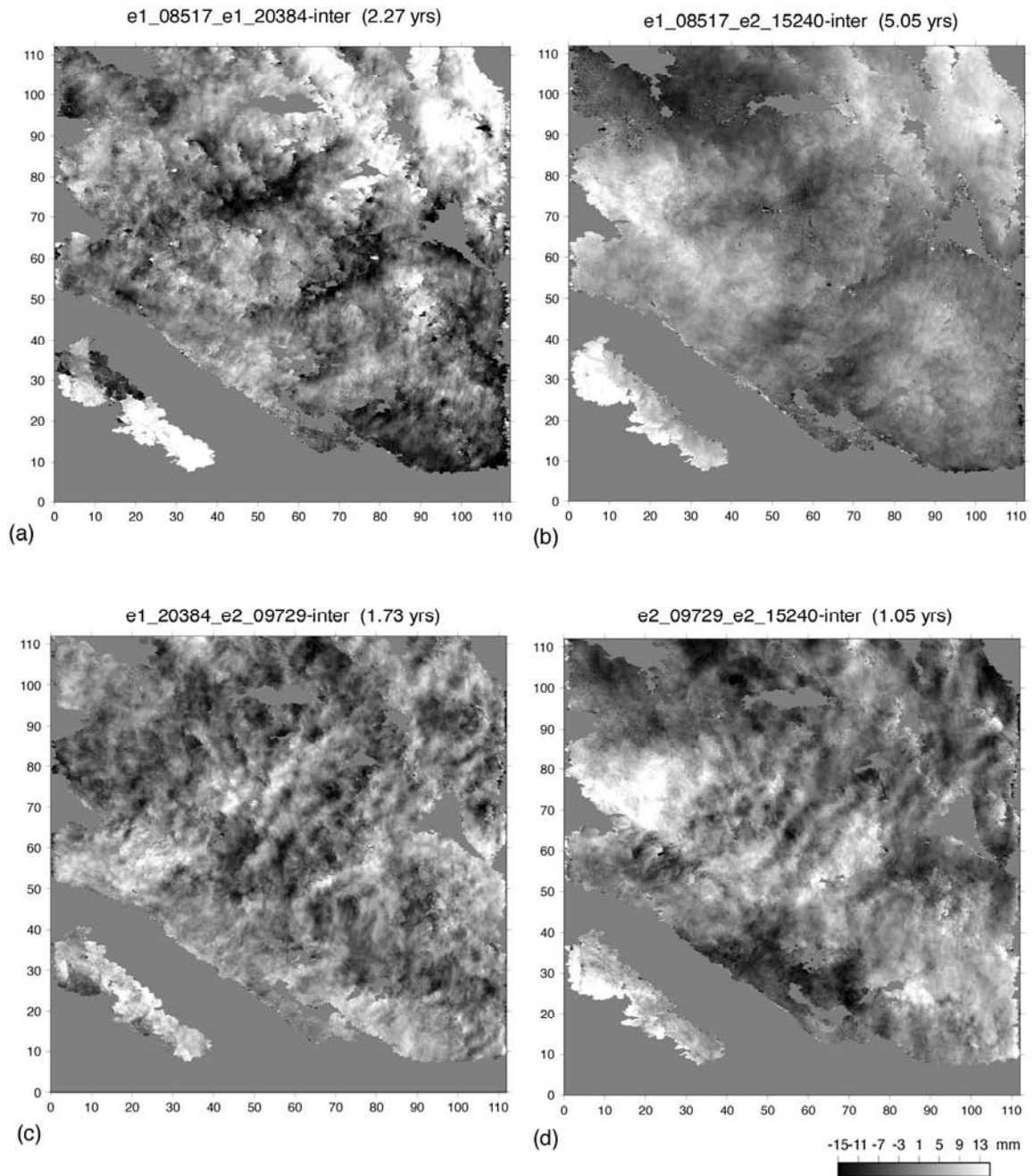
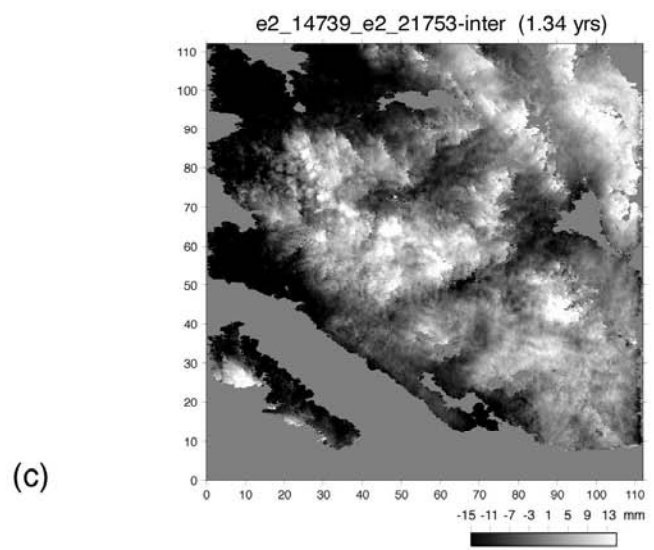
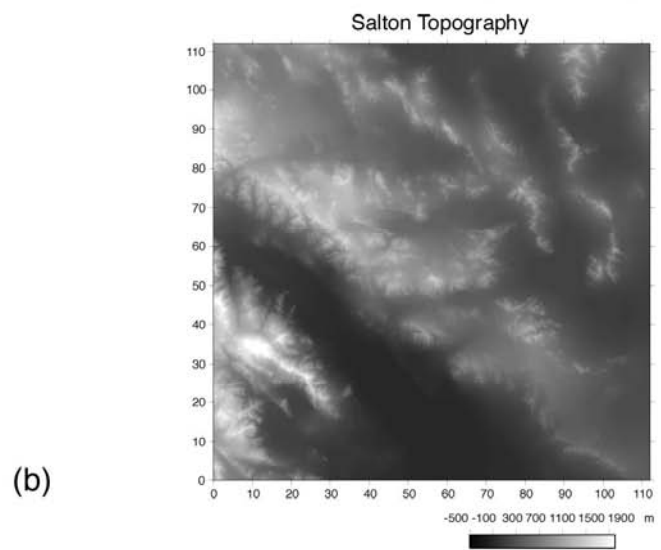
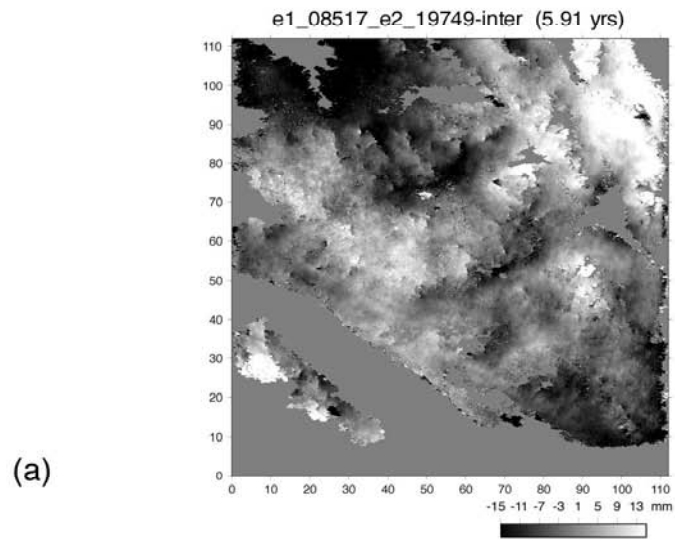


Figure 3.17. Same as Figure 3.15, but for (a) e1\_08517\_e1\_20384, (b) e1\_08517\_e2\_15240, (c) e1\_20384\_e2\_09729 and (d) e2\_09729\_e2\_15240. Comparison indicates some long-wavelength atmospheric signal in images e1\_08517 and e2\_15240 and short-wavelength atmospheric signal in images e1\_20384 and e2\_09729.

Figure 3.18. Atmospheric noise due to topography illustrated in interferograms (a) e1\_08517\_e2\_19749 and (c) e2\_14739\_e2\_21753, compared with (b) the topography (in meters) for the study region. The residuals in (a) and (c) mimic patterns seen in (b), indicating the main contribution to the atmospheric errors in these interferograms is from vertical stratification of the atmosphere due to topography, rather than from water vapor in the troposphere.



quantitative correlation between the residual phase and the topography could be used to isolate the effect due to vertical stratification.

Tables 3.1 and 3.2 provide the mean and variance for each of our 60 interferograms. The values in Table 3.1 were derived from interferograms where the secular deformation derived from the entire stack of 60 interferograms was removed. The standard deviation for the images is less than 15 mm for most of the interferograms and the median of all of the standard deviations is 8.39 mm. Table 3.2 categorizes images into their respective time frames - Interseismic Stack, Hector Stack and Landers Stack - to isolate different types of deformation (triggered slip vs. interseismic creep). When shorter stack intervals are used, the standard deviation is typically less than 10 mm.

### 3.10 CONCLUSIONS

Along the southern San Andreas, InSAR can be used to detect the near-field movement of the fault in regions of little vegetation. For areas of partial decorrelation in the interferograms (cropland, populated areas, etc.), the use of permanent scatterers slightly improves the coherence, which increases the area where the phase can be unwrapped. Since the stack of interferograms is the union of the unwrapped phase of the individuals, slight improvements in coherence can lead to significant improvements in the stack. Further improvements in coherence are provided by multilook averaging, but this reduces the spatial resolution of the final LOS displacement maps.

Near the Salton Sea, we found evidence of triggered slip along the entire section of the San Andreas due to the 1992 Landers earthquake, but saw mostly far-field motion from the 1999 Hector Mine earthquake. The amount of interseismic creep varies both temporally and spatially, with the largest values between Desert Beach and Durmid Hill and the smallest values between Durmid Hill and Bombay Beach. At the far southeast end of the fault, there is a large deflating region near the Coachella Canal that appears to be caused by excess groundwater removal along the unlined section of the canal.

### 3.11 ACKNOWLEDGEMENTS

Some of the figures were created using the GMT software of *Wessel and Smith* [1991]. Duncan Agnew provided a computer program to create a grid interpolating the SCEC velocity model at specific points. Reviews by Roland Bürgmann and Freysteinn Sigmundsson led to a considerable improvement in our slip model and in the organization of this paper. This work was supported by a Department of Defense, National Defense Science and Engineering Graduate Fellowship (S.N. Lyons), NASA Earth Systems Science Fellowship (S.N. Lyons), and NSF Earth Sciences grant NSF EAR-0105896 (D.T. Sandwell).

### 3.12 REFERENCES

Bennett, R.A., W. Rodi, and R.E. Reilinger, Global Positioning System constraints on fault slip rates in southern California and northern Baja, Mexico, *J. Geophys. Res.*, *101*, 21,943-21,960, 1996.

- Bilham, R. and P. Williams, Sawtooth segmentation and deformation processes on the southern San Andreas Fault, California, *Geophys. Res. Lett.*, 12, 557-560, 1985.
- Bodin, P., R. Bilham, J. Behr, J. Gomberg, and K.W. Hudnut, Slip triggered on southern California faults by the 1992 Joshua Tree, Landers and Big Bear earthquakes, *Bull. Seism. Soc. Am.*, 84, 806-816, 1994.
- Bürgmann, R., D. Schmidt, R.M. Nadeau, M. d'Alessio, E. Fielding, D. Manaker, T.V. McEvelly, and M.H. Murray, Earthquake potential along the northern Hayward fault, California, *Science*, 289, 1178-1182, 2000.
- Byerlee, J.D., Friction of rocks, *Pure Appl. Geophys.*, 116, 615-626, 1978.
- Chunchuzov, I., P.W. Vachon, and X. Li, Analysis and modelling of atmospheric gravity waves observed in RADARSAT SAR images, *Remote Sensing of Environment*, 74, 343-361, 2000.
- Coachella Valley Water District, Water and the Coachella Valley, <http://www.cvwd.org/water&cv.htm>, 2001.
- Ferretti, A., C. Prati, and F. Rocca, Nonlinear subsidence rate estimation using permanent scatterers in differential SAR interferometry, *IEEE Trans. Geos. Remote Sens.*, 38, 2202-2212, 2000.
- Ferretti, A., C. Prati, and F. Rocca, Permanent scatterers in SAR interferometry, *IEEE Trans. Geos. Remote Sens.*, 39, 2001.
- Hanssen, R.F., Radar Interferometry: Data interpretation and error analysis, Ph.D. thesis, Technische Universiteit Delft, 2001.
- Hanssen, R.F., T.M. Weckwerth, H.A. Zebker, and R. Klees, High-resolution water vapor mapping from interferometric radar measurements, *Science*, 283, 1297-1299, 1999.
- Harris, R. A., and P. Segall, Detection of a locked zone at depth on the Parkfield, California, segment of the San Andreas fault, *J. Geophys. Res.*, 92, 7945-7962, 1987.
- Hauksson, E., and L.M. Jones, Interseismic background seismicity of the southern San Andreas Fault, California, *Proceedings of the 3<sup>rd</sup> Conference on Tectonic Problems of the San Andreas Fault System*, Stanford, Calif., September 6-8, 2000.
- Haynes, M., New developments in wide-area precision surveying from space, *Mapping Awareness*, 13, 40-43, 1999.

- King, G.C.P., R.S. Stein and J. Lin, Static stress changes and the triggering of earthquakes, *Bull. Seism. Soc. Amer.*, *84*, 935-953, 1994.
- Langbein, J., A. McGarr, M.J.S. Johnston, and P.W. Harsh, Geodetic measurements of postseismic crustal deformation following the 1979 Imperial Valley earthquake, California, *Bull. Seism. Soc. Am.*, *73*, 1203-1224, 1983.
- Lisowski, M. and W.H. Prescott, Short-range distance measurements along the San Andreas fault system in central California, 1975 to 1979, *Bull. Seismol. Soc. Am.*, *71*, 1607-1624, 1981.
- Lorenzetti, E. and T.E. Tullis, Geodetic predictions of a strike-slip fault model: Implications for intermediate- and short-term earthquake prediction, *J. Geophys. Res.*, *94*, 12,343-12,361, 1989.
- Louie, J.N., C.R. Allen, D.C. Johnson, P.C. Haase, and S.N. Cohn, Fault slip in Southern California, *Bull. Seism. Soc. Am.*, *75*, 811-833, 1985.
- Massonnet, D. and K.L. Feigl, Radar interferometry and its applications to changes in the Earth's surface, *Reviews of Geophys.*, *36*, 441-500, 1998.
- Mattar K.E., A.L. Gray, D. Geudtner, and P.W. Vachon, Interferometry for mapping and terrain displacement: Effect of anisotropic propagation, *International Symposium, Geomatics in the Era of RADARSAT (GER'97)*, Ottawa, Canada, 1997.
- Richards-Dinger, K.B. and P.M. Shearer, Earthquake locations in southern California obtained using source specific station terms, *J. Geophys. Res.*, *105*, 10,939-10,960, 2000.
- Rosen, P.A., S. Hensley, I.R. Joughin, F.K. Li, S.N. Madsen, E. Rodriguez, and R.M. Goldstein, Synthetic Aperture Radar Interferometry, *Proceedings of the IEEE*, *88*, 333-382, 2000.
- Rymer, M., Triggered surface slips in the Coachella Valley area associated with the 1992 Joshua Tree and Landers, California, earthquakes, *Bull. Seism. Soc. Am.*, *90*, 832-848, 2000.
- Rymer, M., J. Boatwright, L.C. Seekins, J.D. Yule, and J. Liu, Triggered surface slips in the Salton Trough associated with the 1999 Hector Mine earthquakes, *Bull. Seism. Soc. Am.*, *92*, 1300-1317, 2002.
- Sandwell, D.T. and E.J. Price, Phase gradient approach to stacking interferograms, *J. Geophys. Res.*, *103*, 30,183-30,204, 1998.

- Sandwell, D., and D. Agnew, Strain accumulation and fault creep on the southern San Andreas Fault: 1992 to present, *EOS Trans. AGU, Fall Meet. Suppl.*, 80:F692, 1999.
- Sandwell, D. and L. Sichoix, Topographic recovery from stacked ERS interferometry and a low resolution digital elevation model, *J. Geophys. Res.*, 105, 28,211-28,222, 2000.
- Savage, J.C., Equivalent strike-slip earthquake cycles in half-space and lithosphere-asthenosphere earth models, *J. Geophys. Res.*, 95, 4873-4879, 1990.
- Savage, J.C. and R.O. Burford, Discussion of paper by C. H. Scholz and T. J. Fitch, Strain accumulation along the San Andreas Fault, *J. Geophys. Res.*, 76, 6469-6479, 1971.
- Savage, J.C. and M. Lisowski, Inferred depth of creep on the Hayward Fault, central California, *J. Geophys. Res.*, 98, 787-793, 1993.
- Savage, J.C. and R.W. Simpson, Surface strain accumulation and the seismic moment tensor, *Bull. Seism. Soc. Am.*, 87, 1354-1361, 1997.
- Sieh, K.E., Slip rate across the San Andreas Fault and prehistoric earthquakes at Indio, California, *EOS, AGU Fall Meeting Supplement*, 67, 1200, 1986.
- Southern California Earthquake Center Crustal Dynamics Working Group, SCEC Horizontal Deformation Map v.2.0, [http://www.scecdc.scec.org/group\\_e/release.v2](http://www.scecdc.scec.org/group_e/release.v2), 1999.
- Stein, R.S., G.C.P. King, and J. Lin, Change in failure stress on the southern San Andreas fault system caused by the 1992 Magnitude=7.4 Landers earthquake, *Science*, 258, 1328-1332, 1992.
- Sylvester, A.G., R. Bilham, M. Jackson, and S. Barrientos, Aseismic growth of Durmid Hill, southeasternmost San Andreas Fault, California, *J. Geophys. Res.*, 98, 14,233-14,243, 1993.
- Thatcher, W., Nonlinear strain buildup and the earthquake cycle on the San Andreas Fault, *J. Geophys. Res.*, 88, 5893-5902, 1983.
- Tse, S.T. and J.R. Rice, Crustal earthquake instability in relation to depth variation of frictional slip parameters, *J. Geophys. Res.*, 91, 9452-9572, 1986.
- U.S. Bureau of Reclamation, Coachella Project Description, <http://dataweb.usbr.gov/html/coachella.html>, 2001.

- Vachon, P.W., J.A. Johannessen, and D.B. Browne, ERS-1 SAR images of atmospheric gravity waves, *IEEE Trans. Geos. Remote Sens.*, 33, 1014-1025, 1995.
- Vachon, P.W., O.M. Johannessen, and J.A. Johannessen, An ERS-1 synthetic aperture radar image of atmospheric lee waves, *J. Geophys. Res.*, 99, 22483-22490, 1994.
- Vincent, P., J.B. Rundle, R. Bilham, and S.M. Buckley, Aseismic creep along the San Andreas and Superstition Hills faults with uplift at Durmid Hill, southernmost San Andreas fault, CA measured by radar interferometry, *EOS, AGU Fall Meeting Supplement*, 79, 45, 1998.
- Wdowinski, S., Y. Sudman, and Y. Bock, Distribution of interseismic deformation along the San Andreas fault system, southern California, *Geophys. Res. Lett.*, 28, 2321-2324, 2001.
- Weertman, J., Continuous distribution of dislocations on faults with finite friction, *Bull. Seism. Soc. Am.*, 54, 1035-1058, 1964.
- Wessel, P. and W.H.F. Smith, Free software helps map and display data, *EOS Trans. AGU, Fall Meet. Suppl.*, 72, 445-446, 1991.
- Working Group on California Earthquake Probabilities, Seismic hazard in southern California: probable earthquakes, 1994 to 2024, *Bull. Seism. Soc. Am.*, 85, 379-439, 1995.
- Zebker, H.A., P.A. Rosen, and S. Hensley, Atmospheric effects in interferometric synthetic aperture radar surface deformation and topographic maps, *J. Geophys. Res.*, 102, 7547-7563, 1997.

This chapter, in full, is a reprint of the material as it appears in the *Journal of Geophysical Research*, Lyons, Suzanne; Sandwell, David, 2002 The dissertation author was the primary investigator and author of this paper and the co-authors directed and supervised the research.

## Appendix 3.A

### Salton Sea Photo Survey of Permanent Scatterers

*If we knew what it was we were doing, it would not be called research, would it?*

-Albert Einstein

#### 3.A.1 SURVEY OVERVIEW

In Chapter 3, we introduced the concept of permanent scatterers: points that remain stable in SAR images over long time periods. These points remain coherent over several years and can be used as either weighting values for interferograms (as discussed in Chapter 3) or as a "natural" GPS network (for more information on permanent scatterers in interferometry, see *Haynes, 1999, Ferretti et al., 2000, and Ferretti et al., 2001*).

To determine what types of natural or man-made objects make good point scatterers, on March 15, 2002, David Sandwell, Bridget Smith, and I trekked to the Salton Sea to conduct a photo survey at specific points of varying scattering amplitude. Figure 3.A.1 shows all fifteen of the survey sites, plotted on an image of the average amplitude of a stack of 37 side-look-complex (SLC) images of the Coachella Valley northwest of the Salton Sea. Most sites appear nondescript in the amplitude image, with the exception of sites 14 and 15, which show obvious backscatter saturation. The backscatter at 14 and 15 is similar to that of a corner reflector - an artificial 2-3 meter trihedral metallic structure specifically designed



Figure 3.A.1. The average amplitude of the stack of 37 side-look complex (SLC) images of the Salton Sea/Coachella Valley region, with the survey points labeled.

to reflect the incoming beam straight back to the sensor with relatively little power loss compared to the ground surface in its vicinity [Haynes, 1999].

Figure 3.A.2 shows the survey sites plotted on the scattering amplitude ( $s^2$ , see Chapter 3). Many of the survey sites lie on the boundary between a bright area and a dark area (e.g., sites 2, 3, 6b, and 12), providing the perfect opportunity to compare ground characteristics of both good and poor permanent scatterers.

### 3.A.2 SOUTHEAST REGION

The southeast section of the survey region is highlighted in Figure 3.A.3 and the corresponding photos at each site are in Figures 3.A.4 and 3.A.5. For sites 1-5, the areas of scrub brush and buildings showed high stability (high scattering amplitude), while the tilled fields had very high dispersion (low scattering amplitude). This is not surprising as the climate in the Salton Sea area is such that scrub brush remains basically constant over time, while the plowed fields have variable backscattering characteristics, depending on whether it's time for harvesting, tilling, or cultivating crops.

### 3.A.3 CENTRAL REGION

The central region of our survey is shown in Figure 3.A.6, with its corresponding site photos in Figure 3.A.7. The most prominent feature in the amplitude image is the airport north of site 7. The flat runways return very little backscatter to the satellite (much as a calm lake reflects the beams away at an angle approximately equal to the angle of incidence), while the metallic hangars

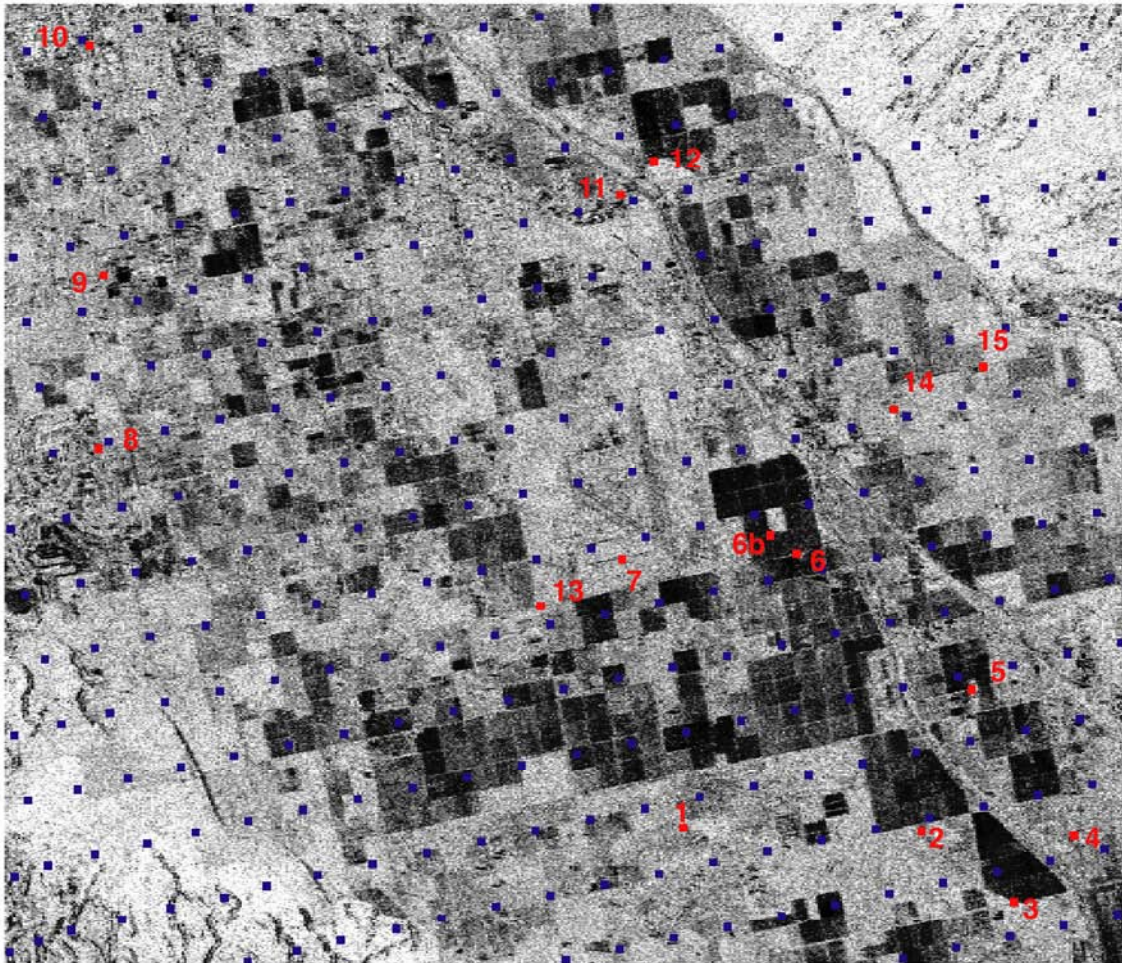
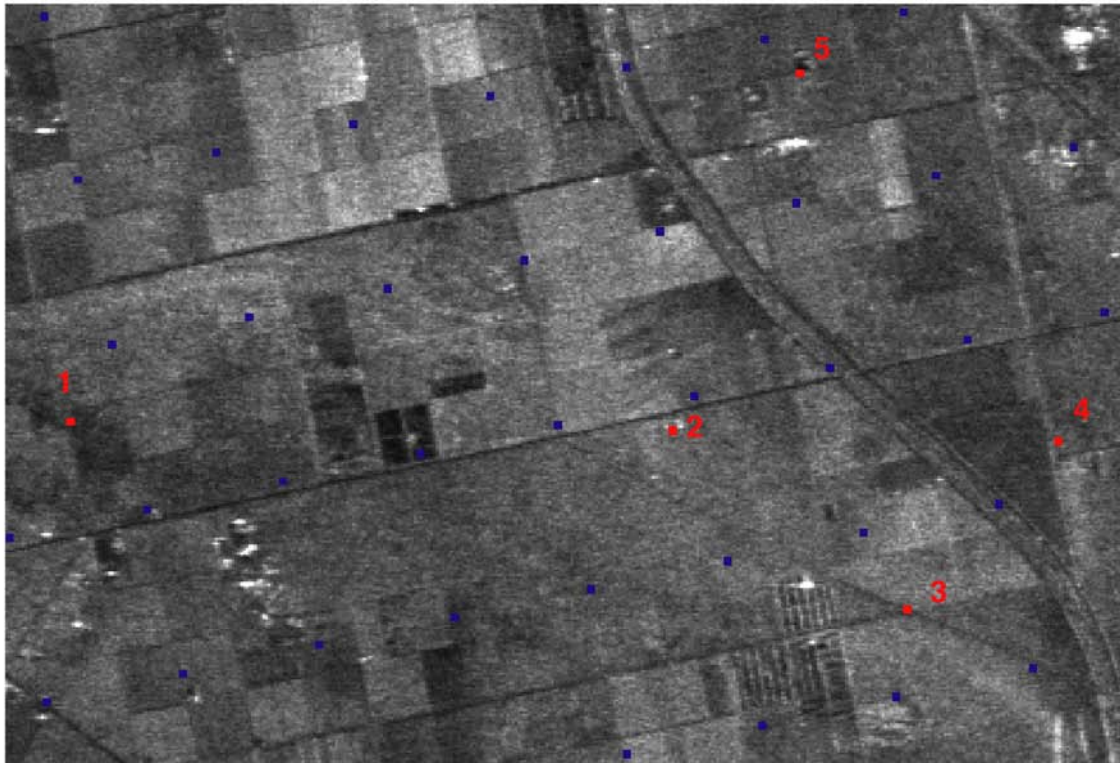
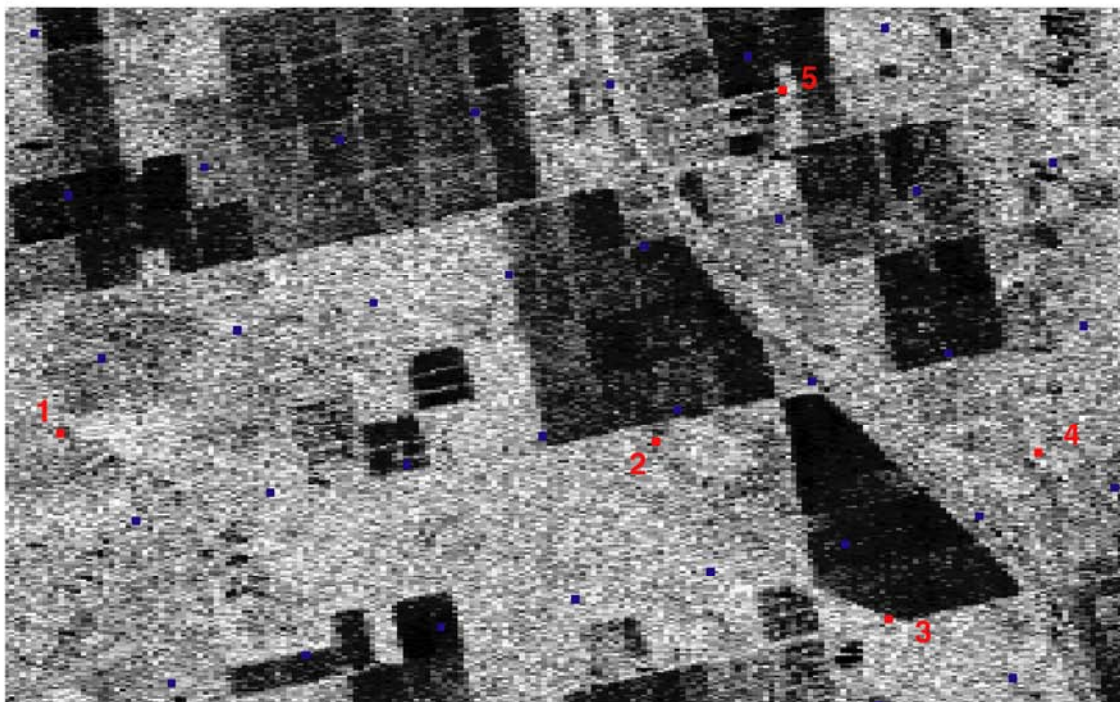


Figure 3.A.2. The scattering amplitude ( $s^2$ ) of the stack of 37 side-look complex (SLC) images of the Salton Sea/Coachella Valley region, with the survey points labeled.



(a)



(b)

Figure 3.A.3. Southeast Salton survey region. Images show (a) average amplitude of SAR stack and (b) average scattering amplitude with survey points labeled.



Site 1: East - dry brush



West - green brush



Site 2: North - junk yard



Site 3: North - tilled field



South - trailer park

Figure 3.A.4. Photos of sites 1-3, southeast survey region.



Site 4: South - trees



Site 5: NE - buildings and crossroads

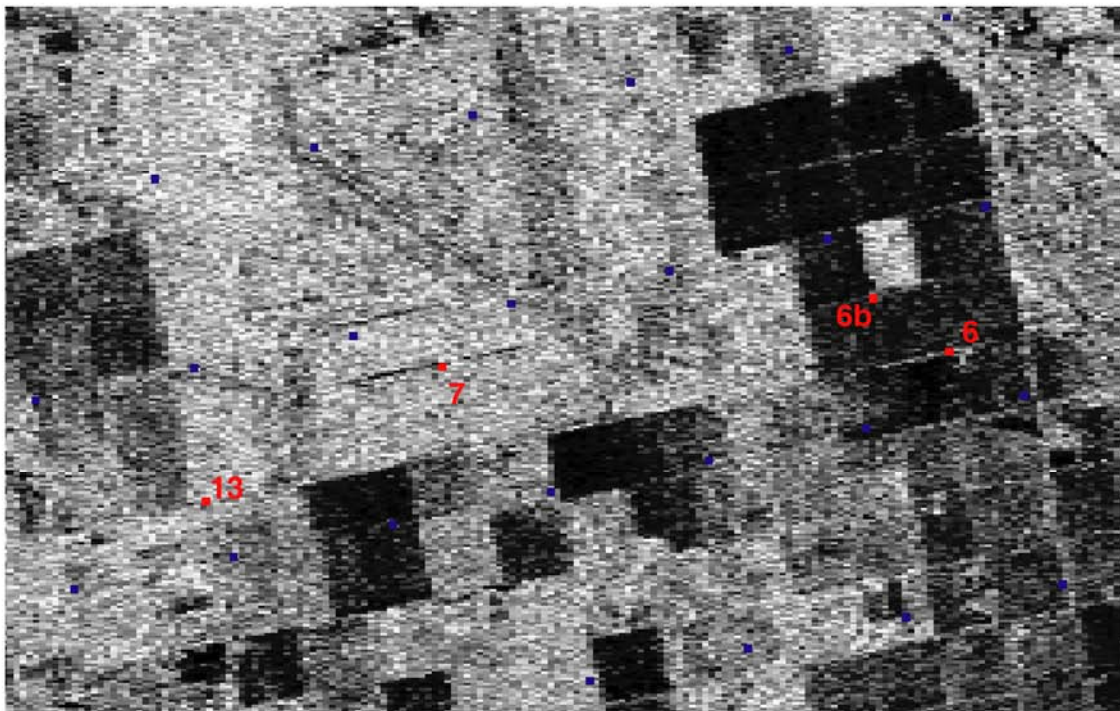


South - grassy patches and road

Figure 3.A.5. Photos of sites 4 and 5, southeast survey region.



(a)



(b)

Figure 3.A.6. Central Salton survey region. Images show (a) average amplitude of SAR stack and (b) average scattering amplitude with survey points labeled.



Site 6: NNE - scrub brush patch in tilled field



South - irrigated field



Site 6b: NNE - Dave trespassing into "public facility"



Site 7: West - abandoned runway



Site 13: NW - palm trees



SW - vineyard

Figure 3.A.7. Photos of sites 6-7 and 13, central survey region.

appear very bright. The scatterer image highlights different features, however. The runways still appear dark because, although they remain stable over time, they do not reflect much of the transmitted energy, and thus the scattering amplitude is still very low. This is dependent on the angle of the road with respect to the satellite. Site 6 lies on a road that is angled such that the backscatter remains fairly consistent and at a higher amplitude than the runways, so the road appears bright in the scattering image.

Site 6b lies on the edge of a sharp contrast between high and low scattering amplitudes. The bright area is the scrub brush seen in Figure 3.A.7a and 3.A.7.c, while the dark areas are irrigated cropland. The prominent dark stripe in the scatterer image at site 7 turned out to be an abandoned runway in the middle of scrub brush, south of the main airport. For site 13, the area just to the southwest of the site has a brighter scattering amplitude than the northwest area, though their average backscatter is similar (Figure 3.A.6). This darker region to the northwest is a palm tree farm, while the southwest region is a vineyard. Presumably, the difference in the scattering amplitude is related to the variation in foliage density at the palm tree farm, while the vineyard remains rather consistent year-round.

#### 3.A.4 NORTHWEST REGION

The northwest section of our survey region is shown in Figure 3.A.8 with the corresponding site photos in Figure 3.A.9. The most distinctive characteristic at site 8 is the strange contoured shapes west of the site, which appear bright in both the average amplitude image and the scattering amplitude image. This turned

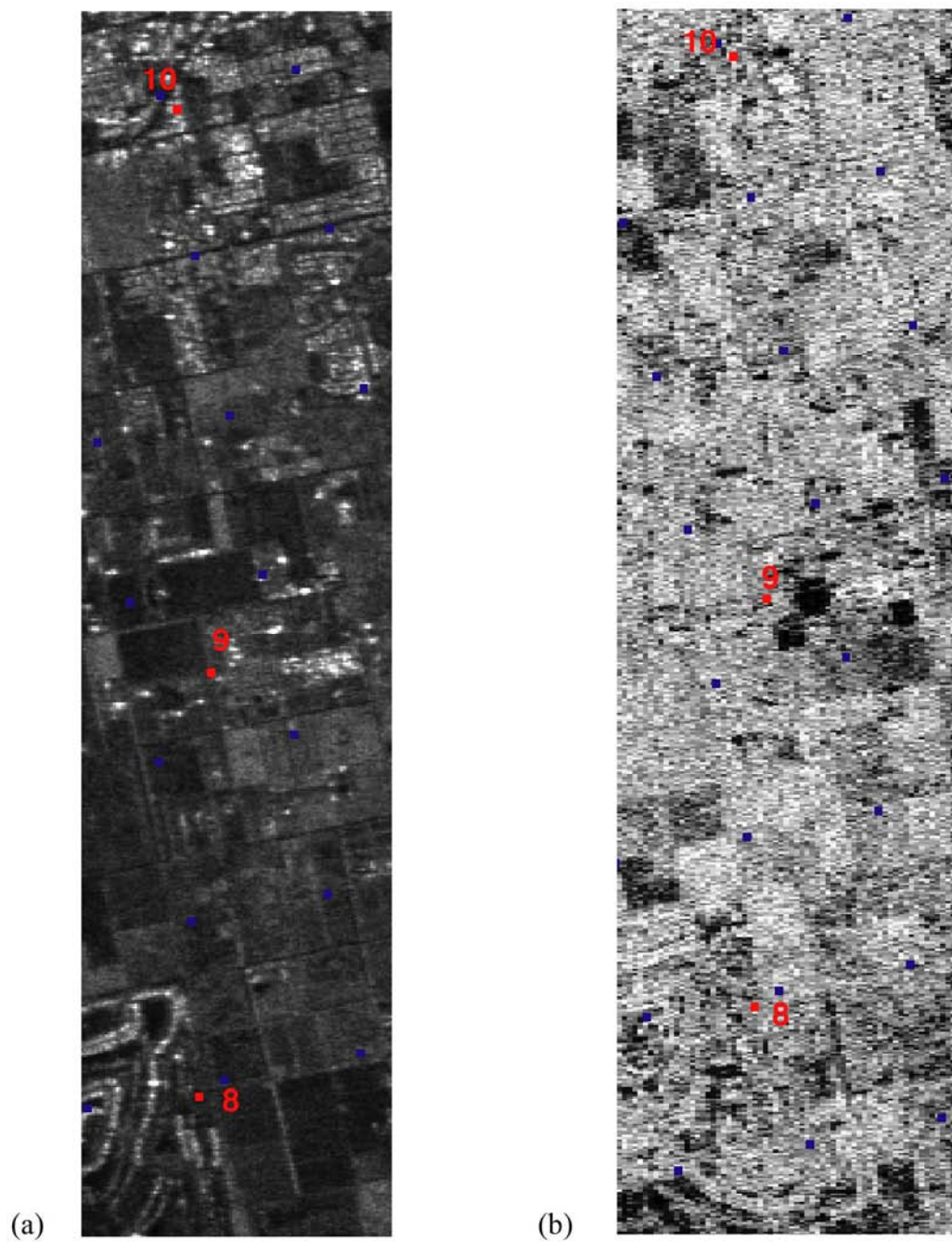


Figure 3.A.8. Northwest Salton survey region. Images show (a) average amplitude of SAR stack and (b) average scattering amplitude with survey points labeled.



Site 8: NW - Bridget on the golf course



Site 9: WNW - polo field



Site 10: East - movie theatre

Figure 3.A.9. Photos of sites 8-10, northwest survey region.

out to be a golf course community with expensive houses and manicured lawns. The water hazards and greens appeared dark in the backscatter image, but had a medium scattering amplitude, while the houses appeared bright in both images.

At site 9, we were interested in the strange ring in the scattering amplitude to the east of the site (Figure 3.A.8b). Unfortunately, during the survey, we could not find any object that appeared to explain this signal and ended up photographing an area too far to the west. The only possible explanation we could find was a horse show arena approximately in the location of the ring, where there were multiple RVs and horse trailers.

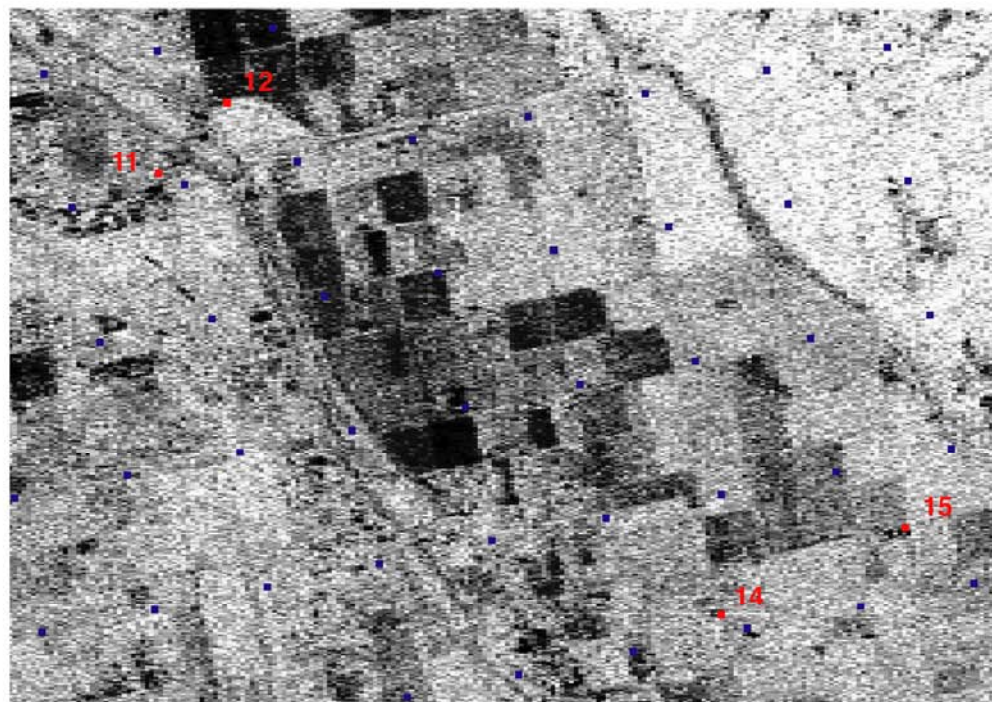
### 3.A.5 NORTHEAST REGION

The final section of our survey, in the northeast quadrant, is shown in Figure 3.A.10, with the corresponding site photos in Figures 3.A.11 and 3.A.12. At site 11, the dark splotches in the scattering image are correlated to a lumberyard. Although the main buildings at the yard remain stable over time, the lumber is constantly being delivered and distributed, thus altering the backscattering characteristics over time and causing high dispersion in the stack of images. For site 12, the scattering contrast is due once again to the difference between cropland (high dispersion over time) and scrub brush (relatively consistent over time).

Sites 14 and 15 have very high backscatter, but appear as dark pixels in the scattering image. This is due to the clipping of saturated pixels in 3.A.10.b and is a result of a very large scattering amplitude. This illustrates the deceptiveness of



(a)



(b)

Figure 3.A.10. Northeast Salton survey region. Images show (a) average amplitude of SAR stack and (b) average scattering amplitude with survey points labeled. Note the high reflections for points 14 and 15 in (a) which saturates the surrounding pixels.



Site 11: South - Lumberyard



Site 12: North - plowed field



South - scrub brush



Site 14: West - Building with collapsed roof

Figure 3.A.11. Photos of sites 11-12 and 14, northeast survey region.



Site 15: ESE - duck pond

Figure 3.A.12. Photos of site 15, northeast survey region.

looking at just the amplitude or the scattering image without cross-referencing with the other. There are many hidden signals at sites like #3, where the amplitude image is completely nondescript, but the scattering image illustrates the variability of the region over time. On the other hand, clipping in the scattering image can hide very strong reflectors, like those at sites 14 and 15. Site 14 is a metallic building with a half-collapsed roof, similar to a typical corner reflector but almost ten times the size. Thus, the backscatter at that pixel is easily saturated by the reflection from the building.

At site 15, the cause of the saturation is a little more obscure. The most prominent feature at that location is the large duck pond. However, bodies of water usually reflect radar signals away from the satellite and thus, typically have very low scattering amplitude. The building could be the source of the high backscatter if its roof were aligned for maximum reflection back toward the satellite. Unfortunately, due to trespassing constraints, we were not able to fully investigate what object might be causing such a strong reflection at this site.

### 3.A.6 CONCLUSIONS

Overall, the pattern of typical reflectors showed that effective permanent scatterers consisted of buildings and scrub brush areas, while poor scatterers were agricultural areas, loading bays (such as the lumberyard), and most roads. This is similar to what we expected, given the backscattering characteristics of each and how they change with time. It does raise the hope, however, that even in agricultural areas, the presence of sheds and buildings might be used to create

natural stable GPS-like networks which can reveal the deformation signal that might otherwise be irrecoverable using InSAR.

### 3.A.7 REFERENCES

Ferretti, A., C. Prati, and F. Rocca, Nonlinear subsidence rate estimation using permanent scatterers in differential SAR interferometry, *IEEE Trans. Geos. Remote Sens.*, 38, 2202-2212, 2000.

Ferretti, A., C. Prati, and F. Rocca, Permanent scatterers in SAR interferometry, *IEEE Trans. Geos. Remote Sens.*, 39, 2001.

Haynes, M., New developments in wide-area precision surveying from space, *Mapping Awareness*, 13, 40-43, 1999.

## Chapter 4

### Conclusions

*...Though I had never before enjoyed a storm of this sort, the strange, wild thrilling motion and rumbling could not be mistaken, and I ran out of my cabin, near Sentinel Rock, both glad and frightened, shouting, "A noble earthquake!" feeling sure I was going to learn something.*

*-John Muir, Our National Parks*

In this dissertation, we have looked at various methods of determining creep rates across faults in southern California. The tectonic implications of fault creep are still debated, with some investigators believing creep is the first step in failure leading to major earthquakes (preseismic slip) [Nason, 1973], while others argue that creep reduces stress buildup along faults, therefore precluding very large earthquakes along the creeping section [Prescott and Lisowski, 1983; Bürgmann *et al.*, 2000]. Regardless, most models of earthquake generation use creep to load asperities on a fault, which subsequently fail in earthquakes. Thus, creep studies are important in determining seismic hazard along active faults in southern California.

#### 4.1 FAULT CREEP ON CALIFORNIA FAULTS

Figure 4.1 shows the distribution of creeping faults in California. From north to south, these faults are: Green Valley, Concord, Hayward, Sargent, Calaveras, San Andreas (from near San Juan Bautista to Cholame and from Indio through the Coachella Valley to its terminus), Superstition Hills, and Imperial. Previous studies have utilized a wide array of geodetic methods to study the creep rates along these faults in an effort to categorize the slip characteristics of the each fault.

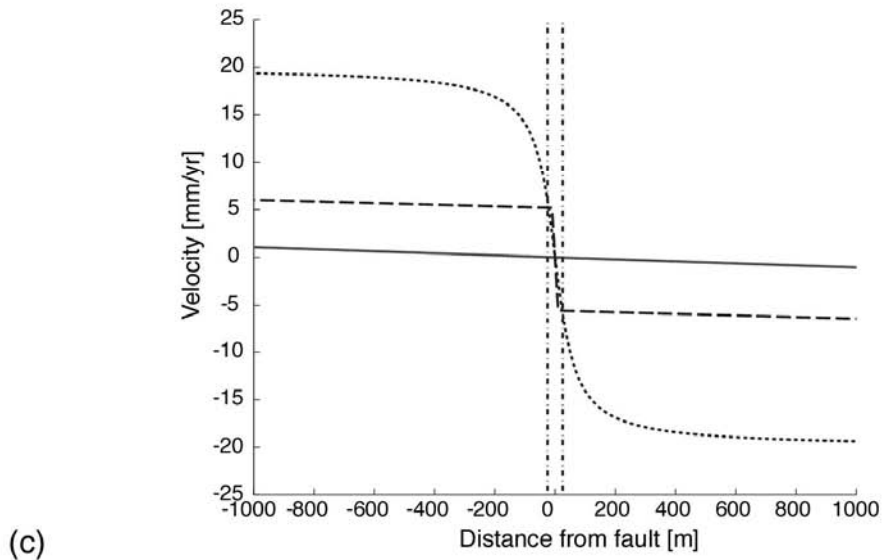
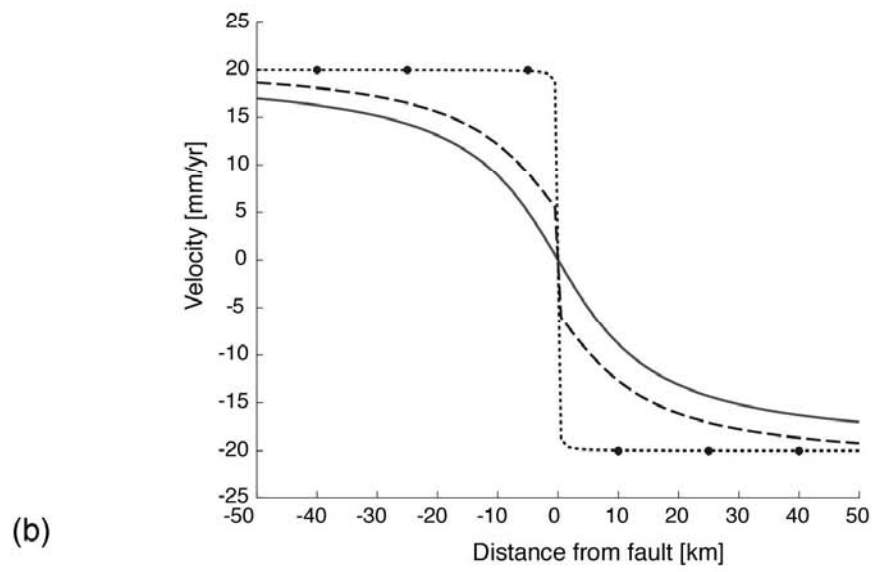
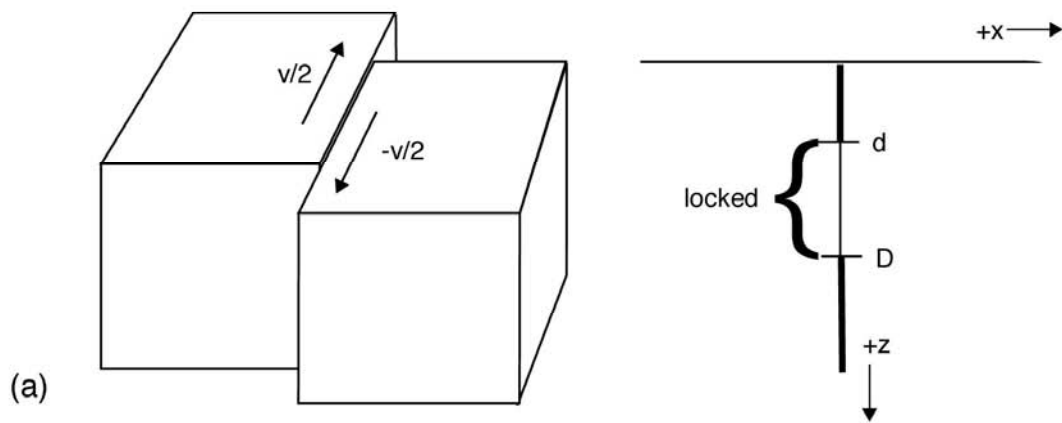
The majority of creep measurements in California have been either through field observations of cracks across a fault (e.g., *Rymer, 2000; Rymer et al., 2002*) or, more commonly, through the use of creepmeters (e.g., *Burford et al., 1973; Nason, 1973; Schulz et al., 1982*). Geologically derived slip measurements generally underestimate the creep rate since the distributed shear across the entire fault zone is not always manifest on the cracks [*Bodin et al., 1994*]. Studies by *Burford and Harsh [1980]* and *Lisowski and Prescott [1981]* showed that creepmeters sampled 80% or more of the displacement measured by alignment and trilateration arrays at only 8 of 16 sites along the San Andreas. Compared with geodetic means, creepmeters usually underestimate the surface slip along a fault [*Lisowski and Prescott, 1981; Langbein et al., 1983*]. This is not surprising when one looks at the typical model of displacement across a strike-slip fault (Figure 4.2).

The usual fault model consists of two plates sliding past each other with a far-field plate velocity of  $V$ . The simplest model has a fault that slips freely between minus infinity and a deep locking depth of  $D$  (Figure 4.2a). If there is no



Figure 4.1. Major faults in California. Creeping faults are shaded gray. Dates of major ( $M > 7$ ) earthquakes are shown at their approximate epicenters. Pink areas indicate faults that slipped during the Great Earthquakes of 1857, 1872, and 1906. CF=Calaveras Fault, GVF=Green Valley/Concord Faults, HF=Hayward Fault, BF=Banning Fault, SHF = Superstition Hills Fault. Image courtesy of the U.S. Geological Survey.

Figure 4.2. (a) Simple model of a strike slip fault. Two plates move past each other with a plate velocity,  $V$ , below a locking depth,  $D$ . (b) Displacement across a fault for a model with slip below  $D$  (solid line), creep from the surface to a depth,  $d$ , and slip below  $D$  (dashed line), and slip from the surface to down to infinity (dotted line). Dots represents spacing of continuous GPS sites. (c) Close-up of (b) within 1 km on each side of the fault. Dash-dot line represents extent of creepmeters.



shallow creep, the displacement follows a smooth arctangent function (Figure 4.2b, solid curve, surface locked). If the fault creeps from the surface all the way to the locking depth, the displacement will be a step at the fault (Figure 4.2b, dotted). The most common case, however, is if the fault is slipping only between the surface of the Earth and some shallow locking depth  $d$ , so there is combined shallow slip and deep slip. The displacement field for this model will have a local abrupt transition superimposed on the broad displacement field (Figure 4.2b, dashed curve, surface creep, from *Savage and Lisowski* [1993] model).

Creepmeters tend to be confined to within 10-50 m across the fault (most are ~30 m long). Thus, they only measure a very small portion (dash-dot lines in Figure 4.2c) of the creeping zone. For faults with shallow creep in a narrow zone, the creepmeters will detect most of this surface slip (solid line). However, in the real world, the creep signature is expressed in a zone that can be greater than 50 meters across, meaning the creepmeters will only detect a portion of this movement (e.g., dotted line), thus underestimating the true value. While geodetic measurements capture the full velocity field, typical GPS site spacing is on the order of 10 km for continuous sites (large dots in Figure 4.2b), which is insufficient for detecting the narrow creep signature.

Dense GPS networks, such as the one in the Imperial Valley [*Mason*, 1987], with a spacing of 500 meters between sites can detect the near-field creep signature while still covering the entire deformation zone to include the far-field deformation (as discussed in Chapter 2). These networks are expensive and labor-

intensive, however, and not practical for assessing the nature of the entire San Andreas Fault System.

Interferometry, on the other hand, has the benefits of fine sampling (~20 m), large area coverage (100 x 100 km per frame) and relatively easy accessibility. Thus, it would seem ideal for wide-area studies of creep along faults. As has been discussed in Chapter 3, there are limitations to this method as well, with the interferograms becoming decorrelated in vegetated and populated regions. Therefore, the best plan of attack for studying creep on California faults is to use a combination of all of these methods, keeping in mind the strengths and limitations of each.

#### 4.2 NORTHERN CALIFORNIA FAULTS

In northern California, creepmeter measurements from 1970 to 1982 [Schulz *et al.*, 1982] revealed creep rates of 3-7 mm/yr for the northern Calaveras Fault and 7-12 mm/yr for the southern Calaveras Fault. Theodolite measurements of creep rates on active faults in the San Francisco Bay region spanning over 20 years yielded creep rates of 3-5 mm/yr along the Green Valley, Concord, Hayward, and northern Calaveras faults, with higher creep rates of 11-18 mm/yr for the southern Calaveras and San Andreas faults near San Juan Bautista, California (Figure 4.1). The other faults in this region exhibited less than one mm/yr of surface slip [Galehouse, 1999].

Creepmeter [Bilham, 1998] and InSAR [Bürgmann *et al.*, 2000] studies of the Hayward Fault have confirmed the theodolite measurements, with creep rates

for the Hayward Fault ranging from 3-8 mm/yr. The interferometric analysis by *Bürgmann et al.* [2000] (Figure 4.3), which also utilized microearthquakes along the fault to constrain the distribution of subsurface fault creep rates, yielded models in which the Hayward Fault creeps over most of the seismogenic zone. This implies that the earthquake potential along the northern Hayward Fault may be lower than previous studies have indicated.

#### 4.3 CENTRAL CREEPING SECTION

Farther south, along the central creeping section of the San Andreas Fault, previous creepmeter measurements from *Schulz et al* [1982] from 1968 to 1982 revealed creep rates of 7-11 mm/yr on the northern end of this section of the San Andreas near San Juan Bautista and the Cienega Winery (Figure 4.1), climbing to almost 28 mm/yr to the south near Slack Canyon and Middle Mountain, and then dropping back down to 3-5 mm/yr just south of Parkfield. South of Twisselman Ranch, the fault appears to be locked to the surface, with <1 mm/yr of creep along the bend and south toward Anza [*Schulz et al.*, 1982]. USGS creepmeter data from 1987 to 1997 has confirmed rates of 21 mm/yr at the northern end of the section near Slack Canyon, decreasing to ~10 mm/yr at Parkfield and 3.5 mm/yr at the southern end near the locked section.

*Rosen et al.* [1998] used interferometry to look for aseismic creep along this central section of the San Andreas Fault. Although their interferograms were limited by atmospheric errors and decorrelation over time, fault creep of almost 8 mm/yr was apparent in the images (Figure 4.4). We have also looked at this

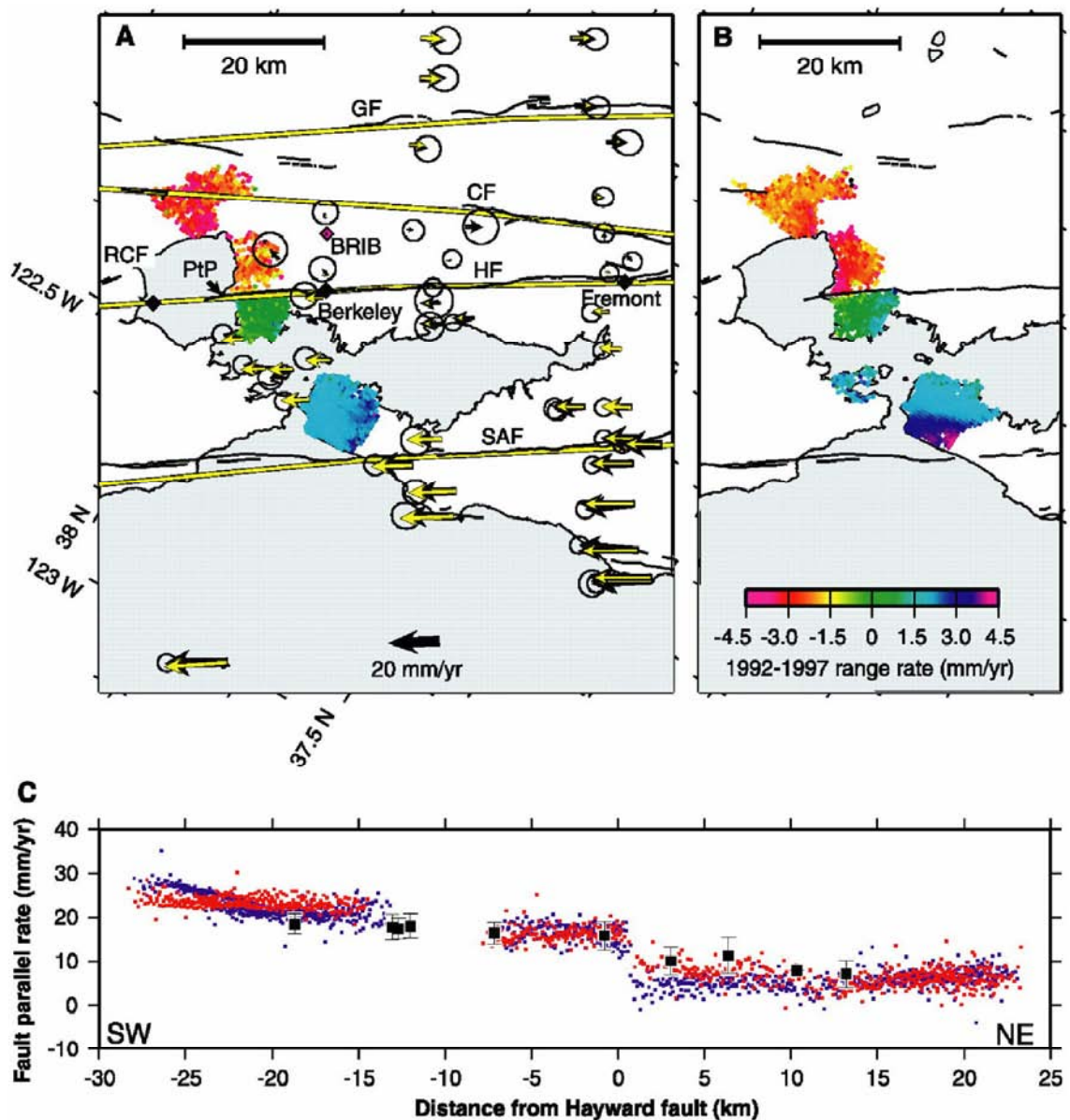


Figure 4.3. (A) Line-of-sight (LOS) displacement for the Hayward Fault from June 1992 to September 1997 interferogram, along with horizontal GPS velocities relative to station BRIB. (B) Interferogram from September 1992 to August 1997. (C) Profiles of GPS velocities within 10 km of the InSAR data in (A) and (B) with  $1\sigma$  error bars. InSAR data from (A) is in blue and data from (B) is in red. From *Burgmann et al.*, 2000.

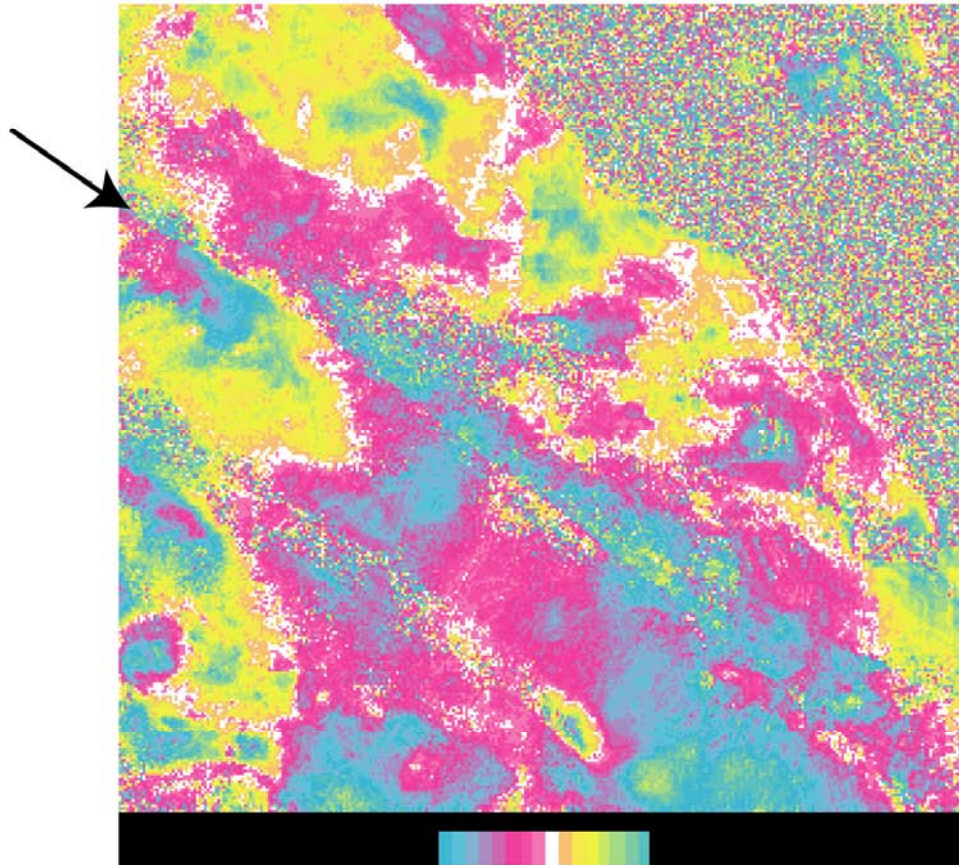


Figure 4.4. Interferogram of the San Andreas Fault (arrow) near Parkfield, California from 1992 to 1993. One color cycle represents 28.4 mm of motion along the line-of-sight (LOS). From *Werner et al.*, 1997.

region using interferometry in an attempt to test the permanent scatterers method introduced in Chapter 3. Initial interferograms are shown in Figures 4.5 and 4.6. Unfortunately, most of the interferograms are highly decorrelated due to the change in vegetation over time. Testing different filters and weighting values (Figure 4.6), we have been able to ascertain viable creep signals from the interferograms. However, there is still much work left to do in this area to determine the most effective scheme for extracting the deformation signal.

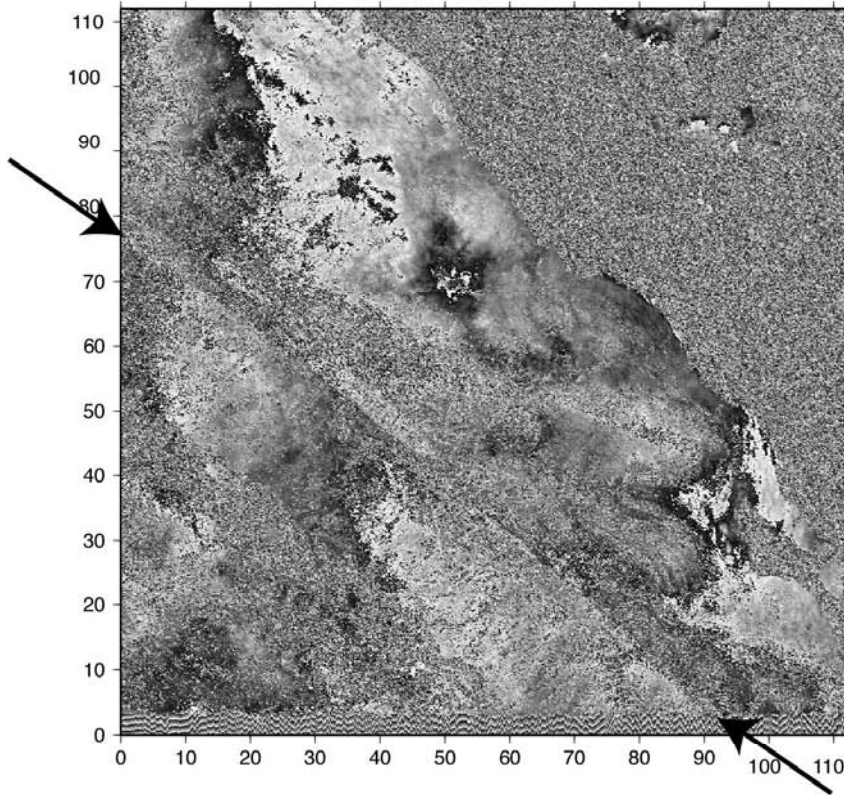
#### 4.4 SOUTHERN CALIFORNIA FAULTS

In southern California, interferometry of the Superstition Hills Fault [Vincent, 2000; Peltzer, personal communication] has revealed episodic surface creep between 1992 and 1997 (Figure 4.7). Although phase decorrelation in the Imperial Valley prevents coherent imaging over the entire fault, a series of interferograms from 1992-1997 [Vincent, 2000] suggests that the Superstition Hills fault underwent 2 cm/yr of creep from 1993-1995, but was not creeping for the rest of the five year period. Vincent [2000] also found signs of creep along the southern San Andreas near the Salton Sea, an area we studied in greater detail in Chapter 3.

Our study of the southern San Andreas used 60 interferograms to determine the spatial variability of creep along the fault. While the quantitative modeling of the fault parameters was not well-constrained (discussed in Chapter 3), our InSAR results showed definitive creep triggered by both the Landers and Hector Mine

Figure 4.5. Interferograms of the San Andreas Fault near Parkfield, California spanning (a) 1995 to 1997 and (b) 1997 to 1999. Arrows indicate location of the fault. Creep is visible in both interferograms, but there is a large amount of noise due to agriculture (upper right corner) and atmospheric effects.

e1\_22560\_e2\_12907



e2\_11905\_e2\_22426

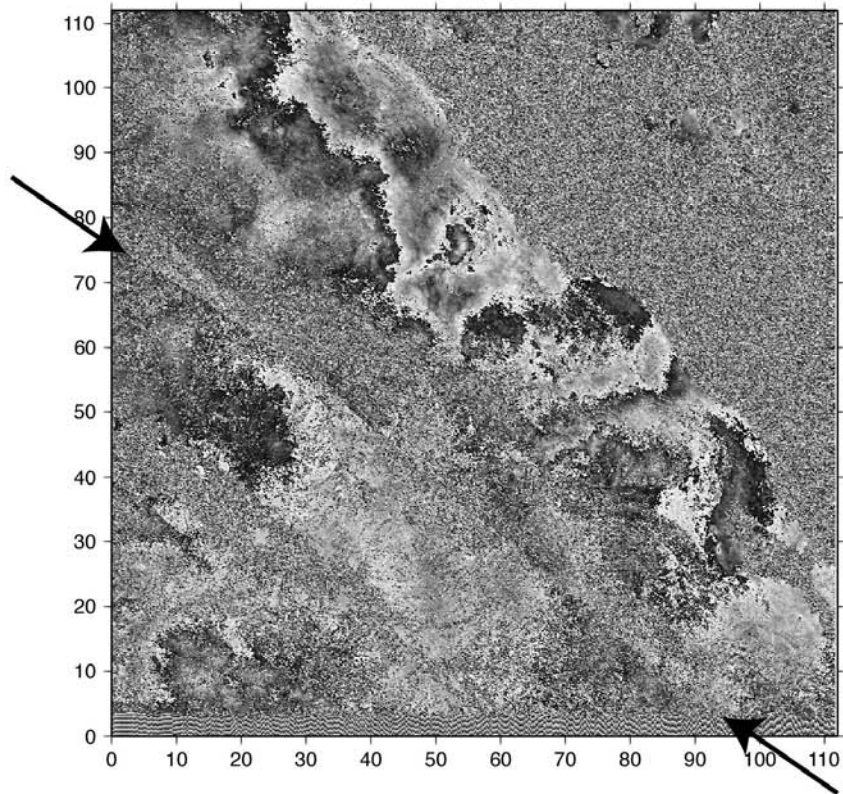
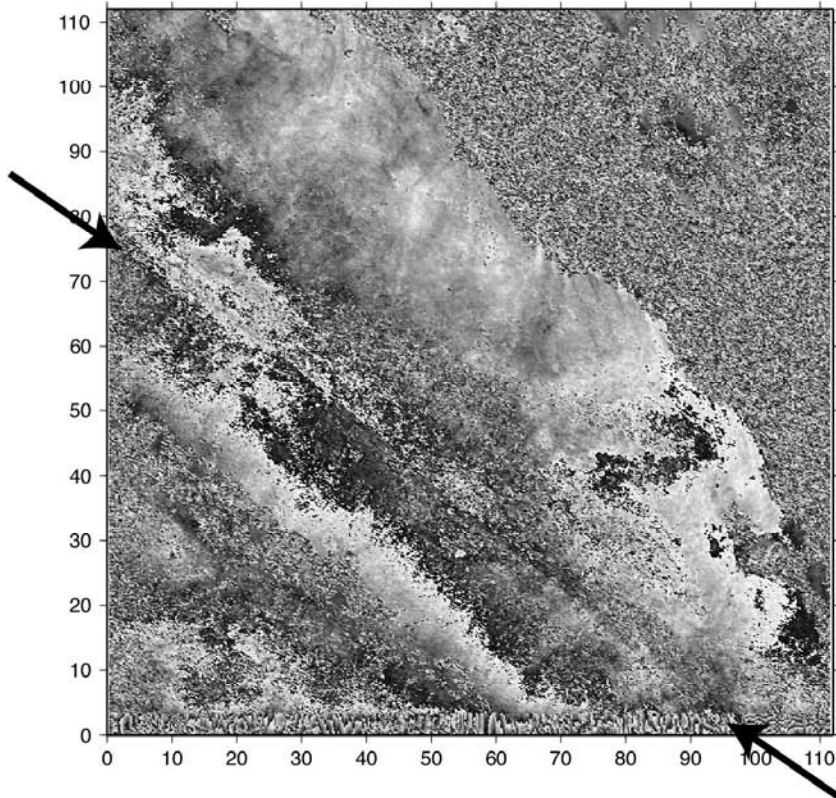
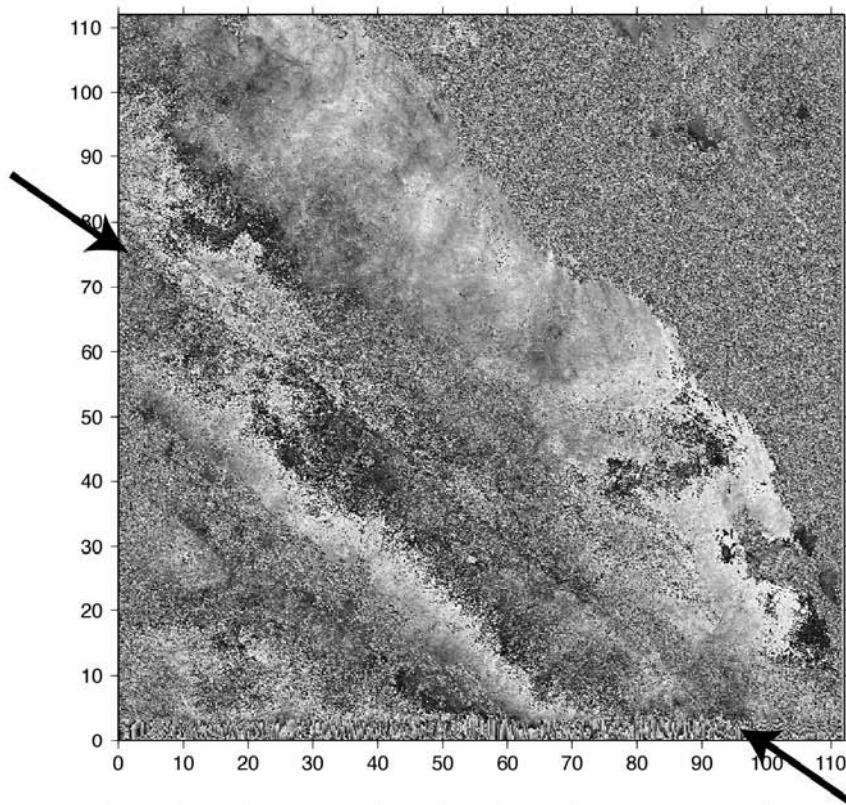


Figure 4.6 Interferogram of the San Andreas Fault near Parkfield, California between 1999 and 2000. (a) Processed using permanent scatterer technique introduced in Chapter 3. (b) Same as (a) except filtered with a filter oriented along the fault such that  $\lambda_{0,5}=570$  m parallel to the fault and  $\lambda_{0,5}=168$  m perpendicular to the fault trace.

e2\_22927\_e2\_27436



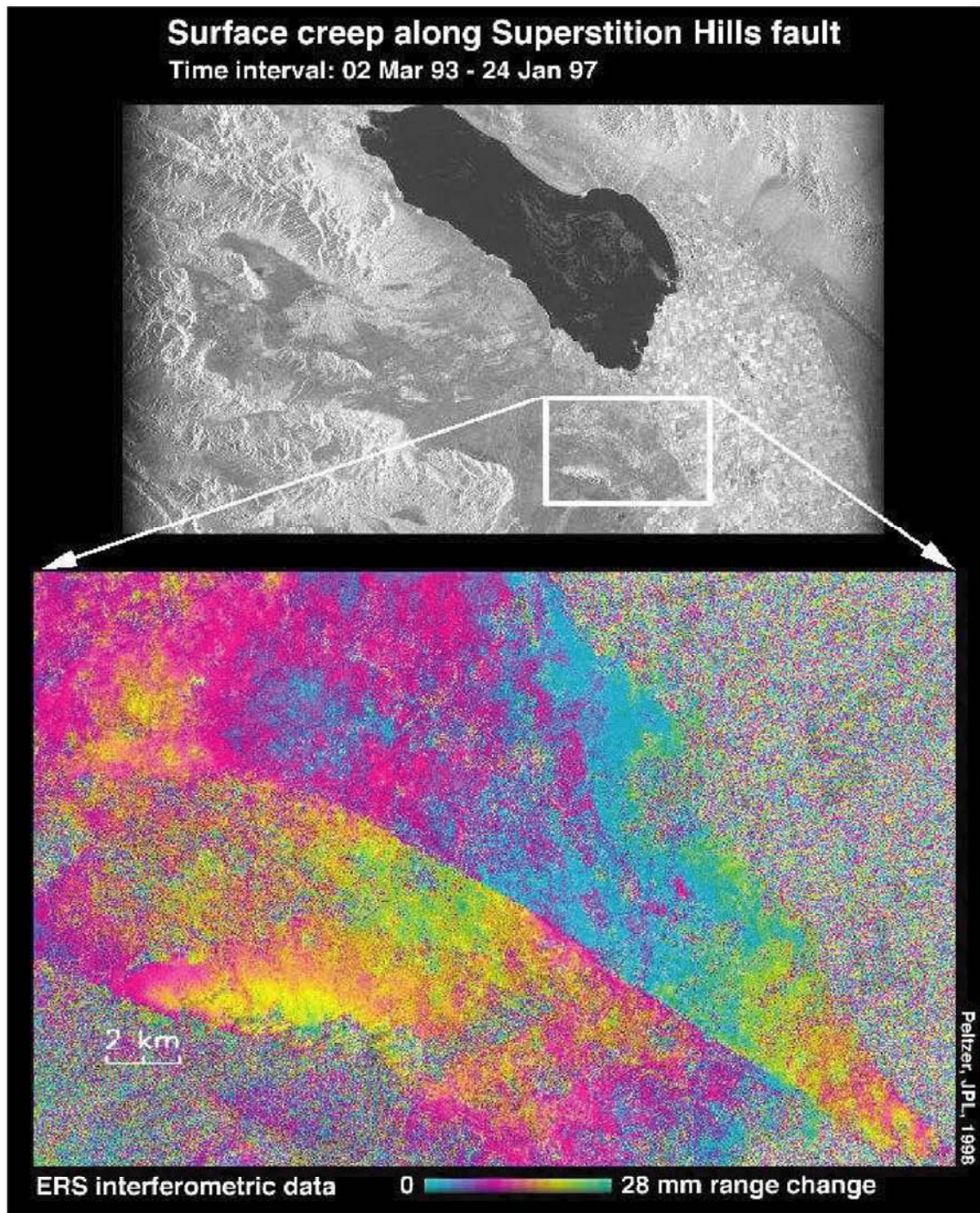


Figure 4.7. Interferogram of the Superstition Hills Fault spanning four years (March 1993-January 1997). The jump in color across the fault indicates aseismic creep in this time period. Image courtesy of Gilles Peltzer, Jet Propulsion Laboratory.

earthquakes, as well as spatially variable interseismic creep of up to 7 mm/yr LOS along the fault.

Finally, on the southernmost California fault, we utilized the dense survey-mode GPS network in the Imperial Valley to detect an average of 9 mm/yr of creep on the Imperial Fault. Although our fault models gave a wide range of parameters that fit the data (discussed in Chapter 2), there was a tradeoff between the locking depth and the creeping depth and our best fit model for the Imperial Fault had a locking depth of 10 km with creep from the surface to 3 km.

#### 4.5 CONCLUSIONS

Various geodetic means have been used to study creep along the faults in California. This dissertation has focused on two: dense GPS networks and Interferometric Synthetic Aperture Radar (InSAR). Both methods have revealed small aseismic surface slip on the order of a centimeter per year on the southern San Andreas and Imperial faults. The characteristics of the survey region (agricultural areas, topography, etc.) and the availability of the InSAR data or GPS sites will determine which method is best for that particular region.

For areas of partial decorrelation in the interferograms (cropland, populated areas, etc.), the use of permanent scatterers slightly improved the coherence, which increased the area of unwrapped phase in our final stacks. We expect the most improvement from this permanent scatterer weighting and filtering method will come from areas where the correlation is marginal ( $\sim 0.2$ ), such as near Parkfield in central California. In highly decorrelated areas, it may be preferable to use only

the permanent scatterer points and discard the other data (similar to *Ferretti et al.* [2001]). Further experimentation is needed in areas of varying correlation to determine the optimum masking, weighting, and filtering technique that will maximize the correlation of the data while still maintaining a useful spatial resolution along the fault. However, this method appears to be a viable and useful one for improving the detection and characterization of small-scale creep along California faults.

#### 4.6 REFERENCES

- Bilham, R., Creepmeters on the Hayward Fault, *USGS Annual Summary, vol. 40*, 1434-HQ-98-GR-00051, 1998.
- Bodin, P., R. Bilham, J. Behr, J. Gomberg, and K.W. Hudnut, Slip triggered on southern California faults by the 1992 Joshua Tree, Landers and Big Bear earthquakes, *Bull. Seism. Soc. Am.*, *84*, 806-816, 1994.
- Burford, R.O., S.S. Allen, R.J. Lamson, and D.D. Goodreau, Accelerated fault creep along the central San Andreas fault after moderate earthquakes during 1971-1973, Proceedings of the Conference on Tectonic Problems of the San Andreas Fault System, *Stanford Univ. Publ. Geol. Sci.*, *13*, 268-274, 1973.
- Burford, R.O., and P.W. Harsh, Slip on the San Andreas fault in central California from alignment array surveys, *Bull. Seism. Soc. Am.*, *70*, 1233-1261, 1980.
- Bürgmann, R., D. Schmidt, R.M. Nadeau, M. d'Alessio, E. Fielding, D. Manaker, T.V. McEvilly, and M.H. Murray, Earthquake potential along the northern Hayward fault, California, *Science*, *289*, 1178-1182, 2000.
- Ferretti, A., C. Prati, and F. Rocca, Permanent scatterers in SAR interferometry, *IEEE Trans. Geos. Remote Sens.*, *39*, 2001.
- Galehouse, J.S., Theodolite measurements of creep rates on San Francisco Bay region faults, *USGS Annual Summary, vol. 42*, 99-HQ-GR-0084, 2000.
- Langbein, J., A. McGarr, M.J.S. Johnston, and P. W. Harsh, Geodetic measurements of postseismic crustal deformation following the 1979 Imperial Valley earthquake, California, *Bull. Seism. Soc. Am.*, *73*, 1203-1224, 1983.

- Lisowski, M. and W.H. Prescott, Short-range distance measurements along the San Andreas fault system in central California, 1975 to 1979, *Bull. Seismol. Soc. Am.*, 71, 1607-1624, 1981.
- Mason, R. G., Geomensor surveys in the Imperial Valley, California, report, Geol. Dept., Imperial College, London, 1987.
- Nason, R. D., Fault creep and earthquakes on the San Andreas Fault, in *Proceedings, Conference of Tectonic Problems of the San Andreas Fault System*, R. L. Kovach and A. Nur, eds., Stanford Univ. Publ. in Geol. Sci. 13, pp. 275-285, 1973.
- Prescott, W. H. and M. Lisowski, Strain accumulation along the San Andreas Fault system east of San Francisco Bay, California, *Tectonophysics*, 97, 41-56, 1983.
- Rosen, P., C. Werner, E. Fielding, S. Hensley, S. Buckley, and P. Vincent, Aseismic creep along the San Andreas fault northwest of Parkfield, California, measured by radar interferometry, *Geophys. Res. Lett.*, 25, 825-828, 1998.
- Savage, J.C., and M. Lisowski, Inferred depth of creep on the Hayward Fault, central California, *J. Geophys. Res.*, 98, 787-793, 1993.
- Schulz, S.S., G.M. Mavko, R.O. Burford, and W.D. Stuart, Long-term fault creep observations in central California, *J. Geophys. Res.*, 87, 6977-6982, 1982.
- Vincent, P., Aseismic slip along the southern San Andreas Fault System captured by radar interferometry, *Proceedings of the 3<sup>rd</sup> Conference on Tectonic Problems of the San Andreas Fault System*, Stanford, Calif., September 6-8, 2000.
- Werner, C.L., P. Rosen, S. Hensley, E. Fielding, and S. Buckley, Detection of aseismic creep along the San Andreas Fault near Parkfield, California with ERS-1 radar interferometry, in *Space at the service of our environment*, ESA Special Publication 414, 521-524, Paris:ESA, 1997.

## Chapter 5

This chapter is based on research from my first two years of graduate studies at Scripps. Early in my studies, I used gravity measurements based on satellite altimetry and shipboard bathymetric data to determine the effective elastic thickness of the lithosphere below the Louisville Ridge. This paper, previously published in the *Journal of Geophysical Research*, describes that project.

### 3-D estimation of elastic thickness under the Louisville Ridge

*I am among those who think that science has great beauty. A scientist in his laboratory is not only a technician: he is also a child placed before natural phenomena which impress him like a fairy tale.*

-Marie Curie

Suzanne N. Lyons, David T. Sandwell, and Walter H.F. Smith

Reprint from *Journal of Geophysical Research*, 2000.

#### 5.1 ABSTRACT

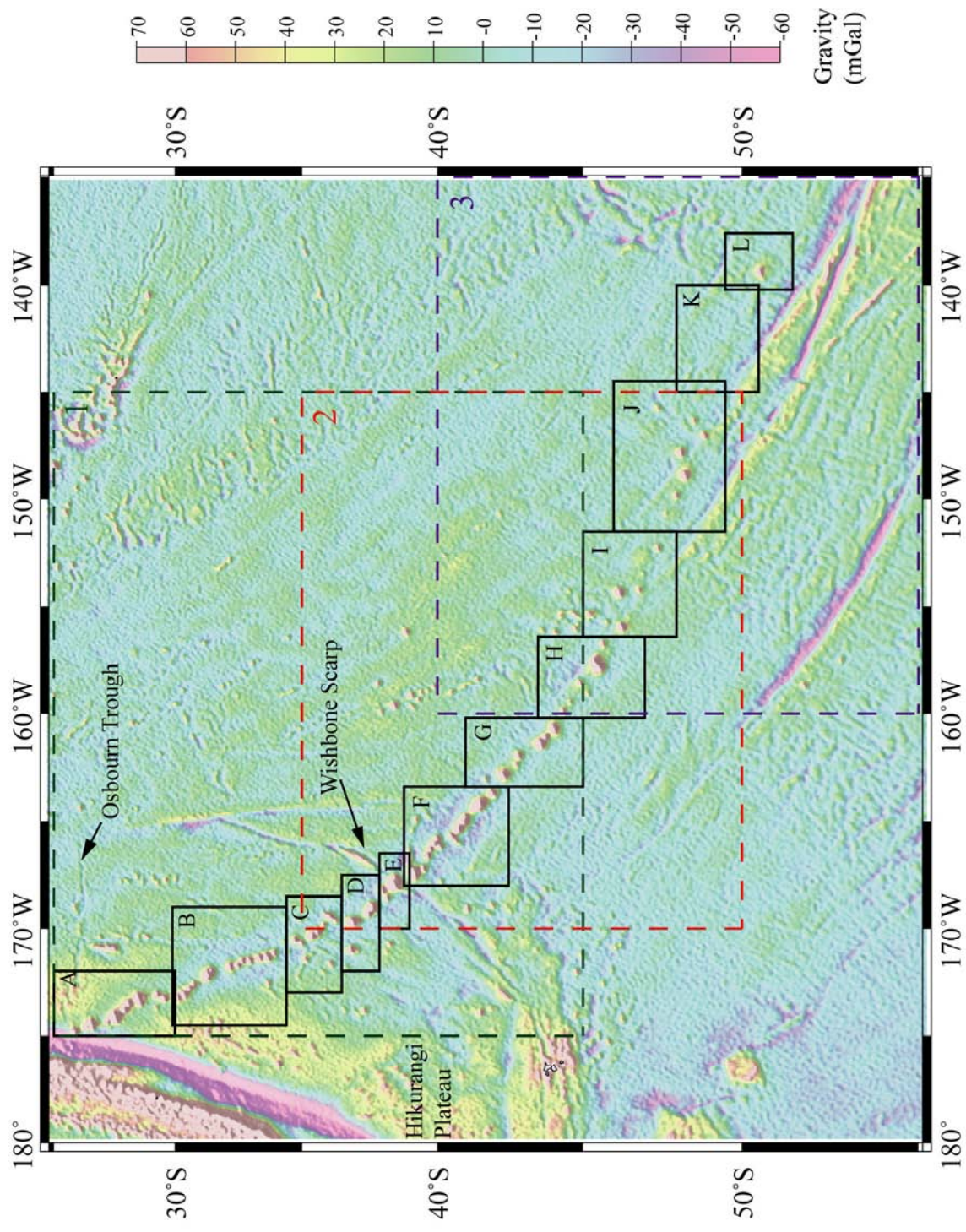
A three-dimensional approach to estimating elastic thickness is presented which uses dense satellite altimetry and sparse ship bathymetry. This technique is applied to the Louisville Ridge system to study the tectonic history of the region. The inversion is performed as both a first-order approximation as well as a

nonlinear relationship between gravity and topography based on *Parker's* equation [1973]. While the higher-order effect on the gravity anomaly is nearly zero for most of the region, the magnitude is significant over the summits of the ridge. Nevertheless, the inclusion of the nonlinear terms has only a minor influence on the elastic thickness estimate within each region, lowering the value by ~1-2 km compared with the linear result. The incorrect assumption of two-dimensionality for circular features exhibits a marked effect on the gravitational anomaly, resulting in false sidelobe structure of nearly 20 mGal for large seamounts. Our elastic thickness estimates are compared with the contradictory values obtained in previous studies by *Cazenave and Dominh* [1984] and *Watts et al.* [1988]. We find an increasing elastic thickness along the chain from southeast to northwest, with a discontinuity along the Wishbone scarp. The jump in elastic thickness values northwest of the scarp appears to be an indication of an age discontinuity caused by an extinct spreading center north of the ridge.

## 5.2 INTRODUCTION

The Hawaiian-Emperor seamount chain serves as the archetype for hotspot volcanism. The Hawaiian chain and its surrounding areas have been the focus of numerous plate flexure studies [e.g., *Vening Meinesz*, 1941; *Moore*, 1970; *Walcott*, 1970; *Watts and Cochran*, 1974; *Suyenaga*, 1979; *Watts*, 1979; *Watts and tenBrink*, 1989; *Wessel*, 1993]. Surprisingly, the Louisville chain (Figure 5.1), second in size to the Hawaiian group, has not attracted nearly as much attention, probably because of its remote location. The only major bathymetric survey of the

Figure 5.1. Gravity anomaly over the Louisville Ridge system, southwest Pacific. Gravity data is taken from *Sandwell and Smith* [1997]. Colored boxes (1-3) represent regions over which gravity was inverted to produce bathymetric predictions. Each box is approximately 1000x1000 km<sup>2</sup> in order to include the very long wavelengths in the inversion. Smaller black boxes (A-L) represent subregions within which predicted bathymetry was compared to available ship data. RMS values were calculated within each subregion and determined the best-fitting parameters for that subregion.



Louisville Ridge system was in 1984 [Lonsdale, 1986; 1988] and there have been just two attempts at calculating the elastic thickness beneath the different sections of the chain [Cazenave and Dominh, 1984; Watts *et al.*, 1988].

*Cazenave and Dominh* [1984] performed a three-dimensional forward model for geoid height using analog bathymetric maps [Mammericx *et al.*, 1974] and constrained the models with widely-spaced Seasat geoid height profiles. However, their study was limited by the relatively low resolution of both the bathymetric maps and the geoid height data. *Watts et al.* [1988] used high-resolution ship bathymetry and gravity anomaly data for their forward model, but they were restricted to modeling along two-dimensional profiles. The two studies yield contradictory values for the elastic thickness under Louisville: *Cazenave and Dominh* estimate the elastic thickness ( $T_e$ ) increasing from southeast (12-19 km) to northwest (15-23 km) while *Watts et al.* estimate  $T_e$  increasing from northwest (12.5-17.5 km) to southeast (32.5-42.5 km). Until now there has been no attempt to reconcile these results.

Higher resolution data from the recent Geosat mission [McConathy and Kilgus, 1987] provides precise gravity (3-7 mGal accuracy) over the world's oceans [Sandwell & Smith, 1997]. This has been used along with available bathymetric profiles to develop a complete model of inferred bathymetry [Smith & Sandwell, 1997]. We introduce a method for determining the elastic thickness which utilizes the complete spatial coverage of the satellite gravity data and sparse ship depth soundings to perform a three-dimensional estimation of elastic

thickness. We assess the importance of nonlinear topography to gravity relationships and we test this method on the Louisville Ridge.

### 5.3 FLEXURE THEORY

In 1970, *Dorman and Lewis* investigated the isostatic compensation of continental landmasses by relating the Bouguer anomaly to elevation in the Fourier transform domain. *Parker* [1973] showed that the gravitational anomaly due to an uneven, non-uniform layer could be written as the sum of an infinite series of Fourier transforms:

$$G(\mathbf{k}) = 2\pi (\rho_1 - \rho_2) e^{-2\pi|\mathbf{k}|s} \sum_{n=1} \frac{|2\pi\mathbf{k}|^{n-1}}{n!} F\{t^n(\mathbf{r})\} \quad (1)$$

where  $s$  is the average depth of the area,  $g$  is the gravitational constant,  $\mathbf{k}$  is the wavenumber vector ( $1/x$ ,  $1/y$ ), and  $F\{t^n(\mathbf{r})\}$  is the two-dimensional Fourier transform of the  $n$ th power of topography of the layer. We use these two approaches, along with the thin-elastic plate flexure model (Figure 5.2a) [e.g. *McKenzie & Bowin*, 1976; *Banks et al.*, 1977; *McNutt*, 1979], to write the gravitational anomaly as the sum of a linear term (a) and two nonlinear terms, (b) and (c):

$$G(\mathbf{k}) = 2\pi (\rho_c - \rho_w) e^{-2\pi|\mathbf{k}|s} B(\mathbf{k}) \left[ 1 - e^{-2\pi|\mathbf{k}|d} R(|\mathbf{k}|) \right] + \quad (a)$$

$$2\pi (\rho_c - \rho_w) e^{-2\pi|\mathbf{k}|s} \sum_{n=2} \frac{|2\pi\mathbf{k}|^{n-1}}{n!} F\{b^n(\mathbf{r})\} + \quad (b) \quad (2)$$

$$2\pi (\rho_m - \rho_c) e^{-2\pi|\mathbf{k}|(s+d)} \sum_{n=2} \frac{|2\pi\mathbf{k}|^{n-1}}{n!} F\{m^n(\mathbf{r})\} \quad (c)$$

where term (a) is due to both the bathymetry of the ocean floor,  $b(\mathbf{r})$ , and the Moho topography,  $m(\mathbf{r})$ , term (b) is due solely to the bathymetry, and term (c) is due entirely to the Moho. Using the thin-elastic plate flexure model, the Moho topography is given by:

$$m(\mathbf{r}) = F^{-1} - \frac{\rho_c - \rho_w}{\rho_m - \rho_c} R(|\mathbf{k}|) B(\mathbf{k}) \quad , \quad (3)$$

with  $R(|\mathbf{k}|)$ , also known as the flexural response function, given by:

$$R(|\mathbf{k}|) = 1 + \frac{D|2\pi\mathbf{k}|^4}{g(\rho_m - \rho_c)}^{-1} \quad . \quad (4)$$

The flexural rigidity of the plate,  $D$ , is defined as  $D = \frac{ETe^3}{12(1-\nu^2)}$ ,  $d$  is the average crustal thickness (6 km),  $E$  is Young's modulus ( $1 \times 10^{11}$  N m<sup>-2</sup>),  $\nu$  is Poisson's ratio (0.25),  $Te$  is called the elastic thickness of the plate, and  $\rho_m$ ,  $\rho_c$ , and  $\rho_w$  are the densities of the mantle (3400 kg m<sup>-3</sup>), bathymetry (2600-3000 kg m<sup>-3</sup>), and seawater (1025 kg m<sup>-3</sup>) respectively.

Our approach for estimating elastic thickness, which uses dense gravity measurements and sparse bathymetric soundings, relies on a linear relationship between gravity and bathymetry so we first assess the nonlinear terms in equation 2. Under the loading conditions of the Louisville ridge we expect that the nonlinear terms due to topography are large and must be accounted for, while the nonlinear terms due to Moho topography are small and can be neglected. To investigate the nonlinear Moho terms (Equation 2c) for this region, we consider a worst-case scenario of a large seamount (Gaussian height=3.6 km,  $\sigma=20$  km,  $\rho_c=2800$  kg m<sup>-3</sup>) loading a weak elastic plate ( $Te$  of only 6 km); this will result in

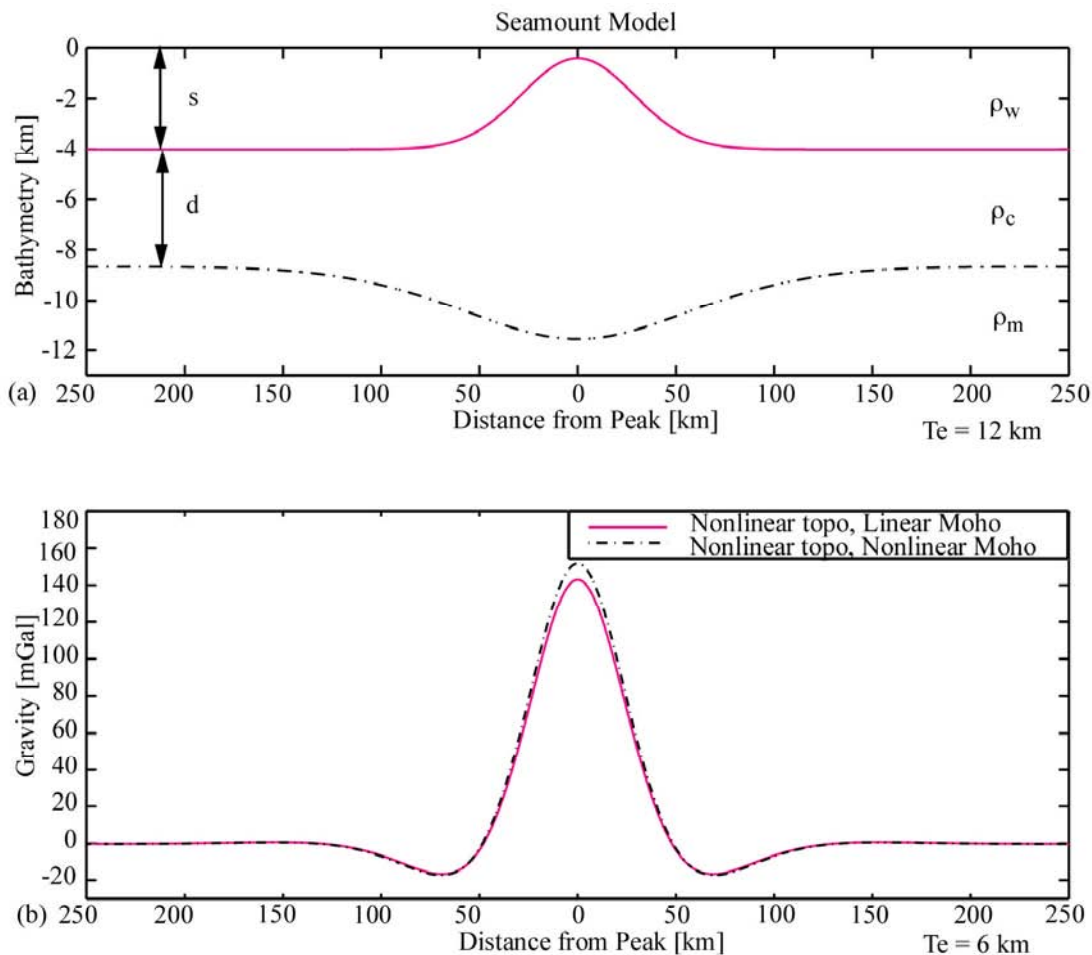


Figure 5.2. (a) Model of a topographic load on an elastic plate overlying a fluid asthenosphere. The load is a Gaussian seamount of height=3.6 km,  $s=20$  km,  $\rho_c=2800$  kg m<sup>-3</sup>,  $\rho_m=3400$  kg m<sup>-3</sup>, and  $Te=12$  km. (b) The nonlinear effects of the Moho for this seamount model, with  $Te=6$  km. The solid line represents the gravity anomaly determined by Equation 2, including term (a), the linear effect of bathymetry and Moho topography, and the first seven terms of (b), the nonlinear effect of bathymetry. The dashed line also includes the first seven terms of (c), the nonlinear effect of the Moho topography. The maximum difference between these two signals is 10 mGal (<7%).

maximum Moho topography and thus maximum nonlinear contribution. This  $Te$  is close to the smallest distinguishable value of 5 km for our method. The maximum difference between the gravity calculated with just the first-order Moho (solid line in Figure 5.2b) and the gravity that includes the nonlinear terms (2-7) (dashed line) is ~10 mGal (7%). This difference drops quickly as  $Te$  increases, though, and for a more reasonable plate thickness of 12 km, the nonlinear effect is only ~2 mGal (<2%). Thus, we are able to justifiably disregard the higher-order effects of the Moho topography. With the nonlinear terms accounted for, Equation 2 becomes:

$$G(\mathbf{k}) = Z(\mathbf{k})B(\mathbf{k}) + N(\mathbf{k}, t) \quad (5)$$

where  $N(\mathbf{k}, t)$  contains the nonlinear contributions from the bathymetry and  $Z(\mathbf{k})$  is called the "admittance function" and represents the gravity anomaly in the wavenumber domain resulting from the compensation of a point load.

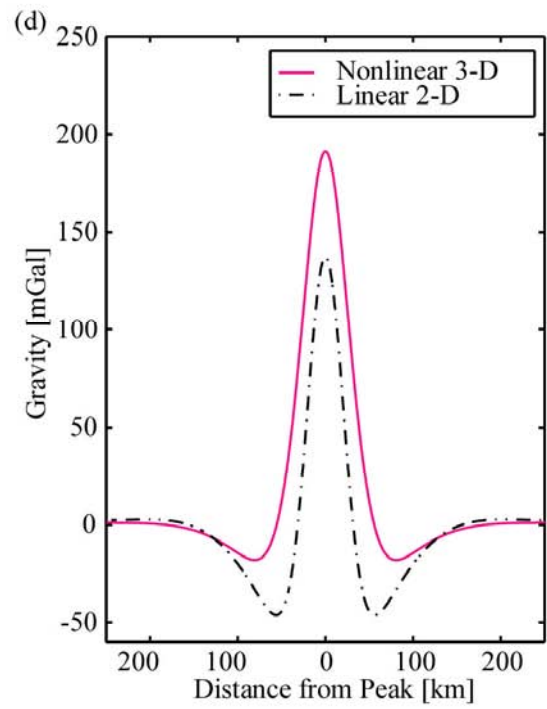
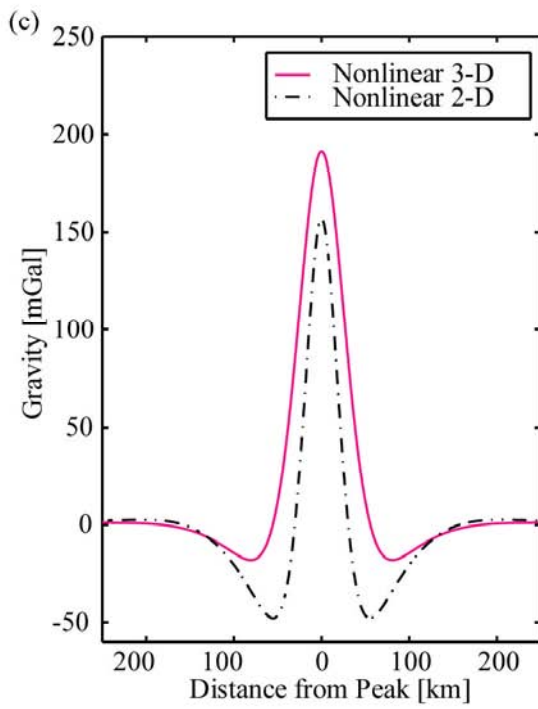
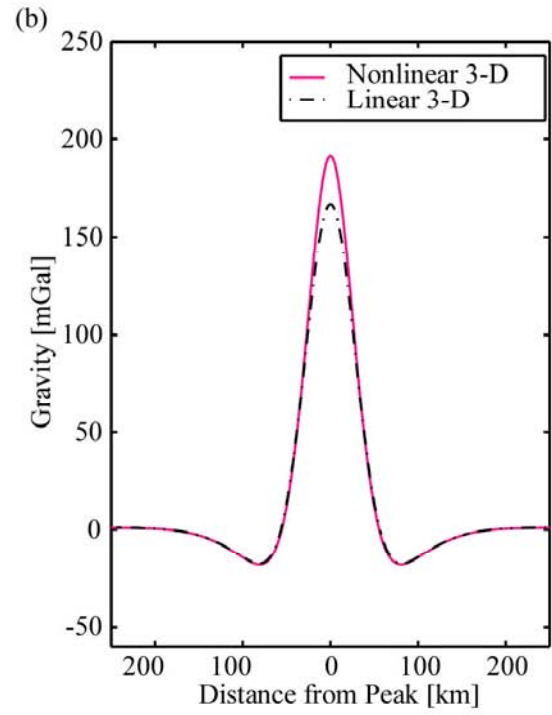
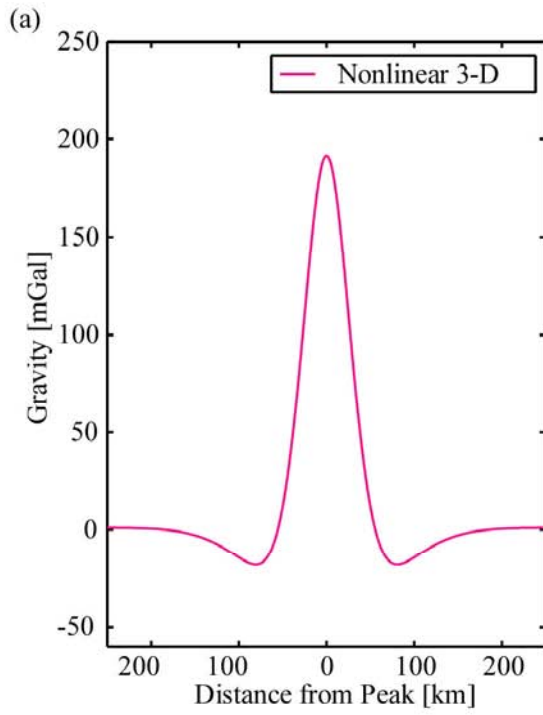
Due to the ease of inverting a linear system, most of the previous elastic thickness studies have ignored the nonlinear contributions [Watts, 1978; Dixon *et al.*, 1983; Cazenave and Dominh, 1984; Watts *et al.*, 1988, and numerous others]. This is, in general, a good approximation, as the linear contribution is usually 85-90% of the total gravity anomaly [McNutt, 1979; Goodwillie, 1995]. However, the omission of nonlinear terms in bathymetric/gravitational modeling could be detrimental in areas where the higher-order terms grow large, such as: regions where the relief of the topography approaches the mean depth [Parker, 1973], areas of short-wavelength, uncompensated topography, or wherever the lithospheric deflection is comparable to the elastic thickness [Ribe, 1982]. As this encompasses numerous regions of the world's oceans, some analyses of the

gravity/topography relationship over volcanic features have included these terms [*Baudry and Calmant, 1991; Goodwillie, 1995; Sichoix and Bonneville, 1996*].

Figures 5.3a and 5.3b demonstrate the importance of the higher-order bathymetric terms when modeling gravitational anomalies due to a topographic load. To investigate an extreme case (large, short-wavelength feature on a thin plate), we again consider the Gaussian model in Figure 5.2, but with an elastic thickness of 12 km. The results are shown in 3a and 3b. The solid profile in both plots includes the nonlinear terms (up to  $N=7$ ), while the dashed profile in 3b is the linear approximation. Note that the inclusion of higher-order terms has very little effect on the flanks of the anomaly, but exerts a strong ( $\sim 13\%$ ) influence on the peak amplitude, suggesting that the inclusion of the nonlinear relationship is important when attempting to fit anomaly peaks, especially in regions where the topography nears the ocean surface, but that the linear approximation should be satisfactory for fitting on the sides.

Figures 5.3c and 5.3d show the effect of correct dimensionality on gravity anomaly models. For the past two decades, flexure modelers have had sufficient spatial coverage in continental data to model the gravity/topography relationship in three dimensions, thus being able to properly account for the dimensionality of the modeled features [e.g. *Lewis and Dorman, 1970; Banks et al., 1977; McNutt and Parker, 1978*]. Marine geophysical studies, however, have, until recently, been limited by the availability of ship data along profiles. This has forced most researchers to perform their modeling techniques either by using bathymetric maps in areas of dense ship tracks [*McNutt, 1979; Sichoix and Bonneville, 1996; Hébert*

Figure 5.3. Model illustrating nonlinear and dimensionality effects. Each model represents the gravity anomaly due to a topographic load placed on a flat surface (no flexure). Plots (a) and (b) were modeled by a Gaussian with the same parameters as Figure 5.2a. Plots (c) & (d) were modeled by a ridge with the same parameters as in (a) & (b). In each plot, the solid line represents the true gravity anomaly over the model Gaussian seamount and is shown for comparison. (b) demonstrates the effect of ignoring the nonlinear terms of *Parker's* [1973] equation for a three-dimensional feature. The linear estimate (dashed) has similar flanks to the nonlinear (solid), but shows a much smaller peak amplitude. (c) shows the effects of improper dimensionality assumptions on the gravitational anomaly in the nonlinear case. The flank structure is noticeably changed, reducing each side by 20 mGals and causing a shift in the peak amplitude of ~30 mGals. The most common inversion techniques assume both linearity and two-dimensionality, yielding a model (d) that has insufficient peak amplitude and a false negative sidelobe, leading to an overestimate in  $T_e$ .



*et al.*, 1999 and others] or by looking at only two dimensions: distance along track and depth [Watts, 1978; Ribe & Watts, 1982; Dixon *et al.*, 1983, and others]. For Parker's equation to hold in two dimensions, two assumptions must be made: the length of the feature is much greater than the width (such as a ridge) and the ship track/profile crosses approximately perpendicular to the feature. In general, the length of the feature should be >250-300 km before the bathymetry can be safely assumed as 2-D [Ribe, 1982]. These assumptions severely limit the number of ship tracks that can be used with any degree of confidence within a given area.

In Figure 5.3c, the solid line again represents the nonlinear seamount model, but is compared with the gravity over a ridge with the same parameters as the seamount (dashed line). Both models contain the nonlinear effects so the differences between the profiles should be due solely to dimensionality. Here both the peak amplitude and the flank shape for the ridge are different from that of the seamount. The assumption of a 2-D structure for a seamount causes a false negative sidelobe in the gravity anomaly, shifting the peak of the anomaly by a significant amount and creating a gravitational low at the base of the signal.

Figure 5.3d shows the combined effects of these two most common assumptions in flexural modeling. The solid line once again represents the true gravity signature over a model seamount, while the dashed line represents an approximation of a linear relationship between topography and gravity over a feature modeled as a two-dimensional structure. By using somewhat extreme parameters (large feature on a plate with low  $T_e$ ), we see that the resultant misfit is almost 20 mGals along the flanks and up to 50 mGals at the peak. Trying to fit

this model by altering the elastic thickness parameter would yield a  $T_e$  higher than the true one if this feature were actually a seamount rather than a ridge. Therefore, much caution should be taken in areas with high-amplitude, circular features and, if possible, both the nonlinear effects as well as the correct dimensionality should be included in any gravitational model.

#### 5.4 METHOD

For the past few decades, limited data meant that marine geophysicists could only perform flexure studies using gravity and bathymetry along sparse ship tracks. However, with the advent of satellite altimetry to determine the earth's geoid, it has been possible to investigate the gravity/bathymetry relationship in three dimensions [Dixon *et al.*, 1983; Kogan *et al.*, 1985; Cazenave and Dominh, 1984; Calmant *et al.*, 1990]. With the recent declassification of the dense Geosat altimetry data, the quality and resolution of the geoid has increased substantially, making it possible to model in three dimensions with much more reliability (see Figure 5.4). In our study, we used the *Sandwell and Smith 2-minute gravity grid*, version 9.2 [1997] to invert for bathymetry on a grid, the *Smith and Sandwell predicted bathymetry*, version 6.2 [1997] to give us an estimation of the nonlinear anomaly contribution, and the available ship bathymetry data along profiles to compare with our predictions.

In order to invert the satellite-derived gravity grid to predict bathymetry, we first divided the Louisville system into three approximately square regions with sides of length  $>1000$  km (see Figure 5.1, dashed boxes 1-3) so we could include

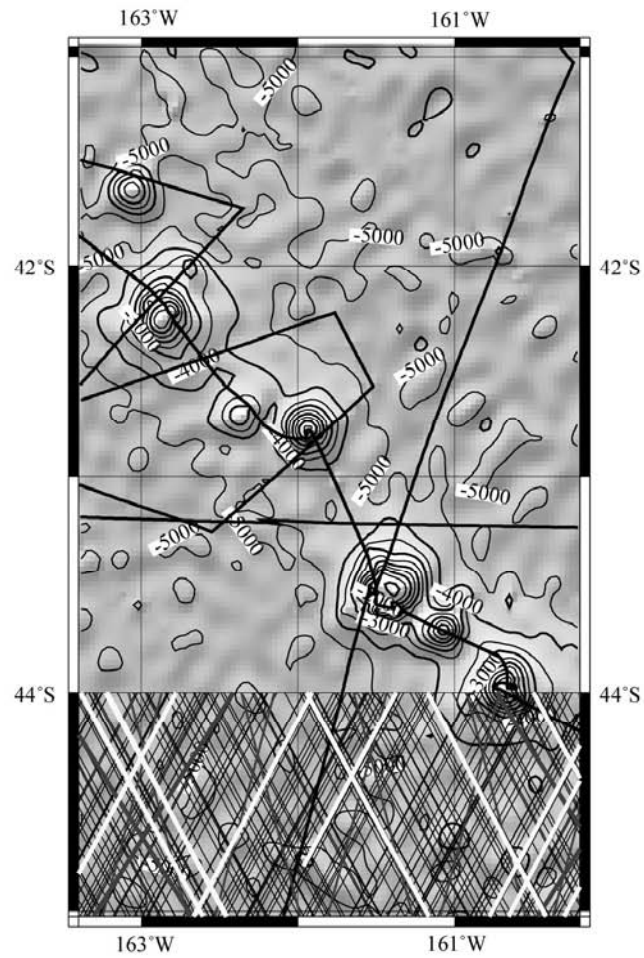


Figure 5.4. Spatial coverage of satellite data vs. ship tracks for region G. Thick black lines represent ship profiles available for the area. Light gray lines are Seasat tracks (used in *Cazenave and Dominh*, 1984). Thin black lines indicate Geosat, Topex, and ERS-1 altimeter tracks used in the *Sandwell and Smith* 2-minute gravity grid, version 9.2 [1997].

wavelengths longer than the maximum expected flexural wavelength in our inversion. For each of these large regions, we performed the same procedure, iterating over a range of both crustal densities ( $\rho_c=2600-3000 \text{ kg m}^{-3}$ ) and elastic thicknesses ( $Te=0-50 \text{ km}$ ). For simplicity, the calculations were performed in the wavenumber domain rather than the spatial domain.

*Oldenburg [1974]* performed a nonlinear inversion for topography using an iterative method along two-dimensional gravity profiles. We used a different approach: removing an estimate of the higher-order gravitational terms ( $N(|\mathbf{k}|,t)$  in Equation 5) to yield a solvable linear approximation. This was achieved by estimating the gravitational contribution of terms 2-7 from the predicted bathymetry of *Smith and Sandwell [1997]*. The *Smith and Sandwell* grid was derived by limiting the waveband to avoid wavelengths where  $Te$  is important and then adjusting the predictions to coincide with the ship bathymetry along surveyed points (for a discussion of this, see *Smith and Sandwell, 1994*). While not exact because of errors in the predicted depths, this should provide a reasonable estimate of the nonlinear contribution as the crests of most seamounts along the chain were surveyed by *Lonsdale [1988]* and included in the *Smith and Sandwell [1997]* bathymetry grid.

This estimate of  $N(|\mathbf{k}|,t)$  was then subtracted from the satellite-derived gravity anomaly, yielding an approximate linear equation,  $G_{\text{first order}}(\mathbf{k})=Z(|\mathbf{k}|)B(\mathbf{k})$ . The admittance function,  $Z(|\mathbf{k}|)$ , was calculated for each value of  $\rho_c$  and  $Te$  and then bandlimited, since  $1/Z(|\mathbf{k}|)$  suffers from instabilities at both very short wavelengths - due to low signal-to-noise ratio - and very long wavelengths - due to

downward continuation [McNutt, 1979; Dixon *et al.*, 1983; Baudry and Calmant, 1991; Sichoix and Bonneville, 1996]. Following the example of Smith and Sandwell [1994], we constructed a spectral window,  $W(\mathbf{k})=W_1(\mathbf{k})*W_2(\mathbf{k})$ , where  $W_1(\mathbf{k})$  is a highpass (with wavenumber) cosine filter which ramps between a value of 1 for  $<571$  km and 0 for  $>800$  km and  $W_2(\mathbf{k})$  is a lowpass filter of the form:

$$W_2(\mathbf{k})=1/(1+A/\mathbf{k}^4 e^{-4\pi/\mathbf{k}/s}) \quad (6)$$

with  $A=5 \times 10^{15} \text{ m}^4$  so that the half-amplitude occurs at 13, 17, and 20 km for  $s=2, 4, \text{ and } 6$  km, respectively. This filter preserves data within the "coherent waveband" (25-250 km) [Ribe and Watts, 1982; Ribe, 1982] in which admittance estimates are of a high reliability (coherence  $> 0.75$ ). Although  $W_1(\mathbf{k})$  places a lower resolution limit of  $\sim 5$  km on elastic thickness estimates [Watts *et al.*, 1980; Smith and Sandwell, 1994], the expected value for  $Te$  within the Louisville system based on age of the crust at time of loading is 20-25 km, so this should not cause any deleterious effects in our inversion.

After solving for bathymetry for the entire  $1000 \times 1000 \text{ km}^2$  region, we inverse Fourier transformed our prediction,  $B_{\text{pred}}(\mathbf{k})$ , to determine misfits within the spatial domain. We compared  $B_{\text{pred}}(\mathbf{x}, \mathbf{y})$  within smaller subregions of the  $1000 \times 1000 \text{ km}^2$  area (see Figure 5.1, boxes A-L) to the measured bathymetry along available ship tracks within that subregion. By using this technique of subdividing, we were able to include the long wavelengths necessary in the inversion for bathymetry, but we constrained our solution with precise ship data within smaller regions of interest.

Within each subregion, A-L, we fit our predictions,  $B_{\text{pred}}(\mathbf{x}, \mathbf{y})$ , only at points where ship data were available. These predictions were compared with both the ship bathymetry data ( $B_{\text{unf}}(\mathbf{x}, \mathbf{y})$ , henceforth called "unfiltered"), which was high-pass filtered to remove the mean depth, and a bandpass-filtered version of the ship data ( $B_{\text{filt}}(\mathbf{x}, \mathbf{y}) = F^{-1}\{W_2(\mathbf{k}) * B_{\text{unf}}(\mathbf{k})\}$ , henceforth called "filtered") which included only the signal within the same waveband as our bandlimited admittance function. The rms values for both comparisons within each box were evaluated and plotted to determine the best fitting values for our parameters,  $\rho_c$  and  $Te$ .

## 5.5 RESULTS AND DISCUSSION

Figure 5.5 shows the magnitude of the gravity anomaly due to terms 2-7 of Parker's equation for subregion G, with a value for  $\rho_c$  of  $2800 \text{ kg m}^{-3}$ . Most of the region yields a nonlinear contribution very close to zero, with a sharp increase in magnitude over the seamounts, peaking to a value of  $>60 \text{ mGal}$  over the summits. This large nonlinear contribution by the short-wavelength features to the total gravity anomaly is not surprising given the results of the model in Figure 5.3b, and demonstrates the importance of these terms in areas with large amplitude features such as the Louisville chain.

To determine the effect of various parameters on elastic thickness estimates, we varied crustal density in our inversion between  $2600$  and  $3000 \text{ kg m}^{-3}$ . An example of rms misfit for varying  $\rho_c$  and  $Te$  within region G is shown in Figure 5.6. As can be seen in this plot, for areas with low elastic thickness, variation in  $\rho_c$  has little effect on misfit. However, for older, thicker plates, a

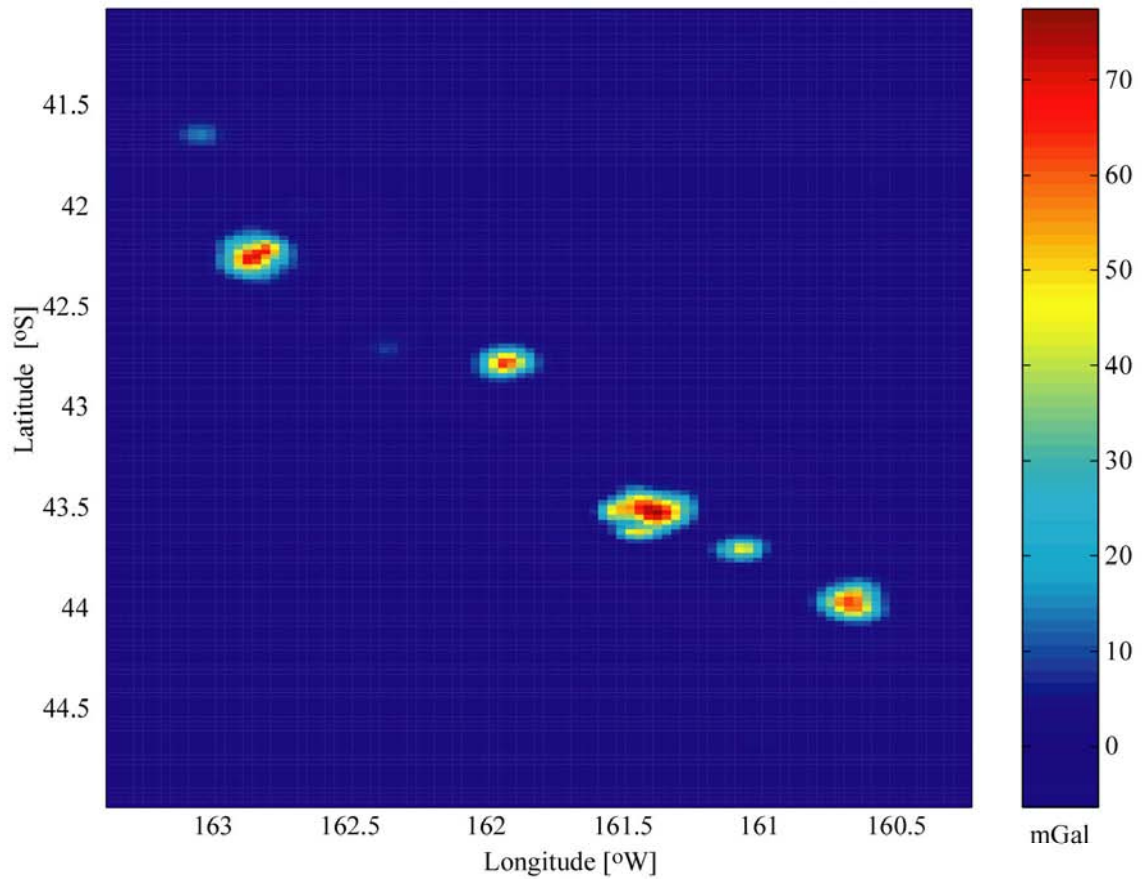


Figure 5.5. Nonlinear contribution of topography to the gravitational anomaly.  $G(k)$  for  $n=2-7$  from *Parker's* [1973] equation is shown for region G of the Louisville Ridge. Most of the region has a negligible nonlinear effect, but over the larger features, gravitational contribution from the higher-order terms grows quite large.

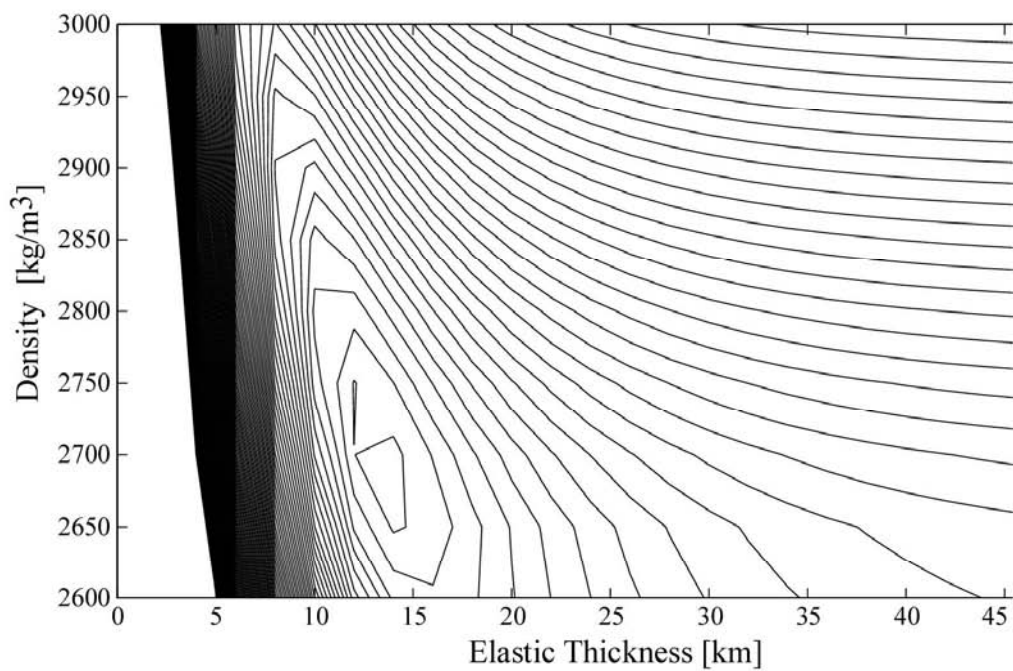


Figure 5.6. RMS misfit for region G plotted against crustal density,  $\rho_c$ , and elastic thickness,  $T_e$ , for the nonlinear case. Mantle density is  $3400 \text{ kg m}^{-3}$ ,  $E=1 \times 10^{11} \text{ N m}^{-2}$ , and  $d=6 \text{ km}$ . Minimum rms is 293 m and the contour interval is 5 m. For low elastic thicknesses, variation in  $\rho_c$  does not affect the misfit. However, for older, thicker plates, a decrease in crustal density translates to an increase in  $T_e$ .

reduction in crustal density forces an increase in the elastic thickness estimate. If it is assumed that the crustal density remains constant along the chain, then a density that is too high or too low will affect the magnitude of  $Te$ , but the trend of values along the chain will remain the same. Variation in the value for Young's modulus yields a similar result. We used  $E=1 \times 10^{11} \text{ N m}^{-2}$  for our calculations, but a smaller value, such as  $E=6.5 \times 10^{10} \text{ N m}^{-2}$  [Sandwell, 1984], increased the  $Te$  for each region by ~6%. Again, by assuming that  $E$  is constant along the chain, only the magnitude of  $Te$  is affected, and the tectonic implications of the estimates should remain the same.

Thus, it should be noted that the trend of elastic thickness estimates along a seamount chain is generally more informative than the magnitude, due to the effects of variation in initial parameters on  $Te$  estimates [e.g., *Calmant et al.*, 1990; *Burov and Diament*, 1995, *Sichoix and Bonneville*, 1996].

The best-fitting  $Te$  values within each region are provided in Table 5.1, compared with the previous results of *Watts et al.* [1988] and *Cazenave and Dominh* [1984]. Even though our best-fit values for crustal density varied somewhat for the regions, we evaluated misfit for  $\rho_c=2800 \text{ kg m}^{-3}$  for consistency of comparison with the previous studies.

In 1984, *Cazenave and Dominh* used analog bathymetric maps from *Mammericx et al.* [1974] to model geoid height in three dimensions, which they compared to geoid values derived from Seasat altimeter data. They also performed 2-D spectral analyses along profiles of ship data for comparison. It is interesting to note that their 3-D estimates yield a  $Te$  that is typically ~4 km higher than their

2-D values. In their discussion, *Cazenave and Dominh* attribute this to the dimensionality issue, positing that a two-dimensional assumption leads to an overestimate of lithospheric deflection (shown by *Watts et al.* [1975] and confirmed in Figure 5.3c) and a corresponding negative geoid anomaly. This, they claim, added to an overestimate of the positive geoid anomaly caused by topography (which we do not see in Figure 5.3c) yields an overestimate of the total anomaly and a smaller derived plate thickness as compared to the 3-D approach.

However, as can be determined from Figure 5.3, and is discussed in *Ribe* [1982] and *Watts et al.* [1988], a feature which is inherently two-dimensional prefers a *higher* elastic thickness than that of a more circular, three-dimensional feature. Therefore, the improper assumption of dimensionality for a seamount would actually result in an *overestimate* of elastic thickness. Thus, the contradictory nature of *Cazenave and Dominh's* results is probably due to the poor quality of the data sets and the insufficient coverage of the earlier altimeter data.

*Watts et al.* [1988] estimated elastic thicknesses for the Louisville chain using two-dimensional ship data, including that obtained during the 1984 survey by the *R/V Thomas Washington*. While the magnitude of their estimates in the northwestern region of the chain appears to agree somewhat with *Cazenave and Dominh's* [1984] results, *Watts et al.* find much higher best-fitting values in the southeast, and the general trend (increasing  $T_e$  from northwest to southeast) is the opposite, which they partially attribute to dimensionality differences.

Our results tend to agree with *Cazenave and Dominh* in trend and show increasing values from southeast to northwest. The rms misfit for the nonlinear

inversion (unfiltered comparison) for all regions is shown in Figure 5.7. The rms is normalized by the standard deviation of the region and represents the ratio of error in our estimate to the variation in topography. Circles represent the best-fit estimate of elastic thickness and are the point of maximum curvature of the misfit. This plot illustrates not only the bimodal nature of the elastic thicknesses under the two sections of the chain (A-D and F-L), but also shows the difficulty in assessing an upper bound on the  $T_e$  estimates. In most cases, the misfit does not significantly increase as  $T_e$  grows large, due to the negligible change in deflection (and, hence, gravitational anomaly) caused by an emplaced bathymetric load once the elastic thickness has passed a critical value.

Table 5.1 shows the estimates and bounds (where possible) for elastic thickness values for both the nonlinear and linear cases within each region. Bounds were determined by  $\pm 5\%$  of the normalized misfit for the best  $T_e$  value. This leads to a lower bound in all cases, but an upper bound in only a few regions. In general, the pattern of best  $T_e$  estimates for all four cases is the same: a relatively low value ( $\sim 11$  km) in the southeast, increasing slightly towards the northwest, with a sharp anomaly (7 km) in region E, followed by a higher value ( $\sim 24$  km) northwest of E which increases toward the northwest.

*Watts* [1978] showed that the elastic thickness for the Hawaiian chain agreed with the depth to the  $450^\circ \pm 150^\circ$  C isotherm based on the cooling model of *Parsons and Sclater* [1977]. This result has been supported by numerous studies since [e.g., *Watts and Ribe, 1984, Calmant et al., 1990*]. Figure 5.8, based on the

Figure 5.7. RMS misfit for each region of the Louisville Ridge, using  $\rho_c=2800 \text{ kg m}^{-3}$ , normalized by the standard deviation of the topography within that region. Values are for the nonlinear inversion and show misfit as a percentage of the variation of topography. The circles represent the best-fit value of the elastic thickness and are at the point of maximum curvature. For region J, the point of maximum curvature for  $Te>6 \text{ km}$  was used due to the anomalous kink in the misfit curve at  $Te=5 \text{ km}$  (the resolution limit of this method). These values are listed in Table 5.1 along with the lower and (where possible) upper bounds. Bounds are at  $\pm 5\%$  misfit from the best-fit value. While the lower bound on  $Te$  can be determined for all regions, the upper bound is complicated by the pseudo-asymptotic behavior as  $Te$  grows large. This is due to the negligible change in deflection caused by an emplaced load once the elastic thickness reaches a critical value.

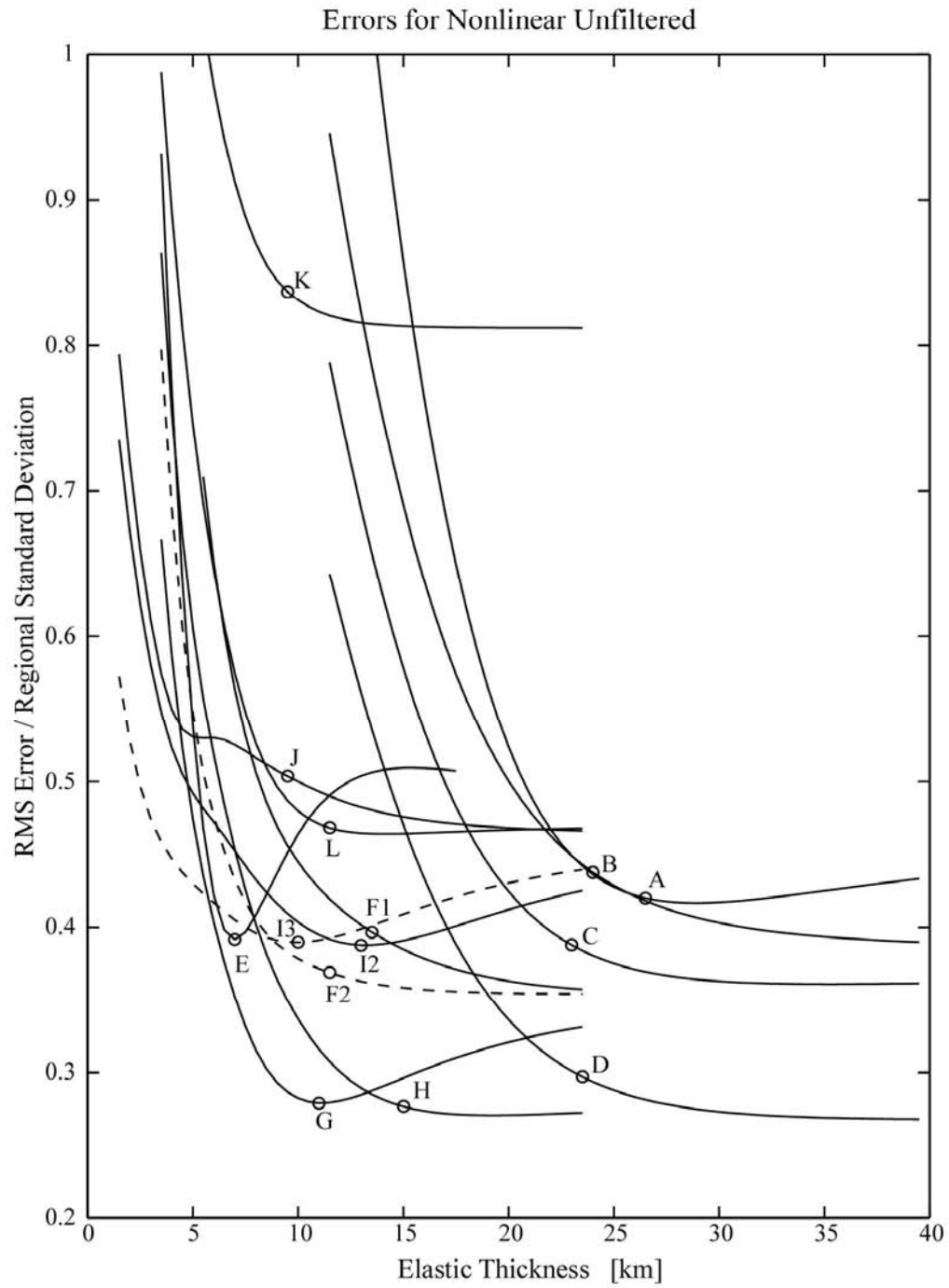


**Table 5.1.** Best Fitting Elastic Thickness Values From *Watts et al.* [1988], *Cazenave and Dominh* [1984], and This Study.

Profile	Expected	Watts	Cazenave 2-D	Cazenave 3-D	Nonlinear			Linear			Region
					Lower	Best	Upper	Lower	Best	Upper	
1	(22)	12.5 - 17.5		21.7 - 23.1	22	26.5		23	27		A
2	(22)	10.0 - 20.0	15.0 - 20.0	18.6 - 21.4	21	24		21.5	24		B
3	(22)	10.0 - 17.0			19.5	24		21.5	24		B
4	(22)	<15.0		12.8 - 18.8	19.5	23		20	23		C
5	(22)	12.5 - 20.0			19.5	23		20	23		C
6	(22)	30.0 - 37.5			19.5	23.5		19.5	23		D
7	(22)				19.5	23.5		19.5	23		D
8	22	34.0 - 41.0	12.0 - 15.0	16.6 - 19.0	6	7	9	6.5	8	12	E
9	22.5				10	13.5		12	15.5		F1
10	22.5	27.5 - 32.5	10.0 - 12.0	16.6 - 17.8	10	13.5		12	15.5		F1
9	22.5				7.5	11.5		9	13		F2
10	22.5	27.5 - 32.5	10.0 - 12.0	16.6 - 17.8	7.5	11.5		9	13		F2
11	23	37.5 - 42.5	12.0 - 15.0	16.6 - 19.0	8	11	22.5	9.5	14		G
12	23	32.5 - 42.5	12.0 - 15.0	16.6 - 19.0	8	11	22.5	9.5	14		G
	23				10.5	15		12	15.5		H
	23				8	13	28	11	14.5		I2
	23				4.5	10	23	8.5	12		I3
	22.5				4	9.5		6.5	10		J
	22				8	9.5		9	9.5		K
	22				8.5	11.5		10	12		L

Ship profile, as used by *Watts et al.* [1988], the regions in this study, including not only the corresponding profiles from the previous studies, but all other ship data available within that area since our technique is not constrained by the requirement of profile alignment perpendicular to the feature. Nonlinear represent bound estimates using the nonlinear approximation for the topographic contribution to gravity, while the Linear represent bounds from the linear approximation as discussed in the text. Best estimate is the point of maximum curvature in Figure 5 for each region. The lower and upper bounds represent  $\pm 5\%$  of the normalized misfit. While our results are in agreement with the general trend of *Cazenave and Dominh's* [1984] 3-D estimate, we find a distinctive jump in elastic thickness at region E. Our results are in general disagreement with values from *Watts et al.* [1988], presumably due to both improved data sets and the inclusion of proper dimensionality.

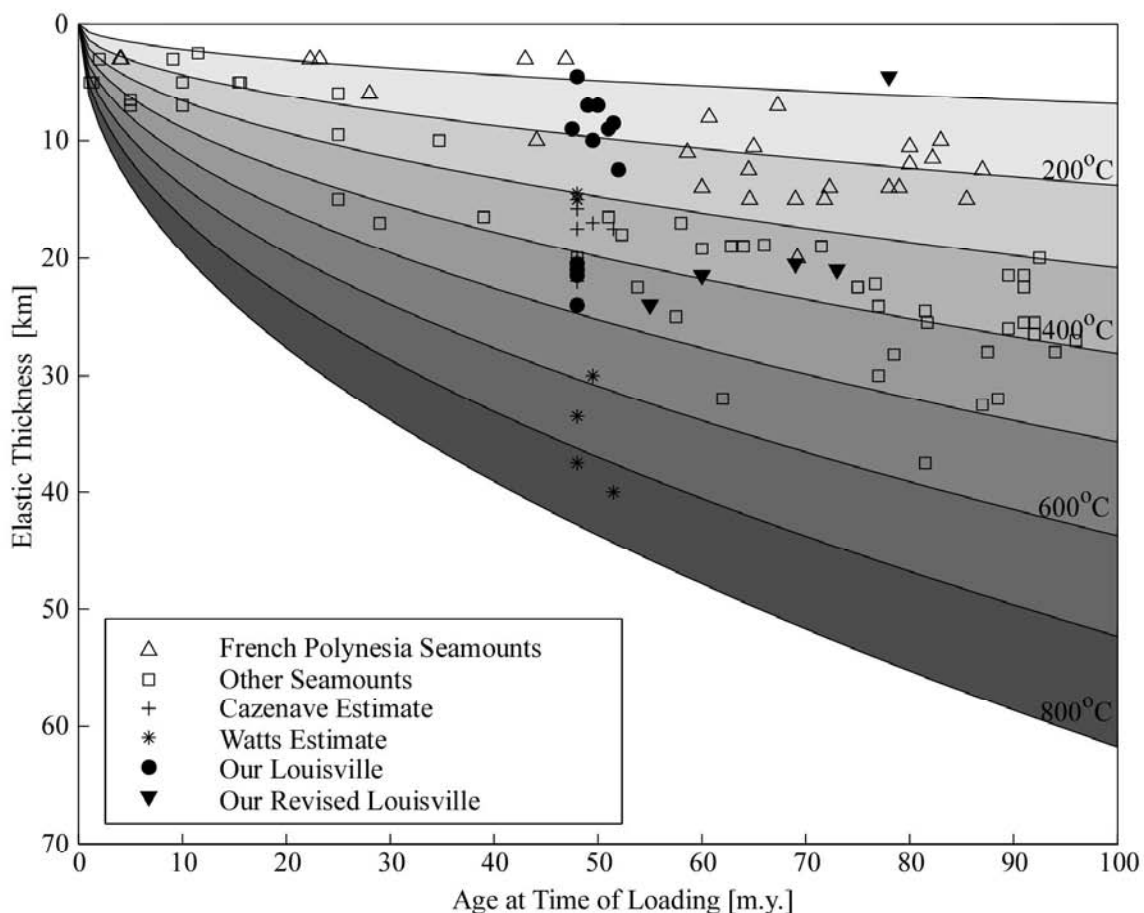


Figure 5.8. Elastic thickness vs. age at time of loading. Data is taken from Figure 1 in *Wessel* [1992] and illustrates the relationship first proposed by *Watts* [1978] which states that the elastic thickness under seamounts follows the  $450^{\circ}\pm 150^{\circ}$  C isotherm based on the cooling plate model of *Parsons and Sclater* [1977]. Although seamounts within French Polynesia (triangles) yield lower-than-expected values, estimates of  $T_e$  from other regions of the world's oceans (squares) fall within these bounds. Solid circles represent our results for the Louisville Ridge. Age at time of loading for Louisville is based on crustal ages taken from *Mueller et al.* [1997] and seamount ages from *Lonsdale* [1988]. North of region E, where data is not available from *Mueller et al.* [1997], age is assumed to increase linearly with distance along the chain. Filled triangles represent our estimates using revised ages approximated from the tentative tectonic history of *Lonsdale* [1997] which places an age discontinuity at  $\sim 39^{\circ}$ S along the ridge.

data in Figure 1 of *Wessel* [1992], shows that, for most seamounts outside of French Polynesia, the elastic thickness does indeed fall between the 300° & 600° C isotherms. The solid circles in Figure 5.8 indicate our estimates for the Louisville region, with crustal ages taken from *Mueller et al.* [1997] and seamount ages from *Lonsdale* [1988]. Along the northwest section (A-D), where age data is not available, we estimated crustal ages based on the assumption of linear age progression with distance along the ridge.

Our elastic thickness estimates for Louisville are lower than expected in the southeastern region (F-L) and are similar to those obtained in French Polynesia. This low  $T_e$  could be due to the presence of the nearby Eltanin Fracture Zone system, which formed prior to the emplacement of the Louisville Ridge [*Watts et al.*, 1988]. However, since the southeastern region of the chain is composed of numerous isolated, circular features, and most of the studies included in Figure 5.8 were performed assuming two-dimensional features, the lower-than-expected elastic thicknesses from our study could also reflect the effect of considering correct dimensionality for these seamounts.  $T_e$  values in the northwest section (A-D) of the Louisville system, when compared to the southern section, are higher than expected, implying that the northern seamounts formed on an older plate than the southern ones and that our assumption of continuous age progression of the plate is not correct. There is an anomaly in the elastic thickness estimates ( $T_e=7$  km) at 39° S, dividing the northern region from the southern.

The location of this  $T_e$  jump is coincident with an anomaly in the gravity field: the signature of the Wishbone Scarp (see Figure 5.1). This scarp is thought

to be a remnant transform fault which had formed from the extinct spreading ridge located at  $\sim 25^\circ$  S, halfway between the Manihiki and Hikurangi plateaus [Lonsdale, 1997]. According to Lonsdale [personal communication, 1999], this remnant boundary could account for a crustal age discontinuity of anywhere from 5 to 25 Ma, which would explain the increased elastic thickness estimates to the northwest of the scarp. Shown in Figure 5.8 (filled triangles) are the revised  $T_e$  vs. age values for the northwestern region based on this tentative new model. These estimates fall very close to the  $400^\circ\text{C}$  isotherm. The 1999 AVON04 cruise by the *R/V Melville* to this region will place better constraints on the crustal age and assist in untangling the complex tectonic history of this area.

Figure 5.9 shows the predicted topography along profile 12 over a seamount in region G ( $43.5^\circ$  S,  $161.5^\circ$  W) using our elastic thickness estimate (11 km, short-dashed), *Cazenave and Dominh's* 3-D result (17.8 km, dotted), and *Watts et al.'s* value (37.5 km, dash-dot) compared with the actual ship bathymetry (solid). Our estimate has the lowest RMS misfit when compared to the actual ship bathymetry (267.43 m), followed by *Cazenave and Dominh* (334.91 m) and *Watts et al.* (393.82 m). Comparison with the band-passed bathymetry yields a much better fit in each case (201.17 m, 299.03 m, and 368.57 m, respectively). While all three methods model the sides of the seamount with similar accuracy, the higher  $T_e$  values do not predict the peak of the seamount as well as our value of 11 km. Inclusion of the nonlinear terms in our inversion did not have a large effect on the elastic thickness estimates, with  $T_e$  values from the linear method exceeding those from the nonlinear by a mean of 0.86 km (median=0.50 km) for unfiltered

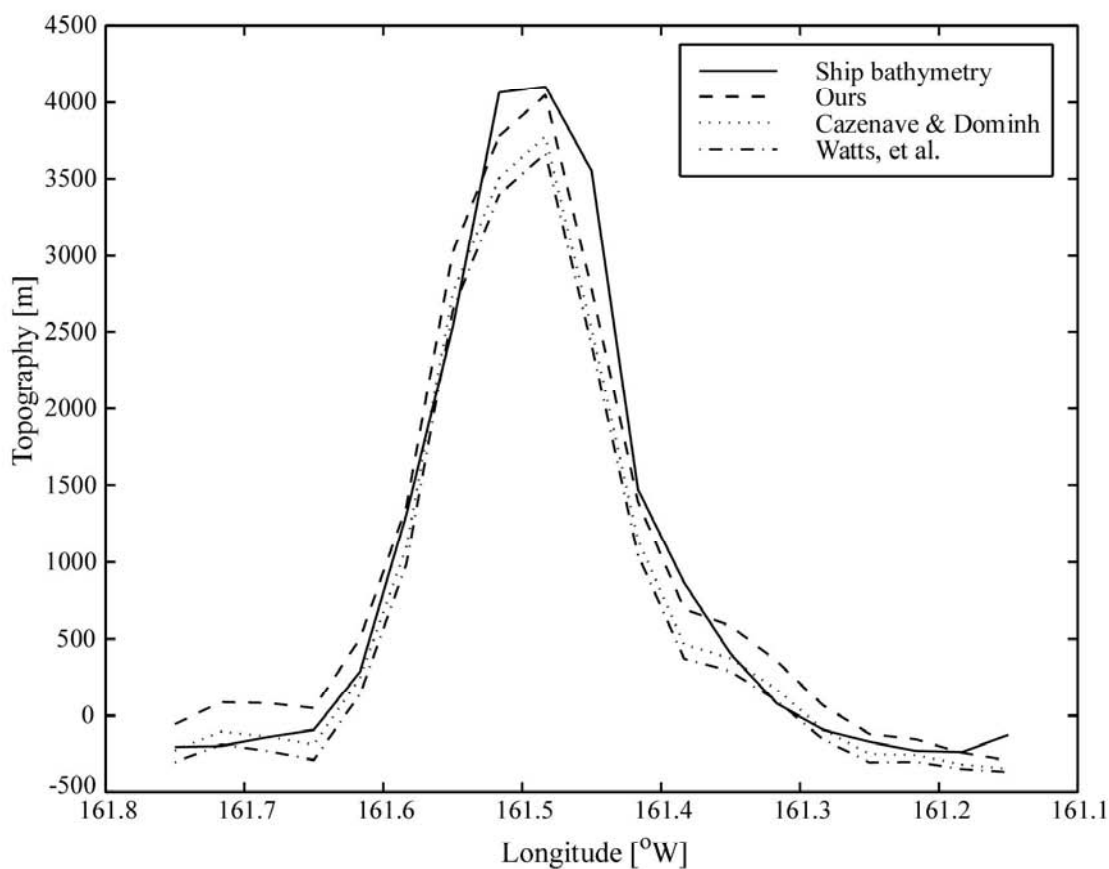


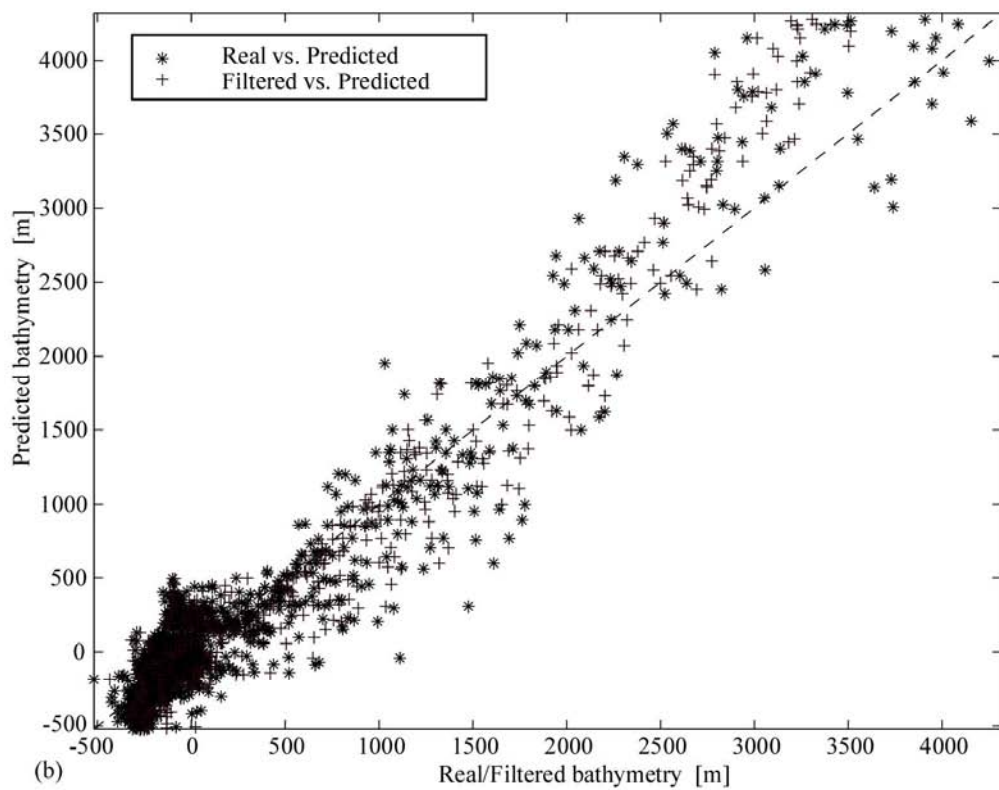
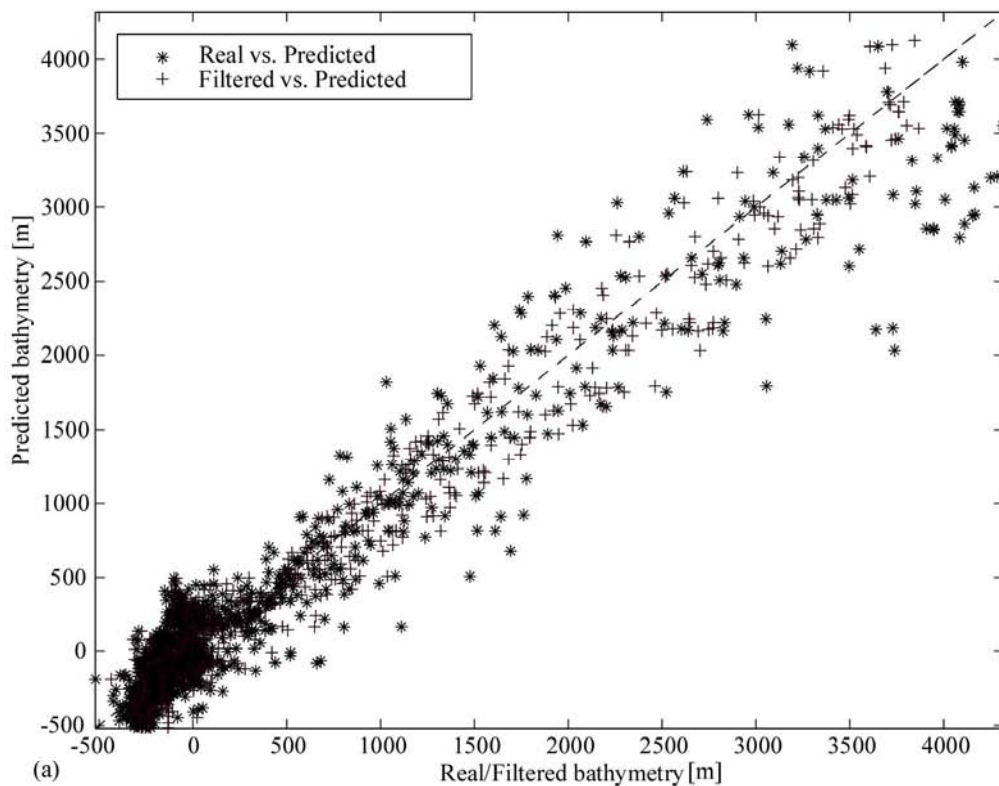
Figure 5.9. Comparison of topographic prediction with ship bathymetry for profile 12 over the seamount in region G. Predicted bathymetry is shown for a range of elastic thickness values: our estimate (11 km, short-dashed), *Cazenave and Dominh's* [1984] (17.8 km, dotted), and *Watts et al.* [1988] (37.5 km, dashed-dot). The actual ship bathymetry (high-pass filtered to remove the mean) is shown as a solid line. RMS misfits between predicted and actual ship bathymetry for this profile are 267.43 m, 334.91 m, and 393.82 m for our study, *Cazenave and Dominh's* [1984], and *Watts et al.* [1988], respectively.

bathymetry and a mean of 0.61 km (median=0.50 km) for filtered bathymetry. The largest discrepancies between the linear and nonlinear estimates (2-3 km) occurred in the middle to southern end of the chain where there are isolated, short-wavelength seamounts on younger, thinner crust than in the northwest.

Figures 5.10a and 5.10b show the correlation between the real bathymetry and the predicted bathymetry for region G, which contains circular, short-wavelength features. In Figure 5.10a, the nonlinear estimate, predictions are well correlated with both the unfiltered bathymetry (stars) as well as with the bandpassed bathymetry (crosses), with the latter case showing an improved match over the former. The same holds true in general for the linear method (Figure 5.10b), but we see that, for large features on the seafloor ( $> 2$  km), the predicted bathymetry is too high, signifying an elastic thickness value which is too low. Thus, the linear method within this region yields a best-fitting  $T_e$  which is  $\sim 3$  km greater than that by the nonlinear method.

As mentioned previously, the correlation improves for the comparison with bandpass-filtered topography, but the actual effect of filtering on the elastic thickness estimate is quite small, with the filtered  $T_e$  greater than the unfiltered value by a mean of 0.61 km (median=0.50 km) for the nonlinear case and a mean of 0.32 km (median=0.25 km) for the linear case. This difference is not dependent on location along the chain.

Figure 5.10. Real vs. predicted bathymetry for region G. Predicted bathymetric values (calculated with  $T_e=11$  km and  $\rho_c=2800$  kg m<sup>-3</sup>) for each point along tracks in the grid (993 points) are plotted vs. their respective ship value. All ship data has been high-pass filtered to remove the mean value of the region. The dashed line indicates the 1:1 exact-fit value. Stars represent high-pass filtered ship bathymetry. Crosses represent ship values that have also been bandlimited as discussed in the text. For both the nonlinear (a) and linear (b) inversions, the bandlimited comparison confines the points closer to the 1:1 line. However, for large features, the linear inversion overpredicts the bathymetry, signifying a  $T_e$  value that is too low. The best-fit value for the linear case in this region is 14 km.



## 5.6 CONCLUSIONS

Including the nonlinear terms in our inversion improved our elastic thickness fit, reducing the minimum rms misfit by 1-30% in areas with a large standard deviation of topography (see Table 5.2). In the southeast region, however, where the variance in depth for the region is not as great, the linear estimate actually had a somewhat lower minimum rms misfit than the nonlinear when the predictions were compared to the unfiltered bathymetry. The resultant effect of including the nonlinear terms in the estimation of elastic thickness was small, with ~1-2 km greater value for the linear estimates than for the nonlinear determinations.

In contrast, the dimensionality of the features in question appears to have a large effect on elastic thickness determination in flexure studies. Since there is a higher percentage of depth soundings over the broad flanks than the narrow peaks, the dimensionality issue was emphasized and could assist in explaining some of the disparity between our study and previous, two-dimensional ones [Cazenave and Dominh, 1984; Watts *et al.*, 1988]. It also provides a viable reason for the low values of elastic thickness in Figure 5.8, when compared with the  $T_e$  vs. age relationship of other Pacific seamounts.

This approach is particularly effective for estimation of elastic thickness in regions where ship tracks do not cross seamount peaks or where data is sparse. However, our elastic thickness estimates should be considered lower bounds rather than absolute values, as the upper limits can be very difficult to define due to the asymptotic behavior of the misfit for large  $T_e$  (see Figure 5.7). Therefore, the best

**Table 5.2.** Minimum rms Misfit Value Within Each Region.

Region	Regional STD		Unfiltered	Filtered	Linear Unfiltered	Linear Filtered	Difference, %*	
	Unfiltered	Filtered					Unfiltered	Filtered
A	1009	952	418	377	421	413	1%	9%
B	948	889	354	306	352	325	-1%	6%
C	953	888	339	254	331	279	-2%	9%
D	1120	1093	299	230	342	299	13%	23%
E	1523	1508	560	544	566	557	1%	2%
F1	1188	1158	418	371	425	390	2%	5%
F2	1188	1144	418	368	455	432	8%	15%
G	1075	1026	293	208	301	275	3 %	24%
H	1067	1037	288	209	337	294	15%	30%
I2	779	716	275	217	251	210	-10%	-3%
I3	779	687	275	209	248	216	-11%	3%
J	600	527	274	182	257	188	-7%	3%
K	247	107	196	128	194	127	-1%	-1%
L	654	569	301	163	272	151	-11%	-8%

\*Percent decrease in minimum rms by including nonlinear terms  $[(\text{linear}-\text{nonlinear})/\text{linear} * 100]$ .

Values represent the minimum misfit for the region for each of the four inversion cases. Percent difference illustrates the decrease in misfit attained by including the nonlinear terms. Misfit is reduced by up to 30% by including the higher-order effect in areas with large variance in topography, but misfit increases by up to 10% in areas where the variance is small.

constraint for a reasonable upper bound would usually be found using the age of the crust at the time of loading

## 5.7 ACKNOWLEDGMENTS

The authors would like to thank Peter Lonsdale for providing information on the crustal ages and spreading history of the Louisville region. We also thank R.L. Parker for his questions and constructive comments on the first draft of this manuscript. Many of the figures were created using the GMT software of *Wessel and Smith* [1991]. Reviews and suggestions by M. Diament, C. Ebinger, and P. Wessel led to a considerably improved final version of this paper. This work was supported by a Department of Defense, National Defense Science and Engineering Graduate Fellowship (S.N. Lyons), National Science Foundation grant #OCE-9521518, and NASA grant #NAG5-5176.

## 5.8 REFERENCES

- Banks, R.J., R.L. Parker, and S.P. Huestis, Isostatic compensation on a continental scale: local versus regional mechanisms, *Geophys. J. R. Astr. Soc.*, 51,431-452, 1977.
- Baudry, N. and S. Calmant, 3-D modelling of seamount topography from satellite altimetry, *Geophys. Res. Lett.*, 18,1143-1146, 1991.
- Calmant, S., J. Francheteau, and A. Cazenave, Elastic layer thickening with age of the oceanic lithosphere: A tool for prediction of the age of volcanoes or oceanic crust, *Geophys. J.*, 100, 59-67, 1990.
- Cazenave, A. and K. Dominh, Geoid heights over the Louisville Ridge (South Pacific), *J. Geophys. Res.*, 89, 11,171-11,179, 1984.

- Dixon, T.H., M. Naraghi, M.K. McNutt, and S.M. Smith, Bathymetric prediction from SEASAT altimeter data, *J. Geophys. Res.*, 88, 1563-1571, 1983.
- Dorman, L.M. and B.T.R. Lewis, Experimental isostasy: 1, Theory of the determination of the Earth's isostatic response to a concentrated load, *J. Geophys. Res.*, 75, 3357-3365, 1970.
- Goodwillie, A.M., Short-wavelength gravity lineations and unusual flexure results at the Puka Puka volcanic ridge system, *Earth Planet. Sci. Lett.*, 136, 297-314, 1995.
- Hébert, H., B. Villemant, C. Deplus, and M. Diament, Contrasting geophysical and geochemical signatures of a volcano at the axis of the Wharton fossil ridge (N-E Indian Ocean), *Geophys. Res. Lett.*, 26, 1053-1056, 1999.
- Kogan, M.G., M. Diament, A. Bulot, and G. Balmino, Thermal isostasy in the South Atlantic Ocean from geoid anomalies, *Earth Planet. Sci. Lett.*, 74, 280-290, 1985.
- Lewis, B.T.R. and L.M. Dorman, Experimental isostasy: 2, An isostatic model for the USA derived from gravity and topographic data, *J. Geophys. Res.*, 75, 3367-3386, 1970.
- Lonsdale, P., A multibeam reconnaissance of the Tonga Trench Axis and its intersection with the Louisville Guyot Chain, *Mar. Geophys. Res.*, 8, 295-327, 1986.
- Lonsdale, P., Geography and history of the Louisville hotspot chain in the southwest Pacific, *J. Geophys. Res.*, 93, 3078-3104, 1988.
- Lonsdale, P., An incomplete geologic history of the southwest Pacific basin, *GSA Abstracts With Programs*, 29:5, 25, 1997.
- Mammericx, J., S.M. Smith, I.L. Taylor, and T.E. Chase, Bathymetry of the South Pacific, *I M R TR-45 Sea Grant Publ. 12*, Scripps Inst. of Oceanogr., La Jolla, Calif., 1974.
- McConathy, D.R. and C.C. Kilgus, The Navy GEOSAT mission: an overview, *Johns Hopkins APL Tech. Digest*, 8, 170-175, 1987.
- McKenzie, D. and C. Bowin, The relationship between bathymetry and gravity in the Atlantic Ocean, *J. Geophys. Res.*, 81, 1903-1915, 1976.
- McNutt, M.K. and R.L. Parker, Isostasy in Australia and the evolution of the compensation mechanism, *Science*, 199, 773-775, 1978.

- McNutt, M.K., Compensation of oceanic topography: an application of the response function technique to the Surveyor area, *J. Geophys. Res.*, *84*, 7589-7598, 1979.
- Moore, J.G., Relationship between subsidence and volcanic load, Hawaii, *Bull. Volcanol.*, *34*, 562-576, 1970.
- Mueller, R.D., W.R. Roest, J.-Y. Royer, L.M. Gahagan, and J.G. Sclater, Digital isochrons of the world's ocean floor, *J. Geophys. Res.*, *102*, 3211-3214, 1997.
- Oldenburg, D.W., The inversion and interpretation of gravity anomalies, *Geophysics*, *39*, 526-536, 1974.
- Parker, R.L., The rapid calculation of potential anomalies, *Geophys. J. R. Astr. Soc.*, *31*, 447-455, 1973.
- Parsons, B. and J.G. Sclater, An analysis of the variation of ocean floor bathymetry and heat flow with age, *J. Geophys. Res.*, *82*, 803-827, 1977.
- Ribe, N.M., On the interpretation of frequency response functions for oceanic gravity and bathymetry, *Geophys. J. R. Astr. Soc.*, *70*, 273-294, 1982.
- Ribe, N.M. and A.B. Watts, The distribution of intraplate volcanism in the Pacific Ocean basin: a spectral approach, *Geophys. J. R. Astr. Soc.*, *71*, 333-362, 1982.
- Sandwell, D.T., Thermomechanical evolution of oceanic fracture zones, *J. Geophys. Res.*, *89*, 11,401-11,413, 1984.
- Sandwell, D. T., E.L. Winterer, J. Mammert, R.A. Duncan, M.A. Lynch, D. Levitt, and C. Johnson, Evidence for diffuse extension of the Pacific Plate from Pukapuka Ridges and cross-grain gravity lineations, *J. Geophys. Res.*, *100*, 15,087-15,099, 1995.
- Sandwell, D.T. and W.H.F. Smith, Marine gravity anomaly from Geosat and ERS-1 satellite altimetry, *J. Geophys. Res.*, *102*, 10,039-10,054, 1997.
- Sichoix, L. and A. Bonneville, Prediction of bathymetry in French Polynesia constrained by shipboard data, *Geophys. Res. Lett.*, *23*, 2469-2472, 1996.
- Smith, W.H.F. and D.T. Sandwell, Bathymetric prediction from dense satellite altimetry and sparse ship bathymetry, *J. Geophys. Res.*, *99*, 21,803-21,824, 1994.

- Smith, W.H.F. and D.T. Sandwell, Global seafloor topography from satellite altimetry and ship depth soundings, *Science*, 277, 1956-1962, 1997.
- Suyenaga, W., Isostasy and flexure of the lithosphere under the Hawaiian Islands, *J. Geophys. Res.*, 84, 5599-5604, 1979.
- Vening Meinesz, F.A., Gravity over the Hawaiian Archipelago and over the Madeira area: Conclusions about the earth's crust, *Proc. Kon. Ned. Akad. Wetensch.*, 44, 1, 1941.
- Walcott, R.I., Flexure of the lithosphere at Hawaii, *Tectonophysics*, 9,435-446, 1970.
- Watts, A.B. and J.R. Cochran, Gravity anomalies and flexure of the lithosphere along the Hawaiian-Emperor Seamount Chain, *Geophys. J. Roy. Astr. Soc.*, 39, 119-141, 1974.
- Watts, A.B., J.R. Cochran, and G. Selzer, Gravity anomalies and flexure of the lithosphere: A three-dimensional study of the Great Meteor seamount, northeast Atlantic, *J. Geophys. Res.*, 80, 1391-1398, 1975.
- Watts, A.B., An analysis of isostasy in the world's oceans, 1, Hawaiian-Emperor seamount chain, *J. Geophys. Res.*, 83, 5989-6004, 1978.
- Watts, A.B., On geoid heights derived from Geos-3 altimeter data and flexure along the Hawaiian-Emperor seamount chain, *J. Geophys. Res.*, 84, 3817-3826, 1979.
- Watts, A.B., J.H. Bodine, and N.M. Ribe, Observations of flexure and the geological evolution of the Pacific Ocean basin, *Nature*, 283, 532-537, 1980.
- Watts, A.B., J.K. Weissel, R.A. Duncan, and R.L. Larson, Origin of the Louisville Ridge and its relationship to the Eltanin Fracture Zone system, *J. Geophys. Res.*, 93, 3051-3077, 1988.
- Watts, A.B. and U.S. tenBrink, Crustal structure, flexure, and subsidence history of the Hawaiian islands, *J. Geophys. Res.*, 89, 10,473-10,500, 1989.
- Wessel, P. and W.H.F. Smith, Free software helps map and display data, *EOS Trans. AGU, Fall Meet. Suppl.*, 72, 445-446, 1991.
- Wessel, P., Thermal stresses and the bimodal distribution of elastic thickness estimates of the oceanic lithosphere, *J. Geophys. Res.*, 97, 14,177-14,193, 1992.

Wessel, P., A reexamination of the flexural deformation beneath the Hawaiian Islands, *J. Geophys. Res.*, 98, 12,177-12,190, 1993.

This chapter, in full, is a reprint of the material as it appears in the *Journal of Geophysical Research*, Lyons, Suzanne; Sandwell, David; Smith, Walter, 2000.

The dissertation author was the primary investigator and author of this paper and the co-authors directed and supervised the research.

## Epilogue

The Road goes ever on and on  
Down from the door where it began.  
Now far ahead the Road has gone,  
And I must follow, if I can,  
Pursuing it with eager feet,  
Until it joins some larger way  
Where many paths and errands meet.  
And whither then? I cannot say.

The Road goes ever on and on  
Out from the door where it began.  
Now far ahead the Road has gone,  
Let others follow it who can!  
Let them a journey new begin,  
But I at last with weary feet  
Will turn towards the lighted inn,  
My evening-rest and sleep to meet.

- J.R.R. Tolkein, *The Lord of the Rings*